## Enhancing visualization of gastrointestinal tumors

Molecular targets and tracers for intraoperative optical imaging

## Enhancing visualization of gastrointestinal tumors

Molecular targets and tracers for intraoperative optical imaging

Ruben D. Houvast

### © R.D. Houvast, 2025

### DESIGN

Caroline de Lint, Den Haag (caro@delint.nl)

### **COVER IMAGE**

Hannah Bremer

### FINANCIAL SUPPORT

Publication of this thesis was financially supported by the Centre for Human Drug Research (CHDR) foundation in Leiden, the Netherlands.

All rights reserved. No part from this thesis may be reproduced, distributed or transmitted in any form or by any means, without prior written permission of the author.

### Enhancing visualization of gastrointestinal tumors

Molecular targets and tracers for intraoperative optical imaging

### Proefschrift

ter verkrijging van de graad van doctor aan de Universiteit Leiden, op gezag van rector magnificus prof. dr. ir. H. Bijl, volgens besluit van het college voor promoties te verdedigen op dinsdag 4 november 2025 klokke 14:30 uur

> door Ruben Douwe Houvast geboren te Zwolle in 1996

### **Promotores**

Prof. dr. J. Burggraaf Prof. dr. A.L. Vahrmeijer

### Co-promotor

Dr. P.J.K. Kuppen

### **Promotiecommissie**

Prof. dr. J.E. van Hooft, MBA Prof. dr. L.F. de Geus-Oei Prof. dr. S. Kruijff – UMCG Dr. S. Keereweer – Erasmus MC Chapter 1 General introduction and thesis outline – 9

PART I Evaluation of biomarkers for molecular imaging of gastrointestinal tumors

Chapter 2 Targeting glycans and heavily glycosylated proteins for tumor imaging – 21

Chapter 3 An immunohistochemical evaluation of tumor-associated glycans and mucins as targets for molecular imaging of pancreatic ductal adenocarcinoma – 49

**Chapter 4** Targets for molecular imaging of gastric adenocarcinoma and metastases: an immunohistochemical evaluation – 71

Chapter 5 Prediction of biomarker expression on primary pancreatic ductal adenocarcinoma tissues using fine-needle biopsies: paving the way for a patient-tailored molecular imaging approach – 93

PART II Preclinical evaluation of novel tracers for near-infrared fluorescence and photoacoustic imaging of gastrointestinal tumors

**Chapter 6** Glycan-based near-infrared fluorescent (NIRF) imaging of gastrointestinal tumors: a preclinical proof-of-concept *in vivo* study – 115

Chapter 7 Preclinical evaluation of glycan-targeting monoclonal antibodies for bimodal near-infrared fluorescence and photoacoustic imaging of gastrointestinal cancers – 135

Chapter 8 Preclinical evaluation of EpCAM-binding designed ankyrin repeat proteins (DARPins) as targeting moieties for bimodal near-infrared fluorescence and photoacoustic imaging of cancer – 161

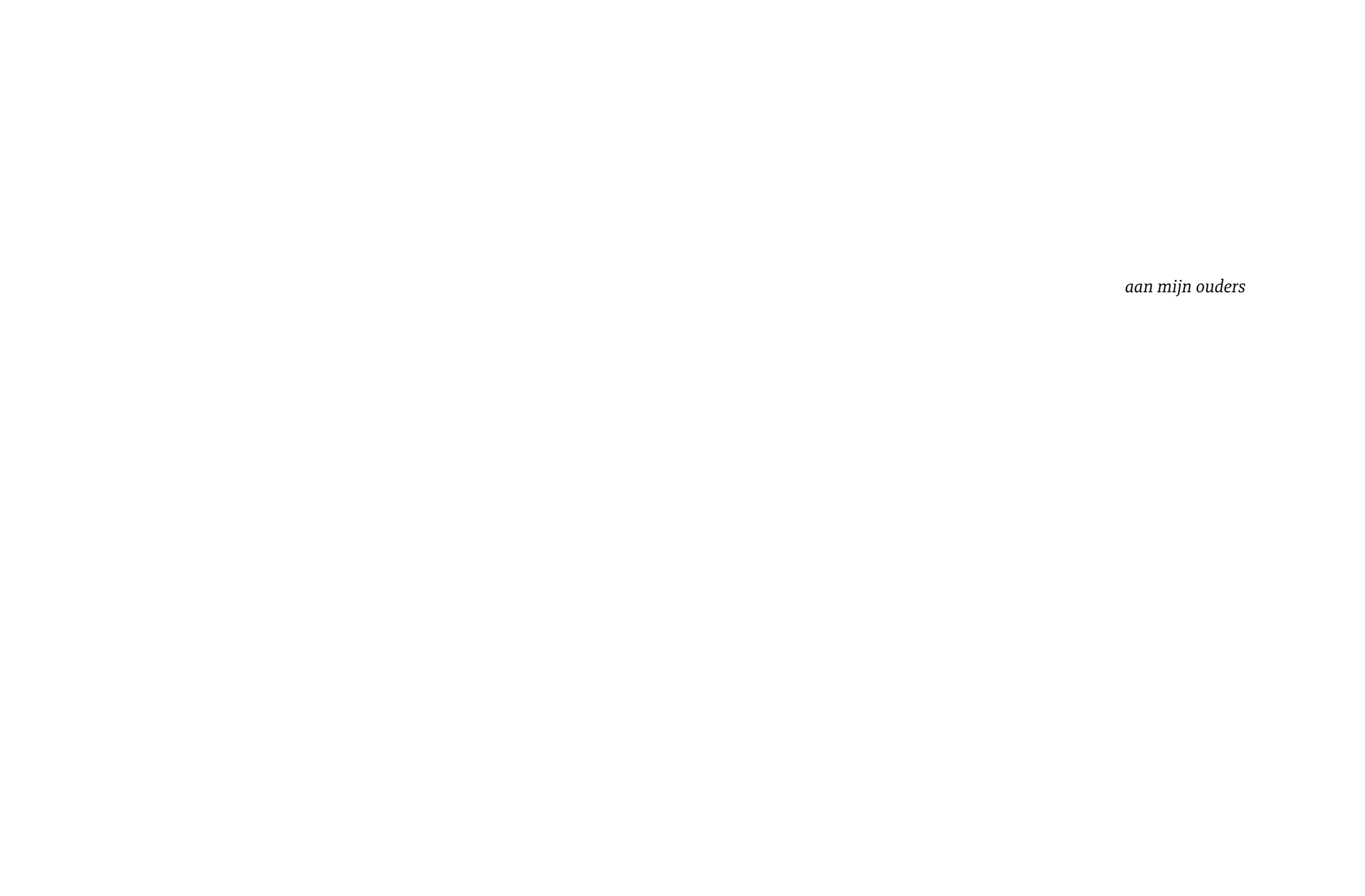
PART III Summary, general discussion and future perspectives

Chapter 9 Summary – 187

**Chapter 10** General discussion and future perspectives – 195

### **Appendices**

Nederlandse samenvatting – 212 List of publications – 218 Curriculum vitae – 221 Dankwoord – 222



### **CHAPTER 1**

General introduction and thesis outline



Cancer is a leading cause of death globally, accounting for over 10 million deaths, and with 19 million new cases annually worldwide, it is likely to be a main driver of death in the foreseeable future. Gastrointestinal cancers, including esophageal, gastric, pancreatic and colorectal cancer are among the most prevalent cancer types and together account for approximately 20% of all cancer cases. 1,2 Although arising from related origins, clinical features of these cancer type vary greatly. For instance, the 5-year overall survival rate for colorectal cancer in developed countries is about 65%, whereas pancreatic cancer has a 5-year survival rate of approximately 10%.<sup>3,4</sup> Recent advances within the therapeutic arena, including the increased application of neoadjuvant chemo(radio)therapy (NAT) and emergence of novel targeted therapies, have significantly improved cancer prognosis.<sup>3,5-7</sup> Nonetheless, achieving local control through radical surgery remains the foundation of curative cancer treatment. Preoperatively, accurate staging is pivotal to assess resectability of tumors and adequately identify patients that may benefit from surgery. However, several diagnostic and surgical challenges are encountered that must be addressed to optimize multidisciplinary treatment of gastrointestinal cancers.

### Diagnostic challenges

Accurate preoperative staging is pivotal to assess resectability of tumors and adequately identify candidates for surgery. Current diagnostic work-up of gastrointestinal cancers consists of endoscopy-guided biopsy, followed by staging using computed tomography (CT) or magnetic resonance imaging (MRI; rectal and pancreatic cancer), and in some cases diagnostic laparoscopy (gastric cancer and pancreatic cancer). For pancreatic cancer, endoscopic ultrasound (EUS)-guided fineneedle biopsy (FNB) may be used for histological diagnosis.8 Despite the increased application of [18F]Fluorodeoxyglucose (FDG)-positron emission tomography (PET) combined with CT, its routine employment for preoperative staging in these cancer types remains controversial.<sup>9,10</sup> Each imaging modality has its limitations for accurate tumor detection. For instance, CT-imaging, has reasonable sensitivity of 83-100% and approximately 60% for T-staging and N-staging in gastric cancer, respectively, while detection of peritoneal metastases is limited at 23-76%. 11-13 Moreover, ~20% of gastric cancers do not show FDG-PET avidity. 14 For pancreatic cancer, 20-47% of patients who are eligible for surgery based on preoperative imaging, have irresectable disease at the time of surgery. 15,16 Approximately 7% of resections for suspected pancreatic cancer are performed for benign diseases, including chronic pancreatitis, and are, therefore, redundant.<sup>17</sup> Erroneous tumor staging can result in unnecessary resections or biopsies, additional imaging procedures, and futile administration of systemic therapy, thereby increasing patient burden and healthcare costs. Tumor-targeted PET imaging, thus directed at a molecular target expressed in the tumor, has emerged as a promising technique that could enhance detection of gastrointestinal cancers and response monitoring after (neo)adjuvant therapy.<sup>9,18</sup>

### Surgical challenges

Intraoperatively, surgeons rely on visual inspection and tactile feedback to delineate cancerous tissue and avoid critical anatomical structures, such as nerves and the ureters. 19,20 Although the advent of minimally invasive surgical techniques, such as laparoscopy and robotics, has decreased postoperative morbidity and mortality, it deprived the ability of surgeons to use tactile information.<sup>21</sup> Moreover, particularly after NAT, tumor tissue may be surrounded by fibrotic and necrotic tissue, which cannot be straightforwardly discriminated. Inadequate estimation of tumor localization may lead to irradical (R1) resections, which increases local recurrence rates for most tumor types and negatively impacts patient survival.<sup>22-25</sup> For instance, tumor-positive margins are reported in up to 80% of patients in pancreatic cancer, while this is 7% in gastric cancer. 26,27 Also, irradical resections may necessitate adjuvant therapy, causing additional burden for patients. Efforts to address these challenges have resulted in the development and clinical introduction of real-time intraoperative imaging techniques that can guide surgeons during tumor resection. Near-infrared fluorescence (NIRF) imaging is a promising technique aimed at achieving this endeavor.

### Near-infrared fluorescence (NIRF) imaging

NIRF imaging, also referred to as fluorescence-guided surgery, is an optical imaging method that provides real-time intraoperative guidance to surgeons for identification of tissue of interest.<sup>28</sup> This technique typically employs an exogenous contrast agent that emits light in the near-infrared red (NIR) region (700–900 nm), which is visualized through a dedicated NIR camera system. As NIR light suffers less from absorption and scattering compared to visible light (~380-700 nm), it travels further through tissues, namely up to approximately 7 mm, and has lower autofluorescence in tissue.<sup>28</sup> These characteristics increase the contrast between the NIR signal and surrounding (untargeted) tissue. Notably, NIR light is not visible to the human eye and does therefore not interfere with the surgical field. Simplified, NIRF imaging systems consist of a white light camera, a NIR light source which excites a fluorophore and a NIRF camera. Several NIRF camera systems for open surgery, laparoscopy or robotics are currently available on the market.<sup>29</sup>

11

Depending on the application and tissue of interest, NIRF contrast agents can be either untargeted or targeted. Untargeted contrast agents, such as U.S. Food and Drug Administration/European Medicines Agency-approved indocyanine green (ICG), are used for perfusion assessment and, due to its hepatic clearance, for visualization of biliary tree anatomy or hepatic metastases. On Targeted NIRF contrast agents typically consist of fluorophores conjugated to targeting moieties that specifically bind a molecular target, making them more suitable for tumor imaging. Examples of targeting moieties include monoclonal antibodies (mAbs), antibody fragments (e.g. Fab, F(ab')2 or scFvs), nanobodies, protein scaffolds, peptides and classical small molecules. On the circulation and bind avidly to their target of interest, while unbound tracer is cleared rapidly from the systemic circulation. This reduces the background signal and increases the contrast between regions bound and unbound by the tracer, facilitating the detection of targeted structures.

The applications of (targeted) NIRF imaging tracers in gastrointestinal cancer surgery can be broadly subdivided into 1) assessment of tumor-free resection margin and 2) detection of clinically occult disease, including nodal involvement or distant metastases. Practically, the second application could be particularly employed during diagnostic laparoscopy. Other applications of particular interest, but beyond the scope of this thesis are 3) identification of critical structures, such as nerves or ureters, and 4) assessment of tissue perfusion.<sup>20,29,32,33</sup>

Although NIRF may allow excellent visualization of superficially located lesions, it may be supplemented with photoacoustic imaging for imaging of deeper lesions. Photoacoustic (PA) imaging utilizing high-resolution ultrasound (US) detects acoustic waves generated by the thermoelastic effect experienced by NIRF dyes when subjected to a nanosecond pulsed NIR laser.<sup>34</sup> PA imaging offers superior spatial resolution compared to optical NIRF imaging and can penetrate tissues to a depth of up to 7 cm. Integrating 3D data from PA imaging with NIRF imaging allows for more effective imaging of tumor lesions. Practically, a tumor could be identified and approached using the 3D image of PA imaging, followed by NIRF imaging-guided tumor resection and assessment of tumor-free margins by overlaying the surgical field (white light) with real-time fluorescence. Moreover, this approach could be applied during intraoperative staging or intraoperative ultrasound as detection of deeper-located lesions not visible using with the naked eye or using fluorescence, such as deeply seated hepatic metastases.<sup>35,36</sup>

### Challenges in targeted molecular imaging of tumors: biomarkers

As outlined above, molecular imaging techniques, such as targeted PET and fluorescence-guided surgery may address current diagnostic and surgical challenges in these cancer types. Although technically distinct, similar (preclinical) challenges are encountered for both techniques.

The appropriate selection and alignment of an imaging biomarker for the respective tumor type is a key prerequisite for successful tumor visualization. An ideal molecular target is abundantly and homogenously expressed on the cell membrane of all tumor cells in all patients, including lymph node and distant metastases, with absent expression in healthy surrounding tissue.<sup>37</sup> Moreover, in the era of increased application of NAT, tumor expression should remain present in remaining cancerous tissue after NAT and is absent in benign conditions, such as chronic inflammation. However, the targets of NIRF imaging tracers evaluated in phase 3 clinical trials, namely CEACAM5 (SGM-101, colorectal cancer) and cathepsins (LUMo15, breast cancer) appear to have limitations, including intra- and intertumoral heterogeneity and expression on non-malignant tissue. 32,38-41 This is also true for integrin  $\alpha v \beta_6$ , epidermal growth factor receptor (EGFR), epithelial cell adhesion molecule (EpCAM), growth-factor receptor-2 (HER-2), mesothelin and vascular endothelial growth factor (VEGF), all considered promising biomarkers for molecular imaging in gastrointestinal cancers. Several critical gaps in knowledge regarding imaging biomarkers persist that should be addressed to advance molecular imaging in gastrointestinal cancers.

Firstly, it seems critical to simultaneously look beyond the current molecular target arsenal and explore novel, perhaps non-protein-based molecular targets. Examples of two promising classes of such biomarkers may be tumor-associated carbohydrates also known as glycans, and heavily glycosylated proteins, including mucins. Aberrant glycosylation of proteins and lipids represents a major characteristic of cancer and glycan-targeting, which is currently in its infancy, may have advantages over protein targeting.

Secondly, for most of the current biomarkers, the differential expression between tumor and healthy (surrounding) tissues is not well understood, while it is crucial information to establish their potential for molecular imaging. Moreover, their expression in cancerous tissue after NAT and in lymph node and distant metastases, also key determinants of their molecular imaging potential, remain understudied.

Thirdly, as the targets of the emerging molecular imaging tracers are not expressed in all patients, it could be beneficial to preoperatively screen for biomarker expression, for instance using biopsy material routinely obtained for histological diagnosis. However, the predictive value of biomarker expression in biopsies for primary tumor expression is not studied for most biomarkers, especially not after administration of NAT.

The thesis aims to address these challenges by further exploring the expression of known and lesser-known targets that are promising for molecular imaging in gastrointestinal cancers, with a focus on pancreatic and gastric cancer. Once the suitability of such biomarkers for molecular imaging in gastrointestinal cancers is established, further preclinical evaluation of tracers targeting these antigens is warranted. This is also demonstrated in this thesis, focusing on bimodal NIRF/PA imaging. Another challenge addressed in this thesis relates to the targeting moiety of an imaging tracer.

### Challenges in targeted molecular imaging of tumors: targeting moieties

A second topic of research in targeted molecular imaging involves the targeting moiety incorporated into a molecular imaging tracer. As outlined before, a wide array of targeting moieties is available, each with its strengths and weaknesses for molecular imaging. The Mass (~150 kDa) are the most frequently used targeting moiety for molecular imaging, but, despite their high specificity, affinity and stability, mAbs have limitations such as a long serum half-life and reduced tumor penetration due their size. Smaller-sized tracers, such as antibody-fragments or peptides provide a shorter time window between injection and imaging but may be less stable and require higher affinities to achieve similar tumor uptake. It is pivotal to take such characteristics into account when selecting the appropriate targeting moiety. After all, two differently designed molecular imaging tracers directed at the same molecular target can provide substantially different results *in vivo*.

Novel classes of targeting vehicles have been introduced that may offer an improved comprise regarding the advantages and disadvantages of targeting moieties. One example are Designed Ankyrin Repeat Proteins (DARPins; ~14 kDa).<sup>51</sup> Their high affinity, thermodynamic stability, solubility, low aggregation tendency, and easy engineerability have made DARPins a promising tumortargeting alternative to mAbs.<sup>52</sup> However, the potential of DARPins as targeting moieties for molecular imaging in gastrointestinal cancer is underexplored. This thesis provides the first preclinical evaluation of such tracers, focusing on fluorescence-guided surgery.

### THESIS OUTLINE

This thesis aims to address diagnostic and surgical challenges for gastrointestinal intestinal cancers by expanding knowledge on biomarkers and novel NIRF/PA imaging tracers that are promising for imaging in gastrointestinal cancers, with a focus on pancreatic and gastric cancer. Ultimately, this knowledge provides the preclinical groundwork for further development, optimization, clinical translation and employment of molecular imaging tracers for gastrointestinal cancers. Part I of this thesis delves into the evaluation of novel and existing biomarkers for molecular imaging in gastrointestinal cancers. Chapter 2 provides a background on the current evidence on targeting of tumor-associated glycans and heavily glycosylated proteins for tumor imaging. Chapter 3 evaluates the potential of several glycans and heavily glycosylated proteins identified as promising in Chapter 1 for molecular imaging of pancreatic cancer. Chapter 4 evaluates the potential of several current imaging biomarkers, all promising for imaging of gastrointestinal cancers, for gastric cancer. **Chapter 5** aims to evaluate whether preoperative screening for the most optimal molecular imaging biomarkers is feasible by comparing the expression of several glycan- and protein-based biomarkers between FNB and primary tumor tissues of pancreatic cancer. While the findings of Part I of this thesis may be extrapolatable to both NIRF and targeted PET imaging, Part II focuses on NIRF/PA imaging of gastrointestinal cancers, in which Chapter 6 and 7 present the preclinical evaluation of glycan-based tracers for bimodal NIRF/PA imaging of gastrointestinal cancers and Chapter 8 provides the first preclinical evaluation on DARPins as targeting moieties for bimodal NIRF/PA imaging of gastrointestinal cancers.

### REFERENCES

- 1 Bray F, Laversanne M, Sung H, Ferlay J, Siegel RL, Soeriomataram I. et al. Global cancer statistics 2022: GLOBOCAN estimates of incidence and mortality worldwide for 36 cancers in 185 countries. CA Cancer I Clin. 2024;74(3):229-63.
- 2 Xie Y. Shi L. He X. Luo Y. Gastrointestinal cancers in China, the USA, and Europe. Gastroenterol Rep (Oxf). 2021;9(2):91-104.
- 3 Hemminki K, Försti A, Hemminki A. Survival in colon and rectal cancers in Finland and Sweden through 50 years. BMJ Open Gastroenterol. 2021;8(1).
- 4 Mizrahi JD, Surana R, Valle JW, Shroff RT. Pancreatic cancer. The Lancet. 2020;395(10242):2008-20.
- 5 Versteijne E, van Dam JL, Suker M, Janssen QP, Groothuis K, Akkermans-Vogelaar JM, et al. Neoadjuvant Chemoradiotherapy Versus Upfront Surgery for Resectable and Borderline Resectable Pancreatic Cancer: Long-Term Results of the Dutch Randomized PREOPANC Trial. J Clin 19 Vahrmeijer AL, Frangioni JV. Seeing the invisible during Oncol. 2022:40(11):1220-30.
- 6 Noordman BJ, Verdam MGE, Lagarde SM, Hulshof M, van Hagen P. van Berge Henegouwen MI, et al. Effect of Neoadjuvant Chemoradiotherapy on Health-Related Ouality of Life in Esophageal or Junctional Cancer: Results From the Randomized CROSS Trial, I Clin Oncol. 2018;36(3):268-75.
- 7 Rha SY, Oh DY, Yañez P, Bai Y, Ryu MH, Lee J, et al. Pembrolizumab plus chemotherapy versus placebo plus chemotherapy for HER2-negative advanced gastric cancer (KEYNOTE-859): a multicentre, randomised, double-blind, phase 3 trial. Lancet Oncol. 2023;24(11):1181-95.
- 8 Iqbal S, Friedel D, Gupta M, Ogden L, Stavropoulos SN. Endoscopic-ultrasound-guided fine-needle aspiration and the role of the cytopathologist in solid pancreatic lesion diagnosis. Patholog Res Int. 2012;2012;317167.
- van Dam MA, Vuijk FA, Stibbe IA, Houvast RD, Luelmo SAC, Crobach S, et al. Overview and Future Perspectives on Tumor-Targeted Positron Emission Tomography and Fluorescence Imaging of Pancreatic Cancer in the Era of Neoadjuvant Therapy. Cancers. 2021;13(23):6088.
- 10 Howard BA, Wong TZ. 18F-FDG-PET/CT Imaging for Gastrointestinal Malignancies. Radiol Clin North Am. 2021;59(5):737-53.
- 11 Borggreve AS, Goense L, Brenkman HJF, Mook S, Meijer GJ, Wessels FJ, et al. Imaging strategies in the management of gastric cancer: current role and future potential of MRI. 27 Jiang Z, Liu C, Cai Z, Shen C, Yin Y, Yin X, et al. Impact of Br J Radiol. 2019;92(1097):20181044.
- 12 Giandola T, Maino C, Marrapodi G, Ratti M, Ragusi M, Bigiogera V, et al. Imaging in Gastric Cancer: Current Practice and Future Perspectives. Diagnostics (Basel). 2023;13(7).
- 13 Kim SH, Kim JJ, Lee JS, Kim SH, Kim BS, Maeng YH, et al. Preoperative N staging of gastric cancer by stomach protocol computed tomography. J Gastric Cancer. 2013;13(3):149-56.
- 14 Gertsen EC, Brenkman HJF, van Hillegersberg R, van Sandick JW, van Berge Henegouwen MI, Gisbertz SS, et al. 18F-Fludeoxyglucose-Positron Emission Tomography/ Computed Tomography and Laparoscopy for Staging of Locally Advanced Gastric Cancer: A Multicenter

- Prospective Dutch Cohort Study (PLASTIC). JAMA Surg. 2021;156(12):e215340.
- 15 Versteijne E, Vogel JA, Besselink MG, Busch ORC, Wilmink JW, Daams JG, et al. Meta-analysis comparing upfront surgery with neoadjuvant treatment in patients with resectable or borderline resectable pancreatic cancer. Br I Surg. 2018;105(8):946-58.
- 16 Papalezova KT, Tyler DS, Blazer DG, 3rd, Clary BM, Czito BG, Hurwitz HI, et al. Does preoperative therapy optimize outcomes in patients with resectable pancreatic cancer? I Surg Oncol. 2012;106(1):111-8.
- 17 Gerritsen A, Molenaar IQ, Bollen TL, Nio CY, Dijkgraaf MG, van Santvoort HC, et al. Preoperative characteristics of patients with presumed pancreatic cancer but ultimately benign disease: a multicenter series of 344 pancreatoduodenectomies. Ann Surg Oncol. 2014;21(12):3999-4006.
- 18 Arçay Öztürk A, Flamen P. FAP-targeted PET imaging in gastrointestinal malignancies: a comprehensive review. Cancer Imaging. 2023;23(1):79.
- surgery. Br J Surg. 2011;98(6):749-50.
- 20 Lauwerends LJ, van Driel P, Baatenburg de Jong RJ, Hardillo IAU, Kolienovic S. Puppels G. et al. Real-time fluorescence imaging in intraoperative decision making for cancer surgery, Lancet Oncol, 2021;22(5):e186-e95.
- 21 Sun V, Fong Y. Minimally Invasive Cancer Surgery: Indications and Outcomes. Semin Oncol Nurs. 2017;33(1):23-36.
- 22 Gertler R, Richter J, Stecher L, Nitsche U, Feith M. What to do after R1-resection of adenocarcinomas of the esophagogastric junction? J Surg Oncol. 2016;114(4):428-33.
- 23 Hirata Y, Agnes A, Estrella JS, Blum Murphy M, Das P, Minsky BD, et al. Clinical Impact of Positive Surgical Margins in Gastric Adenocarcinoma in the Era of Preoperative Therapy. Ann Surg Oncol. 2023;30(8):4936-45.
- 24 Rau BM, Moritz K, Schuschan S, Alsfasser G, Prall F, Klar E. R1 resection in pancreatic cancer has significant impact on long-term outcome in standardized pathology modified for routine use. Surgery. 2012;152(3 Suppl 1):S103-11.
- 25 Khan MA, Hakeem AR, Scott N, Saunders RN, Significance of R1 resection margin in colon cancer resections in the modern era. Colorectal Dis. 2015;17(11):943-53.
- 26 Tummers WS, Groen JV, Sibinga Mulder BG, Farina-Sarasqueta A, Morreau J, Putter H, et al. Impact of resection margin status on recurrence and survival in pancreatic cancer surgery. Br J Surg. 2019;106(8):1055-65.
- Surgical Margin Status on Survival in Gastric Cancer: A Systematic Review and Meta-Analysis. Cancer Control. 2021;28:10732748211043665.
- 28 Vahrmeijer AL, Hutteman M, van der Vorst JR, van de Velde CJH, Frangioni JV. Image-guided cancer surgery using near-infrared fluorescence. Nature reviews Clinical oncology. 2013;10(9):507-18.
- 29 Mieog JSD, Achterberg FB, Zlitni A, Hutteman M, Burggraaf J, Swijnenburg R-J, et al. Fundamentals and developments in fluorescence-guided cancer surgery. Nature Reviews Clinical Oncology. 2021.
- 30 van Manen L, Handgraaf HJM, Diana M, Dijkstra J, Ishizawa T, Vahrmeijer AL, et al. A practical guide for the use of indocyanine green and methylene blue in

- fluorescence-guided abdominal surgery. J Surg Oncol. 2018;118(2):283-300.
- 31 Renna MS, Grzeda MT, Bailey J, Hainsworth A, Ourselin S, Ebner M. et al. Intraoperative bowel perfusion assessment methods and their effects on anastomotic leak rates: meta- 47 Munkley J, Elliott DJ. Hallmarks of glycosylation in cancer. analysis. Br J Surg. 2023:110(9):1131-42.
- 32 Hernot S, van Manen L, Debie P, Mieog JSD, Vahrmeijer AL. 48 Ryman JT, Meibohm B. Pharmacokinetics of Monoclonal Latest developments in molecular tracers for fluorescence image-guided cancer surgery. The Lancet Oncology. 2019;20(7):e354-e67.
- 33 Vahrmeijer AL, Frangioni JV. Seeing the invisible during surgery. Br J Surg. 2011;98(6):749.
- 34 Attia ABE, Balasundaram G, Moothanchery M, Dinish US, Bi R, Ntziachristos V, et al. A review of clinical photoacoustic imaging: Current and future trends. Photoacoustics. 2019;16:100144.
- 35 Zhao J, Chen J, Ma S, Liu Q, Huang L, Chen X, et al. Recent developments in multimodality fluorescence imaging probes. Acta Pharm Sin B. 2018;8(3):320-38.
- 36 Vermeulen I, Isin EM, Barton P, Cillero-Pastor B, Heeren RMA. Multimodal molecular imaging in drug discovery and development. Drug Discov Today. 2022;27(8):2086-99.
- 37 van Oosten M. Crane LM. Bart I. van Leeuwen FW. van Dam GM. Selecting Potential Targetable Biomarkers for Imaging Purposes in Colorectal Cancer Using TArget Selection Criteria (TASC): A Novel Target Identification Tool. Transl Oncol. 2011;4(2):71-82.
- 38 Tummers WS, Farina-Sarasqueta A, Boonstra MC, Prevoo HA, Sier CF, Mieog JS, et al. Selection of optimal molecular targets for tumor-specific imaging in pancreatic ductal adenocarcinoma. Oncotarget. 2017;8(34):56816-28.
- 39 Vuijk FA, de Muynck L, Franken LC, Busch OR, Wilmink JW, Besselink MG, et al. Molecular targets for diagnostic and intraoperative imaging of pancreatic ductal adenocarcinoma after neoadiuvant FOLFIRINOX treatment. Sci Rep. 2020;10(1):16211.
- 40 Muynck L, Gaarenstroom KN, Sier CFM, Duijvenvoorde MV. Bosse T. Mieog ISD, et al. Novel Molecular Targets for Tumor-Specific Imaging of Epithelial Ovarian Cancer Metastases, Cancers (Basel), 2020;12(6).
- 41 Linders DGJ, Bijlstra OD, Fallert LC, Hilling DE, Walker E, Straight B, et al. Cysteine Cathepsins in Breast Cancer: Promising Targets for Fluorescence-Guided Surgery. Mol Imaging Biol. 2023;25(1):58-73.
- 42 Gonzalez-Conchas GA, Rodriguez-Romo L, Hernandez-Barajas D, Gonzalez-Guerrero JF, Rodriguez-Fernandez IA, Verdines-Perez A, et al. Epidermal growth factor receptor overexpression and outcomes in early breast cancer: A systematic review and a meta-analysis. Cancer Treat Rev. 2018:62:1-8.
- 43 Linders D, Deken M, van der Valk M, Tummers W, Bhairosingh S, Schaap D, et al. CEA, EpCAM, ανβ6 and uPAR Expression in Rectal Cancer Patients with a Pathological Complete Response after Neoadjuvant Therapy. Diagnostics (Basel). 2021;11(3).
- 44 Hamilton E, Shastry M, Shiller SM, Ren R. Targeting HER2 heterogeneity in breast cancer. Cancer Treat Rev. 2021;100:102286.
- 45 Pinho SS, Reis CA. Glycosylation in cancer: mechanisms and clinical implications. Nature Reviews Cancer. 2015;15:540.

- 46 Kaur S, Kumar S, Momi N, Sasson AR, Batra SK. Mucins in pancreatic cancer and its microenvironment. Nature reviews Gastroenterology & hepatology. 2013:10(10):607-20.
- Oncotarget. 2016;7(23):35478-89.
- Antibodies. PETT: Pharmacometrics & Systems Pharmacology. 2017;6(9):576-88.
- 49 Bates A, Power CA. David vs. Goliath: The Structure, Function, and Clinical Prospects of Antibody Fragments. Antibodies (Basel, Switzerland). 2019;8(2):28.
- 50 Baart VM, van Manen L, Bhairosingh SS, Vuijk FA, Iamele L, de Jonge H, et al. Side-by-Side Comparison of uPAR-Targeting Optical Imaging Antibodies and Antibody Fragments for Fluorescence-Guided Surgery of Solid Tumors. Mol Imaging Biol. 2021.
- 51 Stumpp MT, Amstutz P. DARPins: a true alternative to antibodies. Curr Opin Drug Discov Devel. 2007;10(2):153-9.
- 52 Plückthun A. Designed Ankyrin Repeat Proteins (DARPins): Binding Proteins for Research, Diagnostics, and Therapy. Annual Review of Pharmacology and Toxicology. 2015;55(1):489-511.

16 CHAPTER 1 • General introduction and thesis outline 17

# PART I **Evaluation of biomarkers** for molecular imaging of gastrointestinal tumors

### **CHAPTER 2**

# Targeting glycans and heavily glycosylated proteins for tumor imaging

Ruben D. Houvast, Mireille Vankemmelbeke, Lindy G. Durrant, Manfred Wuhrer, Victor M. Baart, Peter J. K. Kuppen, Lioe-Fee de Geus-Oei, Alexander L. Vahrmeijer, Cornelis F. M. Sier

Cancers (Basel). 2020;12(12).



### ABSTRACT

Real-time tumor imaging techniques are increasingly used in oncological surgery, but still need to be supplemented with novel targeted tracers, providing specific tumor tissue detection based on intra-tumoral processes or protein expression. To maximize tumor/non-tumor contrast, targets should be highly and homogenously expressed on tumor tissue only, preferably from the earliest developmental stage onward. Unfortunately, most evaluated tumor-associated proteins appear not to meet all of these criteria. Thus, the quest for ideal targets continues. Aberrant glycosylation of proteins and lipids is a fundamental hallmark of almost all cancer types and contributes to tumor progression. Additionally, overexpression of glycoproteins that carry aberrant glycans, such as mucins and proteoglycans, is observed. Selected tumor-associated glyco-antigens are abundantly expressed and could, thus, be ideal candidates for targeted tumor imaging. Nevertheless, glycanbased tumor imaging is still in its infancy. In this review, we highlight the potential of glycans, and heavily glycosylated proteoglycans and mucins as targets for multimodal tumor imaging by discussing the preclinical and clinical accomplishments within this field. Additionally, we describe the major advantages and limitations of targeting glycans compared to cancer-associated proteins. Lastly, by providing a brief overview of the most attractive tumor-associated glycans and glycosylated proteins in association with their respective tumor types, we set out the way for implementing glycan-based imaging in a clinical practice.

### INTRODUCTION

Cancer is a leading cause of death worldwide, accompanied by a high burden on society. Biomedical imaging of malignant tissue plays a pivotal role in cancer detection, biopsy/therapeutic guidance and monitoring, and thus is a major contributor in defining treatment and surgical planning.¹ Current imaging methodologies such as X-ray, ultrasound (US) computed tomography (CT), (functional) magnetic resonance imaging ((f)MRI), positron emission tomography (PET), single-photon emission computed tomography (SPECT) are routinely applied within standard of care, mostly before surgery takes place.¹² Untargeted techniques, such as X-ray, US and CT, detect tissue irregularities based on anatomy and are therefore not exclusively specific for neoplastic tissue. As tumor-targeted contrast agents provide a more specific indication of molecular processes in both premalignant lesions and tumors, their employment is of particular interest for preoperative staging, intraoperative detection and postoperative monitoring of cancer.

An adequate tumor-to-background ratio (TBR), which allows clear differentiation between healthy and malignant tissue, is the cornerstone of tumor imaging.<sup>3</sup> To maximize the TBR, an imaging target should be highly and homogenously expressed, ideally confined to tumor tissue only. As most available protein-based imaging targets appear to have limitations, for instance substantial expression on normal surrounding tissues or lack of (over)expression in early disease stages, the search for novel targets is an ever-continuing topic of research.

Aberrant glycosylation represents a hallmark of cancer, offering a set of novel tumor-specific targets.<sup>4</sup> In man, more than half of all membrane-bound or soluble, secreted proteins carry sugar molecules, referred to as glycans. These proteins are therefore categorized as glycosylated proteins or, in short, glycoproteins. Glycans can also be attached to lipids, forming glycolipid structures, such as gangliosides.<sup>5,6</sup> Of note, particular glycoproteins, such as proteoglycans and mucins, carry an extensive amount of glycans that accounts for the majority of their molecular weight and size, while extensively orchestrating their function. These glycoproteins are further referred to as heavily glycosylated proteins.

In cancer and other pathological process, including infection, and chronic inflammation glycans and heavily glycosylated proteins, that are intricately linked to disease progression, become overexpressed. Despite the tumor-specific expression of these structures, only a few of these determinants have so far been validated as targets for tumor imaging. Table 1 summarizes the recent studies evaluating tumor-associated glycans and heavily glycosylated proteins as targets for molecular imaging of cancer and provides an overview of the most promising targets with respect to their tumor type. In this review, we provide a background on the most promising glycome targets and highlight the great potential of these structures as imaging targets by discussing the recent preclinical and clinical research into glycan-related tumor imaging.

TABLE 1 An overview of recent imaging studies evaluating glycans, heavily glycosylated proteins.

			Preclinical studies	ies			
Target	Targeting moiety	Appl.	Conjugate	Cancer type	Cell line	Mouse model or phase	Ref.
Thomsen- Friedenreich	PNA-coated nano- beacon	Ħ	Coumarin 6	Colon	HCT 116	Subcutaneous	11
	TF peptide	PET	64Cu-NO2A	Breast	MDA-MB-435	Subcutaneous	12
	A38C tetramer	NIRF	AF647	Ovarian peritoneal carcinomatosis	IGROV-1	Orthotopic	13
Thomsen-nouveau	2154F12A4 mAb	NIRF	Qdot-800	Breast	MCF7	Subcutaneous	14
sialyl-Thomsen- nouveau	3E8 scFv	NIRF	IRDye 800	Colon	LS174T	Orthotopic	15
	CC49 mAb HuCC49 ACH2 mAb	NIRF	Cy7	Colon	LS174T	Subcutaneous	16
	HuCC49∆CH2	PET	124I-DOTA	Colon	LS174T	Subcutaneous	17
	Pretarget: CC49-Halo- Tag	SPECT	<sup>111</sup> In-Halo Tag ligands	Colon	LS174T	Subcutaneous	18
	HuCC49∆CH2	SPECT/γ-scin	$\mathbf{u}_{\mathrm{I}\tau\tau\tau}$	Colon	LS174T	Subcutaneous	19
	CC49 mAb-benza- mide-TCO	SPECT/γ-scin	$^{111}$ In-Tz	Colon	LS174T	Subcutaneous	20
	CC49 mAb-acet- amide-TCO	SPECT/γ-scin	$^{ m LL-LZ}$	Colon	LS174T	Subcutaneous	21
Lewis <sup>a/c/x</sup>	CH88.2	NIRF	IRDye 800CW	Colon, pancreas	HT-29, BxPC-3	Subcutaneous	22
sialyl-Lewis <sup>a</sup>	Anti-CA19-9 mAb	FI	AF488 dye	Pancreas	BxPC-3	Subcutaneous, orthotopic	23
	Anti-CA 199 mAb	FI	DyLight 650	Pancreas	PDOX	Orthotopic	24
	Anti-CA19-9 diabody	PET	154 <u>I</u>	Pancreas	BxPc-3, Capan-2, MIA PaCa-2	Subcutaneous	25
	Anti-CA19-9 cys- diabody	PET	154I	Pancreas	BxPC-3	Subcutaneous	26
	HuMAb-5B1 mAb	PET	$^{89}\mathrm{Zr\text{-}DFO}$	Bladder	HT 1197	Subcutaneous	27
	Pretargeted: 5B1 mAb	PET	$^{1268}$	Pancreas	Capan-2	Subcutaneous, orthotopic	28
	5B1 mAb-TCO	PET	64Cu-NOTA- PEG7-Tz	Pancreas	BxPC-3, Capan-2	Subcutaneous, orthotopic	29
	PEGPH20 and HuMab-5B1 mAb	PET	89Zr-DFO	Pancreas	BxPC3-HAS3	Subcutaneous	30

			Preclinical studies	sa			
	5B1 mAb	PET/ NIRF	<sup>89</sup> Zr-DFO FL dye	Pancreas	BxPC-3, MIA PaCa-2, Suit-2	Subcutaneous, orthotopic	31
yl-Lewis <sup>x</sup>	sLeX-carrying lipo- somes	NIRF	Cy5.5	1	Ehrlich Ascites tumor	Subcutaneous	32
Lewisy	hu3S193 mAb	PET, SPECT/y-scin	111 <sup>1</sup> In, 86Y	Colon	HCT-15	Subcutaneous	33
	hu3S193 diabody, F(ab') <sub>2</sub>	SPECT/γ-scin	111In-CHX-A"-DTPA	Breast	MCF-7	Subcutaneous	34
GD2	ch14.18-CHO	NIRF	IRDye 800CW	Neuroblastoma	KCNR, patient-de- rived	Orthotopic	35
	hu14.18K322A mAb	PET	<sup>64</sup> Cu- <i>p</i> -NH2- Вп-DOTA	Neuroblastoma, melanoma	M21, PC-3.	Subcutaneous	36
	hu14.18K322A mAb	PET	64Cu-Bn-NOTA	Osteosarcoma	SJOS072	Subcutaneous	37
ndecan-1	Recombinant syndecan-1	MSOT	CF750 succinyl ester	Pancreas	S2VP10	Orthotopic	38
	9E7.4 mAb	PET	64Cu-TE2A	Multiple myeloma	5T33	Subcutaneous, orthotopic	39
ypican-1	Glypican-1 mAb	FI /MRI	Gd-Au-nanoclusters	Pancreas	COLO-357	Subcutaneous	40
ypican-3	Pretarget: L5 peptide	MRI	SA-PEG-USPIO	HCC	HepG2	Subcutaneous	41
	TJ12P1 peptide	NIRF	Cy5.5	HCC, Prostate	HepG2, PC3	Subcutaneous	45
	αGPC3 mAb	PET	1Z68	HCC	HepG2	Orthotopic	43
	αGPC3 F(ab') <sub>2</sub>	PET	1Z68	HCC	HepG2	Orthotopic	44
MUC1	EPPT peptide	MRI/NIRF	Magnetic NP-Cy5.5	Colon	MC38 MUC1	Orthotopic	45
	EPPT peptide	MRI/NIRF	Magnetic NP-Cy5.5	Breast	Spontaneous	Orthotopic	46
	EPPT peptide	MRI/NIRF	Magnetic NP-Cy5.5	Pancreas	Spontaneous	Orthotopic	47
	EPPT peptide	MRI/NIRF	Magnetic NP-Cy5.5	Colon	LS174T	Subcutaneous	48
	CT2 mAb	NIRF	DyLight 650	Pancreas	Panc-1, BxPC-3	Subcutaneous, orthotopic	49
	hMUC1 mAb	NIRF	DyLight 755	Pancreas	Capan-2	Subcutaneous	20
	CD227 mAb	NIRF	Fluorescein-Cy5.5	Ovary	OVCAR3	Subcutaneous	51
	MUC1 aptamer	NIRF	MPA-PEG	Breast, liver	MCF-7, HepG2	Subcutaneous	52
	TAB 004 mAb	NIRF	ICG	Breast	PyMT, MMT, spontaneous	Orthotopic	23
	GGSK-1/30	PET/MRI	1Z68	Breast	PyMTxhuMUC1	Subcutaneous	54
	PR81 mAb	PET/ SPECT	64Cu-DOTA	Breast	MCF-7	Subcutaneous	22

# [CONTINUATION TABLE 1]

			Preclinical studies	es			
	PR81 mAb	SPECT/y-scin	<sup>99m</sup> Tc	Breast	Spontaneous	Orthotopic	56
MUC1/ MUC5AC	Pretarget: TF10 bispecific mAb	y-scin	<sup>125</sup> I-IMP-288	Pancreas	Capan-1	Subcutaneous	57
	bsPAM4 F(ab') <sub>2</sub>	y-scin	I521	Pancreas	Capan-1	Subcutaneous	28
	Pretarget: bsPAM4 F(ab') <sub>2</sub>	γ-scin	111In-IMP-156 99mTc-IMP-192	Pancreas	Capan-1	Subcutaneous	28
MUCSAC	60C peptide	MRI	USPIO	Colon	HT-29, HCT 116	Subcutaneous	59
MUC16	AR9.6 mAb	NIRF	IRDye 800CW	Pancreas	COLO 357, T3M4	Subcutaneous, orthotopic	09
	B43.13 mAb B43.13 scFv	PET	64Cu	Ovary	OVCAR3, SKOV3	Subcutaneous	61
	B43.13 mAb	PET	$^{1\mathrm{Z}_{68}}$	Ovary	OVCAR3, SKOV3	Subcutaneous	62
I	B43.13 mAb B43.13 scFv	PET	<sup>18</sup> F (FBz)	Ovary	OVCAR3, SKOV3	Subcutaneous	63
			Clinical studies				
sTn	B72.3 mAb	RIGS	I521	Colon, rectum		Phase 1/2	64
I	CC49 mAb	RIGS	I521	Colon, rectum	ı	Phase 1	99
	CC49 mAb	RIGS	1251	Colon, rectum	-	Phase 1	99
	HuCC49∆CH2 mAb	RIGS	1251	Colon, rectum	•	Phase 1	67
I	HuCC49ΔCH2 mAb	RIGS	I521	Colon, rectum	ı	Phase 1	89
sialyl-Lewis <sup>a</sup>	HuMAb-5B1 mAb	PET	$^{89}\mathrm{Zr\text{-}DFO}$	Pancreas	ı	Phase 1	69
	B3 mAb	SPECT	$\mathbf{n}^{111}$	Various	-	Phase 1	70
Lewisy	hu3S193 mAb	SPECT/y-scin	$^{111}$ In	Lung	-	Phase 1	71
GD2	ch14.18 mAb	y-scin	$^{20}\mathrm{mTc}$	Neuroblastoma	ı	Phase 1	72
. !	3F8 mAb	y-scin	I181	Neuroblastoma	ı	Phase 1	73
	3F8 mAb	PET	154I	Neuroblastoma	ı	Case report	74
MUC1	C595 mAb	y-scin	$\mathbf{n}^{111}$	Bladder	-	Phase 1	75
	C595 mAb	y-scin	$^{99}\mathrm{mTc}$	Bladder	•	Phase 1	2/2
MUC1/	hPAM4 mAb	y-scin	$\mathbf{u}_{\mathrm{I}_{111}}$	Pancreas	ı	Phase 1	77

Appl.: application, CHX-A"-DTPA: C-functionalized trans-cyclohexyl diethylenetriaminepentaacetic acid., y-scin. gamna scintigraphy, DFO: desferrioxamine, DOTA: 11,47,10-tetraazacyclododecane-1,4,7,10-tetra- acetic acid, GSC: Gly-Ser-Gly, FI: fluorescence imaging, HCC: hepatocellular carcinoma, ICC: indocyanine green, PEG: polyethylene glycol, mAb: monoclonal antibody, MSOT: multispectral optoacoustic imaging, MRI: magnetic resonance imaging, NIRF: near-infrared fluorescence, NP: nanoparticle NOTA: 1,4,7-Triazacyclononane-1,4,7-triazacyclononane-1,4,7-triazacyclononane-1,4,7-triazacyclononane-1,4,7-triazacyclononane-1,4-diacetate, PDOX: patient-derived orthotopic xenograft, PNA: Arachis hypogaea agglutinin, RIGS: radioimmunoguided surgery, SA: streptavidin,, TCO: trans-Cyclooctene, Tz: Tetrazine, USPIO: ultrasmall superparamagnetic iron oxide.

### **GLYCANS**

### Background

The attachment of glycans to proteins occurs mainly in two forms, namely *O*- and *N*-linked. O-linked glycosylation occurs via the attachment of a sugar molecule to the hydroxyl group of mainly serine (Ser) or threonine (Thr) residue side chains in a protein, whereas *N*-linked glycosylation occurs via the attachment of an oligosaccharide consisting of multiple sugar molecules to the nitrogen atom of asparagine (Asn) side chains (Figure 1A-B)." *N*-glycans, which all share a common glycan core, can be grouped into high-mannose, hybrid and complex *N*-glycan structures, as depicted in Figure 1A. However, as the development of *N*-glycan-specific targeting vehicles is challenging due to the extensive structural similarity of *N*-glycans, therapeutic and imaging tracer development generally focusses on O-linked glycans (explained in detail in section: "targeting the glycome: opportunities and challenges").

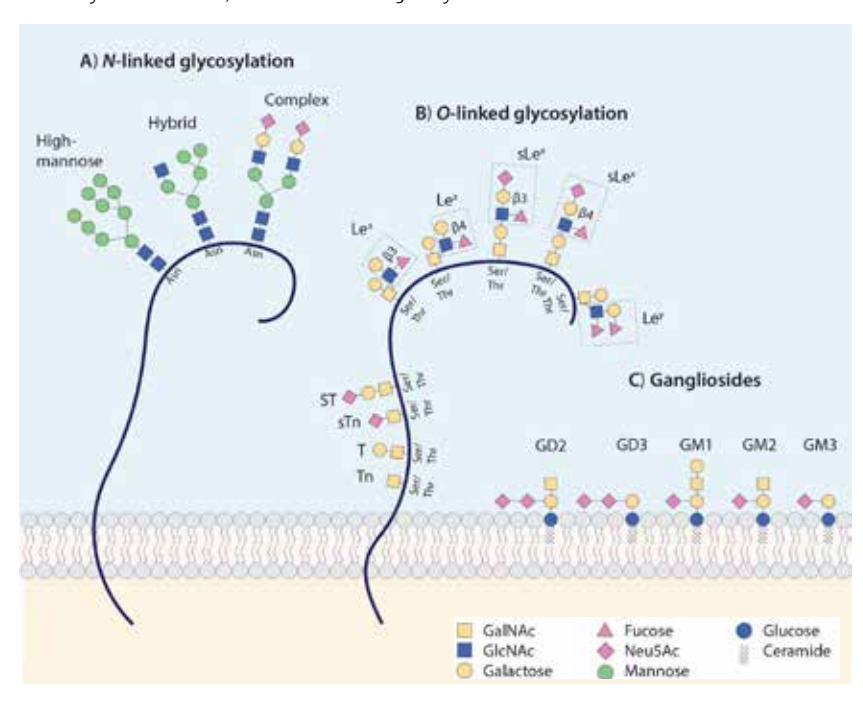
The most abundant form of *O*-glycosylation is mucin-type (GalNAc) *O*-glycosylation, in which extracellular or secreted glycoproteins are modified with *N*-acetylgalactosamine residues (GalNAc-alpha-*O*-Ser/Thr) that by addition of Galactose and *N*-acetylglucosamine (GlcNAc) residues constitute different *O*-GalNAc core structures. *O*-glycan cores can be further elongated by the addition of additional monosaccharides which results in specific terminal glycan motifs, of which some are shown in Figure 1B. These structures play roles in biological processes such as cell adhesion, receptor activation, cell growth, signal transduction, apoptosis and endocytosis and may confer antigenicity or provide cell protection by contributing to the glycocalyx formation.<sup>79-81</sup>

### Aberrant glycosylation in cancer

In cancer, aberrant glycosylation is mainly characterized by increased *N*-glycan branching, augmented O-glycan density, incomplete glycan synthesis, and, in more advanced cancers, synthesis of neo-glycan determinants that carry large amounts of sialic acids or fucose residues.<sup>10,82</sup> This leads to the appearance of immature truncated GalNAc/mucin-type *O*-glycans, such as sialyl-Thomsennouveau (sTn) and complex versions of Lewis glycans, such as sialyl-di-Lewisa (sdi-Lea).<sup>83</sup> Also, overexpression of normally expressed Lewis glycan antigens, such as sialyl-Lewisa (sLea, known as CA19-9) and its structural isomer sialyl-Lewisx (sLex), is observed. sTn, its non-sialylated counterpart Tn, and Lewis glycans are extensively expressed in a wide variety of epithelial-derived cancers,<sup>84,85</sup> of

e.g. the digestive tract, 8,86-88 breast, 87,89-91 lung, 87,92,93 bladder, 87,91,94 and ovaries. 87,88,95 Figure 1B depicts the schematic structure of these and other tumor-associated *O*-glycoantigens and illustrates the most frequently observed *O*-GalNAc core structures from which they extend.

FIGURE 1 Schematic structures of oligosaccharides (A) N-Linked glycans are covalently attached to proteins via asparagine (Asn). N-Glycans are assigned to three groups in which all share the same Pentasaccharide, Trimannosyl core structure: (1) High-Mannose N-glycans (2) Hybrid N-glycans in which the core is extended via both mannose and N-Acetylglucosamine (GlcNAc) residues and (3) complex N-glycans in which GlcNAc-initiated antennae are present. (B) O-linked glycans are covalently attached to proteins via Serine (Ser) or Threonine (Thr). Mucin-type O-Glycans are initiated by N-Acetylgalactosamine (GalNAc), while elongated, GlcNAc-containing glycans (displayed in dashed boxes) contribute to Type 1 (GalO1, 3GlcNAc) and Type 2 (GalO1, 4GlcNAc) structures. In this figure, sLeO2 and sLeO3 extructure (GalO1, 3GlcNAc)GalNAc), while LeO3, and LeO4 are attached to a core 2 structure (GalO1, 3[O1, 6lcNAc]GalNAc). Both O1 and O2-glycan antigens can carry O3-Acetylneuraminic (Neu5Ac) acids, categorizing these structures as sialylated antigens. (C) Gangliosides consist of varying arrangement of sialic acid-containing glycan chain attached to the cell membrane via a lipid anchor, the ceramide. GM1 to GM3 are initiated by glucose and carry one sialic acid, while GD2 and GD3 carry two sialic acids.



Tumor-associated glycans are heavily involved in tumor progression both directly or indirectly by influencing its protein or lipid carrier's function.<sup>96</sup> For instance, both sLe<sup>x</sup> and sLe<sup>a</sup> can serve as ligands for E- and P-selectins present on endothelial cells, thereby facilitating cell adhesion, extravasation and metastasis.<sup>86</sup> sLe<sup>a</sup> is overexpressed on a wide variety of tumor-associated glycoproteins, including mucin-1 (MUC1), MUC5AC and MUC16 (CA125).<sup>97,98</sup> Moreover, sLe<sup>x</sup>, also called CD15s, is overexpressed on liver acute-phase proteins, including haptoglobin,<sup>99</sup> and ceruloplasmin,<sup>100</sup> and on mucins MUC1, MUC5AC, MUC6 in, for example, pancreatic cancer.<sup>98,101</sup> This suggests a major advantage of targeting glycans in relation to protein targeting, as multiple tumor-associated proteins can be targeted simultaneously via a single glycan motif (described in detail in section: "targeting the glycome: opportunities and challenges"). Moreover, glycans are, in relation to proteins, very densely distributed on the outermost layer of the cell membrane,<sup>102</sup> making them easily accessible for targeting vehicles and, consequently, attractive targets for imaging.

### Imaging of sTn

Despite its abundant expression in a wide variety of carcinomas, e.g. lung, ovarian, bladder, breast, and almost all gastrointestinal cancers with low normal tissue distribution (reviewed in<sup>85</sup>), studies into sTn-targeted molecular imaging have particularly focused on colorectal tumors and reported clear tumor delineation. sTn, which is overexpressed on mucins MUC1,<sup>103,104</sup> MUC2,<sup>98</sup> MUC5AC<sup>98</sup> and MUC6,<sup>98</sup> and oncoprotein CD44(v6),<sup>104,105</sup> has been evaluated as a target in several imaging studies aiming to optimize SPECT imaging contrast in colorectal cancer. For instance, Rossin et al. described a strategy using anti-sTn monoclonal antibody (mAb) CC49 to pretarget tumor cells prior to administration of two mAb-clearing agents followed by administration of the CC49-binding radiolabel. Pretargeting could theoretically provide higher tumor-to-background contrast by clearing unbound CC49 mAbs from the circulation.<sup>20</sup> LS174T colon carcinomacarrying mice that were administered with clearing agents showed a remarkable 125-fold improvement of the tumor-to-blood ratio at 3 hours post injection, compared to administration of (non-pretargeted) <sup>177</sup>Lu-NOTA-CC49.

Apart from SPECT imaging, sTn has been evaluated as a target for real-time intraoperative imaging using near-infrared fluorescent (NIRF) light. For instance, murine CC49 and its humanized, CH2-deleted variant HuCC49 $\Delta$ CH2, were conjugated to NIR dye Cy7 and evaluated for NIRF imaging in a subcutaneous mouse model of colorectal cancer. Administration of murine CC49-Cy7 allowed clear

tumor visualization with a tumor-to-blood ratio of 15.5 at 96h post injection. Even though its humanized counterpart was cleared roughly twice as fast, it showed a tumor-to-blood ratio of 12.0 at 18 hours post injection with low specific uptake in other organs, confirming the great potential of sTn as a target for imaging of colorectal tumors. However, as Cy7 has not been clinically approved, the translational potential of the CC49-Cy7 tracer in this confirmation is currently limited. Apart from NIRF imaging, the same research group conjugated HuCC49 $\Delta$ CH2 to 124 and showed excellent tumor delineation using PET imaging in the same mouse model. 17

The low immunogenicity of glycans has both challenged therapeutic efficacy as well as the development of specific and high-affinity IgG mAbs (described in detail in section: "targeting the glycome: opportunities and challenges"). 106,107 For instance, sTn antibodies have been shown to additionally react with the non-sialylated Tn epitope and binding to sTn was dependent on the glycoprotein it was expressed on. Thus, the need for novel antibodies that could serve as a sTn-targeting moiety arose. 87,108 For example, Loureiro et al. developed and characterized the novel sTn mAb L2A5, that showed tumor-specific reactivity with all included bladder and colorectal cancer tissues, and 20% of triple-negative breast cancer tissues.91 Moreover, Prendergast et al. developed a panel of murine, high-affinity, internalizing sTn antibodies that showed positive immunohistochemical staining of the majority of human ovarian, bladder, colorectal, pancreatic, lung and gastric tumor tissues, with low reactivity to normal human tissues.87 Two mAbs, 5G2-1B3 and 2G12-2B2 were subsequently humanized, whilst maintaining limited reactivity with normal human tissues. Of these mAbs, 2G12-2B2-MMAE showed effective tumor targeting by inhibiting tumor growth in both an ovarian cancer cell line and patient-derived ovarian xenograft mouse models.88 Thus sTn, although underexplored, may pose a very suitable target considering its potential employment for imaging of a wide range of tumor types.85

### Imaging of sLe<sup>a</sup>/CA19-9

Considering its clinically applied tumor-specific upregulation in tissues and sera of pancreatic cancer patients, sLea/CA19-9 has been exploited as a target for imaging and therapy.<sup>23,25,26,28.31</sup> Houghton et al. have used the humanized mAb 5B1 conjugated to a NIRF dye and radionuclide <sup>89</sup>Zr <sup>109</sup> for bimodal fluorescence/PET imaging of pancreatic tumors, resulting in excellent tumor, positive lymph node, and metastases localization in both a subcutaneous and orthotopic metastasizing mouse model.<sup>31</sup> To improve tumor/non-tumor contrast even further, several

studies using anti-sLe<sup>a</sup> mAbs to pretarget tumor cells before radiolabel administration have been developed, which have led to remarkable improvements in TBR via various techniques.<sup>28,29</sup>

Interestingly, during malignant transformation, sLe<sup>a</sup>, but also sLe<sup>x</sup>, become expressed on the glycoprotein CEA (carcinoembryonic antigen),<sup>110,111</sup> which is currently undergoing clinical translation facilitated by our group as a target for NIRF imaging of colorectal cancer (SGM-101, SurgiMab).<sup>112</sup> Given their wide expression across different tumor types and multiple tumor-associated proteins, sLe<sup>a</sup> and sLe<sup>x</sup> may be very suitable candidates for pan-carcinoma tumor imaging.

Several mAbs recognizing alternative Lewis glycans have been developed and described. Noble et al. described the mAb 692/29, that recognizes a unique set of Lewis<sup>y</sup> and Lewis<sup>b</sup> glyco-epitopes. Despite some reactivity with normal gastro-intestinal epithelia, 696/29 bound to 82% of colorectal tumors and showed inhibition of cell growth *in vivo* that was further supplemented by chemotherapy.<sup>113</sup> More recently, the novel murine/chimeric IgG mAbs FG88.2 and FG129/CH129 were described, that bound to Lewis<sup>3</sup>/c/x-related and sialyl-di-Lewis<sup>a</sup> glyco-epitopes, respectively, that were highly expressed on pancreatic, colorectal, stomach, lung and ovarian carcinomas with restricted expression on normal tissues.<sup>83</sup>,114 Subsequently, our group evaluated IRDye 800CW-conjugated FG88.2 and its chimeric mouse/human counterpart, CH88.2, for real-time NIRF imaging in subcutaneous mouse models of colon and pancreatic cancer, which provided excellent tumor localization and delineation using a clinical camera system.<sup>22</sup>

Lastly, Shimomura et al. described an alternative approach for glycan-targeting by using glycan-binding lectin rBC2LC-N, which binds to type 1 (Fuc $\alpha$ 1-2 Gal $\beta$ 1-3GlcNAc) and type 3/4 fucosylated glycans (Fuc $\alpha$ 1-2 Gal $\beta$ 1-3GalNAc; see also Figure 1A), showed reactivity with almost all tested human pancreatic ductal adenocarcinoma (PDAC) specimens. After conjugation with a bacterial exotoxin, a remarkable cytotoxicity was observed in several patient-derived models, suggesting excellent tumor penetration. Most importantly, the authors excluded that rBC2LC-N caused human serum agglutination *in vitro*, which is a frequently observed phenomenon after lectin administration. These results not only pave the way for a potential imaging strategy for PDAC, but also provide a novel explorable approach to glycan targeting.

### Glycan imaging in the clinic

Several glycan-targeting imaging tracers have already been evaluated in a clinical setting. For instance, anti-sTn mAb CC49 and its predecessor mAb B72.3 were

conjugated to <sup>125</sup>I and used as a tracer for radioimmunoguided surgery (RIGS) of colorectal cancer. <sup>64-68</sup> Intraoperatively, RIGS using <sup>125</sup>I-CC49 allowed detection of 86% and 97% of primary and recurrent tumors respectively, while the surgical resection was influenced in roughly half of the cases. <sup>65</sup> However, routine clinical implementation of RIGS is limited by the inconveniently long period between tracer administration and surgery (one week) and handling of the long-lived <sup>125</sup>I isotope, and therefore RIGS has been overtaken by other imaging strategies, such as NIRF imaging. <sup>117</sup> Also, the anti-CA19.9 tracer <sup>89</sup>Zr-DFO-HuMab-5B1 (MVT-2163) has recently been evaluated in a phase I trial for PET imaging of pancreatic cancer and allowed high-contrast imaging of tumors and metastases, including lesions that were not detected with traditional imaging methods. <sup>69</sup> Administration of MVT-2163 was safe causing mild to moderate side effects on the first day, including nausea, fever and hypertension, in 50% of patients.

### **GANGLIOSIDES**

### **Background**

Gangliosides are sialic acid-containing glycosphingolipids (a glycolipid subclass) that are attached to the cell membrane via a lipid portion: the ceramide (Figure 1C). These structures are abundantly present in the central nervous system where they serve pivotal roles in its development and maintenance. Simple ganglioside structures such as GD2, GD3 or GM1-3, are aberrantly expressed in several neuroectodermal-derived cancers, including melanoma, osteosarcoma and neuroblastoma, and in breast cancer. Several studies have shown that gangliosides are involved in tumor cell proliferation, mobilization and metastasis. 123,124

In 2015, the human/mouse chimeric anti-GD2 mAb ch14.18 (dinutuximab) became the first and only FDA-approved therapeutic anti-glycan antibody. Administered in combination with IL-2, GM-CSF and isotretinoin, dinutuximab increased 2-year event-free and overall survival (OS) rates of high-risk neuroblastoma patients with 20 and 10.9%, respectively. Phase II and III dinutuximab trials in neuroblastoma (NCT02743429, NCT01704716), osteosarcoma (NCT02484443) and small cell lung cancer (NCT03098030) are underway.

### Imaging of GD2

32

Several studies have validated the humanized variant of dinutuximab, hu14.18, as a targeting moiety for tumor imaging. For instance, Vāvere et al. validated the hu14.18K322A variant of hu14.18, that was developed to decrease neuropathic

pain after administration while maintaining cytotoxicity, as a targeting moiety for PET imaging. Administration of <sup>64Cu</sup>-labeled hu14.18K322A to GD2-postive M21 melanoma xenograft-carrying mice, allowed excellent tumor delineation and localization with low tracer uptake in other organs.<sup>36</sup> More recently, the same group additionally validated the tracer in a patient-derived and metastatic orthotopic in vivo model of osteosarcoma and observed similar tumor-specificity related to GD2 expression and detected tumor lesions as small as 29 mm<sup>3</sup> at 48 hours post injection.37 Dinutuximab-beta (ch18.18/CHO), an FDA-approved biosimilar variant of ch14.18, was recently conjugated to IRDye 800CW and evaluated for NIRF imaging of neuroblastoma in a mouse model.<sup>35</sup> At 4 days post-injection, the tracer showed high-contrast tumor accumulation in both orthotopic transplanted human KCNR cells and patient-derived organoid xenograft mouse models. Moreover, the authors showed that neoadjuvant anti-GD2 immunotherapy did not influence tracer uptake, supporting an application of the tracer in a clinical setting. Alternatively, Jiao et al. used gold nanoparticles (GNPs) conjugated to hu14.18K322A as NK-cell activators as well as CT contrast agents. 127 After incubating NB1691 neuroblastoma cells and M21 melanoma cells with the construct, the authors observed a two-fold higher antibody-dependent cellular cytotoxicity efficacy, along with a 5- to 8-fold increase in CT imaging contrast compared to controls, proposing a potent bimodal application of the tracer. Of note, none of the aforementioned studies evaluated neurotoxicity following administration of anti-GD2 contrast agents administration, however, providing that imaging tracers are administrated in a substantially lower dose than therapeutic agents, one may expect that neurotoxicity will not pose a limiting factor for GD2-based imaging.

### Ganglioside-based nerve imaging

Although other gangliosides have been established as not specific for tumor cells, they might still be of use as targets for imaging during oncological surgery. For instance, to avoid nerve injury during prostatectomy, surgeons may be assisted by a real-time nerve monitoring system, based on a ganglioside specific NIRF tracer. Massaad et al. used the anti-GT1b-2b mAb, that has been shown to bind axons in spinal roots, peripheral nerves and neurons of dorsal root ganglia and the spinal cord, as a targeting moiety. <sup>128</sup> Conjugated to fluorescent dye Dylight550, peripheral nerves could be imaged using the tracer from 24 hours up to 20 days after intravenous administration to wild-type mice. Furthermore, the authors reported that GT1b-2b-induced nerve fiber damage was not present.

### **PROTEOGLYCANS**

### Background

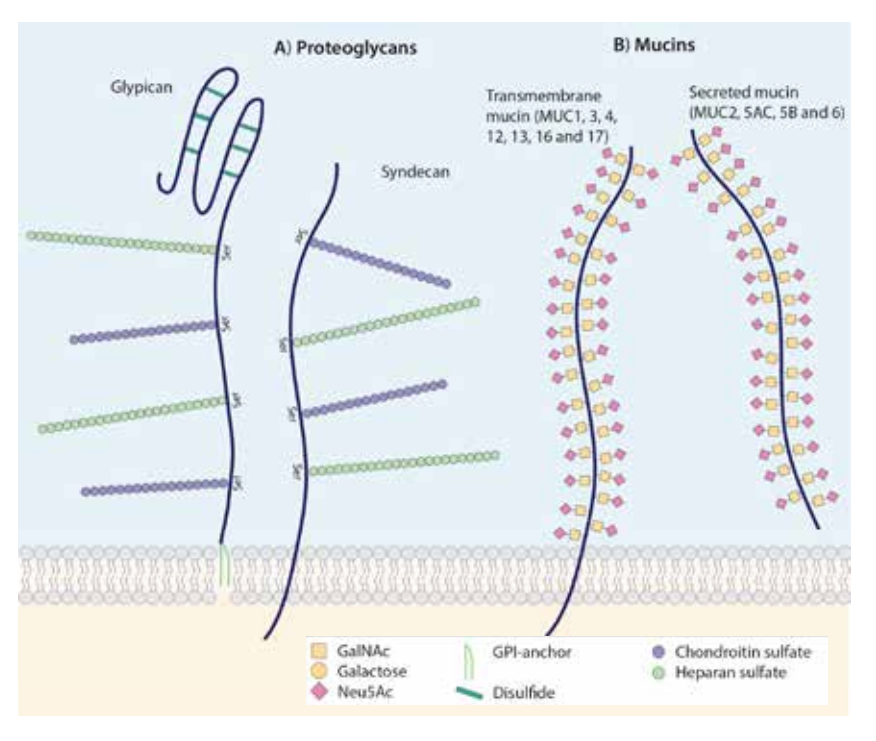
Heavily glycosylated proteins, such as proteoglycans, also form an interesting array of targets for tumor imaging, in addition to tumor-associated glycans (Figure 2A). Proteoglycans (PGs) consist of linear polysaccharide chains (glycosaminoglycans, GAGs) that are covalently attached to a protein core. PGs form a major component of the extracellular matrix and contribute significantly to the structural integrity of tissues. 129 Moreover, PGs play multifaceted roles in the regulation of essential signaling pathways that are involved in cell proliferation, adhesion and migration, apoptosis and angiogenesis. 130 Especially heparan sulfate proteoglycans (HSPGs), such as syndecans and glypicans, have gained significant scientific interest within the oncological field. 131,132 Indeed, syndecans and glypicans are localized at the cell surface, allowing them to be heavily involved in respectively integrin and growth factor signaling and regulation of Wnt and Hedgehog signaling, pathways known to be dysregulated in cancer. 133-136 Many recent studies reported overexpression 132 and, understandably, great involvement of HSPGs in carcinogenesis and tumor progression in a wide range of tumors, making these structures potential targets for molecular imaging of cancer. 130,132,136-139

### Imaging of syndecan-1

Syndecan-1 (CD138) was evaluated as a target for bimodal NIRF imaging and multispectral optoacoustic tomography (MSOT, also known as photoacoustic imaging) in an orthotopic *in vivo* model of pancreatic cancer.<sup>38</sup> At 6 hours post injection, the fluorescent tumor signal was undetectable, while MSOT provided a clear high-contrast imaging of tumor location with inferior liver and kidney uptake. Taken together, these results underline both the advantage of MSOT imaging in relation to NIRF imaging, i.e. deeper imaging depth, as well as the great potential of this syndecan-1 tracer for combined MSOT/NIR imaging of a wide arrange of tumors, given the broad tumor expression of syndecan-1.<sup>139</sup>

More recently, Bailly et al. compared the mAb-based syndecan-1 tracer <sup>64</sup>Cu-TE2A-9E7.4 with the conventional tracer <sup>18</sup>F-FDG and <sup>64</sup>CuCl<sub>2</sub> for PET imaging of primary multiple myeloma lesions and metastases using a syngeneic mouse model.<sup>39</sup> Although <sup>64</sup>Cu-TE2A-9E7.4 was found to accumulate in the liver, spleen, kidneys, and digestive tract, the tracer outperformed both <sup>18</sup>F-FDG and <sup>64</sup>CuCl<sub>2</sub> in terms of non-tumor uptake and tumor-to-blood contrast (41 at 24h post-injection). Moreover, the tracer allowed high-contrast imaging of most metastatic depositions, of which one was not observed using <sup>18</sup>F-FDG.

FIGURE 2 Schematic structure of heavily glycosylated glycoproteins. (A) Proteoglycans are transmembrane glycoproteins that consist of a core protein decorated with glycosaminoglycan (GAG) chains. In glypicans, the protein core is stabilized by disulphide bridges and linked to the cell membrane via GPI-anchors. Both glypicans and syndecans contain serine-linked heparin sulphate and chondroitin sulphate GAGs at both sides of the protein (here only depicted on one side), classifying them as HSPGs. (B) Mucins are high-molecular weight proteins that are extensively decorated with mucin-type O-glycans, schematically illustrated here by the sTn epitope. Mucins are subdivided into transmembrane (MUC1, MUC3, MUC4, MUC12, MUC13, MUC16 and MUC17) and secreted mucins (MUC2, MUC5AC, MUC5B and MUC6).



### **MUCINS**

### Background

Mucins form another class of high molecular weight proteins that are heavily gly-cosylated with truncated *O*-glycans (Figure 2B).<sup>140</sup> These often negatively charged sugar branches on both transmembrane (MUC1, MUC4, MUC13 and MUC16) and secreted mucins (MUC2, MUC5AC, MUC5B and MUC6) form a physical barrier, protecting the underlying epithelium.<sup>140-142</sup> In cancer, aberrantly glycosylated mucins become overexpressed and are, directly or indirectly via their truncated sTn/

Tn/TF (Thomsen-Friedenreich) glyco-epitopes, heavily involved in proliferation, migration, invasion, metastasis, and chemo- and radioresistance of tumor cells. 143- 148 For instance, both MUC1, also called epithelial membrane antigen (EMA), and MUC16, also called CA125, are overexpressed in a wide variety of cancer types, including breast, 149 lung, 150,151 gastrointestinal, 142,147,152,153 head-and-neck, 154,155 ovarian 156,157 and other gynecological malignancies, 158,159 making them potential targets for pan-carcinoma imaging.

### **Imaging of MUC1**

Several preclinical studies described MUC1 as a promising target for molecular imaging.  $^{45,47.49,52,53,55,160.162}$  For instance, Chen et al. evaluated MUC1-specific aptamers, conjugated to indocyanine green (ICG) as a fluorescence imaging tracer in breast, non-small cell lung or hepatocellular carcinoma-bearing mice.  $^{52}$  The tracer showed fast clearance via the kidneys, while still providing tumor-to-background ratios of  $4.0 \pm 0.2$  in low MUC1-expressing HepG2 tumor cells. Tumors could be clearly localized and delineated in all models.

The expression of MUC1 on the apical surface of normal glandular epithelial cells may reduce tumor-to-background contrast, thus limiting the application of MUC1-targeting contrast agents. 163 Although most mAbs recognize MUC1 irrespective of its glycosylation pattern, several targeting moieties target a highly tumor-specific conformational MUC1 epitope induced through increased expression of truncated O-glycans sTn and Tn; the so-called under-glycosylated (u) MUC1 or (tumor-associated) TA-MUC1 epitope, which becomes expressed on the entire cell surface. Zhao et al. described a promising alternative for serum marker-based therapeutic response monitoring by developing the bimodal MR/fluorescence imaging probe MN-EPPT, which targets uMUC1. 45,47,48,161 Using spontaneous, human uMUC1-expressing mouse models of breast and pancreatic cancer, uMUC1 expression was detected using MR and fluorescence imaging as early as from ductal carcinoma in situ (DCIS) and pancreatic intraepithelial neoplasia (PanIN) lesions onward. 46,47 Tracer uptake decreased after treatment with chemotherapy, suggesting a decrease of uMUC1 expression.<sup>45,47,161</sup> Conversely, increased tracer uptake after chemotherapy was observed in unresponsive tumors, even before anatomical changes were present, indicating uMUC1 as a marker for in vivo imaging of in situ lesions and chemoresistance and or tumor progression. 45,47 Meanwhile, positive TA-MUC1 expression has been shown in non-small cell lung, ovarian, breast, gastric, colorectal, liver, cervical, kidney, thyroid, and other (non-epithelial) cancers. 164,165 Administration of gatipotuzumab (previously known as PankoMab-GEX), a humanized mAb that binds TA-MUC1 in a Tn/ TF-dependent manner, was found safe and was well-tolerated in patients with advanced carcinomas, suggesting a potential pan-carcinoma imaging application of the targeting moiety.<sup>166</sup>

Alternatively, GGSK-1/30, a murine mAb specific for an alternative MUC1 gly-coprotein epitope, was conjugated to <sup>89</sup>Zr and evaluated for combined PET/MRI imaging of breast cancer-bearing human MUC1-expressing transgenic mice.<sup>54</sup> At 72h post-injection, administration of <sup>89</sup>Zr-GGSK-1/30 revealed high tracer tumor uptake with lower uptake in excreting organs and healthy mammary tissue, providing high-contrast tumor delineation. Considering its expression in 90% of breast tumors, including triple-negative breast carcinomas, GGSK-1/30 also seems an promising targeting moiety for pan-breast cancer detection.<sup>54</sup>

### Imaging of MUC1/MUC5AC:PAM4-based systems

The PAM4 mAb, which recognizes a carbohydrate-induced conformational epitope on MUC1 and MUC5AC, has been evaluated as a targeting vehicle for therapy and imaging of pancreatic cancer. PAM4 stained approximately 85% of pancreatic carcinomas, while reactivity with pancreatitis and healthy pancreatic tissue was respectively less than 25% and absent. Moreover, the PAM4-epitope is abundantly expressed in PDAC precursor lesions, namely in intraductal papillary mucinous neoplasms and from earliest PanIN lesions (PanIN-1A) onward, suggesting a role for PAM4 in early pancreatic cancer detection. 168

Several studies evaluated PAM4-based contrast agents for y-scintigraphy of PDAC. Cardillo et al. used bsPAM4to pretarget Capan-1 pancreatic tumor cells, following administration of histamine-succinyl-glycine peptide haptens 111In-IMP-156 or 99mTc-IMP-192, that were developed to interact with bsPAM4.58 Subcutaneous Capan-1 xenografts could be imaged as early as 0.5 h after peptide hapten administration. At 3 h post injection, high tumor-to-blood ratios of  $36.5 \pm 8.3$  and  $5.2 \pm 0.5$  were achieved using <sup>111</sup>In-IMP-156 and <sup>99m</sup>Tc-IMP-192, respectively, which was significantly higher compared to administration of directlabeled bsPAM4 F(ab')2. More recently, the same group developed the bispecific, trivalent mAb TF10, which consists of two PAM4-derived Fab' fragments and one mAb-679-derived Fab', enabling interaction with the radiolabeled haptenpeptide <sup>111</sup>In-IMP-288.<sup>57</sup> At 3 h post-injection to Capan-1 tumor-bearing mice, a tumor-to-blood ratio of 915.2 ± 404.3 was observed (vs. 5.2 ± 1.0 using 111 In-DOTA-PAM4 IgG at 24 h), allowing clear delineation of small tumor lesions. These results clearly show the advantages of a pretargeting regime both most importantly demonstrate the feasibility of PAM4-based systems for molecular imaging of PDAC.

### **Imaging of MUC16**

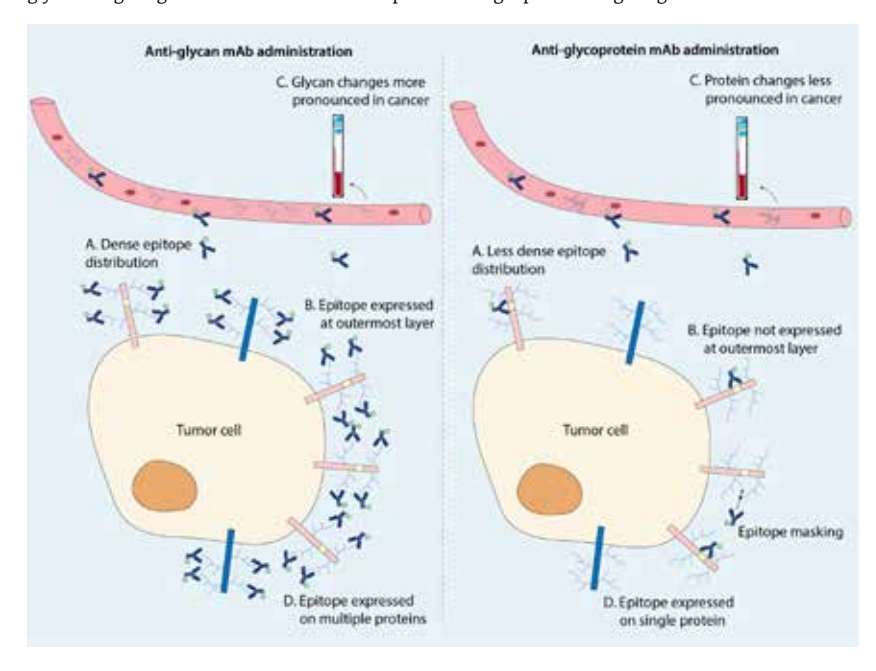
MUC16 has been preclinically evaluated as a target for PET imaging of ovarian tumors, using the mAb B43.13 (oregevomab) or derived fragments conjugated to radionuclides <sup>64</sup>Cu or <sup>89</sup>Zr.<sup>61.63</sup> In human OVCAR3 tumor-bearing mice, <sup>89</sup>Zr-B43.13 provided higher TBRs when compared to <sup>18</sup>F-FDG, which is the gold standard for PET imaging in ovarian cancer.<sup>62</sup> Moreover, the tracer showed uptake in adjacent lymph nodes, which correlated with lymphatic spread of tumor cells. As a one-day imaging protocol is more attractive in a clinical setting, the authors attempted using a faster-clearing scFv fragment of B43.13 conjugated to <sup>18</sup>F in the same *in vivo* model.<sup>63</sup> Unfortunately, only a modest OVCAR3 tumor uptake was observed. In addition, as mouse B43.13 has been administered to patients and was well tolerated despite human-anti-mouse responses based on serum analysis, clinical application of the tracer seems feasible.<sup>62,169</sup>

### Targeting the glycome: opportunities and challenges

Glycan targeting may offer major advantages in relation to protein targeting. Firstly, tumor-associated glycans may be very suitable targets for both therapy and imaging, taking into account their often low abundance or absence on normal tissues and very dense expression on a wide range of tumors (Figure 3A). <sup>170,171</sup> Secondly, as glycans are expressed on the outermost layer on the cell surface, they are highly likely to be accessible by administrated targeting vehicles, in contrast to membrane-bound proteins, that may even be masked by glycans (Figure 3B). Thirdly, glycosylation changes may be more pronounced as a response to disease compared to changes in the proteome, with atypically-expressed glycans potentially present on many glycoproteins, essentially amplifying their expression. 172,173 These characteristics provide major advantages for imaging of early cancer stages onward, but also for the employment as a serum biomarker for diagnosis, follow-up, monitoring of therapeutic response or patient stratification, with CA19.9/sLea as the most illustrative example for monitoring of pancreatic cancer (Figure 3C). 171,174,175 But most importantly, glycan-directed tracers target multiple tumor-associated proteins simultaneously and provide a broader tumor-targeting strategy than individual protein targeting (Figure 3D). Within this context, especially mucin-type O-glycan sTn poses a suitable pan-carcinoma glycotarget, given its high, tumorspecific expression on oncoprotein CD44 as well as MUC1, MUC2, MUC5AC, and MUC6.85

Nevertheless, despite over 50 years of glycobiology, glycan-targeting seems still in its infancy. There may be several reasons for this, probably related to difficulties in anti-glycan mAb development. <sup>176</sup> Glycans are not very immunogenic,

FIGURE 3 Schematic comparison of glycan-targeting versus traditional (glyco)protein targeting for molecular imaging of tumors. (A) Tumor-associated glycans (dark blue branches) are densely packed on multiple proteins (displayed in pink and dark blue) with higher density than binding epitopes on tumor-associated proteins (displayed in yellow). This may result in a denser accumulation of conjugated antibodies, subsequently enhancing tumor signal during imaging. (B) Glycans form the outer layer of proteins, making them easily accessible to administered targeting moieties. Noteworthily, glycans may mask binding domains on proteins, challenging specific binding of protein-directed targeting moieties. (C) As aberrantly expressed glycans may be expressed on many glycoproteins (amplified expression), changes in glycoprotein glycosylation are more attractive for use as serum biomarkers than targeting of individual glycoproteins. (D) As similar tumor-associated glycan structures are expressed on multiple tumor-associated proteins, glycan-targeting can be more efficient compared to single protein targeting.



which results in a major disadvantage: hybridoma-produced mAbs against glycans are often IgM pentamers that are less optimal, if not unsuitable, for *in vivo* targeting due to their low affinity and large size, essentially preventing extravasation.<sup>107,177-179</sup> Of note, several *N*-glycans are intrinsically expressed by host species used in mAb production, which may explain low glycan immunogenicity. Thus, non-immunoglobin-derived targeting moieties, for which production is less dependent on sufficient immunogenicity, such as aptamers, lectins and boronic acid derivatives, may represent promising alternatives to mAbs.<sup>176</sup> Alternatively,

efforts have been made to improve glycan immunogenicity via various complex immunization protocols, with several successes.83,87 Also, the current lack of high-throughput screening methods, which are essential considering the extraordinarily high number of glycan structures, challenges the development of anti-glycan mAbs. 176,180 As groups of glycans - and particularly N-glycans - may be structurally highly related, mAbs are often promiscuous to a certain extent and may thus interact with multiple glyco-epitopes, some of which might be present on normal tissues. 181,182 *N*-glycan targeting is therefore regularly overshadowed by the potential of O-glycans. However, as novel techniques such as MALDI-TOF-MSI have recently improved N-glycan detection, and are estimated to increasingly contribute to the identification of novel tumor-specific N-glycans, the development of tracers targeting a very specific *N*-glycan structure seems feasible in the near future. 183 In fact, various studies have already indicated that several serum *N*-glycan profiles have extraordinarily high sensitivities and specificities for diagnosis of diverse cancer types. 184-186 Lastly, the translation of the results of preclinical glycan-based imaging studies to the human situation is often confounded. As mice do not express fucosyltransferase-3, a major enzyme involved in Lewis glycan synthesis, 187 and their glycome is in various respects not directly comparable to humans, this undoubtedly results in overestimation of TBR imaging contrast in studies evaluating these glycans as an imaging target. Therefore, the use of transgenic mice seems inevitable, but the same is true for virtually all protein-directed tracers.

### CONCLUSION

The search for novel tumor-specific targets for targeted therapy and molecular imaging is an ever-continuing topic of research. Aberrant glycosylation of proteins and lipids, and overexpression of mucins and proteoglycans is an increasingly relevant feature of cancer, providing tumor cells with unique attributes associated with disease progression. Although, the perfect pan-carcinoma target may not exist, tumor-associated glycans and heavily glycosylated proteins form a panel of targets that deserves extensive attention. As described here, glycan targeting, whilst remaining challenging, potentially offers major advantages over protein targeting for imaging and therapy. Several promising targeting moieties are currently available, of which some have been already evaluated for imaging and therapeutic purposes. In this review, we summarized the ongoing research within the field of glycan imaging and intended to provide a firm foundation for glycan-based improvement of cancer care in the near future.

### REFERENCES

- 1 Fass L. Imaging and cancer: a review. Molecular oncology. 2008;2(2):115-52.
- Weissleder R. Molecular Imaging in Cancer. 2006;312(5777):1168-71.
- Clin Oncol. 2008;26(24):4012-21.
- Munkley J, Elliott DJ. Hallmarks of glycosylation in cancer. Oncotarget. 2016;7(23):35478-89.
- 5 Wong CH. Protein glycosylation: new challenges and opportunities. J Org Chem. 2005;70(11):4219-25.
- Varki A, Kornfeld S. Historical Background and Overview. In: Varki A, Cummings RD, Esko JD, Stanley P, Hart GW, Aebi M, et al., editors. Essentials of Glycobiology. Cold Spring Harbor (NY): Cold Spring Harbor Laboratory Press; 2015. p. 1-18.
- Pinho S, Marcos NT, Ferreira B, Carvalho AS, Oliveira MJ, Santos-Silva F, et al. Biological significance of cancerassociated sialyl-Tn antigen: modulation of malignant phenotype in gastric carcinoma cells. Cancer Lett. 2007;249(2):157-70.
- Munkley I. The Role of Sialvl-Tn in Cancer, Int I Mol Sci. 2016;17(3):275.
- Blanas A. Sahasrabudhe NM. Rodríguez E. van Koovk Y. van Vliet SJ. Fucosylated Antigens in Cancer: An Alliance toward Tumor Progression, Metastasis, and Resistance to Chemotherapy. Front Oncol. 2018;8:39.
- 10 Reily C, Stewart TJ, Renfrow MB, Novak J. Glycosylation in health and disease. Nature reviews Nephrology. 2019;15(6):346-66.
- 11 Sakuma S, Yu JY, Quang T, Hiwatari K, Kumagai H, Kao S, et al. Fluorescence-based endoscopic imaging of Thomsen-Friedenreich antigen to improve early detection of colorectal cancer. Int J Cancer. 2015;136(5):1095-103.
- 12 Kumar SR, Gallazzi FA, Quinn TP, Deutscher SL. (64)Culabeled peptide for PET of breast carcinomas expressing the Thomsen-Friedenreich carbohydrate antigen. J Nucl Med. 2011;52(11):1819-26.
- 13 Coustets M. Ladurantie C. Bellard E. Prat M. Rols MP. Ecochard V, et al. Development of a near infrared protein nanoprobe targeting Thomsen-Friedenreich antigen for intraoperative detection of submillimeter nodules in an ovarian peritoneal carcinomatosis mouse model. Biomaterials. 2020;241:119908.
- 14 Danussi C, Coslovi A, Campa C, Mucignat MT, Spessotto P, Uggeri F, et al. A newly generated functional antibody identifies Tn antigen as a novel determinant in the cancer cell-lymphatic endothelium interaction. Glycobiology. 2009;19(10):1056-67.
- 15 Gong L, Ding H, Long NE, Sullivan BJ, Martin EW, Jr., Magliery TJ, et al. A 3E8.scFv.Cys-IR800 Conjugate Targeting TAG-72 in an Orthotopic Colorectal Cancer Model. Mol Imaging Biol. 2018;20(1):47-54.
- 16 Zou P, Xu S, Povoski SP, Wang A, Johnson MA, Martin EW, Ir., et al. Near-infrared fluorescence labeled anti-TAG-72 monoclonal antibodies for tumor imaging in colorectal cancer xenograft mice. Mol Pharm. 2009;6(2):428-40.
- 17 Zou P, Povoski SP, Hall NC, Carlton MM, Hinkle GH, Xu RX, et al. 124I-HuCC49deltaCH2 for TAG-72 antigendirected positron emission tomography (PET) imaging of

- LS174T colon adenocarcinoma tumor implants in xenograft mice: preliminary results. World J Surg Oncol. 2010;8:65.
- 18 Knight JC, Mosley M, Uyeda HT, Cong M, Fan F, Faulkner S, et al. In Vivo Pretargeted Imaging of HER2 and TAG-72 Expression Using the HaloTag Enzyme. Molecular pharmaceutics. 2017;14(7):2307-13.
- Frangioni JV. New technologies for human cancer imaging. 19 Chinn PC, Morena RA, Santoro DA, Kazules T, Kashmiri SV. Schlom I. et al. Pharmacokinetics and tumor localization of (111)in-labeled HuCC49DeltaC(H)2 in BALB/c mice and athymic murine colon carcinoma xenograft. Cancer Biother Radiopharm. 2006;21(2):106-16.
  - 20 Rossin R, Läppchen T, van den Bosch SM, Laforest R, Robillard MS. Diels-Alder reaction for tumor pretargeting: in vivo chemistry can boost tumor radiation dose compared with directly labeled antibody. J Nucl Med. 2013;54(11):1989-95.
  - 21 Rossin R, van Duijnhoven SMJ, Läppchen T, van den Bosch SM, Robillard MS. Trans-Cyclooctene Tag with Improved Properties for Tumor Pretargeting with the Diels-Alder Reaction. Molecular Pharmaceutics. 2014;11(9):3090-6.
  - 22 Houvast RD, Baart VM, Bhairosingh SS, Cordfunke RA, Chua JX, Vankemmelbeke M, et al. Glycan-Based Nearinfrared Fluorescent (NIRF) Imaging of Gastrointestinal Tumors: a Preclinical Proof-of-Concept In Vivo Study. Mol
  - 23 McElroy M, Kaushal S, Luiken GA, Talamini MA, Moossa AR, Hoffman RM, et al. Imaging of primary and metastatic pancreatic cancer using a fluorophore-conjugated anti-CA19-9 antibody for surgical navigation. World J Surg. 2008;32(6):1057-66.
  - 24 Hiroshima Y, Maawy A, Zhang Y, Murakami T, Momiyama M, Mori R, et al. Metastatic recurrence in a pancreatic cancer patient derived orthotopic xenograft (PDOX) nude mouse model is inhibited by neoadjuvant chemotherapy in combination with fluorescence-guided surgery with an anti-CA 19-9-conjugated fluorophore. PLoS One. 2014:9(12):e114310.
  - 25 Girgis MD, Kenanova V, Olafsen T, McCabe KE, Wu AM, Tomlinson JS. Anti-CA19-9 diabody as a PET imaging probe for pancreas cancer, I Surg Res. 2011;170(2):169-78.
  - 26 Girgis MD, Federman N, Rochefort MM, McCabe KE, Wu AM, Nagy JO, et al. An engineered anti-CA19-9 cysdiabody for positron emission tomography imaging of pancreatic cancer and targeting of polymerized liposomal nanoparticles. J Surg Res. 2013;185(1):45-55.
  - Escorcia FE, Steckler JM, Abdel-Atti D, Price EW, Carlin SD, Scholz WW, et al. Tumor-Specific Zr-89 Immuno-PET Imaging in a Human Bladder Cancer Model. 2018;20(5):808-15.
  - 28 Houghton JL, Abdel-Atti D, Scholz WW, Lewis JS. Preloading with Unlabeled CA19.9 Targeted Human Monoclonal Antibody Leads to Improved PET Imaging with 89Zr-5B1. Mol Pharm. 2017;14(3):908-15.
  - 29 Houghton IL, Zeglis BM, Abdel-Atti D, Sawada R, Scholz WW, Lewis JS. Pretargeted Immuno-PET of Pancreatic Cancer: Overcoming Circulating Antigen and Internalized Antibody to Reduce Radiation Doses. J Nucl Med. 2016;57(3):453-9.
  - 30 Rainey J, Maffuid P, Scholz WW, Ostrowski J, Jun HT, Resnick P, et al. Abstract 3036: PEGylated hyaluronidase increases tumor uptake of 89Zr-DFO-HuMab-5B1

- (MVT-2163) in a CA19-9 positive hyaluronanaccumulating pancreatic cancer model. Cancer Research. 2018;78(13 Supplement):3036-.
- 31 Houghton JL, Zeglis BM, Abdel-Atti D, Aggeler R, Sawada R, Agnew BJ, et al. Site-specifically labeled CA19.9-targeted immunoconjugates for the PET. NIRF, and multimodal PET/NIRF imaging of pancreatic cancer. Proc Natl Acad Sci USA. 2015;112(52):15850-5.
- 32 Hirai M, Minematsu H, Kondo N, Oie K, Igarashi K, Yamazaki N. Accumulation of liposome with Sialyl Lewis X to inflammation and tumor region: application to in vivo bio-imaging. Biochem Biophys Res Commun.
- 33 Lovqvist A, Humm JL, Sheikh A, Finn RD, Koziorowski J. Ruan S, et al. PET imaging of (86)Y-labeled anti-Lewis Y monoclonal antibodies in a nude mouse model: comparison between (86)Y and (111)In radiolabels. J Nucl Med. 2001;42(8):1281-7.
- 34 Tahtis K, Lee FT, Smyth FE, Power BE, Renner C, Brechbiel MW, et al. Biodistribution properties of (111) indium-labeled C-functionalized trans-cyclohexyl diethylenetriaminepentaacetic acid humanized 3S193 diabody and F(ab')(2) constructs in a breast carcinoma xenograft model. Clin Cancer Res. 2001;7(4):1061-72.
- 35 Wellens LM, Deken MM, Sier CFM, Johnson HR, de la Jara 50 Wu G, Maharjan S, Kim D, Kim JN, Park BK, Koh Ortiz F, Bhairosingh SS, et al. Anti-GD2-IRDye8ooCW as a targeted probe for fluorescence-guided surgery in neuroblastoma. Sci Rep. 2020;10(1):17667.
- 36 Vavere AL, Butch ER, Dearling JL, Packard AB, Navid F, Shulkin BL, et al. 64Cu-p-NH2-Bn-DOTA-hu14.18K322A, a 51 Zhang Q, Wang F, Wu Y-S, Zhang K-K, Lin Y, Zhu X-Q, et PET radiotracer targeting neuroblastoma and melanoma. J Nucl Med. 2012;53(11):1772-8.
- 37 Butch ER, Mead PE, Amador Diaz V, Tillman H, Stewart E, Mishra JK, et al. Positron Emission Tomography Detects In Vivo Expression of Disialoganglioside GD2 in Mouse Models of Primary and Metastatic Osteosarcoma. Cancer Res. 2019;79(12):3112-24.
- 38 Kimbrough CW, Hudson S, Khanal A, Egger ME, McNally LR. Orthotopic pancreatic tumors detected by optoacoustic tomography using Syndecan-1. I Surg Res. 2015;193(1):246-54.
- 39 Bailly C, Gouard S, Lacombe M, Remaud-Le Saëc P, Chalopin B, Bourgeois M, et al. Comparison of Immuno-PET of CD138 and PET imaging with (64)CuCl(2) and (18)F-FDG in a preclinical syngeneic model of multiple myeloma. Oncotarget. 2018;9(10):9061-72.
- 40 Huang X, Fan C, Zhu H, Le W, Cui S, Chen X, et al. Glypican-1-antibody-conjugated Gd-Au nanoclusters for FI/MRI dual-modal targeted detection of pancreatic cancer. Int J Nanomedicine. 2018;13:2585-99.
- 41 Li W, Xiao X, Li X, Xu Y, Ma L, Guo L, et al. Detecting GPC3-Expressing Hepatocellular Carcinoma with L5 Peptide-Guided Pretargeting Approach: In Vitro and In Vivo MR Imaging Experiments. Contrast Media Mol Imaging. 2018;2018:9169072.
- 42 Zhu D, Qin Y, Wang J, Zhang L, Zou S, Zhu X, et al. Novel Glypican-3-Binding Peptide for in Vivo Hepatocellular Carcinoma Fluorescent Imaging. Bioconjugate Chemistry. 2016:27(3):831-9.
- 43 Sham JG, Kievit FM, Grierson JR, Miyaoka RS, Yeh MM, Zhang M, et al. Glypican-3-targeted 89Zr PET imaging of

- hepatocellular carcinoma. J Nucl Med. 2014;55(5):799-804. 44 Sham JG, Kievit FM, Grierson JR, Chiarelli PA, Miyaoka
- RS, Zhang M, et al. Glypican-3-targeting F(ab')2 for 89Zr PET of hepatocellular carcinoma, I Nucl Med. 2014;55(12):2032-7.
- 45 Zhao H. Richardson R. Talebloo N. Mukheriee P. Wang P. Moore A. uMUC1-Targeting Magnetic Resonance Imaging of Therapeutic Response in an Orthotropic Mouse Model of Colon Cancer. Mol Imaging Biol. 2019;21(5):852-60.
- 46 Ghosh SK, Uchida M, Yoo B, Ross AW, Gendler SJ, Gong J, et al. Targeted imaging of breast tumor progression and therapeutic response in a human uMUC-1 expressing transgenic mouse model. Int J Cancer. 2013;132(8):1860-7.
- 47 Wang P, Yoo B, Sherman S, Mukherjee P, Ross A, Pantazopoulos P, et al. Predictive imaging of chemotherapeutic response in a transgenic mouse model of pancreatic cancer. Int J Cancer. 2016;139(3):712-8.
- 48 Moore A, Medarova Z, Potthast A, Dai G. In vivo targeting of underglycosylated MUC-1 tumor antigen using a multimodal imaging probe. Cancer Res. 2004;64(5):1821-7.
- 49 Park JY, Hiroshima Y, Lee JY, Maawy AA, Hoffman RM, Bouvet M. MUC1 Selectively Targets Human Pancreatic Cancer in Orthotopic Nude Mouse Models, PLoS One, vol. 32015.
- H, et al. A Novel Monoclonal Antibody Targets Mucini and Attenuates Growth in Pancreatic Cancer Model. International journal of molecular sciences. 2018;19(7):2004.
- al. Dual-color labeled anti-mucin 1 antibody for imaging of ovarian cancer: A preliminary animal study. Oncology letters. 2015;9(3):1231-5.
- 52 Chen H, Zhao J, Zhang M, Yang H, Ma Y, Gu Y. MUC1 aptamer-based near-infrared fluorescence probes for tumor imaging. Mol Imaging Biol. 2015;17(1):38-48.
- 53 Moore LI, Roy LD, Zhou R, Grover P, Wu ST, Curry IM, et al. Antibody-Guided In Vivo Imaging for Early Detection of Mammary Gland Tumors. Transl Oncol. 2016;9(4):295-305.
- 54 Stergiou N. Nagel I. Pektor S. Heimes AS, Jäkel I. Brenner W, et al. Evaluation of a novel monoclonal antibody against tumor-associated MUC1 for diagnosis and prognosis of breast cancer. Int J Med Sci. 2019;16(9):1188-98.
- 55 Alirezapour B, Rasaee MJ, Jalilian AR, Rajabifar S, Mohammadnejad J, Paknejad M, et al. Development of [(6) (4)Cul-DOTA-PR81 radioimmunoconjugate for MUC-1 positive PET imaging. Nucl Med Biol. 2016;43(1):73-80.
- 56 Salouti M, Rajabi H, Babaei MH, Rasaee MJ. Breast tumor targeting with (99m)Tc-HYNIC-PR81 complex as a new biologic radiopharmaceutical, Nucl Med Biol. 2008;35(7):763-8.
- 57 Gold DV, Goldenberg DM, Karacay H, Rossi EA, Chang C-H, Cardillo TM, et al. A Novel Bispecific. Trivalent Antibody Construct for Targeting Pancreatic Carcinoma. Cancer Research. 2008;68(12):4819-26.
- 58 Cardillo TM, Karacay H, Goldenberg DM, Yeldell D, Chang C-H, Modrak DE, et al. Improved Targeting of Pancreatic Cancer. Clinical Cancer Research. 2004;10(10):3552.
- 59 Rossez Y. Burtea C. Laurent S. Gosset P. Leonard R. Gonzalez W, et al. Early detection of colonic dysplasia by magnetic resonance molecular imaging with a contrast

- agent raised against the colon cancer marker MUC5AC. Contrast Media Mol Imaging. 2016;11(3):211-21.
- 60 Olson MT, Wojtynek NE, Talmon GA, Caffrey TC, Radhakrishnan P, Ly QP, et al. Development of a MUC16-Targeted Near-Infrared Fluorescent Antibody Conjugate for Intraoperative Imaging of Pancreatic Cancer. Mol Cancer Ther. 2020;19(8):1670-81.
- 61 Sharma SK, Wuest M, Wang M, Glubrecht D, Andrais B, Lapi SE, et al. Immuno-PET of epithelial ovarian cancer: harnessing the potential of CA125 for non-invasive imaging. EJNMMI Res. 2015;4(1):60.
- 62 Sharma SK, Sevak KK, Monette S, Carlin SD, Knight JC, Wuest FR, et al. Preclinical 89Zr Immuno-PET of High-Grade Serous Ovarian Cancer and Lymph Node Metastasis. J Nucl Med. 2016;57(5):771-6.
- 63 Sharma SK, Wuest M, Way JD, Bouvet VR, Wang M, Wuest FR. Synthesis and pre-clinical evaluation of an (18) F-labeled single-chain antibody fragment for PET imaging of epithelial ovarian cancer. Am J Nucl Med Mol Imaging. 2016;6(3):185-98.
- 64 Cohen AM, Martin EW, Jr., Lavery I, Daly J, Sardi A, Aitken D, et al. Radioimmunoguided surgery using iodine 76 Simms M, Perkins A, Price M, Scholfield D, Bishop M. 125 B72.3 in patients with colorectal cancer. Arch Surg. 1991;126(3):349-52.
- 65 Arnold MW, Schneebaum S, Berens A, PETty L, Moizisik C, Hinkle G, et al. Intraoperative detection of colorectal cancer with radioimmunoguided surgery and CC49. a second-generation monoclonal antibody. Ann Surg. 1992;216(6):627-32.
- 66 Nag S, Martinez-Monge R, Nieroda C, Martin E, Jr. Radioimmunoguided-intraoperative radiation therapy in colorectal carcinoma: a new technique to precisely define the clinical target volume. Int J Radiat Oncol Biol Phys. 1999;44(1):133-7.
- 67 Xiao J, Horst S, Hinkle G, Cao X, Kocak E, Fang J, et al. Pharmacokinetics and clinical evaluation of 125I-radiolabeled humanized CC49 monoclonal antibody (HuCC49deltaC(H)2) in recurrent and metastatic colorectal cancer patients. Cancer Biother Radiopharm. 2005;20(1):16-26.
- 68 Fang L, Holford NHG, Hinkle G, Cao X, Xiao JJ, Bloomston M, et al. Population Pharmacokinetics of Humanized Monoclonal Antibody HuCC49∆CH2 and Murine Antibody CC49 in Colorectal Cancer Patients. The Journal of Clinical Pharmacology. 2007;47(2):227-37.
- 69 Lohrmann C, O'Reilly EM, O'Donoghue JA, Pandit-Taskar N, Carrasquillo JA, Lyashchenko SK, et al. Retooling a Blood-Based Biomarker: Phase I Assessment of the High-Affinity CA19-9 Antibody HuMab-5B1 for Immuno-PET Imaging of Pancreatic Cancer. Clin Cancer Res. 2019;25(23):7014-23.
- 70 Pai-Scherf LH, Carrasquillo JA, Paik C, Gansow O, Whatley 85 Julien S, Videira PA, Delannoy P. Sialyl-tn in cancer: (how) M, Pearson D, et al. Imaging and phase I study of 111Inand 90Y-labeled anti-LewisY monoclonal antibody B3. Clin 86 Trinchera M. Aronica A. Dall'Olio F. Selectin Ligands Cancer Res. 2000;6(5):1720-30.
- 71 Ouaia E. Krug LM, Pandit-Taskar N, Nagel A, Reuter VE. Humm J, et al. The value of gamma camera and computed tomography data set coregistration to assess Lewis Y antigen targeting in small cell lung cancer by (111)Indiumlabeled humanized monoclonal antibody 3S193. Eur J Radiol. 2008:67(2):292-9.

- 72 Reuland P, Geiger L, Thelen MH, Handgretinger R, Haase B, Müller-Schauenburg W, et al. Follow-up in neuroblastoma: comparison of metaiodobenzylguanidine and a chimeric anti-GD2 antibody for detection of tumor relapse and therapy response. J Pediatr Hematol Oncol. 2001;23(7):437-42.
- 73 Yeh SD, Larson SM, Burch L, Kushner BH, Laquaglia M, Finn R, et al. Radioimmunodetection of neuroblastoma with iodine-131-3F8: correlation with biopsy, iodine-131-metaiodobenzylguanidine and standard diagnostic modalities. J Nucl Med. 1991;32(5):769-76.
- 74 Larson SM, Pentlow KS, Volkow ND, Wolf AP, Finn RD, Lambrecht RM, et al. PET scanning of iodine-124-3F9 as an approach to tumor dosimetry during treatment planning for radioimmunotherapy in a child with neuroblastoma. I Nucl Med. 1992;33(11):2020-3.
- 75 Hughes O, Perkins A, Frier M, Wastie M, Denton G, Price M, et al. Imaging for staging bladder cancer: a clinical study of intravenous 111indium-labelled anti-MUC1 mucin monoclonal antibody C595. BJU international. 2001;87(1):39-46.
- 99mTechnetium-C595 radioimmunoscintigraphy: a potential staging tool for bladder cancer. BJU international. 2001:88(7):686-91.
- 77 Gulec SA, Cohen SJ, Pennington KL, Zuckier LS, Hauke RI. Horne H. et al. Treatment of advanced pancreatic carcinoma with 90Y-Clivatuzumab Tetraxetan: a phase I single-dose escalation trial. Clin Cancer Res. 2011;17(12):4091-100.
- 78 Li M, Song L, Qin X. Glycan changes: cancer metastasis and anti-cancer vaccines. J Biosci. 2010;35(4):665-73.
- 79 Ohtsubo K, Marth JD. Glycosylation in cellular mechanisms of health and disease. Cell. 2006;126(5):855-67.
- 80 Varki A. Biological roles of glycans. Glycobiology. 2017;27(1):3-49.
- 81 Brockhausen I. Pathways of O-glycan biosynthesis in cancer cells. Biochim Biophys Acta. 1999;1473(1):67-95.
- 82 Vankemmelbeke M, Chua JX, Durrant LG. Cancer cell associated glycans as targets for immunotherapy. Oncoimmunology. 2016;5(1):e1061177.
- 83 Tivadar ST, McIntosh RS, Chua JX, Moss R, Parsons T, Zaitoun AM, et al. Monoclonal Antibody Targeting Sialyl-di-Lewisa - Containing Internalizing and non-Internalizing Glycoproteins with Cancer Immunotherapy Development Potential. Mol Cancer Ther. 2019.
- 84 Blanas A, Sahasrabudhe NM, Rodríguez E, van Kooyk Y, van Vliet SJ. Fucosylated Antigens in Cancer: An Alliance toward Tumor Progression, Metastasis, and Resistance to Chemotherapy. 2018;8(39).
- did we miss the target? Biomolecules. 2012;2(4):435-66.
- Sialyl-Lewis a and Sialyl-Lewis x in Gastrointestinal Cancers. Biology, 2017;6(1):16.
- 87 Prendergast JM, Galvao da Silva AP, Eavarone DA, Ghaderi D, Zhang M, Brady D, et al. Novel anti-Sialyl-Tn monoclonal antibodies and antibody-drug conjugates demonstrate tumor specificity and anti-tumor activity. MAbs. 2017;9(4):615-27.

- 88 Eavarone DA, Al-Alem L, Lugovskoy A, Prendergast JM, Nazer RI, Stein JN, et al. Humanized anti-Sialyl-Tn antibodies for the treatment of ovarian carcinoma. PLoS One. 2018;13(7):e0201314.
- 89 Madjd Z, Parsons T, Watson NF, Spendlove I, Ellis I, Durrant LG. High expression of Lewis v/b antigens is associated with decreased survival in lymph node negative breast carcinomas. Breast Cancer Res. 2005;7(5):R780-7.
- 90 Lottich SC, Johnston WW, Szpak CA, Delong ER, Thor A, Schlom J. Tumor-associated antigen TAG-72: correlation of expression in primary and metastatic breast carcinoma lesions. Breast Cancer Res Treat. 1985;6(1):49-56.
- 91 Loureiro LR, Sousa DP, Ferreira D, Chai W, Lima L, Pereira C, et al. Novel monoclonal antibody L2A5 specifically targeting sialyl-Tn and short glycans terminated by alpha-2-6 sialic acids. Scientific Reports. 2018;8(1):12196.
- 92 Johnston WW, Szpak CA, Thor A, Schlom J. Phenotypic characterization of lung cancers in fine needle aspiration biopsies using monoclonal antibody B72.3. Cancer Res. 1986;46(12 Pt 1):6462-70.
- 93 Kadota A, Masutani M, Takei M, Horie T. Evaluation of expression of CD15 and sCD15 in non-small cell lung cancer. Int I Oncol. 1999;15(6):1081-9.
- 94 Kajiwara H, Yasuda M, Kumaki N, Shibayama T, Osamura Y. Expression of carbohydrate antigens (SSEA-1, sialyl-Lewis X, DU-PAN-2 and CA19-9) and E-selectin in urothelial carcinoma of the renal pelvis, ureter, and urinary bladder. Tokai J Exp Clin Med. 2005;30(3):177-82.
- 95 Pochechueva T, Jacob F, Fedier A, Heinzelmann-Schwarz V. Tumor-associated glycans and their role in gynecological cancers: accelerating translational research by novel highthroughput approaches. Metabolites. 2012;2(4):913-39.
- 96 Contessa JN, Bhojani MS, Freeze HH, Rehemtulla A, Lawrence TS. Inhibition of N-linked glycosylation disrupts receptor tyrosine kinase signaling in tumor cells. Cancer Res. 2008;68(10):3803-9.
- 97 Yue T, Maupin KA, Fallon B, Li L, Partyka K, Anderson MA, et al. Enhanced discrimination of malignant from benign pancreatic disease by measuring the CA 19-9 antigen on specific protein carriers. PLoS One. 2011:6(12):e29180.
- 98 Pinto R, Carvalho AS, Conze T, Magalhães A, Picco G, Burchell JM, et al. Identification of new cancer biomarkers based on aberrant mucin glycoforms by in situ proximity ligation. J Cell Mol Med. 2012;16(7):1474-84.
- 99 Sarrats A, Saldova R, Pla E, Fort E, Harvey DJ, Struwe WB, et al. Glycosylation of liver acute-phase proteins in pancreatic cancer and chronic pancreatitis. Proteomics Clin Appl. 2010;4(4):432-48.
- 100 Balmaña M, Sarrats A, Llop E, Barrabés S, Saldova R, Ferri MI, et al. Identification of potential pancreatic cancer serum markers: Increased sialyl-Lewis X on ceruloplasmin. Clinica Chimica Acta. 2015;442:56-62.
- 101 Balmaña M, Duran A, Gomes C, Llop E, López-Martos R, Ortiz MR, et al. Analysis of sialyl-Lewis x on MUC5AC and MUC1 mucins in pancreatic cancer tissues. International Journal of Biological Macromolecules. 2018;112:33-45.
- 102 Buffone A, Weaver VM. Don't sugarcoat it: How glycocalyx composition influences cancer progression. J Cell Biol. 2020;219(1).
- 103 Burdick MD, Harris A, Reid CJ, Iwamura T, Hollingsworth MA. Oligosaccharides expressed on MUC1 produced

- by pancreatic and colon tumor cell lines. J Biol Chem. 1997;272(39):24198-202.
- 104 Ozaki H, Matsuzaki H, Ando H, Kaji H, Nakanishi H, Ikehara Y, et al. Enhancement of metastatic ability by ectopic expression of ST6GalNAcI on a gastric cancer cell line in a mouse model. Clinical & experimental metastasis. 2012;29(3):229-38.
- 105 Singh R, Campbell BJ, Yu LG, Fernig DG, Milton JD, Goodlad RA, et al. Cell surface-expressed Thomsen-Friedenreich antigen in colon cancer is predominantly carried on high molecular weight splice variants of CD44. Glycobiology. 2001;11(7):587-92.
- 106 Loureiro LR, Carrascal MA, Barbas A, Ramalho JS, Novo C, Delannoy P, et al. Challenges in Antibody Development against Tn and Sialyl-Tn Antigens. Biomolecules. 2015;5(3):1783-809.
- 107 Rabu C, McIntosh R, Jurasova Z, Durrant L. Glycans as targets for therapeutic antitumor antibodies. Future Oncol. 2012;8(8):943-60.
- 108 Zhang S, Walberg LA, Ogata S, Itzkowitz SH, Koganty RR, Reddish M. et al. Immune sera and monoclonal antibodies define two configurations for the sialyl Tn tumor antigen. Cancer Res. 1995;55(15):3364-8.
- 109 Sawada R, Sun SM, Wu X, Hong F, Ragupathi G, Livingston PO. et al. Human monoclonal antibodies to sialvl-Lewis (CA19.9) with potent CDC, ADCC, and antitumor activity. Clin Cancer Res. 2011;17(5):1024-32.
- 110 Ferreira IG, Carrascal M, Mineiro AG, Bugalho A, Borralho P, Silva Z, et al. Carcinoembryonic antigen is a sialyl Lewis x/a carrier and an E-selectin ligand in non-small cell lung cancer. International journal of oncology. 2019;55(5):1033-48.
- 111 Gomes C, Almeida A, Barreira A, Calheiros J, Pinto F, Abrantes R, et al. Carcinoembryonic antigen carrying SLe(X) as a new biomarker of more aggressive gastric carcinomas. Theranostics. 2019;9(24):7431-46.
- 112 Boogerd LSF, Hoogstins CES, Schaap DP, Kusters M. Handgraaf HJM, van der Valk MJM, et al. Safety and effectiveness of SGM-101, a fluorescent antibody targeting carcinoembryonic antigen, for intraoperative detection of colorectal cancer: a dose-escalation pilot study. Lancet Gastroenterol Hepatol. 2018;3(3):181-91.
- 113 Noble P, Spendlove I, Harding S, Parsons T, Durrant LG. Therapeutic targeting of Lewis(y) and Lewis(b) with a novel monoclonal antibody 692/29. PLoS One. 2013;8(2):e54892.
- 114 Chua JX, Vankemmelbeke M, McIntosh RS, Clarke PA, Moss R, Parsons T, et al. Monoclonal Antibodies Targeting LecLex-Related Glycans with Potent Antitumor Activity. Clin Cancer Res. 2015;21(13):2963-74.
- 115 Shimomura O, Oda T, Tateno H, Ozawa Y, Kimura S, Sakashita S, et al. A Novel Therapeutic Strategy for Pancreatic Cancer: Targeting Cell Surface Glycan Using rBC2LC-N Lectin-Drug Conjugate (LDC). Mol Cancer Ther. 2018;17(1):183-95.
- 116 Mishra A, Behura A, Mawatwal S, Kumar A, Naik L, Mohanty SS, et al. Structure-function and application of plant lectins in disease biology and immunity. Food Chem Toxicol, 2019:134:110827.
- 117 Tiernan JP, Ansari I, Hirst NA, Millner PA, Hughes TA, Jayne DG. Intra-operative tumour detection and

- staging in colorectal cancer surgery. Colorectal Disease. 2012;14(9):e510-e20.
- 118 Ohmi Y. Kambe M. Ohkawa Y. Hamamura K. Tajima O, Takeuchi R, et al. Differential roles of gangliosides in malignant properties of melanomas. PloS one. 2018:13(11):e0206881-e.
- 119 Marquina G, Waki H, Fernandez LE, Kon K, Carr A, Valiente O, et al. Gangliosides expressed in human breast cancer. Cancer Res. 1996;56(22):5165-71.
- 120 Kong Y, Yu J, Si L, Chi Z, Cui C, Sheng X, et al. Abstract 2303: The expression of gangliosides GD2 is associated with worse prognosis in melanoma patients. Cancer Research. 2016;76(14 Supplement):2303-.
- 121 Roth M, Linkowski M, Tarim J, Piperdi S, Sowers R, Geller D, et al. Ganglioside GD2 as a therapeutic target for antibody-mediated therapy in patients with osteosarcoma. 140 Kufe DWJNRC. Mucins in cancer: function, prognosis and Cancer. 2014;120(4):548-54.
- 122 Schulz G, Cheresh DA, Varki NM, Yu A, Staffileno LK. Reisfeld RA. Detection of ganglioside GD2 in tumor tissues and sera of neuroblastoma patients. Cancer Res. 1984;44(12
- 123 Alessandri G. Filippeschi S. Sinibaldi P. Mornet F. Passera P. Spreafico F. et al. Influence of gangliosides on primary and metastatic neoplastic growth in human and murine cells. Cancer Res. 1987;47(16):4243-7.
- 124 Sarkar TR, Battula VL, Werden SJ, Vijay GV, Ramirez-Peña EO. Taube IH. et al. GD3 Synthase regulates epithelialmesenchymal transition and metastasis in breast cancer. Oncogene. 2015;34(23):2958-67.
- 125 Ploessl C, Pan A, Maples KT, Lowe DK. Dinutuximab: An Anti-GD2 Monoclonal Antibody for High-Risk Neuroblastoma. Ann Pharmacother. 2016;50(5):416-22.
- 126 Sait S, Modak S. Anti-GD2 immunotherapy for neuroblastoma. Expert review of anticancer therapy. 2017;17(10):889-904.
- 127 kJiao P, Otto M, Geng Q, Li C, Li F, Butch ER, et al. Enhancing both CT imaging and natural killer cellmediated cancer cell killing by a GD2-targeting nanoconstruct. J Mater Chem B. 2016;4(3):513-20.
- 128 Massaad CA, Zhang G, Pillai L, Azhdarinia A, Liu W, Sheikh KA. Fluorescently-tagged anti-ganglioside antibody 147 Muniyan S, Haridas D, Chugh S, Rachagani S, Lakshmanan selectively identifies peripheral nerve in living animals. Sci Rep. 2015;5:15766.
- 129 Yanagishita M. Function of proteoglycans in the extracellular matrix. Acta Pathol Jpn. 1993;43(6):283-93.
- 130 Elfenbein A, Simons M. Auxiliary and autonomous proteoglycan signaling networks. Methods Enzymol. 2010;480:3-31.
- 131 Wang S, Qiu Y, Bai B. The Expression, Regulation, and Biomarker Potential of Glypican-1 in Cancer. Front Oncol. 2019;9:614.
- 132 Nikitovic D, Berdiaki A, Spyridaki I, Krasanakis T, Tsatsakis A, Tzanakakis GN. Proteoglycans-Biomarkers and Targets in Cancer Therapy, Front Endocrinol (Lausanne). 2018;9:69.
- 133 Fico A. Maina F. Dono R. Fine-tuning of cell signaling by glypicans. Cell Mol Life Sci. 2011;68(6):923-9.
- 134 Filmus J, Capurro M. The role of glypicans in Hedgehog signaling. Matrix Biology. 2014;35:248-52.
- 135 Matsuo I, Kimura-Yoshida C. Extracellular distribution of diffusible growth factors controlled by heparan sulfate

- proteoglycans during mammalian embryogenesis. Philos Trans R Soc Lond B Biol Sci. 2014;369(1657).
- 136 Nagarajan A, Malvi P, Wajapeyee N. Heparan Sulfate and Heparan Sulfate Proteoglycans in Cancer Initiation and Progression. Front Endocrinol (Lausanne). 2018;9:483.
- 137 Sanderson RD, Yang Y, Purushothaman A, Khotskaya YB, Ritchie JP, Ramani VC. Proteoglycans and Cancer. In: Zent R, Pozzi A, editors. Cell-Extracellular Matrix Interactions in Cancer. New York, NY: Springer New York; 2010. p. 191-215.
- 138 Nishida T, Kataoka H. Glypican 3-Targeted Therapy in Hepatocellular Carcinoma. Cancers (Basel). 2019;11(9).
- 139 Szatmari T, Otvos R, Hjerpe A, Dobra K. Syndecan-1 in Cancer: Implications for Cell Signaling, Differentiation, and Prognostication. Dis Markers. 2015;2015:796052.
- therapy. 2009;9(12):874.
- 141 Nath S, Mukherjee P. MUC1: a multifaceted oncoprotein with a key role in cancer progression. Trends Mol Med. 2014;20(6):332-42.
- 142 Kaur S, Kumar S, Momi N, Sasson AR, Batra SK. Mucins in pancreatic cancer and its microenvironment. Nat Rev Gastroenterol Hepatol. 2013;10(10):607-20.
- 143 Tréhoux S, Duchêne B, Jonckheere N, Van Seuningen I. The MUC1 oncomucin regulates pancreatic cancer cell biological properties and chemoresistance. Implication of p42-44 MAPK, Akt, Bcl-2 and MMP13 pathways, Biochem Biophys Res Commun. 2015;456(3):757-62.
- 144 Zhou R, Curry JM, Roy LD, Grover P, Haider J, Moore LJ, et al. A novel association of neuropilin-1 and MUC1 in pancreatic ductal adenocarcinoma: role in induction of VEGF signaling and angiogenesis. Oncogene. 2016;35(43):5608-18.
- 145 Sahraei M, Roy LD, Curry JM, Teresa TL, Nath S, Besmer D, et al. MUC1 regulates PDGFA expression during pancreatic cancer progression. Oncogene. 2012;31(47):4935.
- 146 Grover P. Nath S. Nye MD. Zhou R. Ahmad M. Mukherjee P. SMAD4-independent activation of TGF-β signaling by MUC1 in a human pancreatic cancer cell line. Oncotarget. 2018;9(6):6897-910.
- I, Gupta S, et al. MUC16 contributes to the metastasis of pancreatic ductal adenocarcinoma through focal adhesion mediated signaling mechanism. Genes & cancer. 2016;7(3-4):110-24.
- 148 Inaguma S. Kasai K. Ikeda H. GLI1 facilitates the migration and invasion of pancreatic cancer cells through MUC5AC-mediated attenuation of E-cadherin. Oncogene. 2010;30:714.
- 149 Lakshmanan I, Ponnusamy MP, Das S, Chakraborty S, Haridas D, Mukhopadhyay P, et al. MUC16 induced rapid G2/M transition via interactions with JAK2 for increased proliferation and anti-apoptosis in breast cancer cells. Oncogene. 2012;31(7):805-17.
- 150 Awaya H, Takeshima Y, Yamasaki M, Inai K. Expression of MUC1, MUC2, MUC5AC, and MUC6 in atypical adenomatous hyperplasia, bronchioloalveolar carcinoma, adenocarcinoma with mixed subtypes, and mucinous bronchioloalyeolar carcinoma of the lung. Am I Clin Pathol. 2004;121(5):644-53.
- 151 Situ D, Wang J, Ma Y, Zhu Z, Hu Y, Long H, et al. Expression

- and prognostic relevance of MUC1 in stage IB non-small cell lung cancer. Med Oncol. 2011;28 Suppl 1:S596-604.
- 152 Hinoda Y, Ikematsu Y, Horinochi M, Sato S, Yamamoto K, Nakano T, et al. Increased expression of MUC1 in advanced pancreatic cancer. J Gastroenterol. 2003;38(12):1162-6.
- 153 Streppel MM, Vincent A, Mukherjee R, Campbell NR, Chen SH, Konstantopoulos K, et al. Mucin 16 (cancer antigen 125) expression in human tissues and cell lines and correlation with clinical outcome in adenocarcinomas of the pancreas, esophagus, stomach, and colon. Hum Pathol. 2012;43(10):1755-63.
- 154 Rabassa ME, Croce MV, Pereyra A, Segal-Eiras A. MUC1 expression and anti-MUC1 serum immune response in head and neck squamous cell carcinoma (HNSCC): a multivariate analysis. BMC cancer. 2006;6:253-.
- 155 Kannan A, Hertweck KL, Philley JV, Wells RB, Dasgupta S. Genetic Mutation and Exosome Signature of Human Papilloma Virus Associated Oropharyngeal Cancer. Scientific Reports. 2017;7(1):46102.
- 156 Sato S, Kato T, Abe K, Hanaoka T, Yano Y, Kurosaki A, et al. Pre-operative evaluation of circulating KL-6 levels as a biomarker for epithelial ovarian carcinoma and its correlation with tumor MUC1 expression. Oncol Lett. 2017;14(1):776-86.
- 157 Peters IT, Hilders CG, Sier CF, Vahrmeijer AL, Smit VT, Baptist Trimbos J, et al. Identification of cell-surface markers for detecting breast cancer cells in ovarian tissue. Arch Gynecol Obstet. 2016;294(2):385-93.
- 158 Heublein S, Friese K, Kost B, Marmé F, Kuhn C, Mahner S, et al. TA-MUC1 as detected by the fully humanized, therapeutic antibody Gatipotzumab predicts poor prognosis in cervical cancer. J Cancer Res Clin Oncol. 2018;144(10):1899-907.
- 159 Ginath S, Menczer J, Fintsi Y, Ben-Shem E, Glezerman M, Avinoach I. Tissue and serum CA125 expression in endometrial cancer. Int J Gynecol Cancer. 2002;12(4):372-5.
- 160 Wu G, Maharjan S, Kim D, Kim JN, Park BK, Koh H, et al. A Novel Monoclonal Antibody Targets Mucin1 and Attenuates Growth in Pancreatic Cancer Model. Int J Mol Sci. 2018;19(7).
- 161 Ghosh SK, Uchida M, Yoo B, Ross AW, Gendler SJ, Gong J, et al. Targeted imaging of breast tumor progression and therapeutic response in a human uMUC-1 expressing transgenic mouse model. 2013;132(8):1860-7.
- 162 Zhang Q, Wang F, Wu YS, Zhang KK, Lin Y, Zhu XQ, et al. Dual-color labeled anti-mucin 1 antibody for imaging of ovarian cancer: A preliminary animal study. Oncol Lett. 2015;9(3):1231-5.
- 163 Wang P, Yoo B, Sherman S, Mukherjee P, Ross A, Pantazopoulos P, et al. Predictive imaging of chemotherapeutic response in a transgenic mouse model of pancreatic cancer. International Journal of Cancer. 2016;139(3):712-8.
- 164 Fan XÑ, Karsten U, Goletz S, Cao Y. Reactivity of a humanized antibody (hPankoMab) towards a tumorrelated MUC1 epitope (TA-MUC1) with various human carcinomas. Pathol Res Pract. 2010;206(8):585-9.
- 165 Dian D, Lenhard M, Mayr D, Heublein S, Karsten U, Goletz S, et al. Staining of MUC1 in ovarian cancer tissues with PankoMab-GEX detecting the tumour-associated epitope, TA-MUC1, as compared to antibodies HMFG-1 and 115D8.

- Histol Histopathol. 2013;28(2):239-44.
- 166 Fiedler W, DeDosso S, Cresta S, Weidmann J, Tessari A, Salzberg M, et al. A phase I study of PankoMab-GEX, a humanised glyco-optimised monoclonal antibody to a novel tumour-specific MUC1 glycopeptide epitope in patients with advanced carcinomas. Eur J Cancer. 2016;63:55-63.
- 167 Gold DV, Lew K, Maliniak R, Hernandez M, Cardillo T. Characterization of monoclonal antibody PAM4 reactive with a pancreatic cancer mucin. Int J Cancer. 1994;57(2):204-10.
- 168 Gold DV, Karanjawala Z, Modrak DE, Goldenberg DM, Hruban RH. PAM4-reactive MUC1 is a biomarker for early pancreatic adenocarcinoma. Clin Cancer Res. 2007;13(24):7380-7.
- 169 Berek JS, Taylor PT, Gordon A, Cunningham MJ, Finkler N, Orr J, Jr., et al. Randomized, placebo-controlled study of oregovomab for consolidation of clinical remission in patients with advanced ovarian cancer. J Clin Oncol. 2004;22(17):3507-16.
- 170 Kudelka MR, Ju T, Heimburg-Molinaro J, Cummings RD. Simple sugars to complex disease—mucin-type O-glycans in cancer. Adv Cancer Res. 2015;126:53-135.
- 171 Stowell SR, Ju T, Cummings RD. Protein glycosylation in cancer. Annu Rev Pathol. 2015;10:473-510.
- 172 Fuster MM, Esko JD. The sweet and sour of cancer: glycans as novel therapeutic targets. Nat Rev Cancer. 2005;5(7):526-42.
- 173 Lebrilla CB, An HJ. The prospects of glycan biomarkers for the diagnosis of diseases. Mol Biosyst. 2009;5(1):17-20.
- 174 Tang H, Singh S, Partyka K, Kletter D, Hsueh P, Yadav J, et al. Glycan motif profiling reveals plasma sialyl-lewis x elevations in pancreatic cancers that are negative for sialyllewis A. Mol Cell Proteomics. 2015;14(5):1323-33.
- 175 Tang Y, Cui Y, Zhang S, Zhang L. Chapter Five The sensitivity and specificity of serum glycan-based biomarkers for cancer detection. In: Zhang L, editor. Progress in Molecular Biology and Translational Science. Academic Press; 2019. p. 121-40.
- 176 Tommasone S, Allabush F, Tagger YK, Norman J, Köpf M, Tucker JHR, et al. The challenges of glycan recognition with natural and artificial receptors. Chem Soc Rev. 2019;48(22):5488-505.
- 177 Adams GP, Weiner LM. Monoclonal antibody therapy of cancer. Nature Biotechnology. 2005;23(9):1147-57.
- 178 Eisen HN. Affinity enhancement of antibodies: how low-affinity antibodies produced early in immune responses are followed by high-affinity antibodies later and in memory B-cell responses. Cancer Immunol Res. 2014;2(5):381-92.
- 179 Cao Y, Lan Y, Qian J, Zheng Y, Hong S, Li H, et al. Targeting cell surface  $\beta_2$  -microglobulin by pentameric IgM antibodies. Br J Haematol. 2011;154(1):111-21.
- 180 Manimala JC, Roach TA, Li Z, Gildersleeve JC. Highthroughput carbohydrate microarray profiling of 27 antibodies demonstrates widespread specificity problems. Glycobiology. 2007;17(8):17c-23c.
- 181 Sterner E, Flanagan N, Gildersleeve JC. Perspectives on Anti-Glycan Antibodies Gleaned from Development of a Community Resource Database. ACS Chem Biol. 2016;11(7):1773-83.

- 182 Cummings RD, Darvill AG, Etzler ME, Hahn MG. Glycan-Recognizing Probes as Tools. In: Varki A, Cummings RD, Esko JD, Stanley P, Hart GW, Aebi M, et al., editors. Essentials of Glycobiology. Cold Spring Harbor (NY): Cold Spring Harbor Laboratory Press; 2015. p. 611-25.
- 183 Heijs B, Holst-Bernal S, de Graaff MA, Briaire-de Bruijn IH, Rodriguez-Girondo M, van de Sande MAJ, et al. Molecular signatures of tumor progression in myxoid liposarcoma identified by N-glycan mass spectrometry imaging. Lab Invest. 2020.
- 184 Liu Y, Wang C, Wang R, Wu Y, Zhang L, Liu BF, et al. Isomer-specific profiling of N-glycans derived from human serum for potential biomarker discovery in pancreatic cancer. J Proteomics. 2018;181:160-9.
- 185 Gebrehiwot AG, Melka DS, Kassaye YM, Gemechu T, Lako W, Hinou H, et al. Exploring serum and immunoglobulin G N-glycome as diagnostic biomarkers for early detection of breast cancer in Ethiopian women. BMC Cancer. 2019;19(1):588.
- 186 Oikawa M, Hatakeyama S, Yoneyma T, Tobisawa Y, Narita T, Yamamoto H, et al. Significance of Serum N-glycan Profiling as a Diagnostic Biomarker in Urothelial Carcinoma. Eur Urol Focus. 2018;4(3):405-11.
- 187 Gersten KM, Natsuka S, Trinchera M, Petryniak B, Kelly RJ, Hiraiwa N, et al. Molecular cloning, expression, chromosomal assignment, and tissue-specific expression of a murine alpha-(1,3)-fucosyltransferase locus corresponding to the human ELAM-1 ligand fucosyl transferase. J Biol Chem. 1995;270(42):25047-56.

### **CHAPTER 3**

An immunohistochemical evaluation of tumor-associated glycans and mucins as targets for molecular imaging of pancreatic ductal adenocarcinoma

Ruben D. Houvast, Kira Thijse, Jesse V. Groen, JiaXin Chua, Mireille Vankemmelbeke, Lindy G. Durrant, J. Sven D. Mieog, Bert A. Bonsing, Alexander L. Vahrmeijer, Peter J. K. Kuppen, A. Stijn L. P. Crobach, Cornelis F. M. Sier

Cancers (Basel). 2021;13(22).



### ABSTRACT

**BACKGROUND** Targeted molecular imaging may overcome current challenges in the preoperative and intraoperative delineation of pancreatic ductal adenocarcinoma (PDAC). Tumor-associated glycans Le<sup>a/c/x</sup>, sdi-Le<sup>a</sup>, sLe<sup>a</sup>, sLe<sup>x</sup>, sTn as well as mucin-1 (MUC1) and mucin-5AC (MU5AC) have gained significant interest as targets for PDAC imaging.

**METHODS** To evaluate their PDAC molecular imaging potential, biomarker expression was determined using immunohistochemistry on PDAC, (surrounding) chronic pancreatitis (CP), healthy pancreatic, duodenum, positive (LN<sup>+</sup>) and negative lymph node (LN<sup>-</sup>) tissues, and quantified using a semi-automated digital image analysis workflow.

**RESULTS** Positive expression on PDAC tissues was found on 83% for Le<sup>a</sup>/c/x, 94% for sdi-Le<sup>a</sup>, 98% for sLe<sup>a</sup>, 90% for sLe<sup>x</sup>, 88% for sTn, 96% for MUC1 and 67% for MUC5AC, where all were not affected by the application of neoadjuvant therapy. Compared to PDAC, all biomarkers were significantly lower expressed on CP, healthy pancreatic and duodenal tissues, except for sTn and MUC1, which showed a strong expression on duodenum (sTn tumor:duodenum ratio: 0.6, p < 0.0001) and healthy pancreatic tissues (MUC1 tumor:pancreas ratio: 1.0, p > 0.9999), respectively. All biomarkers are suitable targets for correct identification of LN<sup>+</sup>, as well as the distinction of LN<sup>+</sup> from LN<sup>-</sup> tissues.

**CONCLUSION** To conclude, this study paves the way for the development and evaluation of Le<sup>a/c/x</sup>-, sdi-Le<sup>a</sup>, sLe<sup>a</sup>-, sLe<sup>x</sup>- and MUC5AC-specific tracers for molecular imaging of PDAC imaging and their subsequent introduction into the clinic.

### INTRODUCTION

Pancreatic ductal adenocarcinoma (PDAC) is the seventh leading cause of cancerrelated mortality in the Western world, with a dismal 5-year survival of only 9%.1 As 80–90% of patients present with locally advanced or metastatic disease, radical surgical resection, which is the only curative therapy, is often not feasible. Extensive preoperative imaging using endoscopic ultrasound (EUS), magnetic resonance imaging (MRI) and positron emission tomography/computed tomography (PET/CT) is crucial for accurate selection and stratification of patients for surgery. Nevertheless, 20–47% of patients who qualify for surgery present with an irresectable disease at the time of surgery,<sup>2,3</sup> whereas R1 (microscopic residual disease) resections are reported in up to 80% of patients, both of which are associated with worse overall survival. 4-6 On the other hand, approximately 7% of resections for suspected pancreatic cancer are performed for benign diseases, such as chronic pancreatitis (CP).7 Considering the abundance of desmoplasia in both PDAC and CP, which may be further induced by the application of neoadjuvant therapy (NAT), distinguishing malignant from healthy or benign tissue is challenging in both a preoperative and real-time intraoperative setting.<sup>8-10</sup> By facilitating high-contrast visualization of tumor cells, targeted molecular imaging may play a key role in overcoming these challenges, potentially avoiding resection for benign and irresectable disease, while simultaneously aiming to increase radical resection rates in resectable patients.

Within the continuing search for novel targets for molecular imaging, tumorassociated glycans and mucins have gained significant interest (reviewed in<sup>11</sup>). In cancer, many proteins and lipids are aberrantly glycosylated, which results in the appearance of truncated *O*-glycans, such as sialyl-Thomsen-Nouveau (sTn) and Lewis glycans, such as sialyl-Lewis<sup>a</sup> (sLe<sup>a</sup>) and sialyl-Lewis<sup>x</sup> (sLe<sup>x</sup>), Lewis<sup>a/c/x</sup> (Le<sup>a/c/x</sup>), sialyl-di-Lewis<sup>a</sup> (sdi-Le<sup>a</sup>) and related glyco-epitopes.<sup>12-15</sup> Some of these structures, such as sLe<sup>a</sup> and sLe<sup>x</sup>, are involved in tumor progression, both directly and indirectly by applying conformational changes to their carrier protein.<sup>16,17</sup>

In reference to glycans, mucins, which are high-molecular-weight proteins that are extensively coated with *O*-glycans, seem interesting tumor-specific targets based on their high expression on tumor tissues, low abundance in healthy tissues and pivotal roles in carcinogenesis<sup>18,19</sup> Especially, transmembrane mucin-1 (MUC1) and secreted mucin-5AC (MUC5AC), which are both, directly and indirectly, involved in tumor progression via their truncated sTn glycans, are considered promising targets for PDAC targeting.<sup>18</sup> As a result of mucin overexpression, tumor-associated glycans become strongly amplified on the outermost layer of multiple proteins simultaneously, making them a set of high-potential molecular

imaging targets with advantages for targeting beyond proteins.<sup>11,20</sup> Although the aforementioned tumor-associated *O*-glycans and mucins are strongly expressed on pancreatic cancers cells, their relative expression on (surrounding) chronic pancreatitis as well as on healthy pancreas and duodenum and metastatic lymph nodes, which defines their molecular imaging suitability, is underexplored.

Therefore, the current study aims to evaluate and compare the potential of tumor-associated glycans Le<sup>a/c/x</sup>, sdi-Le<sup>a</sup>, sLe<sup>a</sup>, sLe<sup>x</sup> and sTn, and mucins MUC1 and MUC5AC for molecular imaging of PDAC using a semi-automated, machine learning-based digital image analysis workflow.

### MATERIALS AND METHODS

### Patient and tissue selection

Medical records and pathology reports from patients who underwent pancreatic resection in the Leiden University Medical Center (LUMC) between August 2011 and July 2020 were retrospectively reviewed. Patients older than 18 years diagnosed with PDAC or CP were considered suitable for inclusion in the study. Representative formalin-fixed paraffin-embedded tissue blocks containing PDAC, CP, healthy pancreatic, healthy duodenum, LN+ and LN- tissues were obtained from the Pancreas Biobank of the LUMC. All tissue samples were assessed by a hepatopancreaticobiliary pathologist (ASLPC) before inclusion in the study. Both peritumoral pancreatitis and primary CP tissues were categorized as CP. Clinicopathological data were retrospectively collected from hospital records. R1 resection was defined as the presence of tumor cells at ≤1 mm from the surgical margin. Pathological T (pT) and pathological N (pN) stages were defined according to the 8th edition of the American Joint Committee on Cancer/Union for International Cancer Control (AJCC/UICC) TNM staging system for pancreatic cancer. The study protocol was approved by the Gastroenterology Biobank Review Committee (protocol reference: 2020-16) and local medical ethical review committee (protocol reference: B20.052). The research was conducted in accordance with the Dutch code of conduct for responsible use of human tissue in medical research. Tissue samples and patient data were used anonymously and in compliance with the Declaration of Helsinki (1964).

### Monoclonal antibodies and reagents

Le<sup>a/c/x</sup>, sdi-Le<sup>a</sup>, sLe<sup>a</sup>, sLe<sup>x</sup>, sTn, MUC1 and MUC5AC were selected based on their expected specificity for PDAC. The primary and secondary mAbs and other reagents are listed in Table S1 (see Supplementary Materials).

### Immunohistochemistry (IHC)

The 4-µm-thick formalin-fixed paraffin-embedded tissue sections were placed on glass slides. The sections were deparaffinized in xylene for 15 min, rehydrated in a series of 100%, 50%, 25% ethanol dilutions and rinsed in demineralized water. Next, endogenous peroxidase was blocked for 20 min using 0.3% hydrogen peroxide in demineralized water. Antigen retrieval was subsequently performed as described in Table S1. After cooling in phosphate-buffered saline (PBS, pH 7.4), sections were incubated overnight in a humidified chamber at room temperature with 150 μL primary antibody using a predetermined optimal dilution (see Table S1). Next, slides were washed three times in PBS for 5 min and incubated with appropriate secondary antibodies, followed by an additional washing step. Staining was visualized through incubation with 3,3-diaminobenzidine tetrahydrochloride solution (DAB, K3468, Agilent Technologies, Inc., Santa Clara, CA, USA) for 10 min at room temperature. Sections were then counterstained with Mayer's hematoxylin solution (Sigma-Aldrich, Saint Louis, MO, USA). After dehydration in an incubator for 1 h at 37 °C, slides were mounted with Pertex (Leica Microsystems, Wetzlar, Germany).

### Semi-automated imaging analysis

Whole slide images of tissue sections were captured using a PANNORAMIC® 250 Flash III DX scanner (3DHISTECH Ltd., Budapest, Hungary) and imported into QuPath v.o.2.3.<sup>21</sup> All tissue slides were scanned using similar settings to exclude variability during image analysis. A detailed description and graphic representation of the object classifier training, validation and semi-automated image analysis workflow is included in the Supplementary Materials. Briefly, random forest object classifiers for PDAC, pancreatic (healthy pancreas and CP), healthy duodenal, positive lymph node (LN<sup>+</sup>) and negative lymph node (LN<sup>-</sup>) tissue classes were built for each biomarker.<sup>22</sup> QuPath parameters used for automated cell detection are listed in Table S2. Object classifiers were trained until they provided detection of their respective cell type with a sensitivity, specificity, positive predictive value (PPV), negative predictive value (NPV) and accuracy of ≥85%, as depicted in Figure S1. Next, tissue class-, biomarker-specific scripts allowing semi-automated cell detection, segmentation, object classifier application and classification of DAB staining intensity were generated as shown in Figure S2. DAB staining intensity was classified as negative, low (1+), moderate (2+) or strong (3+). Next, PDAC, CP, healthy pancreas, healthy duodenum, LN<sup>+</sup> and LN<sup>-</sup> regions were then annotated on the full cohort by a pathologist (ASLPC), after which the respective script was run (Figure S2). Staining was quantified using the H-score (formula:  $1 \times (\% \text{cells 1+}) + 2 \times (\% \text{cells 2+}) + 3 \times (\% \text{cells 3+})$ , range: 0-300). Immunohistochemical staining with an H-score  $\geq 51$  was regarded positive.<sup>23</sup>

### **Statistical Analysis**

Statistical analysis and graph generation were performed using IBM SPSS statistics (version 25, IBM Corporation, Somer, NY, USA) and GraphPad Prism (version 8, GraphPad Software, La Jolla, CA, USA). Baseline characteristics between groups were compared using a Chi-square test for categorical data, an unpaired t-test for normally distributed data or Mann–Whitney U test for nonparametric data. Mean H-scores were compared using one-way ANOVA with Bonferroni correction ( $\geq$ 3 groups) or an unpaired t-test (2 groups). Receiver operating characteristic (ROC) curves were drawn to calculate area under the curve (AUC) for LN<sup>+</sup> vs. LN<sup>-</sup> detection based on H-score. Differences with a *p*-value < 0.05 were considered statistically significant.

### RESULTS

### **Patient characteristics**

Tissues from 53 patients primarily diagnosed with PDAC and 9 patients diagnosed with CP were obtained. The clinicopathological data of this cohort are summarized in Table 1. Of the PDAC cohort, 22 patients received NAT, of which 15 patients received chemoradiotherapy and 7 patients received chemotherapy. NAT patients were significantly younger (p = 0.033) had significantly lower pN stages (p < 0.001), smaller tumors (p = 0.024) and lower serum CA19-9 levels (p = 0.007) compared to PDAC patients who did not receive NAT. Slides containing PDAC tissue were not available for 5 patients. In total, tissue blocks containing 48 PDAC, 28 CP, 31 healthy pancreatic, 10 healthy duodenal, 27 LN<sup>+</sup> and 41 LN<sup>-</sup> tissues derived of 62 patients (53 PDAC and 9 CP patients) were included in the study.

### Object classifier training and validation

To prepare the scripts for semi-automated image analysis, thirty-five tissue class, biomarker-specific object classifiers were trained and validated as described in the Supplementary Materials. Briefly, after extensive training, sensitivity, specificity, PPV, NPV and accuracy were above the predetermined threshold of 85% for all object classifiers separately, allowing highly accurate detection and classification of its cell type of interest (Table S<sub>3</sub>).

**TABLE 1** Characteristics of PDAC patients (n = 53) and CP patients (n = 9)\*. PDAC patients are categorized into NAT and no NAT patients. *p*-values represent differences between NAT and no NAT patients.

Characteristic	Total PDAC $(n = 53)$	NAT (n = 22)	No NAT (n = 31)	<i>p</i> -value	CP (n = 9)
Age, years, mean (SD)	64.7 (9.8)	61.3 (9.1)	67.1 (9.7)	0.033	53.5 (10.9)
Gender, <i>n</i> (%)					
Male	26 (49)	9 (41)	17 (55)	0.406	8 (89)
Female	27 (51)	13 (59)	14 (45)		1 (11)
Surgery type, $n$ (%)					
Pancreaticoduodenectomy	41 (77)	16 (73)	25 (81)	0.632	4 (44)
Pancreatic corpus/tail resection	9 (17)	4 (18)	5 (16)		5 (56)
Total pancreatectomy	3 (6)	2 (9)	1(3)		0 (0)
Tumor differentiation, $n$ (%)					
Good	6 (11)	1(5)	5 (16)	0.607	-
Moderate	12 (23)	1 (5)	11 (36)		-
Poor	18 (34)	4 (18)	14 (45)		-
Missing	17 (32)	16 (73)	1(3)		-
Primary tumor, n (%)					
pT1	18 (34)	10 (46)	8 (26)	0.275	-
pT2	27 (51)	10 (46)	17 (55)		-
pT3	8 (15)	2 (9)	6 (19)		-
Regional lymph nodes, n (%)					
pN0	18 (34)	13 (59)	5 (16)	< 0.001	-
pN1	21 (40)	9 (41)	12 (39)		-
pN2	14 (26)	0 (0)	14 (45)		-
Surgical margin status, n (%)					
RO	29 (55)	15 (68)	14 (45)	0.161	-
R1	24 (45)	7 (32)	17 (55)		-
NAT, n (%)					
No	31 (59)	0 (0)	31 (100)	-	8 (89)
Yes, chemoradiotherapy	15 (28)	15 (68)	0 (0)	-	0 (0)
Yes, chemotherapy	7 (13)	7 (32)	0 (0)	-	1 (11)
Tumor size, mm, mean (SD)	26 (13)	22 (11)	30 (13)	0.024	-
Serum CEA, μg/L, median (IQR)	3.2 (5.9)	3.2 (6.5)	3.5 (5.2)	0.349	-
Serum CA19-9, kU/L, median (IQR)	74.5 (377.5)	48.4 (69.7)	322.8 (371.6)	0.007	-

<sup>\*</sup> Patients primarily diagnosed with CP are listed in the table as a separate cohort next to PDAC patients. CP: chronic pancreatitis, IQR: interquartile range, NA: not applicable, NAT: neoadjuvant therapy, PDAC: pancreatic ductal adenocarcinoma, SD: standard deviation.

### Biomarker expression on PDAC, CP, healthy pancreatic and duodenal tissues

The cohort was stained for Le<sup>a/c/x</sup>, sdi-Le<sup>a</sup>, sLe<sup>a</sup>, sLe<sup>x</sup>, sTn, MUC1 and MUC5AC (Figure 1), followed by semi-automated imaging analysis. H-scores scatter plots showing IHC staining of all biomarkers on PDAC, CP, healthy pancreatic and duodenal tissues are depicted in Figure 2.

Positive biomarker expression on PDAC tissues was found on 83% for Le<sup>a/c/x</sup> (4o/48), 94% for sdi-Le<sup>a</sup> (45/48), 98% for sLe<sup>a</sup> (47/48), 90% for sLe<sup>x</sup> (43/48), 88% for sTn (42/48), 96% for MUC1 (46/48) and 67% for MUC5AC (32/48), as shown in Table 2. Categorized IHC staining distributions on PDAC tissues and biomarker expression for each PDAC case separately are represented in Table 3 and in heatmap format in Figure S3, respectively. All biomarkers were highly expressed on tumor tissues and showed a tumor-specific, membranous staining pattern of PDAC cells. Le<sup>a/c/x</sup>, sdi-Le<sup>a</sup>, sLe<sup>a</sup> and sTn showed a more heterogenous staining distribution, while sLe<sup>x</sup>, MUC1 and MUC5AC staining was slightly more homogenous. Moreover, strong luminal staining was occasionally observed for Le<sup>a/c/x</sup>, sdi-Le<sup>a</sup>, sLe<sup>a</sup> and sLe<sup>x</sup>, but not for MUC1 and MUC5AC.

In CP, staining was homogenous and mainly located on acinar and ductal cells of the pancreas. Low to moderate staining was observed for  $Le^{a/c/x}$ ,  $sdi-Le^a$ ,  $sLe^a$  and MUC1, while  $sLe^x$ , sTn and MUC5AC expression was virtually absent. For all biomarkers, expression in CP was significantly lower than in PDAC, although tumor:CP ratios of only 1.7 and 1.4 were observed for  $Le^{a/c/x}$  and MUC1, respectively (Table 2).

Low to moderate Lea/c/x, sdi-Lea and sLea expression was found in healthy acinar cells, while MUC1 was highly expressed. As for CP, expression in healthy pancreatic tissue was mainly located on acinar and ductal cells. sLex, sTn and MUC5AC expression was virtually absent. Compared to PDAC, a significantly lower healthy pancreas expression was found for all biomarkers (p < 0.0001), except for MUC1 (tumor:pancreas ratio: 1.0, p > 0.9999).

In healthy duodenal tissues, low to moderate expression of  $Le^{a/c/x}$ ,  $sdi-Le^a$ ,  $sLe^a$  and MUC1 on cells of the glandular epithelium was observed, in which  $Le^{a/c/x}$  expression was more abundant relative to  $sdi-Le^a$ ,  $sLe^a$  and MUC1. Moreover, strong sTn staining was observed. Of note, occasional staining of Brunner's glands was present for  $sLe^a$ ,  $sLe^x$ , sTn, MUC1, MUC5AC, but to a lesser extent for  $Le^{a/c/x}$  and  $sdi-Le^a$  Expression on healthy duodenal tissue was significantly lower compared to PDAC for all biomarkers (p < 0.0001), except for sTn (tumor:duodenum ratio: 0.6, p < 0.0001), as shown in Table 2.

**FIGURE 1** Representative (immuno)histochemical staining of HE, Lea/c/x, sdi-Lea, sLea, sLea, sLex, sTn, MUC1 and MUC5AC expression on PDAC, CP, pancreas and duodenum tissues. Overview images and inserts are taken at  $5\times$  and  $25\times$  magnification, respectively. Scale bars represent 100  $\mu$ M. HE: hematoxylin-eosin, CP: chronic pancreatitis, PDAC: pancreatic ductal adenocarcinoma.

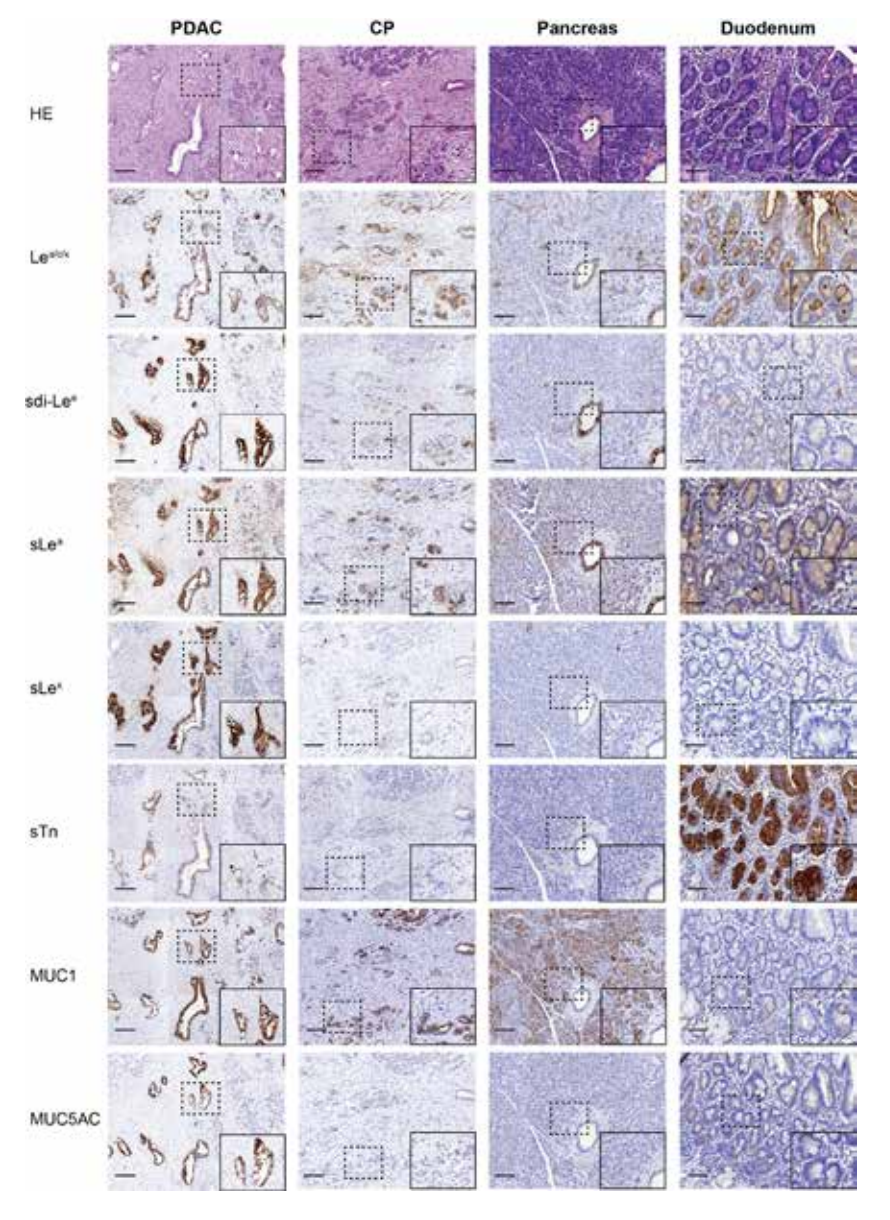


**FIGURE 2** H-score scatter plots of immunohistochemical staining of (A)  $Le^{a/c/x}$ , (B)  $sdi-Le^a$ , (C)  $sLe^a$ , (D)  $sLe^x$ , (E) sTn, (F) MUC1 and (G) MUC5AC expression on PDAC, CP, pancreas and duodenum tissues. Mean H-scores are represented by the horizontal line together with their error bars representing the 95% confidence interval. Within each tissue category, every dot represents immunohistochemical staining on one case. CP: chronic pancreatitis, Duo: duodenum, ns: not significant, Panc: pancreas, PDAC: pancreatic ductal adenocarcinoma, \*\*: p < 0.001, \*\*\*: p < 0.0001.

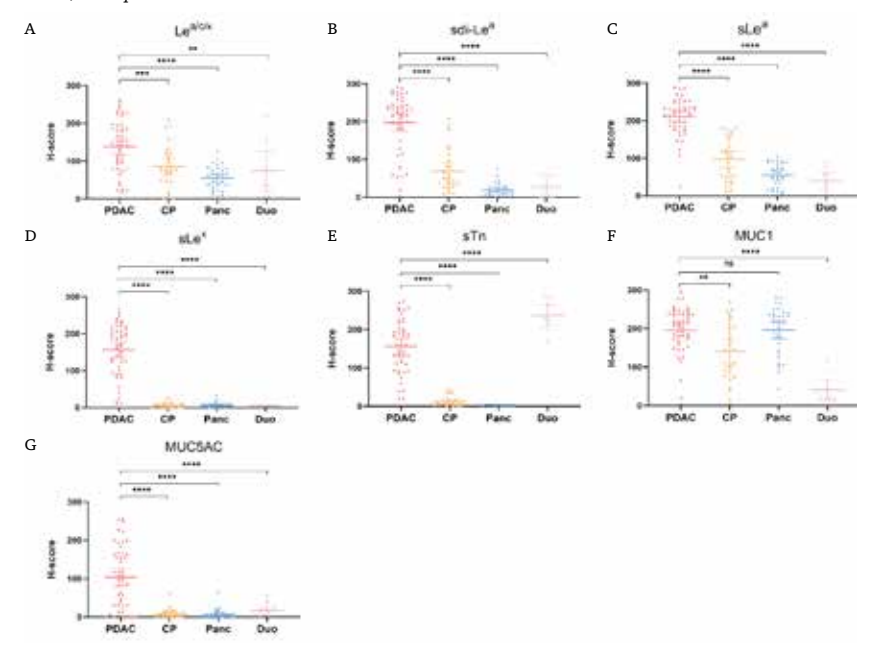


**TABLE 2** Percentage of PDAC tissues with positive immunohistochemical staining (H-score  $\geq 51$  out of 300) and mean tumor:CP, tumor:pancreas and tumor:duodenum H-score ratios, along with the *p*-value of the H-score difference.

Biomarker	PDAC Positive n (%)	Tumor: CP	<i>p</i> -value	Tumor: Pancreas	<i>p</i> -value	Tumor: Duodenum	<i>p</i> -value
I.ea/c/x			0.0010		0.0001		0.0072
Lea/c/x	40 (83)	1.7	0.0010	2.5	<0.0001	1.9	0.0073
sdi-Le <sup>a</sup>	45 (94)	2.9	< 0.0001	10.3	< 0.0001	10.0	< 0.0001
sLea	47 (98)	2.2	< 0.0001	3.8	< 0.0001	5.9	< 0.0001
sLe <sup>x</sup>	43 (90)	33.2	< 0.0001	20.9	< 0.0001	53.0	< 0.0001
sTn	42 (88)	15.6	< 0.0001	100.9	< 0.0001	0.6	< 0.0001
MUC1	46 (96)	1.4	0.0012	1.0	>0.9999	4.8	< 0.0001
MUC5AC	32 (67)	11.5	<0.0001	13.6	< 0.0001	5.6	< 0.0001

CP: chronic pancreatitis, PDAC: pancreatic ductal adenocarcinoma.

**TABLE 3** Distribution of biomarker expression on 48 PDAC tissues (*n* (%)). Expression was categorized as negative (H-score: o–50), low (H score: 51–100), moderate (H-score: 101–200) or high (H-score 201–300).

		PDAC expression		
Biomarker	Negative n (%)	Low n (%)	Moderate n (%)	High n (%)
Lea/c/x	8 (17)	8 (17)	23 (48)	9 (19)
sdi-Le <sup>a</sup>	3 (6)	5 (10)	11 (23)	29 (60)
sLea	1(2)	0 (0)	15 (31)	32 (67)
sLe <sup>x</sup>	5 (10)	7 (15)	20 (42)	16 (33)
sTn	6 (13)	7 (15)	23 (48)	12 (25)
MUC1	2 (4)	1 (2)	18 (38)	27 (56)
MUC5AC	16 (33)	9 (19)	17 (35)	6 (13)

PDAC: pancreatic ductal adenocarcinoma.

### Biomarker expression on PDAC tissues after NAT

As we found that all biomarkers showed high expression on PDAC tissues, subgroup analyses were performed to study the effect of NAT on biomarker expression on PDAC tissues. H-score scatter plots showing biomarker expression in NAT and no NAT patients are shown in Figure 3. Although sLex, sTn and MUC5AC expression seemed slightly lower in the NAT group, no statistically significant differences in biomarker expression between NAT and no NAT patients were observed, suggesting that NAT does not influence the (over)expression of these biomarkers.

### Biomarker co-expression on PDAC tissues

Biomarker co-expression on tumor tissues was analyzed to evaluate the potential added value of targeting two biomarkers simultaneously. The percentage of patients with positive expression of at least one biomarker along with the percentage of cases with biomarker co-expression are shown in Table 4. Although co-expression was present in the majority of patients, virtually all patients expressed at least one of two biomarkers of any panel, with the least-performing biomarker combination being sTn-MUC5AC that was, alone and or combined, expressed in 90% of PDAC tissues. The highest co-expression panel was sLe<sup>a</sup> and MUC1, which were simultaneously expressed in 94% of patients.

**FIGURE 3** H-score scatter plots of immunohistochemical staining of (A) Le<sup>a/c/x</sup>, (B) sdi-Le<sup>a</sup>, (C) sLe<sup>a</sup>, (D) sLe<sup>x</sup>, (E) sTn, (F) MUC1 and (G) MUC5AC expression on PDAC tissues of patients who received NAT or no NAT. Mean H-scores are represented by the horizontal line together with their error bars representing the 95% confidence interval. Each dot represents immunohistochemical staining on one case. NAT: neoadjuvant treatment, ns: not significant.

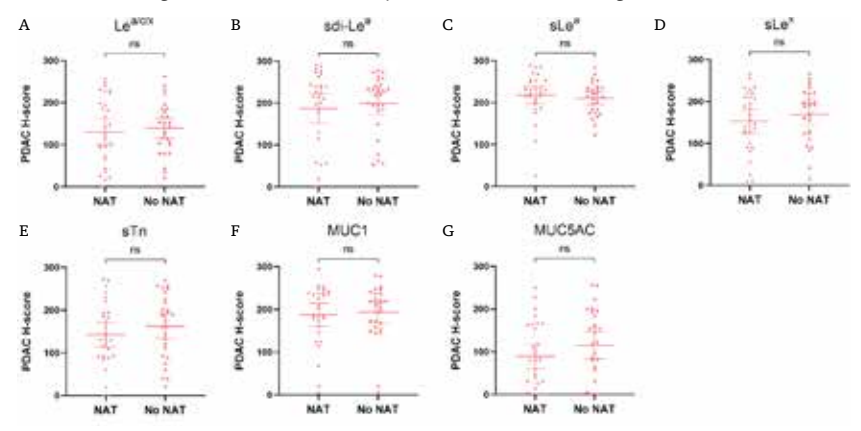


**TABLE 4** Percentage of cases with positive expression for at least one of two biomarker combinations (panel:  $\geq 1$ ) along with the percentage of cases with expression of both biomarkers (panel: both). Immunohistochemical staining with an H-score of  $\geq 51.0$  was considered positive.

Biomarker	Panel	Le <sup>a/c/x</sup> (%)	sdi-Le <sup>a</sup> (%)	sLe <sup>a</sup> (%)	sLe <sup>x</sup>	sTn (%)	MUC1	MUC5AC
		(%)	(%)	(%)	(%)	(%)	(%)	(%)
Le <sup>a/c/x</sup>	≥1	-	-	-	-	-	-	-
	Both							
sdi-Le <sup>a</sup>	≥1	94	-	-	-	-	-	-
	Both	83						
sLea	≥1	100	100	-	-	-	-	-
	Both	81	92					
sLex	≥1	98	100	100	-	-	-	-
	Both	75	83	88				
sTn	≥1	100	100	100	98	-	-	-
	Both	71	81	85	79			
MUC1	≥1	100	100	100	100	100	-	-
	Both	79	90	94	85	83		
MUC5AC	≥1	96	96	98	96	90	96	-
	Both	54	65	67	60	65	67	

### Detection of lymph node metastases

LN+ and LN− tissues were stained to evaluate the biomarkers' potential for identification of lymph node metastases in addition to primary PDAC lesions. Representative IHC images for biomarker expression on LN+ tissues are depicted in Figure 4, which shows that all biomarkers were highly expressed on PDAC cells in LN+ tissues. For LN− tissues, biomarker expression was mostly absent, although low to moderate expression was occasionally observed for Lea/c/x, sdi-Lea and sLe.a Despite the latter, mean LN+ expression was significantly higher compared to LN− expression for all biomarkers (p < 0.0001), as shown in Figure 5. In addition, sensitivity, specificity, PPV, NPV and AUC for correct LN+ detection were calculated based on positive or negative biomarker expression on LN+ and LN− tissues. Although sensitivity for LN+ detection was lower for sLex and sTn, Lea/c/x, sdi-Lea, sLea, MUC1 and MUC5AC showed high LN+ identification potential, with limited false-positive and false-negative staining. Accuracy for identification of LN+ and LN− tissues together was 90% for Lea/c/x, 81% for sdi-Lea, 81% for sLea, 81% for sTn, 97% for MUC1, and 91% for MUC5AC (Table 5).

**FIGURE 4** Representative images of (immuno)histochemical staining of (A)  $Le^{a/c/x}$ , (B)  $sdi-Le^a$ , (C)  $sLe^a$ , (D)  $sLe^x$ , (E) sTn, (F) MUC1 and (G) MUC5AC expression on  $LN^+$  tissues of primary PDAC patients. Overview images and inserts are taken at  $5\times$  and  $25\times$  magnification, respectively. Scale bars represent 100  $\mu$ M. HE: hematoxylin-eosin,  $LN^+$ : positive lymph node.

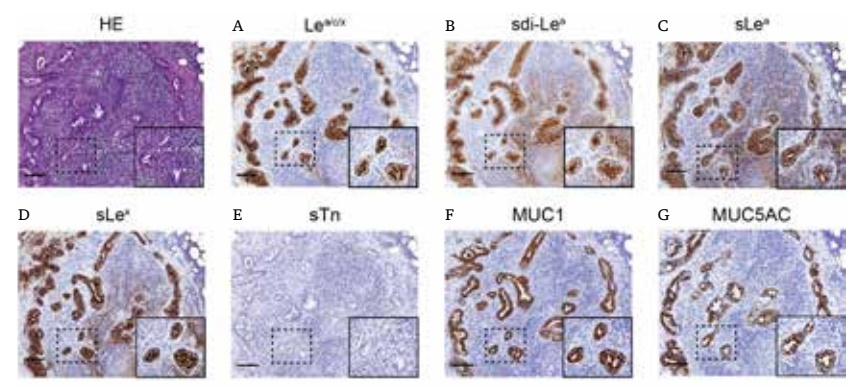


**FIGURE 5** H-score scatter plots of immunohistochemical staining of (A)  $Le^{a/c/x}$ , (B)  $sdi-Le^a$ , (C)  $sLe^a$ , (D)  $sLe^x$ , (E) sTn, (F) MUC1 and (G) MUC5AC expression on  $LN^+$  and  $LN^-$  tissues. Mean H-scores are represented by the horizontal line together with their error bars representing the 95% confidence interval. Within each tissue category, every dot represents immunohistochemical staining on one case.  $LN^+$ : positive lymph node,  $LN^-$ : negative lymph node, \*\*\*\*: p < 0.0001.

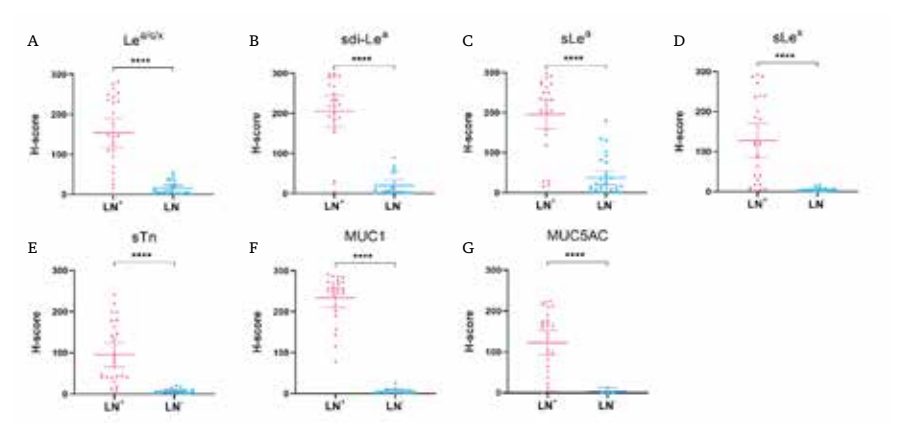


**TABLE 5** Biomarker sensitivity, specificity, PPV, NPV and accuracy along with the AUC and p-value for identification of LN $^+$ . Immunohistochemical staining with an H-score of  $\ge 51.0$  was considered positive.

Biomarker	Sens. (%)	Spec. (%)	PPV (%)	NPV (%)	Accuracy (%)	AUC (95% CI)	<i>p</i> -value
Le <sup>a/c/x</sup>	78	98	96	87	90	0.929 (0.846-1.000)	<0.0001
sdi-Le <sup>a</sup>	70	88	79	82	81	0.955 (0.896-1.000)	<0.0001
sLea	78	83	75	85	81	0.927 (0.858-0.995)	<0.0001
sLe <sup>x</sup>	59	100	100	79	84	0.960 (0.913-1.000)	<0.0001
sTn	52	100	100	76	81	0.954 (0.894-1.000)	< 0.0001
MUC1	93	100	100	95	97	1.000 (1.000-1.000)	< 0.0001
MUC5AC	78	100	100	87	91	0.972 (0.912-1.000)	<0.0001

AUC: area under the curve, PPV: positive predictive value, NPV: negative predictive value, Sens.: sensitivity, Spec.: specificity, 95% CI: 95% confidence interval.

### **DISCUSSION**

Through specific binding to and (real-time) visualization of tumor cells, targeted molecular imaging agents can play a key role in overcoming current challenges during diagnosis, resection, and monitoring of PDAC. In this study, we evaluated the potential of tumor-associated glycans Lea/c/x, sdi-Lea, sLea, sLea and sTn, and mucins MUC1 and MUC5AC as a molecular imaging target for PDAC using a

semi-automated, machine-learning-based image analysis workflow. Our results show that all biomarkers are highly expressed on PDAC cells. Importantly, subgroup analyses showed that biomarker expression was similar in patients who received NAT and patients who did not receive NAT, suggesting that NAT does not influence biomarker expression. This finding is particularly promising in view of the ever-increasing application of neoadjuvant chemoradiotherapy for PDAC and paves the way for PDAC targeting using these biomarkers in a clinically relevant setting.<sup>24</sup> We additionally showed that simultaneous targeting of two targets using, for instance, a bispecific tracer could be attractive in order to allow targeting of the entire PDAC population. High tumor:CP ratios were observed for all biomarkers, although tumor:CP ratios for MUC1 and Lea/c/x were closer to 1 (1.4 and 1.7, respectively). In addition, high tumor:pancreas ratios were observed for all biomarkers, except for MUC1 (tumor:pancreas ratio 1.0). These results suggest that all biomarkers, besides MUC1, have a high potential to serve as molecular imaging targets to solve current challenges in the delineation of primary PDAC lesions from surrounding CP and healthy pancreatic tissue. We additionally evaluated biomarker expression on healthy duodenal tissues to evaluate their potential for delineating locally advanced primary pancreatic head carcinomas invading the duodenum, which can be present in 47-58% of patients. 25,26 In contrast to the other biomarkers, sTn's abundant expression on healthy duodenal tissues limits its suitability for molecular imaging of primary PDAC invading the duodenum.

In addition to primary PDAC detection, both pre- and intraoperative imaging of lymph node metastases is pivotal for disease staging and monitoring.  $^{27,28}$  Therefore, we evaluated the potential of the biomarker panel to detect lymph node metastases and found that all biomarkers are significantly upregulated on LN+ compared to LN- tissues. All biomarkers showed a high detection potential for LN+ tissues and distinction of LN+ from LN- tissues, which was comparable to the performance of established protein-based molecular imaging targets, such as CEACAM5, PSMA,  $\alpha_V\beta_6$  and uPAR, further strengthening their potential as molecular imaging targets.  $^{28,29}$ 

Due to their tumor-specific (over)expression and excellent *in vivo* accessibility, tumor-associated glycans, which are present on the outermost layer of the cell membrane, are of particular interest for molecular imaging. <sup>11</sup> Several glycan-specific tracers were successfully evaluated for molecular imaging of PDAC in a preclinical setting, but only a few studies have described glycan-based imaging in a clinical context. For instance, <sup>89</sup>Zr-DFO-HuMab-5B1 (MVT-2163), which targets sLe<sup>a</sup> (more commonly known as CA19-9), was successfully evaluated in a phase

1 trial for PET imaging of PDAC and provided clear delineation of primary tumors and metastases, some of which were not identified using standard imaging modalities. See a is also employed as a serum biomarker for diagnosis and monitoring of PDAC within standard-of-care. However, despite its strong overexpression in PDAC, targeting of sLea in PDAC is limited by its presence in the healthy pancreas, CP and other benign pancreaticobiliary diseases, which is confirmed by the relatively low tumor: CP, tumor: pancreas and tumor: duodenum ratios found in the current study. Noteworthy, we showed that sdi-Lea, which is a Lewis glycan structurally related to sLea, had a more restricted expression on CP, healthy pancreas and duodenal tissues with similar PDAC expression, which strengthens the major potential of sdi-Lea over sLea for specific PDAC targeting.

Le<sup>a/c/x</sup> and sdi-Le<sup>a</sup> were recently described by Chua and Tivadar et al., respectively, showing high expression on PDAC tissues with low to moderate abundance on healthy tissues.<sup>13,15</sup> Once employed *in vivo*, the Le<sup>a/c/x</sup>-specific mAb FG88.2 subsequently displayed remarkable tumor targeting.<sup>13</sup> Recently, our group conducted a proof-of-concept evaluation of the chimeric (human/mouse) counterpart of the FG88.2 mAb, CH88.2, as a targeting moiety for fluorescence-guided surgery of colon carcinoma and PDAC. Conjugated to IRDye 800CW, the tracer allowed clear visualization of subcutaneous HT-29 (colon carcinoma) and BxPC-3 (PDAC) tumor xenografts using a clinical near-infrared fluorescence imaging system.<sup>32</sup> Although additional IHC exploration of expression on other gastrointestinal tumors along with their normal counterparts and metastases is required to evaluate the tracer employability beyond PDAC, the current findings strongly support previous data on FG88.2 staining, paving the way for a clinical translation of the tracer.<sup>13,15</sup>

In addition to glycans, mucins, that are heavily coated with glycans, may form attractive targets for molecular imaging of PDAC due to their tumor-specific expression, some of which from the earliest in situ stage onward. Although in our study MUC1 seems to be a less suitable candidate for molecular imaging of PDAC, it should be noted that alternative conformational epitopes on MUC1, induced by the presence of (truncated) *O*-glycans, were described.<sup>33,34</sup> As their accessibility is dependent on conformational changes, induced by tumor-specific aberrant glycosylation, their expression on healthy tissues might be minimized, making them more attractive for tumor-specific targeting. For instance, the PAM4-reactive epitope, which is present on both MUC1 and MUC5AC, was shown to have a low abundance on healthy pancreatic and CP tissues, while expression on PDAC and pancreatic intraepithelial neoplasia (PanIN)-1A lesions onward was high.<sup>35,36</sup>

Evaluation of PAM4-reactive epitope expression on the current cohort would be an interesting continuation in order to establish its potential as a PDAC imaging target, while simultaneously putting the current findings into perspective.

A strong methodological point of the study is the inclusion of tissues derived from the entire PDAC context, i.e., the primary tumor, healthy/benign tissue counterparts, surrounding organs and metastatic and healthy lymph nodes, which is paramount for a complete and accurate biomarker comparison. Our semi-automated image analysis workflow provided highly accurate cell classification, allowing an objective, reproducible and precise evaluation of biomarker expression. In contrast, accurate manual scoring of heterogeneous biomarker stainings may be challenging and consequently suffers from both intraobserver and interobserver variability.<sup>37,39</sup> Moreover, to the best of our knowledge, this study is the first to evaluate the expression of the current biomarkers on both PDAC tissues of patients who received NAT and on metastatic PDAC lymph node tissues.

This study has some limitations. Application of the current QuPath workflow for this relatively small cohort is limited by its labor intensity and still does not avoid the involvement of a specialized pathologist. In addition, erroneous classification of out-of-focus tissue areas and staining artifacts, although mostly avoided during tissue area annotation, may further compromise accurate semi-automated scoring of digital images. Moreover, we cannot fully exclude that, particularly in patients that received NAT, residual tumor clusters in both primary resection and lymph node tissues were misclassified and subsequently annotated as non-tumorous. It should however be noted that considering manual scoring to be the gold standard may overlook the potential of machine learning-based algorithms to classify cells with superior accuracy relative to the human eye.<sup>40</sup> Furthermore, we feel that the benefits of the highly accurate, semi-automated scoring method, which is of high importance considering the heterogenicity of the observed staining patterns within a complex PDAC morphology, do outweigh the aforementioned disadvantages.

This study identified Lea/c/x, sdi-Lea, sLea, sLex, and MUC5AC as high-potential targets for molecular imaging of PDAC. Future research into glycan- and mucin-targeted imaging should thus focus on the development and evaluation of clinically suitable tracers directed against these glycan and mucin targets. Secondly, although this study showed no difference in biomarker expression on PDAC tissues between NAT and no NAT patients, evaluating the correlation between biomarker expression on PDAC tissues before and after NAT, for instance by using fine-needle aspiration biopsies acquired before NAT, could strengthen

the current finding that NAT does not influence biomarker expression. Thirdly, although this study demonstrates the potential of identifying LN<sup>+</sup> tissues based on the expression of the evaluated biomarkers, future animal models with complex lymph node metastases are required to definitely establish a glycan or mucin-targeting tracer's potential for metastatic lymph node detection. Altogether, this study provides a strong foundation for the development, characterization and preclinical evaluation of tumor-associated glycan- and mucin-specific molecular imaging agents for high-contrast delineation of PDAC.

### CONCLUSION

To conclude, our results show that particularly Lea/c/x, sdi-Lea, sLea, sLea and MUC5AC are high-potential targets for molecular imaging of primary PDAC lesions, regardless of the application of NAT. Due to their strong abundance on duodenum and healthy pancreatic tissues, sTn and MUC1 were considered less suitable targets. All biomarkers are suitable targets for correct identification of LN<sup>+</sup> as well as the distinction of LN<sup>+</sup> from LN<sup>-</sup> tissues. Through this study, we lay the groundwork for the development and evaluation of clinically suitable glycan- and mucin-specific tracers for molecular imaging of PDAC.

### SUPPLEMENTARY MATERIALS

The following Supplementary Materials are available online at: https://bit.ly/42ozZHE.

Supplementary Figure 1: Graphical representation of biomarker training and validation workflow; Supplementary Figure 2: QuPath images and semi-automated image analysis workflow; Supplementary Figure 3: Heatmap of biomarker expression on PDAC tissues for each case separately; Supplementary Table 1: Primary and secondary mAbs, clone, catalog number, provider, isotype and conditions used during IHC; Supplementary Table 2: Automated cell detection parameters used in OuPath; Supplementary Table 3: Mean + SD object classifier sensitivity, specificity, PPV, NPV, accuracy for the detection of tumor, stromal, acinar, immune or glandular cells pooled from all biomarkers (n = 7).

### REFERENCES

- 1 Rawla P, Sunkara T, Gaduputi V. Epidemiology of Pancreatic Cancer: Global Trends, Etiology and Risk Factors. World J Oncol. 2019;10(1):10-27.
- 2 Versteijne E, Vogel JA, Besselink MG, Busch ORC, Wilmink 17 Contessa JN, Bhojani MS, Freeze HH, Rehemtulla A, JW, Daams JG, et al. Meta-analysis comparing upfront surgery with neoadjuvant treatment in patients with resectable or borderline resectable pancreatic cancer. Br J Surg. 2018;105(8):946-58.
- 3 Papalezova KT, Tyler DS, Blazer DG, 3rd, Clary BM, Czito BG, Hurwitz HI, et al. Does preoperative therapy optimize outcomes in patients with resectable pancreatic cancer? I Surg Oncol. 2012;106(1):111-8.
- 4 Pietryga JA, Morgan DE. Imaging preoperatively for pancreatic adenocarcinoma. J Gastrointest Oncol. 2015;6(4):343-57.
- 5 Tummers WS, Groen JV, Sibinga Mulder BG, Farina-Sarasqueta A, Morreau J, Putter H, et al. Impact of resection margin status on recurrence and survival in pancreatic cancer surgery. Br J Surg. 2019;106(8):1055-65.
- Strobel O, Hank T, Hinz U, Bergmann F, Schneider L, Springfeld C, et al. Pancreatic Cancer Surgery: The New R-status Counts. Ann Surg. 2017;265(3):565-73.
- 7 Gerritsen A. Molenaar IO. Bollen TL. Nio CY. Dijkgraaf MG, van Santvoort HC, et al. Preoperative characteristics of patients with presumed pancreatic cancer but ultimately benign disease: a multicenter series of 344 pancreatoduodenectomies. Ann Surg Oncol. 2014;21(12):3999-4006.
- Pandol S, Edderkaoui M, Gukovsky I, Lugea A, Gukovskaya A. Desmoplasia of pancreatic ductal adenocarcinoma. Clin Gastroenterol Hepatol. 2009;7(11 Suppl):S44-S7.
- Chatterjee D, Katz MH, Rashid A, Estrella JS, Wang H, Varadhachary GR, et al. Pancreatic intraepithelial neoplasia and histological changes in non-neoplastic pancreas associated with neoadjuvant therapy in patients with pancreatic ductal adenocarcinoma. Histopathology. 2013;63(6):841-51.
- 10 Vahrmeijer AL, Hutteman M, van der Vorst IR, van de Velde CJH, Frangioni JV. Image-guided cancer surgery using near-infrared fluorescence. Nature reviews Clinical oncology. 2013;10(9):507-18.
- 11 Houvast RD, Vankemmelbeke M, Durrant LG, Wuhrer M, Baart VM, Kuppen PJK, et al. Targeting Glycans and Heavily Glycosylated Proteins for Tumor Imaging. Cancers (Basel). 2020;12(12).
- 12 Fuster MM, Esko JD. The sweet and sour of cancer: glycans as novel therapeutic targets. Nat Rev Cancer. 2005;5(7):526-42.
- 13 Chua JX, Vankemmelbeke M, McIntosh RS, Clarke PA, Moss R, Parsons T, et al. Monoclonal Antibodies Targeting LecLex-Related Glycans with Potent Antitumor Activity. Clin Cancer Res. 2015;21(13):2963-74.
- 14 Dube DH, Bertozzi CR. Glycans in cancer and inflammation—potential for therapeutics and diagnostics. Nat Rev Drug Discov. 2005;4(6):477-88.
- 15 Tivadar ST, McIntosh RS, Chua JX, Moss R, Parsons T, Zaitoun AM, et al. Monoclonal Antibody Targeting Sialyl-di-Lewis(a)-Containing Internalizing and Noninternalizing Glycoproteins with Cancer

- Immunotherapy Development Potential. Mol Cancer Ther. 2020;19(3):790-801.
- 16 Trinchera M, Aronica A, Dall'Olio F. Selectin Ligands Sialyl-Lewis a and Sialyl-Lewis x in Gastrointestinal Cancers. Biology. 2017;6(1):16.
- Lawrence TS. Inhibition of N-linked glycosylation disrupts receptor tyrosine kinase signaling in tumor cells. Cancer Res. 2008;68(10):3803-9.
- 18 Wang S, You L, Dai M, Zhao Y. Mucins in pancreatic cancer: A well-established but promising family for diagnosis, prognosis and therapy. J Cell Mol Med. 2020;24(18):10279-89.
- 19 Kaur S. Kumar S. Momi N. Sasson AR. Batra SK. Mucins in pancreatic cancer and its microenvironment. Nature reviews Gastroenterology & hepatology.
- 20 Lebrilla CB, An HJ. The prospects of glycan biomarkers for the diagnosis of diseases. Mol Biosyst. 2009;5(1):17-20.
- 21 Bankhead P, Loughrey MB, Fernández JA, Dombrowski Y, McArt DG, Dunne PD, et al. QuPath: Open source software for digital pathology image analysis. Sci Rep. 2017;7(1):16878.
- 22 Breiman L. Random forests. Machine learning. 2001;45(1):5-32.
- 23 Thike AA, Chng MJ, Fook-Chong S, Tan PH. Immunohistochemical expression of hormone receptors in invasive breast carcinoma; correlation of results of H-score with pathological parameters. Pathology. 2001;33(1):21-5.
- 24 Janssen OP, van Dam JL, Bonsing BA, Bos H, Bosscha KP. Coene P, et al. Total neoadjuvant FOLFIRINOX versus neoadjuvant gemcitabine-based chemoradiotherapy and adjuvant gemcitabine for resectable and borderline resectable pancreatic cancer (PREOPANC-2 trial): study protocol for a nationwide multicenter randomized controlled trial. BMC Cancer. 2021;21(1):300.
- 25 Park HS, Lee JM, Choi HK, Hong SH, Han JK, Choi BI. Preoperative evaluation of pancreatic cancer: comparison of gadolinium-enhanced dynamic MRI with MR cholangiopancreatography versus MDCT. J Magn Reson Imaging. 2009;30(3):586-95.
- 26 Arvold ND, Niemierko A, Mamon HJ, Fernandez-del Castillo C, Hong TS. Pancreatic cancer tumor size on CT scan versus pathologic specimen: implications for radiation treatment planning. Int I Radiat Oncol Biol Phys. 2011;80(5):1383-90.
- 27 Tummers WS, Miller SE, Teraphongphom NT, Gomez A, Steinberg I, Huland DM, et al. Intraoperative Pancreatic Cancer Detection using Tumor-Specific Multimodality Molecular Imaging. Ann Surg Oncol. 2018;25(7):1880-8.
- 28 Vuijk FA, Hilling DE, Mieog JSD, Vahrmeijer AL. Fluorescent-guided surgery for sentinel lymph node detection in gastric cancer and carcinoembryonic antigen targeted fluorescent-guided surgery in colorectal and pancreatic cancer. Journal of surgical oncology. 2018;118(2):315-23.
- 29 Tummers WS, Farina-Sarasqueta A, Boonstra MC, Prevoo HA, Sier CF, Mieog JS, et al. Selection of optimal molecular targets for tumor-specific imaging in pancreatic ductal adenocarcinoma. Oncotarget. 2017;8(34):56816-28.
- 30 Lohrmann C, O'Reilly EM, O'Donoghue JA, Pandit-Taskar

- N, Carrasquillo JA, Lyashchenko SK, et al. Retooling a Blood-Based Biomarker: Phase I Assessment of the High-Affinity CA19-9 Antibody HuMab-5B1 for Immuno-PET Imaging of Pancreatic Cancer. Clin Cancer Res. 2019;25(23):
- 31 Ballehaninna UK, Chamberlain RS. Serum CA 19-9 as a biomarker for pancreatic cancer—a comprehensive review. Indian J Surg Oncol 2011;2(2):88-100.
- 32 Houvast RD, Baart VM, Bhairosingh SS, Cordfunke RA, Chua JX, Vankemmelbeke M, et al. Glycan-Based Near-infrared Fluorescent (NIRF) Imaging of Gastrointestinal Tumors: a Preclinical Proof-of-Concept In Vivo Study. Mol Imaging Biol. 2020;22(6):1511-22.
- 33 Gold DV, Lew K, Maliniak R, Hernandez M, Cardillo T. Characterization of monoclonal antibody PAM4 reactive with a pancreatic cancer mucin. Int J Cancer. 1994;57(2):204-10.
- 34 Fan XN, Karsten U, Goletz S, Cao Y. Reactivity of a humanized antibody (hPankoMab) towards a tumorrelated MUC1 epitope (TA-MUC1) with various human carcinomas. Pathol Res Pract. 2010;206(8):585-9.
- 35 Gold DV, Karanjawala Z, Modrak DE, Goldenberg DM, Hruban RH. PAM4-reactive MUC1 is a biomarker for early pancreatic adenocarcinoma. Clin Cancer Res. 2007;13(24):7380-7.
- 36 Shi C, Merchant N, Newsome G, Goldenberg DM, Gold DV. Differentiation of pancreatic ductal adenocarcinoma from chronic pancreatitis by PAM4 immunohistochemistry. Arch Pathol Lab Med. 2014;138(2):220-8.
- 37 Loughrey MB, Bankhead P, Coleman HG, Hagan RS, Craig S, McCorry AMB, et al. Validation of the systematic scoring of immunohistochemically stained tumour tissue microarrays using QuPath digital image analysis. Histopathology. 2018;73(2):327-38.
- 38 Adams EJ, Green JA, Clark AH, Youngson JH. Comparison of different scoring systems for immunohistochemical staining. J Clin Pathol. 1999;52(1):75-7.
- 39 Feuchtinger A, Stiehler T, Jütting U, Marjanovic G, Luber B, Langer R, et al. Image analysis of immunohistochemistry is superior to visual scoring as shown for patient outcome of esophageal adenocarcinoma. Histochem Cell Biol. 2015;143(1):1-9.
- 40 Bankhead P, Fernández JA, McArt DG, Boyle DP, Li G, Loughrey MB, et al. Integrated tumor identification and automated scoring minimizes pathologist involvement and provides new insights to key biomarkers in breast cancer. Lab Invest. 2018;98(1):15-26.

## **CHAPTER 4**

Selecting targets for molecular imaging of gastric cancer: an immunohistochemical evaluation

Ruben D. Houvast, Maurice van Duijvenvoorde, Kira Thijse, Wobbe O. de Steur, Lioe-Fee de Geus-Oei, A. Stijn. L. P. Crobach, Jacobus Burggraaf, Alexander L. Vahrmeijer, Peter J.K. Kuppen

Molecular Diagnosis & Therapy. 2025;29(2):213-27.



#### ABSTRACT

**BACKGROUND** Tumor-targeted positron emission tomography (PET) and fluorescence-guided surgery (FGS) could address current challenges in pre- and intraoperative imaging of gastric cancer. Adequate selection of molecular imaging targets remains crucial for successful tumor visualization. This study evaluated the potential of integrin  $\alpha_V \beta_6$ , carcinoembryonic antigen (CEACAM5), epidermal growth factor receptor (EGFR), epithelial cell adhesion molecule (EpCAM) and human epidermal growth factor receptor-2 (HER2) for molecular imaging of primary gastric cancer, as well as lymph node and distant metastases.

**METHODS** Expression of  $\alpha_V \beta_s$ , CEACAM5, EGFR, EpCAM and HER2 was determined using immunohistochemistry in human tissue specimens of primary gastric adenocarcinoma, healthy surrounding stomach, esophageal and duodenal tissue, as well as tumor-positive and -negative lymph nodes, and distant metastases, followed by quantification using the total immunostaining score (TIS).

**RESULTS** Positive biomarker expression in primary gastric tumors was observed in 86% for  $\alpha_V\beta_6$ , 72% for CEACAM5, 77% for EGFR, 93% for EpCAM and 71% for HER2. Tumor expression of CEACAM5, EGFR and EpCAM was higher compared to healthy stomach tissue expression, while this was not the case for  $\alpha_V\beta_6$  and HER2. Tumor-positive lymph nodes could be distinguished from tumor-negative lymph nodes with accuracy ranging from 82% to 93% between biomarkers. CEACAM5, EGFR and EpCAM expression were abundantly expressed on distant metastases, with expression in 88% to 95% of tissue specimens.

**CONCLUSION** Our findings show that CEACAM5, EGFR and EpCAM are promising targets for molecular imaging of primary gastric cancer, as well as visualization of both lymph node and distant metastases. Further clinical evaluation of PET and FGS tracers targeting these antigens is warranted.

#### INTRODUCTION

Gastric cancer is the fifth most common malignancy, with a worldwide incidence of more than 1 million cases per year. Despite recent therapeutic advances, prognosis remains poor with a 5-year-survival of approximately 40%, resulting in more than 700,000 deaths worldwide annually. Achieving local control through subtotal or total gastrectomy combined with lymphadenectomy remains the cornerstone of multidisciplinary gastric cancer treatment. Preoperatively, adequate disease staging is pivotal for patient-tailored treatment selection and maximizing its efficacy.

Preoperative work-up of gastric cancers is comprised of endoscopy, computed tomography (CT) imaging,  $^{18}$ F-fluorodeoxyglucose positron emission tomography ( $^{18}$ F-FDG PET) and/or diagnostic laparoscopy in clinically curable locally advanced disease ( $^{18}$ F-FDG PET) and/or N+, Mo).  $^{4.5}$  However, each modality has its limitations for accurate tumor detection, potentially leading to erroneous tumor staging and, consequently, unnecessary tumor resections, futile biopsies, extra imaging procedures and/or unnecessary administration of systemic therapy. For example, CT imaging provides accurate T-staging (sensitivity 83-100% for tumors with serosal involvement), while sensitivity for N-staging is lower at approximately  $^{60}$ M. Importantly, sensitivity for small-sized distant metastases and peritoneal metastases is limited at 23-76%. Also, a significant proportion of gastric cancers has absent  $^{18}$ F-FDG PET-avidity ( $^{18}$ PET-avidity ( $^{18}$ PET-bulke in the stomach wall can also mask tumor presence.  $^{5,8}$  The use of  $^{18}$ F-FDG PET for nodal and of distant metastasis staging is also unsatisfactory, with sensitivity 49%, and 33-56%, respectively.  $^{5,9}$ 

To improve the accuracy of gastric cancer staging, diagnostic laparoscopy with or without peritoneal cytology is frequently performed.<sup>5,10-12</sup> A systematic review highlighted that 9-60% of patients who were preoperatively staged as Mo, had irresectable disease intraoperatively.<sup>10</sup> Recently, the PLASTIC trial reported the limited added value of <sup>18</sup>F-FDG-PET and showed the superiority of diagnostic laparoscopy in accurate staging of locally advanced gastric cancer.<sup>5</sup> Limitations of laparoscopy, however, include its invasiveness, inability to accurately identify non-superficial liver metastases, lymph node metastases or extraperitoneal lesions, as well as the absence of tactile feedback for identifying malignant tissue.<sup>13,14</sup> Besides tumor staging, an intraoperative challenge is encountered when radical resection is considered feasible. Studies showed that presence of microscopically tumor-positive resection margins (i.e. R1 resection) is still observed in approximately 7% of gastric cancer patients, which has been associated with higher peritoneal recurrence rates and poorer survival.<sup>15,16</sup>

To address these challenges, tumor-targeted PET and real-time fluorescence-guided surgery using near-infrared light have emerged as valuable tools to enhance tumor imaging, respectively, by providing high-contrast visualization of malignant tissue. 14,17,18 These molecular imaging technologies could improve assessment of tumor localization, potentially avoiding resection for irresectable disease, as well as assisting surgeons in radical tumor resection. However, the success of molecular imaging hinges on the adequate selection of tumor-specific targets.

An ideal molecular imaging target is abundantly and homogenously expressed on the tumor cell membrane across all patients, while expression in healthy surrounding tissue is absent.<sup>17</sup> Preferably, the target-of-interest is also present on lymph node and distant metastases and its expression remains present in microscopic residual disease after neoadjuvant therapy (NAT). However, governed by tumor heterogeneity, among others, a universal molecular imaging target for gastric cancer has still not been identified.

Over the last years, several targets were recognized as promising for molecular imaging of gastrointestinal cancers, including integrin  $\alpha_V\beta_6$ , carcinoembryonic antigen (CEACAM5), epidermal growth factor receptor (EGFR), epithelial cell adhesion molecule (EpCAM) and human epidermal growth factor receptor-2 (HER2).  $^{19-24}$  Consequently, tracers targeting some of these biomarkers were evaluated in clinical trials for various gastrointestinal tumor types.  $^{25-30}$  However, their potential for molecular imaging of gastric cancer has been underexplored.

This study therefore provides the first crucial step towards application of these tracers in gastric cancer, by evaluating  $\alpha_V\beta_6$ , CEACAM5, EGFR, EpCAM and HER2 as molecular imaging targets for gastric cancer and its metastases. To accomplish this, biomarker expression was evaluated within the full anatomical context of gastric cancer. Biomarker expression was, therefore, determined using immunohistochemistry on human tissue specimens of primary tumors, healthy surrounding stomach, but also on esophageal and duodenal tissue, as well as tumor-positive and -negative lymph nodes, and distant metastases.

## MATERIALS AND METHODS

## Patient and tissue specimen selection

Pathology reports of patients who underwent resection for gastric adenocarcinoma at the Leiden University Medical Center (LUMC) from 2013 to 2020 were retrospectively reviewed. Representative formalin-fixed paraffin-embedded (FFPE) tissues blocks and hematoxylin and eosin (HE) slides of 87 patients containing primary gastric tumor, healthy stomach, esophageal, duodenal and or (metastatic) lymph

node tissue were selected and obtained from the biobank at the LUMC. To allow proper subgroup analyses, the cohort was constituted to contain approximately a 1:1 ratio of patients with diffuse and intestinal type tumors according to the Laurén classification. Patients with mixed type Laurén classification were excluded. Selection of FFPE tissue blocks was performed by a gastrointestinal pathologist (ASLPC) based on the HE slides. Tissue specimens containing gastric adenocarcinoma metastases biopsy tissue were also obtained from 19 patients. Clinicopathological data were obtained from patients' medical records. Pathological tumor (pT) and pathological lymph node (pN) stages were defined according to the 8th edition of the American Joint Committee on Cancer and Union for International Cancer Control (AJCC/ UICC) TNM staging system for gastric cancer. The study protocol was approved by both the Gastroenterology Biobank Review Committee (protocol reference: 2020-16) as well as the local medical Ethical Review Committee (protocol reference: B20.052). This study was conducted in compliance with the Dutch code of conduct for responsible use of human tissue in medical research. Tissue specimens and clinicopathological data were handled in anonymized manner and in compliance with the Declaration of Helsinki (1964).

## Immunohistochemistry

Four-um-thick tissue sections were cut from FFPE tissues and mounted on glass slides. Sections underwent deparaffinization in xylene for 15 minutes followed by rehydration through sequential ethanol concentrations (100%, 50%, and 25%). Subsequently, endogenous peroxidase was blocked using a 0.3% hydrogen peroxide solution. Antigen retrieval was tailored to the primary antibody employed, as outlined in Table 1 of the Electronic Supplementary Material (ESM). Post-antigen retrieval, slides were thoroughly rinsed in phosphate-buffered saline (PBS, pH 7.4). Primary antibodies (see Table 1 of the ESM) targeting  $\alpha_V \beta_6$ , CEACAM5, EGFR, EpCAM or HER2 were applied to the tissue sections which were subsequently left to incubate overnight at room temperature in a humid incubator. After overnight incubation, slides were rinsed in PBS to remove any residual primary antibodies. Anti-mouse-horseradish peroxidase (HRP) or anti-rabbit-HRP secondary antibodies (Envision, Dako, Glostrup, Denmark) were subsequently applied for 30 minutes at room temperature in a humid incubator for 30 minutes. Secondary antibodies were then removed by thorough PBS rinsing. Visualization of antibody binding was achieved using a 3,3-diaminobenzidine tetrahydrochloride solution (DAB, K3468, Agilent Technologies, Inc., Santa Clara, CA, USA) for 10 minutes at room temperature. Finally, slides were counterstained with Mayer's hematoxylin (Klinipath B.V., Olen, Belgium), dehydrated in a dry incubator for 2 hours, and mounted using Pertex (Leica Microsystems, Wetzlar, Germany).

## **Evaluation of immunohistochemical staining**

Whole slide images of the stained tissue slides were captured using the PANNORAMIC® 250 Flash III DX scanner (3DHISTECH Ltd, Budapest, Hungary). DAB staining was quantified using the total immunostaining score, which was computed by multiplying the staining proportion (0 =  $\le$ 9%, 1 = 10-25%, 2 = 26-50%, 3 = 51-75%, 4 =  $\ge$ 76%) by the staining intensity (0 = none, 1 = weak, 2 = moderate, 3 = strong). Staining based on the TIS was categorized as follows: 0 = negative; 1, 2, 3, 4 = weak expression; 6, 8 = moderate expression; 9, 12 = strong expression. A panel of three independent observers (RDH, MvD, ASLPC) conducted the scoring. Instances of disagreement were discussed in a consensus meeting, during which the final score was conclusively determined.

## Statistical analysis

For categorial data, groups at baseline were compared using a Chi-square test. An independent samples t-test was used to compare continuous variables of patient characteristics. TIS values between tumor, healthy surrounding stomach, esophageal and duodenal tissue were compared using Kruskal-Wallis test with Dunn's correction for multiple comparisons. Biomarker expression subgroup analyses were performed using a Mann-Whitney test. IBM SPSS statistics version 29 (IBM Corporation, Armonk, NY, USA) was used for all statistical analyses of patient characteristics. Graphs and statistical analyses for biomarker expression were created and performed using GraphPad Prism version 8 (GraphPad Software, La Jolla, CA, USA). Differences with a *p*-value < 0.05 were considered significant.

## RESULTS

## **Patient characteristics**

Eighty-seven patients diagnosed with gastric adenocarcinoma were included, of which forty-five (52%) had diffuse-type and forty-two (48%) had intestinal-type disease. Clinicopathological characteristics are summarized in Table 1. In the intestinal type group, 17 (40%) patients had well-moderately differentiated tumors, compared to 0 (0%) in the diffuse type group (p < 0.001). NAT consisted of chemotherapy, while one patient received chemoradiotherapy. Albeit not statistically significant, there was a small difference in the number of patients that received NAT in both groups (diffuse type: 32 (71%); intestinal type: 22 (52%); p = 0.097). Other baseline characteristics did not differ between both groups.

**TABLE 1** Patient characteristics of the total gastric cancer cohort (n = 87) as well as diffuse type (n = 45) and intestinal-type (n = 42) subgroups.

Characteristic	Total (n = 87)	Diffuse type $(n = 45)$	Intestinal type $(n = 42)$	<i>p</i> -value
Age, mean (SD)	67.2 (12.7)	64.3 (14.1)	70.3 (10.3)	0.073
Gender, n (%)				0.038
Male	28 (32)	26 (58)	33 (79)	
Female	59 (68)	19 (42)	9 (21)	
Surgery type, n (%)				0.407
Total gastrectomy	35 (40)	20 (44)	15 (36)	
Partial gastrectomy	52 (60)	25 (56)	27 (64)	
Tumor localization, n (%)				
Cardia/fundus	15 (17)	6 (13)	9 (21)	0.298
Corpus	24 (28)	11 (24)	13 (31)	
Antrum	34 (39)	20 (44)	14 (33)	
Pre-pyloric	8 (9)	3 (7)	5 (12)	
Other	6 (7)	5 (11)	1 (2)	
Tumor differentiation, n (%)				
Well-moderate	17 (20)	0 (0)	17 (40)	< 0.001
Poor	51 (59)	27 (60)	24 (57)	
Missing	19 (22)	18 (40)	1 (2)	
Primary tumor, n (%)				
pT1	15 (17)	5 (11)	10 (24)	0.210
pT2	9 (10)	7 (16)	2 (5)	
pT3	37 (43)	19 (42)	18 (43)	
pT4	26 (30)	14 (31)	12 (29)	
Regional lymph nodes, n (%)				
pN0	27 (31)	15 (33)	12 (29)	0.789
pN1	21 (24)	12 (27)	9 (21)	
pN2	16 (18)	8 (18)	8 (19)	
pN3	23 (26)	10 (22)	13 (31)	
Neoadjuvant therapy, n (%)				
Yes, chemotherapy	53 (61)	32 (71)	21 (50)	0.097
Yes, chemoradiotherapy	1(1)	0 (0)	1 (2)	
No	33 (38)	13 (29)	20 (48)	
R-status, n (%)				
RO	76 (87)	38 (84)	38 (90)	0.234
R1	10 (11)	7 (16)	3 (7)	
Missing	1(1)	0 (0)	1(2)	

## Biomarker expression in primary gastric cancer tissue specimens

Tissue slides were stained for  $\alpha_V\beta_6$ , CEACAM5, EGFR, EpCAM and HER2 expression and expression was quantified using the TIS. Representative examples of these stainings are shown in Figure 1. Positive expression (TIS values  $\geq 1$ ) on primary gastric tumors was found in 86% of the tumors for  $\alpha_V\beta_6$ , 72% for CEACAM5, 77% for EGFR, 93% for EpCAM and 71% for HER2 (Table 2). Categorized staining intensities are depicted in Table 3. All biomarkers showed a membranous staining pattern, with  $\alpha_V\beta_6$  and EpCAM showing a mostly homogenous staining pattern, while staining was slightly more heterogeneous for CEACAM5, EGFR and HER2 (Figure 1). Additionally, biomarker co-expression in primary gastric tumors was analyzed (Table 4). The highest co-expressing biomarker combination was  $\alpha_V\beta_6$  and EpCAM that were simultaneously expressed in 84% for primary gastric tumors. The remaining biomarker combinations were always expressed in more than 55% of cases, indicating moderate co-expression. Additionally, for all biomarker combinations, 88-98% of primary tumors was positive for at least one of the two biomarkers ( $\geq 1$ ).

**TABLE 2** Percentages of positive biomarker expression in primary gastric cancer tissue specimens (TIS  $\geq 1$ ).

Biomarker	Positive tumor expression (%)
$ \alpha_{V}eta_{\scriptscriptstyle{6}}$	86
CEACAM5	72
EGFR	77
EpCAM	93
HER2	71

**TABLE 3** Distribution of  $\alpha_V \beta_6$ , CEACAM5, EGFR, EpCAM and HER2 expression on primary gastric cancer as quantified by the TIS values categorized into negative (TIS = 0), weak (TIS = 1, 2, 3, 4) moderate (TIS = 6, 8) or strong expression (TIS = 9, 12).

Biomarker	No. of tissue	Negative n (%)	Weak n (%)	Moderate n (%)	Strong n (%)
$\alpha_V \beta_6$	n = 87	12 (14)	27 (31)	24 (28)	24 (28)
CEACAM5	n = 87	24 (28)	20 (23)	14 (16)	29 (33)
EGFR	n = 84	19 (23)	26 (31)	26 (31)	13 (15)
EpCAM	n = 86	6 (7)	7 (8)	18 (21)	55 (64)
HER2	n = 84	24 (29)	36 (43)	20 (24)	4 (5)

78

**FIGURE 1** Representative images of HE and immunohistochemical staining of  $\alpha v\beta 6$ , CEACAM5, EGFR, EpCAM and HER2 on primary gastric cancer, as well as healthy surrounding stomach, esophageal and duodenal tissue. Overview images and inserts are taken at  $5\times$  and  $20\times$  magnification, respectively. Scale bars represent  $200~\mu M$ .

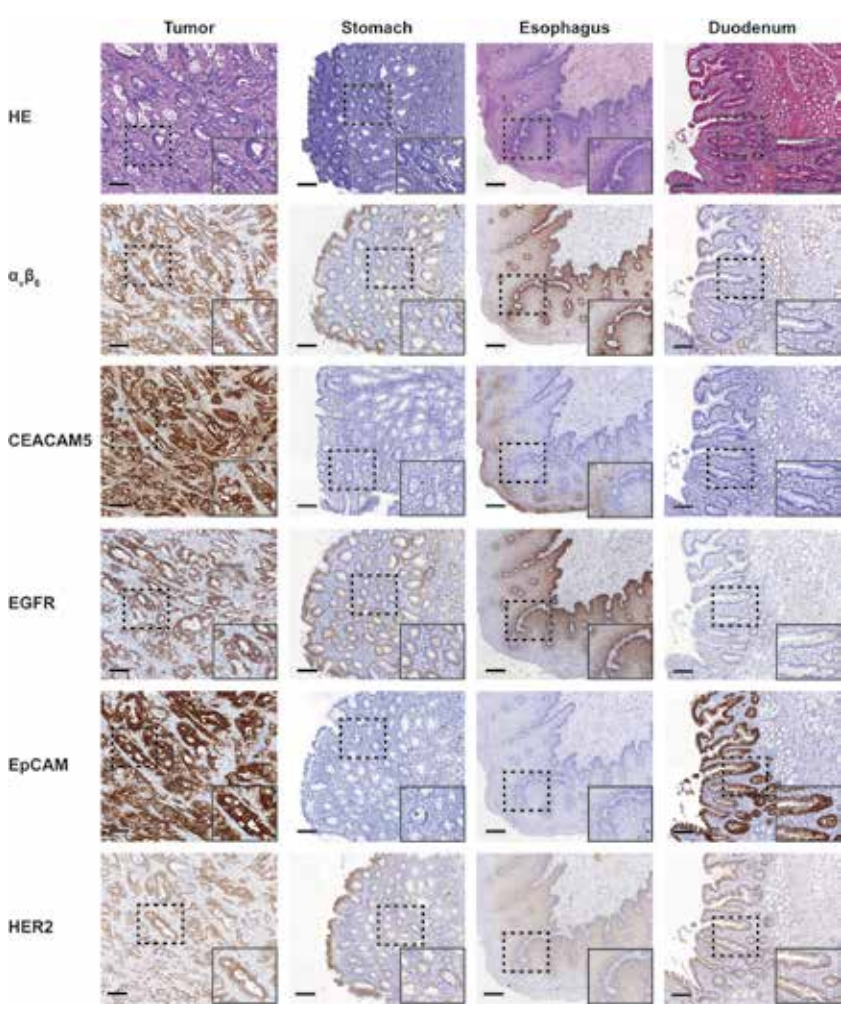


**TABLE 4** Percentage of cases with positive  $\alpha_V \beta_{e_s}$ , CEACAM5, EGFR, EpCAM and HER2 expression for at least one of two biomarker combinations (panel:  $\ge 1$ ) along with the percentage of cases with positive expression of both biomarkers (panel: both), as quantified by a dichotomized TIS (TIS = o: negative, all other TIS values: positive expression).

Biomarker	Panel	$\alpha_{V}\beta_{6}$ (%)	CEACAM5 (%)	EGFR (%)	EpCAM (%)	HER2 (%)
$\alpha_V \beta_6$	≥1	-	93	94	95	94
αγρ <sub>6</sub>	Both		66	77	84	71
CEACAM5	≥1	93	-	93	95	90
CEACAIMS	Both	66		56	70	55
EGFR	≥1	94	93	-	98	88
EGFK	Both	77	56		74	59
EnCAM	≥1	95	95	98	-	94
EpCAM	Both	84	70	74		71
LIEDO	≥1	94	90	88	94	-
HER2	Both	71	55	59	71	

# Subgroup analyses of biomarker expression in primary gastric cancer tissue specimens

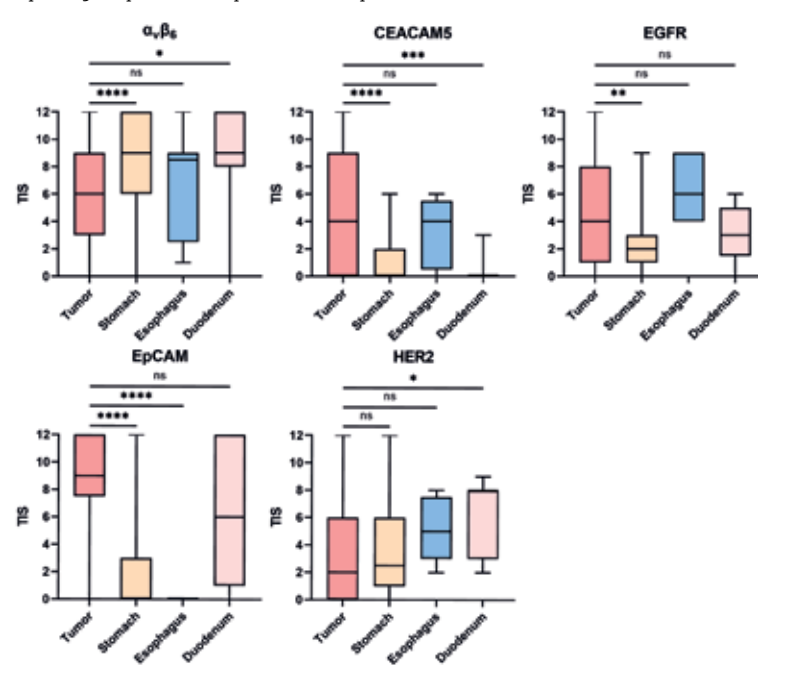
Subgroup analyses revealed that median expression between diffuse and intestinal type tumor did not differ for all biomarkers expect for HER2, which showed a lower median TIS on diffuse-type tumors (median TIS 4.0 vs. 2.0; p = 0.0004, also see Table 2 of the ESM). Moreover, subgroup analyses of biomarker expression in primary tumor tissues between patients that did not receive NAT and received NAT revealed that the median TIS for CEACAM5 and EGFR was lower on tumor specimens derived from patients that received NAT (CEACAM5: median TIS 9.0 vs. 3.5; p = 0.0215; EGFR: median TIS 6.0 vs. 3.0; p = 0.0072, also see Table 3 of the ESM). For the remaining biomarkers, primary tumor expression was similar in patients who received NAT and patients who did not receive NAT.

# Biomarker expression in primary gastric cancer vs. healthy surrounding stomach, esophageal and duodenal tissue specimens

Images of sequential tumor sections showing biomarker expression in primary gastric cancer, and healthy surrounding stomach, esophageal as well as duodenal tissue specimens are shown in Figure 1. Quantified TIS values representing expression of  $\alpha_V\beta_6$ , CEACAM5, EGFR, EpCAM and HER2 as well as the statistical comparison of biomarker expression is depicted in Figure 2 and Table 4 of the ESM. For  $\alpha_V\beta_6$ , median expression in primary gastric cancer tissue was lower compared to healthy surrounding stomach (median TIS 6.0 vs. 9.0; p < 0.0001) and duodenal tissue (median TIS 6.0 vs. 8.5; p = 0.0427), and similar to expression in esophageal

tissue (median TIS 6.0 vs. 9.0; p > 0.9999). For CEACAM5, expression in primary tumor tissue was higher compared to healthy surrounding stomach (median TIS 4.0 vs. 0.0; p < 0.0001) and duodenal tissue (median TIS 4.0 vs. 0.0; p = 0.0003), but comparable to esophageal tissue (median TIS 4.0 vs. 4.0; p > 0.9999). EGFR expression in primary tumor tissue was higher compared to healthy surrounding stomach tissue (median TIS 4.0 vs. 2.0; p = 0.0023) but similar to esophageal (median TIS 4.0 vs. 6.0; p = 0.2235) and duodenal tissue (median TIS 4.0 vs 3.0; p > 0.9999). EpCAM expression in tumor tissue was higher compared to healthy surround stomach (median TIS 9.0 vs. 0.0; p < 0.0001) and esophageal tissue (median TIS 9.0 vs. 6.0; p = 0.7003). Lastly, HER2 expression in primary tumor tissue was not different from healthy surrounding stomach (median TIS 2.0 vs. 2.5; p > 0.9999) and esophageal tissue (median TIS 2.0 vs. 5.0; p = 0.1454) and lower than duodenal tissue (median TIS 2.0 vs. 8.0; p = 0.0152).

FIGURE 2 Box plots representing TIS values of  $\alpha_V \beta_e$ , CEACAM5, EGFR, EpCAM and HER2 staining on primary gastric cancer, as well as healthy surrounding stomach, esophageal and duodenal tissue. Horizontal lines represents the median TIS values, boxes represent interquartile range and brackets represent total TIS range. ns: not significant, TIS: total immunostaining score. \*:  $p \le 0.05$ , \*\*:  $p \le 0.01$ , \*\*\*:  $p \le 0.001$ , \*\*\*\*:  $p \le 0.0001$ .



# Expression of biomarkers in tumor-positive and tumor-negative lymph node tissue specimens

Biomarker expression was evaluated on metastatic lymph nodes (LN<sup>+</sup>) as well as tumor-negative lymph nodes (LN<sup>-</sup>). Representative IHC images showing expression of  $\alpha_V \beta_6$ , CEACAM5, EGFR, EpCAM and HER2 on LN<sup>+</sup> tissue are shown in Figure 3. Sensitivity, specificity, positive predictive value (PPV), negative predictive value (NPV) and area under the curve (AUC) were calculated based on dichotomous (positive/negative) biomarker expression and depicted in Table 5. Although sensitivity for LN<sup>+</sup>vs. LN<sup>-</sup> differentiation was moderate for HER2 and CEACAM5 (both 56%), no false-positive staining was observed. For the remaining biomarkers, higher sensitivity (range 72-82%) and 100% specificity for differentiation between LN<sup>+</sup> and LN<sup>-</sup> was observed, indicating their potential to serve as targets for imaging of metastatic lymph nodes. Accuracy for identifying tumor-positive and tumornegative lymph nodes ranged between 82 and 93% for all biomarkers.

FIGURE 3 Representative images of HE and immunohistochemical staining of  $\alpha_V \beta_6$ , CEACAM5, EGFR, EpCAM and HER2 on lymph node metastases of gastric cancer. Overview images and inserts are taken at 5× and 20× magnification, respectively. Scale bars represent 200  $\mu$ M.

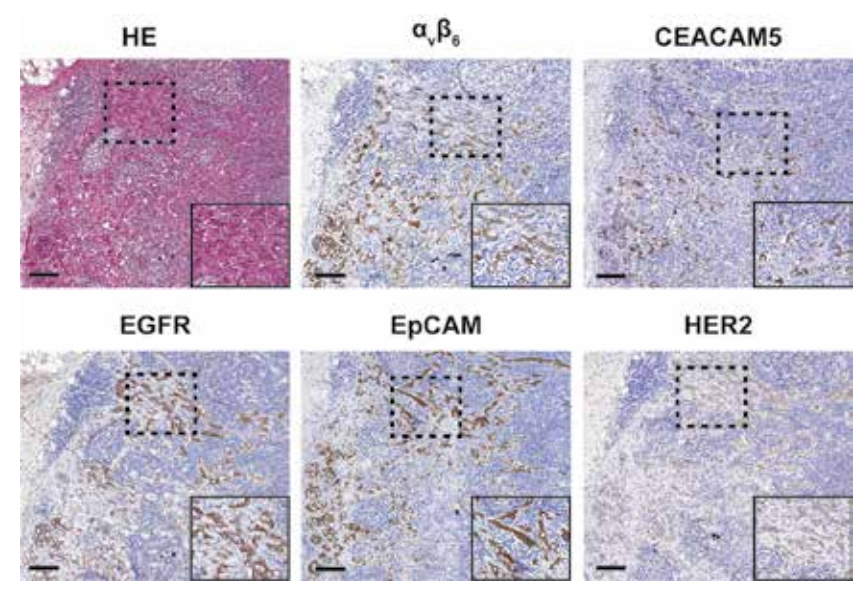


**TABLE 5** Sensitivity, specificity, PPV, NPV and accuracy along with the AUC and *p*-value for identification of LN<sup>+</sup> tissue specimens based on  $\alpha_V \beta_\varepsilon$ , CEACAM5, EGFR, EpCAM and HER2 expression. A dichotomized (positive/negative) TIS was used (TIS = o: negative expression, all other TIS values: positive expression).

Biomarker	Sens. (%)	Spec. (%)	PPV (%)	NPV (%)	Accuracy (%)	AUC (95% CI)	<i>p</i> -value
$\alpha_V\beta_{\scriptscriptstyle 6}$	72	100	100	85	89	0.860 (0.782; 0.938)	< 0.0001
CEACAM5	56	100	100	78	83	0.780 (0.689; 0.872)	< 0.0001
EGFR	74	100	100	86	90	0.872 (0.795; 0.949)	< 0.0001
EpCAM	82	100	100	89	93	0.908 (0.843; 0.974)	< 0.0001
HER2	56	100	100	77	82	0.780 (0.688; 0.872)	< 0.0001

AUC: area under the curve, CI: confidence interval, PPV: positive predictive value, NPV: negative predictive value, Sens.: sensitivity, Spec.: specificity.

# Expression of selected biomarkers in metastatic gastric cancer tissue specimens

Based on their tumor-specific expression pattern and accurate LN<sup>+</sup> detection potential, CEACAM5, EGFR and EpCAM were selected for further analysis of their expression in metastatic gastric cancer tissue specimens derived from 19 patients. Patient characteristics of this cohort are described in Table 5 of the ESM. Tissue specimens were derived from various locations, with the most common locations including the abdominal wall (4/19, 21%), peritoneum (3/19, 16%) and large/small intestine (both 2/19, 11%). Representative IHC images of HE, CEACAM5, EGFR and EpCAM staining are depicted in Figure 4. Positive biomarker expression in metastatic gastric cancer tissue specimens was observed in 94% for CEACAM5, 88% for EGFR and 95% for EpCAM (Table 6). As can be derived from Table 7, CEACAM5 and EpCAM staining was predominantly strong, while EGFR staining was somewhat weaker.

**FIGURE 4** Representative images of HE and immunohistochemical staining of CEACAM5, EGFR and EpCAM on distant metastases of gastric cancer. Overview images and inserts are taken at  $5\times$  and  $20\times$  magnification, respectively. Scale bars represent  $200~\mu$ M.

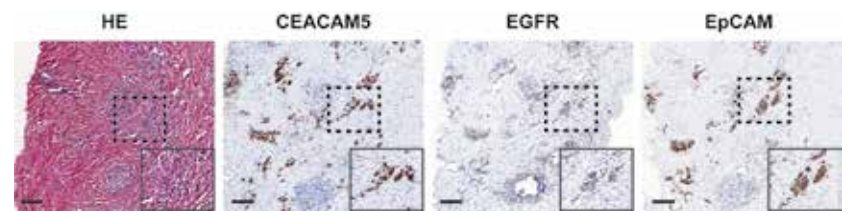


**TABLE 6** Percentages of positive biomarker expression in metastatic gastric cancer tissue specimens (TIS  $\geq$ 1).

Biomarker	Positive tumor expression (%)
CEACAM5	94
EGFR	88
EpCAM	95

**TABLE 7** Distribution of CEACAM5, EGFR and EpCAM expression in metastatic gastric cancer tissue specimens as quantified by the TIS values categorized into negative (TIS = 0), weak (TIS = 1, 2, 3, 4) moderate (TIS = 6, 8) or strong expression (TIS = 9, 12).

Biomarker	No. of tissue	Negative n (%)	Weak n (%)	Moderate n (%)	Strong n (%)
CEACAM5	n = 18	1 (6)	6 (33)	4 (22)	7 (39)
EGFR	n = 16	2 (13)	10 (63)	2 (13)	2 (13)
EpCAM	n = 19	1 (5)	3 (16)	2 (11)	13 (68)

## **DISCUSSION**

Molecular imaging through tumor-targeted PET and FGS can address current limitations in pre- and intraoperative staging as well as resection margin assessment of gastric cancer. Adequate selection and application of molecular imaging targets is the main perquisite for adequate tumor visualization using these techniques. The current study showed that  $\alpha_V \beta_6$ , CEACAM5, EGFR, EpCAM and HER2, all promising tumor-specific targets for gastrointestinal cancers, were abundantly expressed in primary gastric tumor tissue specimens, with positive expression ranging from 71% to 93%. Regarding biomarker co-expression, 88-98% of primary gastric tumors showed positive expression of at least one of two biomarkers for all possible biomarker combinations, indicating the potential added value of bispecific tracers to increase the number of patients eligible for molecular imaging. Additionally, CEACAM5, EGFR and EpCAM showed higher expression in tumor tissue compared to healthy surrounding stomach tissue, classifying these targets as suitable for primary gastric cancer imaging. As  $\alpha_V \beta_{\scriptscriptstyle 6}$  and HER2 expression in healthy surrounding stomach tissue was higher or did not differ from primary tumor expression, respectively, we consider these targets not suitable for molecular imaging of primary gastric cancer. Despite moderate sensitivity for LN<sup>+</sup> detection observed for CEACAM5 and HER2 (both 56%), all biomarkers could distinguish LN<sup>+</sup> and LN with high accuracy, indicating the potential of these targets for pre- and intraoperative N-staging. Lastly, EGFR, EpCAM and CEACAM5 showed moderate to strong expression in virtually all distant (peritoneal) metastases, highlighting their potential as targets for M-staging. Our study therefore demonstrated the feasibility of EGFR, EpCAM and CEACAM5 as molecular imaging targets for gastric cancer in a clinically relevant context.

The abundant tumor expression of the biomarkers reported herein is largely in line with previous studies, albeit we reported higher percentages of positive IHC staining compared to previous research, particularly for  $\alpha_V \beta_6$ , EGFR and HER2. This could, among others, have been caused by the use of different scoring systems, primary antibodies or antigen retrieval techniques during IHC staining, as well as inter- and intratumoral heterogeneity, and the relatively small sample sizes of previous IHC studies. Confirmation of our results in a different or larger cohort of gastric cancer patients could verify validity of the results observed herein, as well as elucidate underlying mechanisms contributing to these discrepancies.

A strong methodological point of this study is the additional evaluation of biomarker expression in healthy surrounding esophageal and duodenal tissue specimens. Similar CEACAM5 and EpCAM expression levels were found on healthy esophageal and duodenal tissue compared to tumor expression, respectively, while EGFR expression in both tissue types did not differ from tumor expression. Consistent with our findings, expression of CEACAM5 and EGFR has been identified in healthy esophageal tissue, while EGFR and EpCAM expression in, respectively, duodenal mucosa, and epithelia of both the small and large intestines was also reported. 21,37-40 Although previous literature described that EpCAM is overexpressed in gastrointestinal tumors compared to healthy surrounding tissue, it should be noted that EpCAM's presence in the small and large intestine might impact the detection of peritoneal metastases of gastric cancer using EpCAM-targeted molecular imaging tracers.<sup>21</sup> Taken further, the absence of EpCAM on esophageal tissue makes EpCAM a more suitable target for delineation of proximal gastric cancers located near the esophageal-gastric junction (EGJ), while absence of CEACAM5 on duodenum epithelium makes this target appropriate for assessing resection margins of distal gastric cancers invading the duodenum. Of note, EGJ and duodenal invasion are frequently present in (sub) cardia (33-50%) and distal gastric cancer (14-33%), respectively.<sup>41-43</sup> Moreover, considering the increased R1 resection rate and reduced patient survival in these locally advanced cancers, adequate intraoperative tumor delineation may be a valuable tool to improve adequate resection margin assessment and, potentially, patient outcomes.44,45

In addition, the inclusion of patients with diffuse- and intestinal-type adenocarcinomas, as well as patients who received neoadjuvant therapy, allowed subgroup analyses to study potential effect of these clinicopathological factors on the biomarkers' expression level. Interestingly, we found similar biomarker expression in diffuse- and intestinal-type adenocarcinomas for all biomarkers, except for HER2 that showed lower TIS values on intestinal-type tumor tissue specimens. This makes the remaining biomarkers broadly applicable as molecular imaging markers in gastric cancer patients. Moreover, this finding is particularly promising for molecular imaging of diffuse-type gastric cancers, given the lower <sup>18</sup>F-FDG-PET avidity, more frequent underestimation of the proximal margin length and increased irradical resection rate in this histological subtype. <sup>44,46-49</sup> Additionally, subgroup analyses revealed that CEACAM5 and EGFR expression was lower in patients who received NAT. Consequently, care should be taken when targeting CEACAM5 and EGFR for molecular imaging of primary gastric tumors after NAT.

Preoperatively, several targeted PET tracers have aimed to address current limitations in staging of gastric cancer in both the preclinical and clinical setting, with a strong focus on fibroblast activation protein (FAP)-targeted agents. FAP is expressed in 55-75% of gastric carcinomas and is associated with increased migration, invasion and reduced survival, while expression in healthy surrounding tissues is virtually absent. Fap. A recent meta-analysis showed that FAPI PET outperformed conventional Fap. Fed. Pet sensitivity for primary tumor, lymph node metastasis and peritoneal dissemination of gastric cancer, thereby indicating the potential of both FAPI PET as well as targeted PET in general. However, the overexpression of FAP in tissue during instances of tissue remodeling, such as wound healing or chronic inflammation, could pose a threat for its potential to delineate benign from malignant tissue. Nevertheless, although our study intended to focus on tumor cell-specific molecular imaging targets, additional evaluation and comparison of FAP expression in our cohort would be an interesting continuation of this study.

Of the targets evaluated herein, only HER2 has been clinically targeted for PET imaging in gastric cancer. Using <sup>89</sup>Zr-trastuzumab, O'Donoghue et al. observed tumor accumulation in 80% of patients with positive HER2-status, however not all known lesions could be visualized in these patients.<sup>56</sup> Interestingly, the authors did not observe significant stomach uptake as one would expect based on our observation of similar HER2 expression in primary tumors and healthy surrounding stomach tissue. It should be noted that, although positive biomarker expression remains a fundamental criterion for successful molecular imaging, it does not invariably correlate with positive tumor uptake in the clinical setting,

underscoring the importance of both tumor heterogeneity and extensive clinical validation of molecular imaging tracers. Noteworthy, significant stomach wall and intestine uptake is commonly reported for  $\alpha v \beta_6$ -targeting PET tracers, thus reflecting our findings of high  $\alpha v \beta_6$  expression in these tissue types.<sup>57</sup>

FGS-related research in gastric cancer has particularly focused on fluorescence-guided lymphadenectomy, as opposed to primary tumor imaging or intra-operative tumor staging. For instance, Chen et al. randomized gastric cancer patients between ICG-guided lymphadenectomy using submucosal injection 1 day preoperatively and conventional laparoscopic gastrectomy. The authors showed that ICG-guided lymphadenectomy yielded more lymph nodes compared to the non-ICG group, leading to less unremoved lymph node stations, while complication rates between both groups were similar. However, sensitivity for metastatic lymph node detection was moderate at 56%. Considering these and previously outlined constraints in accurate intraoperative staging of gastric cancer staging, redirecting focus in FGS-related research towards tumor-targeted imaging could pave the way for novel tracers that address these limitations.

This study has some limitations. For instance, the relatively small sample size may have reduced the robustness of our subgroup analyses. Therefore, the findings of the subgroup analyses reported herein, although relevant for the assessment of a molecular imaging target's suitability, should be interpreted with caution. Secondly, due to the presence of staining artefacts, some slides were not suitable for scoring. Nevertheless, as the amount of excluded tissue slides per marker was limited (maximum 3/87 primary tumor specimens), we do not anticipate this influenced the findings of our study and reproducibility thereof.

Future research into molecular imaging targets for gastric cancer could focus on their expression in premalignant tissue, such as chronic gastritis, intestinal metaplasia or dysplasia, thereby establishing the targets' potential for differentiation between malignant and benign tissue. For Also, as molecular targets are not expressed in all patients, preoperative screening for positive biomarker expression could be performed, followed by application of the most suitable molecular imaging tracer. When feasible, such a strategy would form a robust and efficient way of patient-tailored employment of molecular imaging tracers in gastric cancer, maximizing its potential to improve pre- and intraoperative staging as well as resection margin assessment. This may be performed using biopsy material of primary gastric tumors or metastases, which is routinely obtained for histological diagnosis. Moreover, the predictive value of biomarker expression in tumor biopsies for primary gastric tumor expression remains to be elucidated.

#### CONCLUSION

Our findings show that CEACAM5, EGFR and EpCAM are promising targets for molecular imaging of gastric cancer, as well as lymph node and distant metastases. By improving pre- and intraoperative identification of tumor tissue, targeted PET and FGS could enhance gastric cancer staging and resection, ultimately leading to improved patient outcomes. Further clinical evaluation of PET and FGS tracers targeting these antigens is warranted.

#### SUPPLEMENTARY MATERIALS

88

The following Supplementary Materials are available online at: https://bit.ly/4j3IBDa.

Supplementary Table 1: Primary antibody and immunohistochemical protocol information; Supplementary Table 2: Quantified biomarker expression in primary gastric cancer between diffuse- and intestinal-type carcinomas; Supplementary Table 3: Quantified biomarker expression in primary gastric cancer between patients that received no NAT and patients who received NAT; Supplementary Table 4: Quantified biomarker expression in primary gastric cancer vs. healthy surrounding stomach, esophagus and duodenum; Supplementary Table 5: patient characteristics of the gastric cancer metastases cohort.

#### REFERENCES

- Li Y, Feng A, Zheng S, Chen C, Lyu J. Recent Estimates and Predictions of 5-Year Survival in Patients with Gastric Cancer: A Model-Based Period Analysis. Cancer Control. 2022;29:10732748221099227.
- 2 Sung H, Ferlay J, Siegel RL, Laversanne M, Soerjomataram I, Jemal A, et al. Global Cancer Statistics 2020: GLO-BOCAN Estimates of Incidence and Mortality Worldwide for 36 Cancers in 185 Countries. CA Cancer J Clin. 2021;71(3):209-49.
- 3 Mocan L. Surgical Management of Gastric Cancer: A Systematic Review. J Clin Med. 2021;10(12).
- 4 Borggreve AS, Goense L, Brenkman HJF, Mook S, Meijer GJ, Wessels FJ, et al. Imaging strategies in the management of gastric cancer: current role and future potential of MRI. Br J Radiol. 2019;92(1097):20181044.
- 5 Gertsen EC, Brenkman HJF, van Hillegersberg R, van Sandick JW, van Berge Henegouwen MI, Gisbertz SS, et al. 18F-Fludeoxyglucose-Positron Emission Tomography/Computed Tomography and Laparoscopy for Staging of Locally Advanced Gastric Cancer: A Multicenter Prospective Dutch Cohort Study (PLASTIC). JAMA Surg. 2021;156(12):e215340.
- 6 Giandola T, Maino C, Marrapodi G, Ratti M, Ragusi M, Bigiogera V, et al. Imaging in Gastric Cancer: Current Practice and Future Perspectives. Diagnostics (Basel). 2023;13(7).
- Kim SH, Kim JJ, Lee JS, Kim SH, Kim BS, Maeng YH, et al. Preoperative N staging of gastric cancer by stomach protocol computed tomography. J Gastric Cancer. 2013;13(3):149-56.
- 8 Findlay JM, Antonowicz S, Segaran A, El Kafsi J, Zhang A, Bradley KM, et al. Routinely staging gastric cancer with (18)F-FDG PET-CT detects additional metastases and predicts early recurrence and death after surgery. Eur Radiol. 2019;29(5):2490-8.
- 9 Zhang Z, Zheng B, Chen W, Xiong H, Jiang C. Accuracy of (18)F-FDG PET/CT and CECT for primary staging and diagnosis of recurrent gastric cancer: A meta-analysis. Exp Ther Med. 2021;21(2):164.
- 10 Leake PA, Cardoso R, Seevaratnam R, Lourenco L, Helyer L, Mahar A, et al. A systematic review of the accuracy and indications for diagnostic laparoscopy prior to curativeintent resection of gastric cancer. Gastric Cancer. 2012;15 Suppl 1:538-47.
- 11 Allen CJ, Blumenthaler AN, Das P, Minsky BD, Blum M, Roy-Chowdhuri S, et al. Staging laparoscopy and peritoneal cytology in patients with early stage gastric adenocarcinoma. World J Surg Oncol. 2020;18(1):39.
- 12 Fukagawa T. Role of staging laparoscopy for gastric cancer patients. Ann Gastroenterol Surg. 2019;3(5):496-505.
- 13 Schena CA, Laterza V, De Sio D, Quero G, Fiorillo C, Gunawardena G, et al. The Role of Staging Laparoscopy for Gastric Cancer Patients: Current Evidence and Future Perspectives. Cancers (Basel). 2023;15(13).
- 14 Vahrmeijer AL, Hutteman M, van der Vorst JR, van de Velde CJH, Frangioni JV. Image-guided cancer surgery using near-infrared fluorescence. Nature reviews Clinical oncology, 2013;10(9):507-18.
- 15 Jiang Z, Liu C, Cai Z, Shen C, Yin Y, Yin X, et al. Impact of Surgical Margin Status on Survival in Gastric Cancer: A

- Systematic Review and Meta-Analysis. Cancer Control. 2021;28:10732748211043665.
- 16 Hirata Y, Agnes A, Estrella JS, Blum Murphy M, Das P, Minsky BD, et al. Clinical Impact of Positive Surgical Margins in Gastric Adenocarcinoma in the Era of Preoperative Therapy. Ann Surg Oncol. 2023;30(8):4936-45.
- 17 Hernot S, van Manen L, Debie P, Mieog JSD, Vahrmeijer AL. Latest developments in molecular tracers for fluorescence image-guided cancer surgery. The Lancet Oncology. 2019;20(7):e354-e67.
- 18 Arçay Öztürk A, Flamen P. FAP-targeted PET imaging in gastrointestinal malignancies: a comprehensive review. Cancer Imaging. 2023;23(1):79.
- 19 de Geus SW, Boogerd LS, Swijnenburg RJ, Mieog JS, Tummers WS, Prevoo HA, et al. Selecting Tumor-Specific Molecular Targets in Pancreatic Adenocarcinoma: Paving the Way for Image-Guided Pancreatic Surgery. Mol Imaging Biol. 2016;18(6):807-19.
- 20 Tummers WS, Farina-Sarasqueta A, Boonstra MC, Prevoo HA, Sier CF, Mieog JS, et al. Selection of optimal molecular targets for tumor-specific imaging in pancreatic ductal adenocarcinoma. Oncotarget. 2017;8(34):56816-28.
- 21 Linders D, Deken M, van der Valk M, Tummers W, Bhairosingh S, Schaap D, et al. CEA, EpCAM, ανβ6 and uPAR Expression in Rectal Cancer Patients with a Pathological Complete Response after Neoadjuvant Therapy. Diagnostics (Basel). 2021;11(3).
- 22 Wang L, Liang M, Xiao Y, Chen J, Mei C, Lin Y, et al. NIR-II Navigation with an EGFR-Targeted Probe Improves Imaging Resolution and Sensitivity of Detecting Micrometastases in Esophageal Squamous Cell Carcinoma Xenograft Models. Mol Pharm. 2022;19(10):3563-75.
- 23 Spizzo G, Fong D, Wurm M, Ensinger C, Obrist P, Hofer C, et al. EpCAM expression in primary tumour tissues and metastases: an immunohistochemical analysis. J Clin Pathol. 2011;64(5):415-20.
- 24 Yan M, Schwaederle M, Arguello D, Millis SZ, Gatalica Z, Kurzrock R. HER2 expression status in diverse cancers: review of results from 37,992 patients. Cancer Metastasis Rev. 2015;34(1):157-64.
- 25 Hausner SH, Bold RJ, Cheuy LY, Chew HK, Daly ME, Davis RA, et al. Preclinical Development and First-in-Human Imaging of the Integrin  $\alpha(v)\beta(6)$  with  $[(18)F]\alpha(v)\beta(6)$ -Binding Peptide in Metastatic Carcinoma. Clin Cancer Res. 2019;25(4):1206-15.
- 26 Boogerd LSF, Hoogstins CES, Schaap DP, Kusters M, Hand-graaf HJM, van der Valk MJM, et al. Safety and effectiveness of SGM-101, a fluorescent antibody targeting carcino-embryonic antigen, for intraoperative detection of colorectal cancer: a dose-escalation pilot study. Lancet Gastroenterol Hepatol. 2018;3(3):181-91.
- 27 de Valk KS, Deken MM, Schaap DP, Meijer RP, Boogerd LS, Hoogstins CE, et al. Dose-Finding Study of a CEA-Targeting Agent, SGM-101, for Intraoperative Fluorescence Imaging of Colorectal Cancer. Ann Surg Oncol. 2021;28(3):1832-44.
- 28 Bragina Ö, von Witting E, Garousi J, Zelchan R, Sandström M, Orlova A, et al. Phase I Study of (99m)Tc-ADAPT6, a Scaffold Protein-Based Probe for Visualization of HER2 Expression in Breast Cancer. J Nucl Med. 2021;62(4):493-9.
- 29 Gabriëls RY, van Heijst LE, Hooghiemstra WTR, van der Waaij AM, Kats-Ugurlu G, Karrenbeld A, et al. Detection of

- Early Esophageal Neoplastic Barrett Lesions with Quanti- 45 Kumazu Y, Hayashi T, Yoshikawa T, Yamada T, Hara K, fied Fluorescence Molecular Endoscopy Using Cetuximab-800CW. J Nucl Med. 2023;64(5):803-8.
- 30 Voskuil FJ, de Jongh SJ, Hooghiemstra WTR, Linssen MD, Steinkamp PJ, de Visscher S, et al. Fluorescenceguided imaging for resection margin evaluation in head and neck cancer patients using cetuximab-800CW: A quantitative dose-escalation study. Theranostics. 2020;10(9):3994-4005.
- 31 Lian PL, Liu Z, Yang GY, Zhao R, Zhang ZY, Chen YG, et al. Integrin αvβ6 and matrix metalloproteinase 9 correlate with survival in gastric cancer. World J Gastroenterol.
- 32 Wang W, Seeruttun SR, Fang C, Chen J, Li Y, Liu Z, et al. Prognostic Significance of Carcinoembryonic Antigen Staining in Cancer Tissues of Gastric Cancer Patients. Ann Surg Oncol. 2016;23(4):1244-51.
- 33 Arienti C, Pignatta S, Tesei A. Epidermal Growth Factor Receptor Family and its Role in Gastric Cancer. Front Oncol. 2019;9:1308.
- 34 Dai M, Yuan F, Fu C, Shen G, Hu S, Shen G. Relationship between epithelial cell adhesion molecule (EpCAM) overexpression and gastric cancer patients: A systematic review and meta-analysis. PLoS One. 2017;12(4):e0175357.
- 35 Boku N. HER2-positive gastric cancer. Gastric Cancer. 2014:17(1):1-12.
- 36 Meyerholz DK, Beck AP. Principles and approaches for reproducible scoring of tissue stains in research. Lab Invest.
- 37 Zhou J, Fan X, Chen N, Zhou F, Dong J, Nie Y, et al. Identification of CEACAM5 as a Biomarker for Prewarning and Prognosis in Gastric Cancer. J Histochem Cytochem. 2015;63(12):922-30.
- 38 Patriarca C, Macchi RM, Marschner AK, Mellstedt H. Epithelial cell adhesion molecule expression (CD326) in cancer: a short review. Cancer Treat Rev. 2012;38(1):68-75.
- 39 Shi W, Zhang S. [Expression of epidermal growth factor receptor in human duodenal ulcer]. Hua Xi Yi Ke Da Xue Xue Bao. 1997;28(3):280-3.
- 40 Abedi-Ardekani B. Dar NA. Mir MM. Zargar SA. Lone MM. Martel-Planche G, et al. Epidermal growth factor receptor (EGFR) mutations and expression in squamous cell carcinoma of the esophagus in central Asia. BMC Cancer. 2012;12:602.
- 41 Ito H, Inoue H, Odaka N, Satodate H, Suzuki M, Mukai S, et al. Comparison of Clinicopathological Characteristics in the Patients with Cardiac Cancer with or without Esophagogastric Junctional Invasion: A Single-Center Retrospective Cohort Study. Int J Surg Oncol. 2013;2013:189459.
- 42 Oh SE, Park S, Ahn S, An JY, Lee JH, Sohn TS, et al. Prognostic Significance of Esophagogastric Junction Invasion in Patients with Adenocarcinoma of the Cardia or Subcardia. Cancers (Basel), 2023:15(6).
- 43 Kumagai K, Sano T, Hiki N, Nunobe S, Tsujiura M, Ida S, et al. Survival benefit of "D2-plus" gastrectomy in gastric cancer patients with duodenal invasion. Gastric Cancer. 2018:21(2):296-302.
- 44 Bissolati M, Desio M, Rosa F, Rausei S, Marrelli D, Baiocchi GL, et al. Risk factor analysis for involvement of resection margins in gastric and esophagogastric junction cancer: an Italian multicenter study. Gastric Cancer. 2017;20(1):70-82.

- Shimoda Y, et al. Risk factors analysis and stratification for microscopically positive resection margin in gastric cancer patients. BMC Surg. 2020;20(1):95.
- 46 Smyth EC, Verheij M, Allum W, Cunningham D, Cervantes A. Arnold D. Gastric cancer: ESMO Clinical Practice Guidelines for diagnosis, treatment and follow-up. Ann Oncol. 2016;27(suppl 5):v38-v49.
- 47 Dondi F, Albano D, Giubbini R, Bertagna F. 18F-FDG PET and PET/CT for the evaluation of gastric signet ring cell carcinoma: a systematic review. Nucl Med Commun. 2021;42(12):1293-300.
- 48 Watanabe A, Adamson H, Lim H, McFadden AF, McConnell YJ, Hamilton TD. Intraoperative frozen section analysis of margin status as a quality indicator in gastric cancer surgery. J Surg Oncol. 2023;127(1):66-72.
- 49 Berlth F, Kim WH, Choi JH, Park SH, Kong SH, Lee HJ, et al. Prognostic Impact of Frozen Section Investigation and Extent of Proximal Safety Margin in Gastric Cancer Resection. Ann Surg. 2020;272(5):871-8.
- 50 Puré E, Blomberg R. Pro-tumorigenic roles of fibroblast activation protein in cancer: back to the basics. Oncogene. 2018;37(32):4343-57.
- 51 Kalaei Z, Manafi-Farid R, Rashidi B, Kiani FK, Zarei A, Fathi M. et al. The Prognostic and therapeutic value and clinical implications of fibroblast activation protein- $\alpha$  as a novel biomarker in colorectal cancer. Cell Commun Signal. 2023;21(1):139.
- 52 Wang RF, Zhang LH, Shan LH, Sun WG, Chai CC, Wu HM, et al. Effects of the fibroblast activation protein on the invasion and migration of gastric cancer. Exp Mol Pathol. 2013;95(3):350-56.
- 53 Hathi DK, Jones EF. (68)Ga FAPI PET/CT: Tracer Uptake in 28 Different Kinds of Cancer. Radiol Imaging Cancer. 2019:1(1):e194003.
- 54 Wang Y, Luo W, Li Y. [(68)Ga]Ga-FAPI-04 PET MRI/CT in the evaluation of gastric carcinomas compared with [(18) F]-FDG PET MRI/CT: a meta-analysis. Eur J Med Res. 2023;28(1):34.
- 55 Kessler L. Ferdinandus I. Hirmas N. Zarrad F. Nader M, Kersting D, et al. Pitfalls and Common Findings in (68)Ga-FAPI PET: A Pictorial Analysis. J Nucl Med. 2022;63(6):890-6.
- 56 O'Donoghue JA, Lewis JS, Pandit-Taskar N, Fleming SE, Schöder H, Larson SM, et al. Pharmacokinetics, Biodistribution, and Radiation Dosimetry for (89)Zr-Trastuzumab in Patients with Esophagogastric Cancer. J Nucl Med. 2018;59(1):161-6.
- 57 Kossatz S, Beer AJ, Notni J. It's Time to Shift the Paradigm: Translation and Clinical Application of Non-ανβ3 Integrin Targeting Radiopharmaceuticals. Cancers (Basel). 2021;13(23).
- 58 Chen QY, Xie JW, Zhong Q, Wang JB, Lin JX, Lu J, et al. Safety and Efficacy of Indocvanine Green Tracer-Guided Lymph Node Dissection During Laparoscopic Radical Gastrectomy in Patients With Gastric Cancer: A Randomized Clinical Trial. JAMA Surg. 2020;155(4):300-11.
- 59 Koulis A, Buckle A, Boussioutas A. Premalignant lesions and gastric cancer: Current understanding. World J Gastrointest Oncol. 2019;11(9):665-78.

90 CHAPTER 4 • Targets for molecular imaging of gastric cancer 91

## CHAPTER 5

Prediction of biomarker expression on primary pancreatic ductal adenocarcinoma tissues using fine-needle biopsies: paving the way for a patient-tailored molecular imaging approach

Ruben D. Houvast, Maurice van Duijvenvoorde, JiaXin Chua, Mireille Vankemmelbeke, Lindy G. Durrant, Akin Inderson, Jeanin E. van Hooft, J. Sven D. Mieog, Bert A. Bonsing, Cornelis F. M. Sier, A. Stijn L. P. Crobach, Alexander L. Vahrmeijer, Peter J. K. Kuppen

Molecular Diagnosis & Therapy. 2023;27(2):261-73.



#### ABSTRACT

BACKGROUND Targeted-molecular imaging may improve tumor cell identification during diagnosis and resection of pancreatic ductal adenocarcinoma (PDAC). Although many molecular imaging biomarkers are (over)expressed in PDAC, intertumoral heterogeneity of biomarker expression hampers universal tracer administration. Preoperative, patient-specific screening and selection of the most optimal biomarker could therefore improve tumor delineation. This study evaluates whether fine-needle biopsy (FNB) specimens could be used to preoperatively predict biomarker expression in the corresponding primary PDAC specimen.

**METHODS** Expression of previously identified PDAC biomarkers  $\alpha_V \beta_6$ , CEACAM5, EGFR, mesothelin, Le<sup>a/c/x</sup>, and sdi-Le<sup>a</sup> on FNB and corresponding primary tumor (PT) specimens (n = 45) was evaluated using immunohistochemistry and quantified using a semi-automated image analysis workflow.

**RESULTS** Biomarker expression on FNB and PT tissues showed high concordance ( $\Delta H$ -score  $\leq 50$ ), i.e. was present in 62% of cases for  $\alpha_V \beta_6$ , 61% for CEACAM5, 85% for EGFR, 69% for mesothelin, 76% for Lea/c/x, and 79% for sdi-Lea, indicating high concordance. Except for  $\alpha_V \beta_6$ , biomarker expression on FNB tissues was positively correlated with PT expression for all biomarkers. Subgroup analyses showed that neoadjuvant therapy (NAT) had no major and or significant effect on concordance, expression difference and, except for mesothelin, correlation of biomarker expression between FNB and PT tissues.

**CONCLUSION** To conclude, this study demonstrates that biomarker expression in FNB tissues is predictive for PT expression, irrespective of the application of NAT. These findings thereby provide the foundation for the clinical application of a FNB-based biomarker-screening workflow, eventually facilitating a patient-specific approach of molecular imaging tracer administration in PDAC.

#### INTRODUCTION

Pancreatic ductal adenocarcinoma (PDAC) is the most common type of pancreatic cancer (± 90%), accounting for approximately 450,000 cases each year worldwide.¹ With an 5-year overall-survival rate of merely 2-9%, the malignancy is highly lethal.¹.² To date, surgery offers the only curative treatment for PDAC.¹.³ Unfortunately, due to the asymptomatic course of the disease, PDAC is often diagnosed at an advanced stage and therefore only 15-25% of patients qualify for surgery.⁴ In addition, positive resection margins are observed in up to 75% of patients who underwent surgery for PDAC, leading to early recurrence and shorter survival.⁵.⁶ Neoadjuvant therapy (NAT) has been shown to reduce the number of irradical resections and is therefore increasingly applied.⁵.⁶

Accurate guidance through computed tomography (CT), endoscopic ultrasound (EUS), magnetic resonance imaging (MRI) and/or positron emission tomography (PET) is essential to carefully select and stratify patients for surgery. However, due to the highly infiltrative and discontinuous growth pattern of PDAC, these modalities are not sufficiently able to make a clear distinction between vital tumor cells and benign lesions, such as tumor-associated pancreatitis. 9,10 Moreover, the application of neoadjuvant treatment may induce tissue fibrosis and necrosis, thereby further complicating pre- and intraoperative tumor detection. By providing enhanced contrast between malignant and healthy as well as benign tissues, molecular-targeted imaging agents could provide more reliable visualization of PDAC. 11

Accurate selection of molecular imaging biomarkers remains a key prerequisite for successful tumor delineation. A biomarker is considered suitable for molecular imaging when, among other criteria, it is expressed in a large group of patients within the same tumor type, while expression on surrounding healthy and benign tissues is absent, or at least significantly lower. Previous research by, among others, our group has identified the proteins  $\alpha_V\beta_6$ , CEACAM5, Epidermal Growth Factor Receptor (EGFR), mesothelin, and tumor-associated glycans Lewisa/c/x (Lea/c/x) and sialyl-di-Lewisa (sdi-Lea) as promising tumor-specific biomarkers for molecular imaging in PDAC.  $^{13-17}$ 

Due to the presence of intertumoral heterogeneity and application of NAT, none of these tumor markers is equally expressed in all patients, thereby preventing universal administration of molecular imaging tracers. To address these issues, patients could be preoperatively screened for expression of multiple tumor markers, for instance by using fine-needle biopsies (FNBs). During diagnostic workup, FNBs are routinely obtained via EUS and may provide histological confirmation of PDAC. 18-20 Moreover, FNB material is increasingly used for molecular

and genomic characterization of PDAC, as well as to generate patient-derived xenografts or organoids, thereby providing opportunities for patient-centered therapeutic selection. <sup>21,22</sup> Similarly, preoperative evaluation of biomarker expression on FNBs could form a robust and efficient strategy to select the most suitable molecular imaging tracer in a patient-specific manner. However, it remains to be elucidated whether biomarker expression in FNBs corresponds to the expression on the primary tumor (PT). Moreover, very few studies have examined expression of tumor markers in PDAC after NAT. <sup>14,15,17</sup>

Therefore, this study aims to evaluate whether preoperative FNB specimens can be used to predict biomarker expression in the corresponding primary tumor specimen. To accomplish this, expression of biomarkers  $\alpha_V\beta_6$ , CEACAM5, EGFR, mesothelin, Lea/c/x and sdi-Lea on FNB and PT specimens derived from the same patient is evaluated and compared. Moreover, since FNB specimens are acquired before NAT, the effect of pretreatment on this association between FNB and PT biomarker expression will additionally be studied.

## MATERIALS AND METHODS

## Patient and specimen selection

Pathology reports of patients who underwent a pancreatic EUS-FNB procedure and resection at the Leiden University Medical Center (LUMC) between 2015 and 2020 were retrospectively reviewed. Representative formalin-fixed paraffin-embedded (FFPE) tissue blocks and hematoxylin and eosin (H&E) stained slides of the PT and the FNB of each patient were selected, and obtained from the biobank at the LUMC. FNB samples were processed using the cell-block technique.<sup>23</sup> Selection and suitability of patient material included was determined by a hepatopancreaticobiliary pathologist based on H&E slides (ASLPC). One tissue block per FNB or PT tissue was used for each patient. Clinicopathological data were obtained from patients' medical records. Pathological T (pT) and pathological N (pN) stages were defined according to the 8th edition of the American Joint Committee on Cancer/ Union for International Cancer Control (AJCC/UICC) TNM staging system for pancreatic cancer. Partial and near-complete pathological response were defined as the presence of >5% and ≤5% residual tumor tissue, respectively. The study protocol was approved by the Gastroenterology Biobank Review Committee (protocol reference: 2020-16) and the local medical ethical review committee (protocol reference: B20.052). This study was conducted in agreement with the Dutch code of conduct for responsible use of human tissue in medical research. Tissue specimen and clinicopathological data were used anonymized and in compliance with the Declaration of Helsinki (1964).

## Immunohistochemistry (IHC)

Four mm-thick tissue sections were cut using a microtome from FFPE tissues and placed on glass slides. Tissue sections were deparaffinized in xylene and rehydrated in degrading concentrations of ethanol (100%, 50% and 25%), until reaching demineralized water. Subsequently, endogenous peroxidases were blocked using a 0.3% hydrogen peroxide solution. Antigen retrieval was performed depending on the primary antibody as described in Table 1 of the Electronic Supplementary Material (ESM). After antigen retrieval, slides were rinsed in phosphate-buffered saline (PBS, pH 7.4). Primary antibodies against  $\alpha y \beta_6$ , CEACAM5, EGFR, mesothelin, Lea/c/x and sdi-Lea were applied on the tissue and incubated overnight at room temperature in a humid incubator. For information about primary antibodies, see Table 1 of the ESM. After overnight incubation, primary antibodies were removed by rinsing the slides in PBS and anti-mouse-horseradisch peroxidase (HRP) or anti-rabbit-HRP secondary antibodies (Envision, Dako, Glostrup, Denmark) were applied for 30 minutes at room temperature in a humid incubator. Subsequently, secondary antibodies were removed by rinsing the slides in PBS. Antibody-binding was visualized using a 3,3-diaminobenzidine tetrahydrochloride solution (DAB, K3468, Agilent Technologies, Inc., Santa Clara, CA, USA) for 10 minutes at room temperature. Lastly, the slides were counterstained with Mayer's hematoxylin (Klinipath B.V., Olen, Belgium), dehydrated in a dry incubator for 2 hours and mounted using pertex (Leica Microsystems, Wetzlar, Germany).

## Semi-automatic/digital image analysis

Whole slide images of the stained tissue slides were captured using the PANNORAMIC® 250 Flash III DX scanner (3DHISTECH Ltd., Budapest, Hungary). For quantification of DAB staining, QuPath version 0.2.3 open-access software was used. A detailed description of the QuPath workflow used in this study is provided in the ESM. A graphical representation of the used workflow is depicted in Figure 1 of the ESM. Briefly, random forest object classifiers for PDAC FNB and PT tissues were trained and built for each investigated biomarker separately, yielding a total of 12 object classifiers. Image type settings, color deconvolution stain settings and positive cell detection (DAB staining) parameters were optimized. Object classifiers were trained to specifically recognize and discriminate between tumor cells, stroma cells and red blood cells (RBC), until providing a sensitivity, specificity, negative-predictive value, and positive-predictive value of  $\geq$ 85%. Subsequently, the described workflow was scripted, allowing for semi-automated batch processing of the whole cohort (n = 45). Tumor regions were annotated on FNB and PT tissues by a pathologist (ASLPC), whereafter the corresponding script

was ran. The H-score scoring system was used to quantify per-cell biomarker expression (H-score formula:  $1 \times (\% \text{ cells } 1+) + 2 \times (\% \text{ cells } 2+) + 3 \times (\% \text{ cells } 3+)$ , in which 1+, 2+ and 3+ were defined as low, medium, and high immunohistochemical staining intensity, respectively. Overall tissue staining with an H-score of  $\le 50$  was considered negative, 51-100 as low, 101-200 as moderate, and 201-300 as strong expression of the biomarker. Concordance between FNAB and PT biomarker expression was defined as a FNAB vs. PT H-score difference of  $\le 50$  ( $\Delta$ H-score  $\le 50$ ).

## Statistical analysis

IBM SPSS statistics version 25 (IBM Corp., Somer NY, USA) was used for all statistical analyses. Graphs were created using GraphPad Prism version 8 (La Jolla, USA). For categorial data, groups were compared using a chi-square test. An independent samples *t*-test was used to compare continuous variables of patient characteristics. Correlation analyses were performed using Spearman correlation. Differences or correlations with a *p*-value <0.05 were considered significant.

#### RESULTS

## **Patient characteristics**

Forty-five patients diagnosed with PDAC were included in this study, of which 23 (51%) received NAT and 22 (49%) patients did not receive NAT. Ten (43%) NAT patients received gemcitabine/radiotherapy, while 13 (57%) patients received FOLFIRINOX. Characteristics of patients included in the full cohort and within two subgroups (patients who received NAT and patients who did not receive NAT) are shown in Table 1. No significant differences were observed between the two subgroups for all characteristics.

## Object classifier training and validation

Twelve object classifiers were trained and validated. Each of the object classifiers allowed detection of its cell type-of-interest with sensitivity, specificity, positive predictive value (PPV) and negative predictive values (NPV) of  $\ge 85\%$ , as shown in Table 2 of the ESM Examples of QuPath detection images after batch processing analysis in FNB and PT tissues are shown in Figure 2 of the ESM.

**TABLE 1** Patient characteristics of the total cohort and subgroups of patients who received NAT and patients who did not. *p*-values indicate differences in patient characteristics between no NAT and NAT groups.

Characteristic	Total PDAC $(n = 45)$	NAT (n = 23)	No NAT (n = 22)	<i>p</i> -value
Age, mean (SD)	64.3 (8.5)	62.7 (7.0)	65.8 (10.0)	0.236
Gender, n (%)				
Male	18 (40)	9 (39)	9 (41)	0.903
Female	27 (60)	14 (61)	13 (59)	
Tumor differentiation, n (%)				
Well	4 (9)	1(4)	3 (14)	
Moderate	17 (38)	2 (9)	15 (68)	*
Poor	3 (7)	0 (0)	3 (14)	
Missing	21 (47)	20 (87)	1 (4)	
Primary tumor, n (%)				
pT1	8 (18)	6 (26)	2 (9.0)	
pT2	26 (58)	14 (61)	12 (55)	0.206
pT3	11 (24)	3 (13)	8 (36)	
Regional lymph nodes, n (%)				
pN0	12 (27)	8 (35)	4(18)	0.433
pN1	25 (56)	11 (48)	14 (64)	
pN2	8 (18)	4 (17)	4 (18)	
Distant metastases, n (%)				
MO	43 (96)	22 (96)	21 (96)	0.974
M1	2 (4)	1 (4)	1 (4)	
NAT, n (%)				
None	22 (49)	NA	22 (100)	
Gemcitabine/RT	10 (22)	10 (44)	NA	-
FOLFIRINOX	13 (29)	13 (57)	NA	
Pathological response, n (%)				
No response	2 (4)	2 (9)	NA	
Partial	14 (31)	14 (61)	NA	_
Near complete	6(13)	6 (26)	NA	
Not applicable	22 (49)	0 (0)	22 (100)	
Missing	1 (2)	1 (4)	NA	
Surgery type, n (%)				
Pancreaticoduodenectomy	33 (73)	18 (78)	15 (68)	0.253
Pancreatic corpus/tail resection	10 (22)	5 (22)	5 (23)	
Total pancreatectomy	2 (5)	0 (0)	2 (9)	
Surgical margin status, n (%)				
RO	26 (58)	12 (52)	14 (64)	0.436
R1	19 (42)	11 (48)	8 (36)	
Tumor size in mm, mean (SD)	30 (12)	28 (12)	32 (13)	0.354

<sup>\*</sup>Characteristic is missing for most NAT patients as assessment of tumor differentiation after NAT is not recommended. A statistical comparison of both subgroups is therefore not included. NA, not applicable; NAT, neoadjuvant therapy; PDAC, pancreatic ductal adenocarcinoma; RT, radiotherapy; SD, standard deviation. Biomarker expression on FNB and PT tissues of PDAC.

In total, 45 FNB and 45 PT tissues were included in the study and immunohistochemically stained for  $\alpha_V\beta_s$ , CEACAM5, EGFR, mesothelin, Lea/c/x and sdi-Lea expression, followed by staining quantification using the described semi-automated imaging analysis workflow. Sequential images of staining of FNB and PT tissues derived from one representative patient are shown in Figure 1.

All biomarkers showed a membranous staining pattern on tumor cells in both FNB and PT tissues, with CEACAM5 showing generally more staining on the luminal side of cells.  $\alpha_V\beta_6$  was homogeneously expressed throughout the positive tumors, whereas Lea/c/x and sdi-Lea showed a slightly more heterogeneous staining pattern. Membranous staining of CEACAM5, EGFR and mesothelin on PDAC cells was considerably more heterogeneous compared to the other biomarkers (Figure 1).

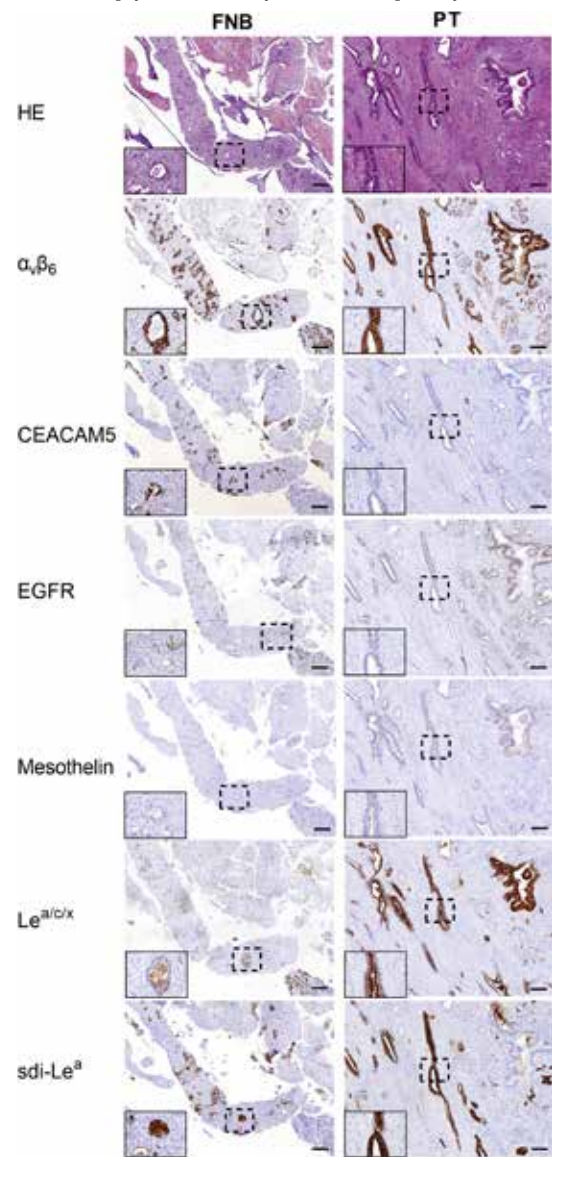
In the FNB specimen, positive biomarker expression (H-score >51) was observed in 41/42 (98%) for  $\alpha_V\beta_6$ , 29/41 (71%) for CEACAM5, 39/39 (100%) for EGFR, 13/39 (33%) for mesothelin, 37/41 (90%) for Lea/c/x, and 39/43 (91%) for sdi-Lea. In the PT specimen, positive biomarker expression was observed in 41/42 (98%) for  $\alpha_V\beta_6$ , 32/41 (78%) for CEACAM5, 35/39 (90%) for EGFR, 17/39 (44%) for mesothelin, 35/41 (85%) for Lea/c/x, and 41/43 (95%) for sdi-Lea. Categorized biomarker staining levels for FNB and PT tissues separately are shown in Table 2. Moderate or strong  $\alpha_V\beta_6$ , Lea/c/x and sdi-Leastaining was observed in most FNB and PT tissues, whereas EGFR was moderately stained in the majority of cases. CEACAM5 and mesothelin staining was generally weaker compared to the other biomarkers.

**TABLE 2** Categorized staining levels of  $\alpha_V \beta_6$ , CEACAM5, EGFR, mesothelin, Le<sup>a/c/x</sup> and sdi-Le<sup>a</sup> investigated targets in PDAC FNB and PT specimens, separated into cases showing negative (H-score o-50), low (H-score 51-100), moderate (H-score 101-200) and strong expression (201-300).

Biomarker	n of pairs	U	ative, (%)		Low, n (%)		oderate, n (%)		ong, (%)
		FNB	PT	FNB	PT	FNB	PT	FNB	PT
ανβ6	42	1 (2)	1 (2)	1 (2)	0 (0)	9 (21)	3 (7)	31 (74)	38 (91)
CEACAM5	41	12 (29)	9 (22)	9 (22)	11 (27)	12 (29)	15 (37)	8 (20)	6 (15)
EGFR	39	0 (0)	4 (10)	7 (18)	6 (15)	30 (77)	24 (62)	2 (5)	5 (13)
Mesothelin	42	26 (62)	22 (52)	7 (17)	10 (24)	9 (21)	8 (19)	0 (0)	2 (5)
Lea/c/x	41	4 (10)	6 (15)	2 (5)	6 (15)	21 (51)	17 (42)	14 (34)	12 (29)
sdi-Le <sup>a</sup>	43	4 (9)	2 (5)	2 (5)	3 (7)	12 (28)	8 (19)	25 (58)	30 (70)

FNB: fine-needle biopsy, PT: primary tumor.

**FIGURE 1** Images of HE and immunohistochemical staining  $\alpha_V \beta_6$ , CEACAM5, EGFR, mesothelin, Lea/c/x and sdi-Lea on FNB and PT tissues derived from one representative patient. Overview images and inserts are taken at 5× and 40× magnification, respectively. Scale bars represent 200  $\mu$ M. FNB; fine-needle biopsy, HE; hematoxylin-eosin, PT; primary tumor.



## Concordance between biomarker expression on PDAC FNB and PT tissues

To assess the concordance between FNB and PT biomarker expression, differences between H-scores on FNB and PT tissue were calculated. Concordance was considered to be present when the difference between FNB and PT H-score was  $\leq$ 50. Concordance rates of all biomarkers are shown in Table 3. For the full cohort, concordance rates were 62% for  $\alpha_V\beta_6$ , 61% for CEACAM5, 85% for EGFR, 69% for mesothelin, 76% for Lea/c/x, and 79% for sdi-Lea, indicating high concordance between biomarker expression on FNB and PT tissues. Next, to study the effect of NAT on concordance between FNB and PT biomarker expression, patients who received NAT and patients who did not receive NAT were divided in two subgroups. In subgroup analyses, medium to high concordance rates between dichotomized IHC staining were observed for patients who received NAT (range: 64-83%) and patients who did not receive NAT (range: 60-90%), suggesting that NAT does not substantially affect concordance between positive or negative FNB and PT biomarker expression (Table 3).

TABLE 3 Concordance rates biomarker expression on FNB and PT tissues for the full cohort as well as NAT and no NAT subgroups, along with the number of FNB and PT pairs. Concordance of biomarker expression was present when the H-score difference between FNB and PT tissues ( $\Delta$ H-score) was  $\leq$ 50.

	Full cohort concordance			Subgroup concordance			
Biomarker	n of pairs	Patients ΔH-score ≤50 n (%)	n of pairs	Treatment	Patients ΔH-score ≤50 n (%)		
$\alpha_V \beta_6$	42	26 (62)	22	NAT	14 (64)		
			20	No NAT	12 (60)		
CEACAM5	41	25 (61)	21	NAT	15 (71)		
			20	No NAT	14 (70)		
EGFR	39	33 (85)	18	NAT	15 (83)		
			21	No NAT	18 (86)		
Mesothelin	42	29 (69)	22	NAT	17 (77)		
			20	No NAT	12 (60)		
Le <sup>a/c/x</sup>	41	31 (76)	22	NAT	18 (82)		
			19	No NAT	13 (68)		
sdi-Le <sup>a</sup>	43	34 (79)	23	NAT	16 (70)		
			20	No NAT	18 (90)		

NAT: neoadjuvant treatment.

## Correlation between biomarker expression on PDAC FNB and PT tissues

To study the predictive value of biomarker expression on FNB tissues for PT expression, the linear relationship of biomarker expression level between FNB and PT specimen was investigated. For the full cohort, H-score scatterplots showing biomarker expression on FNB and PT tissues are shown in Figure 2A-F. Moreover, Spearman's rank correlation coefficients indicating the linear association between the FNB and PT biomarker expression are shown in Table 4 as well as in Figure 2A-F. H-scores on FNB tissues were positively correlated with H-scores on PT tissues for CEACAM5, EGFR, mesothelin, sdi-Lea and Lea/c/x, suggesting that biomarker expression on FNB tissues is predictive for expression level in PT tissues. Correlation coefficients indicated a moderate-strong linear relationship between FNB and PT expression. For  $\alpha_V \beta_6$ , however, no correlation between H-score on FNB and PT tissues was found ( $r_S = 0.041$ , p = 0.795).

**TABLE 4** Correlation scores between biomarker expression on FNB and PT PDAC tissues. Spearman's rank correlation coefficient (rs) along with their corresponding *p*-values are shown.

		Correlation			
Biomarker	n of pairs	$r_{S}$	<i>p</i> -value		
$\alpha_V \beta_{\epsilon}$	42	0.041	0.795		
CEACAM5	41	0.651	<0.001		
EGFR	39	0.628	<0.001		
Mesothelin	42	0.427	0.005		
Lea/c/x	41	0.736	<0.001		
sdi-Le <sup>a</sup>	43	0.672	<0.001		

Next, subgroup analyses were performed to study the effect of NAT on the predictive value of biomarker expression on FNB tissues for PT biomarker expression. As shown in Figure 3A-L and Table 5, H-scores of CEACAM5, EGFR, sdi-Lea and Lea/c/x expression on FNB were positively correlated with H-scores on PT tissues in both NAT and no NAT patients, suggesting that biomarker expression is predictive for PT expression regardless of application of NAT. For  $\alpha_V\beta_{\text{G}}$  and mesothelin, however, biomarker expression on FNB tissues was not predictive for PT expression regardless of application of NAT or in the no NAT subgroup, respectively.

**FIGURE 2** H-score scatterplots showing the relationship between immunohistochemical staining of (A)  $\alpha_V \beta_6$ , (B) CEACAM5 (C) EGFR (D) mesothelin (E) Lea/c/x and (F) sdi-Lea on FNB (x-axis) and PT (y-axis) tissues. Blue dots represent a H-score difference between FNB and PT staining of  $\leq$ 50, whereas the red dots represent a difference of >51, thereby indicating an outlier. Spearman's rank correlation coefficient (rs) with corresponding *p*-values are shown in each graph. FNB: fineneedle biopsy, PT: primary tumor.

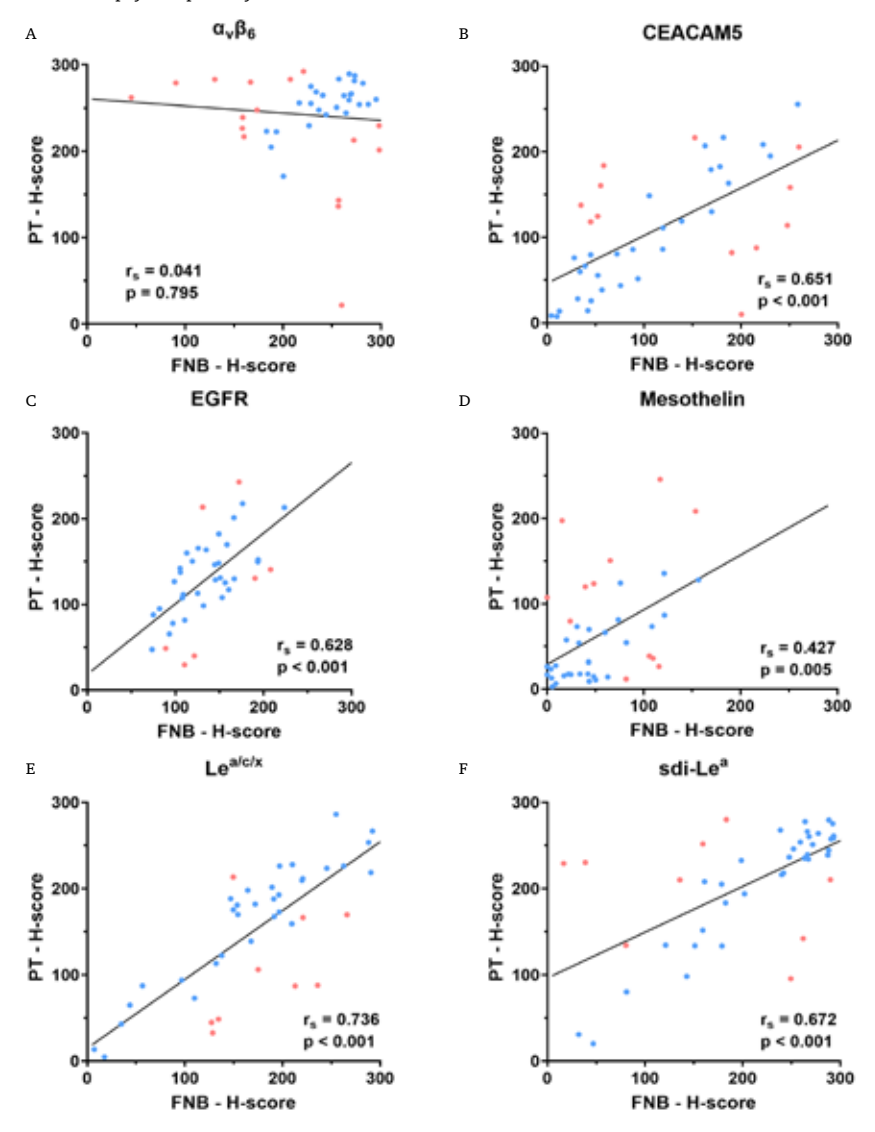
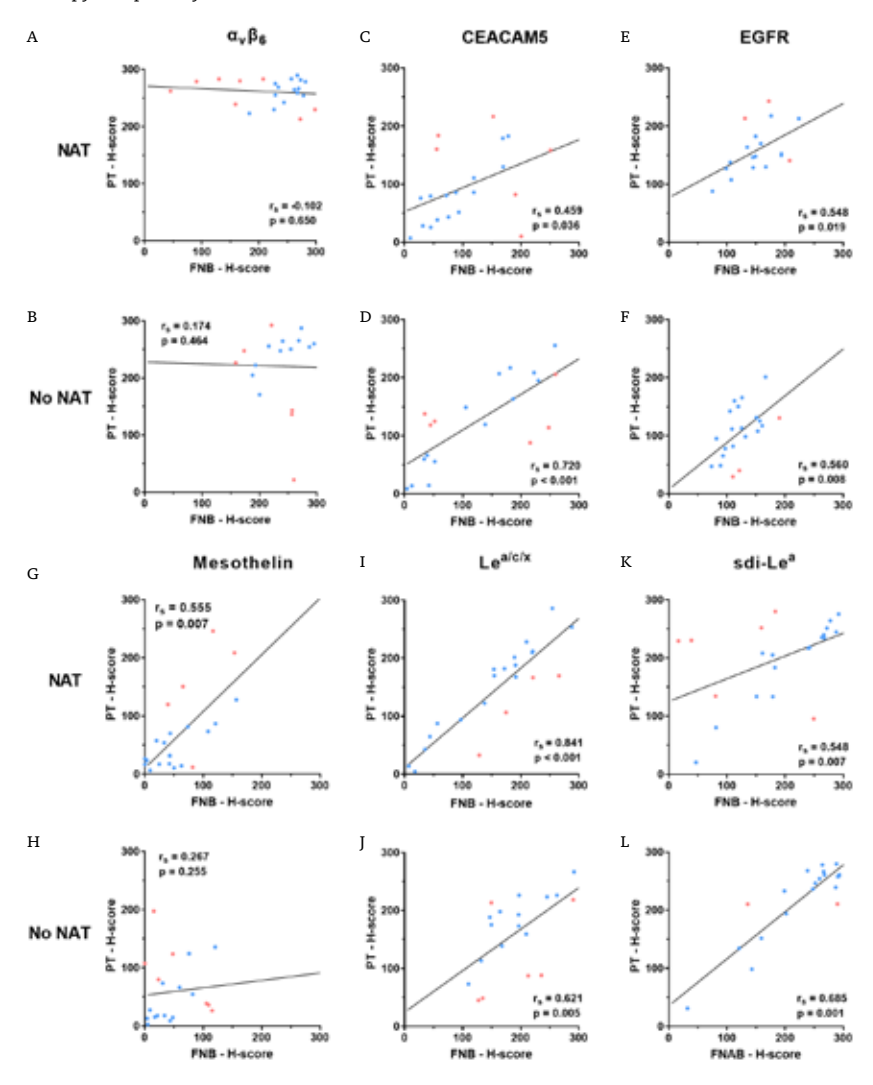


FIGURE 3 H-score scatterplots showing the relationship between immunohistochemical staining of (A-B)  $\alpha_V \beta_6$  (C-D) CEACAM5 (E-F) EGFR (G-H) mesothelin (I-J) Lea/c/x and (K-L) sdi-Lea on FNB (x-axis) and PT (y-axis) tissues for NAT and no NAT patients separately. Blue dots represent a H-score difference between FNB and PT staining of  $\leq 50$ , whereas the red dots represent a difference of > 51, thereby indicating an outlier. Spearman's rank correlation coefficient (rs) with corresponding p-values are shown in each graph. FNB: fine-needle biopsy, NAT: neoadjuvant therapy, PT: primary tumor.



**TABLE 5** Correlation scores between biomarker expression on FNB and PT PDAC tissues, subdivided in patients who received NAT and patients who received no NAT Spearman's rank correlation coefficient ( $r_s$ ) along with their corresponding p-values are shown.

			Corre	lation
Biomarker		n of pairs	$r_S$	<i>p</i> -value
a 8	NAT	22	-0.102	0.650
$\alpha_{\rm V}\beta_{\rm 6}$	No NAT	20	0.174	0.464
CEACAM5 -	NAT	21	0.459	0.036
CEACAMS	No NAT	20	0.720	<0.001
EGFR -	NAT	18	0.548	0.019
EGFK	No NAT	21	0.560	0.008
Mesothelin -	NAT	22	0.555	0.007
Mesotnelin	No NAT	20	0.267	0.255
I.ea/c/x -	NAT	22	0.841	<0.001
Leu/c/A -	No NAT	19	0.621	0.005
. 1: 1 . 3	NAT	23	0.548	0.007
sdi-Le <sup>a</sup> -	No NAT	20	0.685	0.001

NAT: neoadjuvant therapy.

#### DISCUSSION

Tumor-targeted molecular imaging could play a crucial role in solving current challenges during diagnosis, monitoring and resection of PDAC by providing high-contrast delineation of malignant tissues.<sup>11,26</sup> Patient-specific screening and selection of molecular imaging biomarkers using FNB tissues may improve PDAC delineation and prevent unnecessary tracer administration.

Our study shows that  $\alpha_V \beta_6$ , CEACAM5, EGFR, mesothelin, Lea/c/x, and sdi-Lea are highly expressed in FNB and PT tissues of PDAC. The results suggest that there is a high level of association in expression between FNB and PT tissues of PDAC for the biomarkers evaluated herein. Although no correlation was observed for  $\alpha_V \beta_6$ , concordance rate was the highest among the investigated biomarkers. This suggests that  $\alpha_V \beta_6$  expression is similar between FNB and PT, and the biomarker was expressed in homogenous manner, i.e. strongly in most tissues. Moreover, when discriminating between patients that received NAT and patients who received no NAT, no substantial differences between concordance rates and, except for mesothelin, correlations were observed, suggesting that NAT does not affect the expression level of the biomarkers investigated and, therefore, also not the predictive value of biomarker expression on FNB vs. PT tissues. Our study therefore demonstrates the feasibility of a molecular imaging biomarker screening workflow for PDAC in a clinically relevant setting.

The current findings are largely in line with previous studies that showed high expression of  $\alpha_V\beta_6$ , CEACAM5, EGFR, mesothelin, Leal/c/x and sdi-Leal in PDAC tissues. Interestingly, our study found positive mesothelin expression in 48% of PT tissues, while most studies report positive mesothelin expression in 80-85% of PDAC tissues. In 3,27,28 This discrepancy could have been caused by, among others, the use of different antibody clones directed against mesothelin, a lack of staining reproducibility between laboratories, or the use of manual scoring methods in other studies, which may not be sufficiently reproducible. Biopsy specimens have the potential to aid in proper treatment selection, as was previously shown for rectum, lung, breast and gastric cancer. In each of these studies, high levels of concordance between biomarker expression on biopsy and PT tissues was observed. Although PDAC FNB specimens are already used in research into PDAC diagnosis, The association between FNB and PT biomarker expression was, to the best of our knowledge, not yet investigated for PDAC.

The lack of reproducibility of manual scoring was compensated in our study through the use of QuPath, which could provide superior cell detection efficacy, leading to more accurate and reproducible H-scores as opposed to manual scoring. <sup>24,31</sup> However, the QuPath workflow we used herein was more time-consuming compared to manual scoring. We therefore believe that for this study, the advantages outweighed the disadvantages as the workflow allowed us to obtain highly accurate and reproducible results.

Although moderate to strong correlation coefficients between FNB and PT tissues were observed for expression level of most biomarkers, along with high concordance, several H-score outliers were present. A possible explanation may be that, considering the average time of 100 days between the FNB and surgical procedure (data not shown), biomarker expression changed over time. PDAC is a highly progressive disease and distinct (epi)genetic events or remodeling could lead to a certain extent of polyclonality.<sup>17,18</sup> Different subclones of tumor cells could (over) express distinct proteins and, over time, this could result in intra-tumoral heterogeneity and, subsequently, varying expression patterns. Secondly, a biopsy is merely a small fragment of the entire PT specimen. Considering intratumoral heterogeneity, it could very well be possible that a biopsy sample contains an area of the PT that does not express the biomarker of interest, while other parts of the tumor do express the biomarker.<sup>17</sup> Of note and in line with previous research, five out of six biomarkers evaluated herein showed considerable heterogeneity, further substantiating this hypothesis. 13-17,27 Lastly, FNB cell-blocks and FFPE tissues are fixed and processed differently, which can influence the level IHC staining.<sup>40</sup> However, our study shows that, in most cases, biomarker expression on FNB tissues shows considerable predictivity for expression on PT tissues, indicating that biopsy specimens provide a representative sample of PT tissues.

Due to their low abundance in surrounding tissues and also high expression in lymph node metastases, the biomarkers evaluated herein are promising targets for both diagnostic and intraoperative imaging of PDAC. Regarding the former, several studies recently reported the phase I/II evaluation of targeted PET tracers directed against mesothelin and  $\alpha_V \beta_6$  and showed their safety and feasibility for PDAC visualization. 41.43 With regards to the latter, (early-phase) clinical trials have particularly focused on NIRF tracers targeting EGFR and CEA.<sup>44-48</sup> NIRF imaging using anti-EGFR tracers panitumumab-IRDye8ooCW and cetuximab-IRDye8ooCW, and anti-CEA tracer SGM-101 allowed clear delineation of primary PDAC lesions, as well as lymph node and distant metastases intraoperatively. 44-48 Within the preclinical arena, anti- $\alpha_V \beta_6$  tracers Ro1-MG-IRDye8ooCW and anti-Lea/c/x CH88.2-IRDye8ooCW have enabled clear localization and delineation of human PDAC xenografts in mice, thereby strengthening their clinical potential for real-time intraoperative NIRF imaging of PDAC. 16,49 Considering the (pre)clinical availability of molecular tracers directed against these biomarkers, the workflow we evaluated and discuss here may be instantaneously translated towards a clinical setting, where patients with positive biomarker expression in FNB can be selected for patient-specific tracer administration.

This study has some limitations. Firstly, the present study cohort was relatively small for exact estimation of biomarker expression in PT tissues. Therefore, evaluation of the relationship between FNB and PT expression on a larger cohort could strengthen the findings of this study. Secondly, due to the limited number of patients available, the NAT subgroup was small, which allowed no separate evaluation of the effect of gemcitabine/radiotherapy or FOLFIRINOX. Thirdly, due to staining artefacts, the number of pairs available for analysis differed and did not overlap precisely for all biomarkers.

Future research could focus on the expansion of the workflow to other tumor types for which biopsies are obtained, such as breast, (colo)rectal and gastric cancer, and additionally to other tumor biomarkers-of-interest. The workflow evaluated herein can conveniently be integrated within standard pathological workup, as IHC stainings on FNB tissues for markers such as Ki-67, p53 and SMAD4 are regularly performed to guide histological diagnosis. Taken further, this method of biomarker screening can also be applied in the therapeutic arena, where PDAC patients eligible for targeted therapy can be screened for biomarker

expression.<sup>53</sup> Altogether, this study provides the foundation for clinical translation of a patient-specific, FNB-based molecular imaging biomarker selection workflow that may improve PDAC diagnosis, delineation and, ultimately, patient outcomes.

## CONCLUSION

To conclude, our findings show that biomarker expression on FNB is considerably predictive for biomarker expression on corresponding PT tissue, irrespective of the application of NAT. This study thereby provides the foundation for the clinical application of a FNB-based biomarker-screening workflow, eventually facilitating a personalized approach of molecular imaging tracer administration in PDAC.

#### SUPPLEMENTARY MATERIALS

The following Supplementary Materials are available online at: https://bit.ly/3PmzqjO.

Supplementary Table 1: primary antibody and additional immunohistochemical protocol information; Supplementary Table 2: calculated sensitivity, specificity, NPV and PPV for object classifiers created FNB and PT specimen stained for each target; Supplementary Table 3: corresponding values to each parameter considered in the described QuPath workflow; Supplementary Table 4: Object classifier validation calculations of sensitivity, specificity, NPV and PPV; Supplementary Figure 1: Graphical representation of the workflow used for digital image analysis using QuPath; Supplementary Figure 2: Representative QuPath examples of brightfield, cell segmentation, detection and intensity classification, and cell type classification images of PDAC PT and FNB tissue.

#### REFERENCES

- 1 McGuigan A, Kelly P, Turkington RC, Jones C, Coleman HG. McCain RS. Pancreatic cancer: A review of clinical diagnosis, epidemiology, treatment and outcomes. World J Gastroenterol, 2018;24(43);4846-61.
- 2 Latenstein AEJ, van der Geest LGM, Bonsing BA, Groot Koerkamp B. Hai Mohammad N. de Hingh I. et al. Nationwide trends in incidence, treatment and survival of pancreatic ductal adenocarcinoma. Eur J Cancer.
- 3 Stathis A, Moore MJ. Advanced pancreatic carcinoma: current treatment and future challenges. Nat Rev Clin Oncol. 2010;7(3):163-72.
- 4 Barugola G, Partelli S, Marcucci S, Sartori N, Capelli P, Bassi C, et al. Resectable pancreatic cancer: who really benefits from resection? Ann Surg Oncol. 2009;16(12):3316-22.
- 5 Tummers WS, Groen JV, Sibinga Mulder BG, Farina-Sarasqueta A, Morreau J, Putter H, et al. Impact of resection margin status on recurrence and survival in pancreatic cancer surgery. Br J Surg. 2019;106(8):1055-65.
- 6 Verbeke CS. Resection margins in pancreatic cancer, Surg Clin North Am. 2013;93(3):647-62.
- 7 Versteijne E. Suker M. Groothuis K. Akkermans-Vogelaar JM, Besselink MG, Bonsing BA, et al. Preoperative Chemoradiotherapy Versus Immediate Surgery for Resectable and Borderline Resectable Pancreatic Cancer: Results of the Dutch Randomized Phase III PREOPANC Trial. J Clin Oncol. 2020;38(16):1763-73.
- 8 Janssen QP, van Dam JL, Bonsing BA, Bos H, Bosscha KP, Coene P, et al. Total neoadjuvant FOLFIRINOX versus neoadjuvant gemcitabine-based chemoradiotherapy and adjuvant gemcitabine for resectable and borderline resectable pancreatic cancer (PREOPANC-2 trial): study protocol for a nationwide multicenter randomized controlled trial. BMC Cancer. 2021;21(1):300.
- Ferrone CR, Marchegiani G, Hong TS, Ryan DP, Deshpande V, McDonnell EI, et al. Radiological and surgical implications of neoadiuvant treatment with FOLFIRINOX for locally advanced and borderline resectable pancreatic cancer. Ann Surg. 2015;261(1):12-7.
- 10 González-Gómez R, Pazo-Cid RA, Sarría L, Morcillo M, Schuhmacher AJ. Diagnosis of Pancreatic Ductal Adenocarcinoma by Immuno-Positron Emission Tomography. J Clin Med. 2021;10(6).
- 11 Tummers WS, Willmann JK, Bonsing BA, Vahrmeijer AL, Gambhir SS, Swijnenburg RJ. Advances in Diagnostic and Intraoperative Molecular Imaging of Pancreatic Cancer. Pancreas. 2018;47(6):675-89.
- 12 Hernot S, van Manen L, Debie P, Mieog JSD, Vahrmeijer AL. Latest developments in molecular tracers for fluorescence image-guided cancer surgery. Lancet Oncol. 2019;20(7):e354-e67.
- 13 de Geus SW, Boogerd LS, Swijnenburg RJ, Mieog JS, Tummers WS, Prevoo HA, et al. Selecting Tumor-Specific Molecular Targets in Pancreatic Adenocarcinoma: Paving the Way for Image-Guided Pancreatic Surgery. Mol Imaging Biol. 2016;18(6):807-19.
- 14 Tummers WS, Farina-Sarasqueta A, Boonstra MC, Prevoo HA, Sier CF, Mieog JS, et al. Selection of optimal molecular

- targets for tumor-specific imaging in pancreatic ductal adenocarcinoma. Oncotarget. 2017;8(34):56816-28.
- 15 Vuijk FA, de Muynck L, Franken LC, Busch OR, Wilmink IW. Besselink MG. et al. Molecular targets for diagnostic and intraoperative imaging of pancreatic ductal adenocarcinoma after neoadiuvant FOLFIRINOX treatment. Sci Rep. 2020;10(1):16211.
- 16 Houvast RD, Baart VM, Bhairosingh SS, Cordfunke RA, Chua JX, Vankemmelbeke M, et al. Glycan-Based Nearinfrared Fluorescent (NIRF) Imaging of Gastrointestinal Tumors: a Preclinical Proof-of-Concept In Vivo Study. Mol Imaging Biol. 2020;22(6):1511-22.
- 17 Houvast RD, Thijse K, Groen JV, Chua J, Vankemmelbeke M, Durrant LG, et al. An Immunohistochemical Evaluation of Tumor-Associated Glycans and Mucins as Targets for Molecular Imaging of Pancreatic Ductal Adenocarcinoma. Cancers (Basel). 2021;13(22).
- 18 Kalogeraki A, Papadakis GZ, Tamiolakis D, Karvela-Kalogeraki I, Karvelas-Kalogerakis M, Segredakis J, et al. EUS - Fine- Needle Aspiration Biopsy (FNAB) in the Diagnosis of Pancreatic Adenocarcinoma: A Review. Rom J Intern Med. 2016;54(1):24-30.
- 19 Luu TT. Review of Immunohistochemistry Biomarkers in Pancreatic Cancer Diagnosis. Front Oncol. 2021;11:799025.
- 20 Bang IY, Hebert-Magee S, Navaneethan U, Hasan MK, Hawes R, Varadarajulu S. EUS-guided fine needle biopsy of pancreatic masses can yield true histology. Gut. 2018:67(12):2081-4.
- 21 Archibugi L, Testoni SGG, Redegalli M, Petrone MC, Reni M, Falconi M, et al. New era for pancreatic endoscopic ultrasound: From imaging to molecular pathology of pancreatic cancer. World J Gastrointest Oncol. 2019;11(11):933-45.
- 22 Tanaka H, Matsusaki S. The Utility of Endoscopic-Ultrasonography-Guided Tissue Acquisition for Solid Pancreatic Lesions. Diagnostics (Basel). 2022;12(3).
- 23 Ieni A. Barresi V. Todaro P. Caruso RA, Tuccari G. Cellblock procedure in endoscopic ultrasound-guided-fineneedle-aspiration of gastrointestinal solid neoplastic lesions. World I Gastrointest Endosc. 2015;7(11):1014-22.
- 24 Bankhead P, Loughrey MB, Fernández JA, Dombrowski Y, McArt DG, Dunne PD, et al. QuPath: Open source software for digital pathology image analysis. Sci Rep. 2017;7(1):16878.
- 25 Breiman L. Random forests. Machine learning. 2001;45(1):5-32.
- 26 Vahrmeijer AL, Hutteman M, van der Vorst JR, van de Velde CJ, Frangioni JV. Image-guided cancer surgery using near-infrared fluorescence. Nat Rev Clin Oncol. 2013;10(9):507-18.
- 27 Le K, Wang J, Zhang T, Guo Y, Chang H, Wang S, et al. Overexpression of Mesothelin in Pancreatic Ductal Adenocarcinoma (PDAC). Int J Med Sci. 2020;17(4):422-7.
- 28 Montemagno C. Cassim S. Pouvssegur I. Broisat A. Pagès G. From Malignant Progression to Therapeutic Targeting: Current Insights of Mesothelin in Pancreatic Ductal Adenocarcinoma, International Journal of Molecular Sciences. 2020;21(11):4067.
- 29 Adams EJ, Green JA, Clark AH, Youngson JH. Comparison of different scoring systems for immunohistochemical staining. J Clin Pathol. 1999;52(1):75-7.

- 30 Loughrey MB, Bankhead P, Coleman HG, Hagan RS, Craig S, McCorry AMB, et al. Validation of the systematic scoring of immunohistochemically stained tumour tissue microarrays using QuPath digital image analysis. Histopathology. 2018;73(2):327-38.
- 31 Bankhead P. Fernández JA. McArt DG. Boyle DP. Li G. Loughrey MB, et al. Integrated tumor identification and automated scoring minimizes pathologist involvement and provides new insights to key biomarkers in breast cancer. Lab Invest. 2018;98(1):15-26.
- 32 Boogerd LS, van der Valk MJ, Boonstra MC, Prevoo HA, Hilling DE, van de Velde CJ, et al. Biomarker expression in rectal cancer tissue before and after neoadjuvant therapy. Onco Targets Ther. 2018;11:1655-64.
- 33 Okimoto T, Tsubata Y, Sutani A, Fuchita H, Koba N, Hotta T, et al. Immunohistochemical comparison of biomarker expression in biopsy and surgical specimens of non-small cell lung cancer. Anticancer research. 2014;34(6):2755-61.
- 34 Robertson S, Rönnlund C, de Boniface J, Hartman J. Retesting of predictive biomarkers on surgical breast cancer specimens is clinically relevant. Breast Cancer Res Treat. 2019;174(3):795-805.
- 35 Taillade L, Penault-Llorca F, Boulet T, Fouret P, Michiels S, Taranchon E, et al. Immunohistochemichal expression of biomarkers: a comparative study between diagnostic bronchial biopsies and surgical specimens of non-smallcell lung cancer. Ann Oncol. 2007:18(6):1043-50.
- 36 Wang T, Hsieh ET, Henry P, Hanna W, Streutker CJ, Grin A. Matched biopsy and resection specimens of gastric and gastroesophageal adenocarcinoma show high concordance in HER2 status. Hum Pathol. 2014;45(5):970-5.
- 37 Agarwal B, Ludwig OJ, Collins BT, Cortese C. Immunostaining as an adjunct to cytology for diagnosis of pancreatic adenocarcinoma. Clin Gastroenterol Hepatol. 2008;6(12):1425-31.
- 38 Zapata M, Cohen C, Siddiqui MT. Immunohistochemical expression of SMAD4, CK19, and CA19-9 in fine needle aspiration samples of pancreatic adenocarcinoma: Utility and potential role. Cytojournal. 2007;4:13.
- 39 Nguyen NO, Ruszkiewicz A, Chang D, Bambrick I, Biankin 52 Ren B, Liu X, Surjawinata AA, Pancreatic Ductal AV. Biomarker assessment from EUS-guided biopsy to predict outcomes and treatment in pancreatic cancer. American Society of Clinical Oncology; 2014.
- 40 Shidham VB, Layfield LJ. Cell-blocks and immunohistochemistry. Cytojournal. 2021;18:2.
- 41 Lamberts LE, Koch M, de Jong JS, Adams ALL, Glatz J, Kranendonk MEG, et al. Tumor-Specific Uptake of Fluorescent Bevacizumab-IRDye8ooCW Microdosing in Patients with Primary Breast Cancer: A Phase I Feasibility Study. Clin Cancer Res. 2017;23(11):2730-41.
- 42 Kimura RH, Wang L, Shen B, Huo L, Tummers W, Filipp FV, et al. Evaluation of integrin  $\alpha v \beta(6)$  cystine knot PET tracers to detect cancer and idiopathic pulmonary fibrosis. Nat Commun. 2019;10(1):4673.
- 43 Nakamoto R, Ferri V, Duan H, Hatami N, Goel M, Rosenberg I, et al. Pilot-phase PET/CT study targeting integrin  $\alpha(v)\beta(6)$  in pancreatic cancer patients using the cystine-knot peptide-based (18)F-FP-R(0)1-MG-F2. Eur J Nucl Med Mol Imaging. 2021.
- 44 Hoogstins CES, Boogerd LSF, Sibinga Mulder BG, Mieog JSD, Swijnenburg RJ, van de Velde CJH, et al. Image-Guided

- Surgery in Patients with Pancreatic Cancer: First Results of a Clinical Trial Using SGM-101, a Novel Carcinoembryonic Antigen-Targeting, Near-Infrared Fluorescent Agent. Ann Surg Oncol. 2018;25(11):3350-7.
- 45 Tummers WS, Miller SE, Teraphongphom NT, Gomez A, Steinberg I, Huland DM, et al. Intraoperative Pancreatic Cancer Detection using Tumor-Specific Multimodality Molecular Imaging. Ann Surg Oncol. 2018;25(7):1880-8.
- 46 Tummers WS, Miller SE, Teraphongphom NT, van den Berg NS, Hasan A, Longacre TA, et al. Detection of visually occult metastatic lymph nodes using molecularly targeted fluorescent imaging during surgical resection of pancreatic cancer. HPB (Oxford). 2019;21(7):883-90.
- 47 Lu G, van den Berg NS, Martin BA, Nishio N, Hart ZP, van Keulen S. et al. Tumour-specific fluorescence-guided surgery for pancreatic cancer using panitumumab-IRDye8ooCW: a phase 1 single-centre, open-label, singlearm, dose-escalation study. Lancet Gastroenterol Hepatol. 2020;5(8):753-64.
- 48 Boogerd LSF, Hoogstins CES, Schaap DP, Kusters M, Handgraaf HJM, van der Valk MJM, et al. Safety and effectiveness of SGM-101, a fluorescent antibody targeting carcinoembryonic antigen, for intraoperative detection of colorectal cancer: a dose-escalation pilot study. Lancet Gastroenterol Hepatol, 2018;3(3):181-91.
- 49 Tummers WS, Kimura RH, Abou-Elkacem L, Beinat C, Vahrmeijer AL, Swijnenburg RI, et al, Development and Preclinical Validation of a Cysteine Knottin Peptide Targeting Integrin alphavbeta6 for Near-infrared Fluorescent-guided Surgery in Pancreatic Cancer. Clin Cancer Res. 2018;24(7):1667-76.
- 50 Jahng AW, Reicher S, Chung D, Varela D, Chhablani R, Dev A, et al. Staining for p53 and Ki-67 increases the sensitivity of EUS-FNA to detect pancreatic malignancy. World J Gastrointest Endosc. 2010;2(11):362-8.
- 51 Fabbri C, Gibiino G, Fornelli A, Cennamo V, Grifoni D, Visani M. et al. Team work and cytopathology molecular diagnosis of solid pancreatic lesions. Digestive Endoscopy. 2017:29(6):657-66.
- Adenocarcinoma and Its Precursor Lesions: Histopathology, Cytopathology, and Molecular Pathology. Am J Pathol. 2019;189(1):9-21.
- 53 Lundy J, Harris M, Zalcberg J, Zimet A, Goldstein D, Gebski V, et al. EUS-FNA Biopsies to Guide Precision Medicine in Pancreatic Cancer: Results of a Pilot Study to Identify KRAS Wild-Type Tumours for Targeted Therapy. Front Oncol. 2021;11:770022.

## PART II

Preclinical evaluation
of novel tracers for near-infrared
fluorescence and photoacoustic
imaging of gastrointestinal tumors

## CHAPTER 6

Glycan-based near-infrared fluorescent (NIRF) imaging of gastrointestinal tumors: a preclinical proof-of-concept *in vivo* study

Ruben D. Houvast\*, Victor M. Baart\*, Shadhvi S. Bhairosingh, Robert A. Cordfunke, Jia Xin Chua, Mireille Vankemmelbeke, Tina Parsons, Peter J. K. Kuppen, Lindy G. Durrant, Alexander L. Vahrmeijer, Cornelis F. M. Sier \* Shared first authorship

Molecular Imaging and Biology. 2020;22(6):1511-22.



#### ABSTRACT

**BACKGROUND** Aberrantly expressed glycans in cancer are of particular interest for tumor targeting. This proof-of-concept *in vivo* study aims to validate the use of aberrant Lewis glycans as target for antibody-based, real-time imaging of gastro-intestinal cancers.

**METHODS** Immunohistochemical (IHC) staining with monoclonal antibody FG88.2, targeting Lewisa/c/x, was performed on gastrointestinal tumors and their healthy counterparts. Then, FG88.2 and its chimeric human/mouse variant CH88.2 were conjugated with near-infrared fluorescent (NIRF) IRDye 8ooCW for real-time imaging. Specific binding was evaluated *in vitro* on human gastrointestinal cancer cell lines with cell-based plate assays, flow cytometry, and immune-fluorescence microscopy. Subsequently, mice bearing human colon and pancreatic subcutaneous tumors were imaged *in vivo* after intravenous administration of 1 nmol (150 μg) CH88.2-8ooCW with the clinical Artemis NIRF imaging system using the Pearl Trilogy small animal imager as reference. One week post-injection of the tracer, tumors and organs were resected and tracer uptake was analyzed *ex vivo*.

**RESULTS** IHC analysis showed strong FG88.2 staining on colonic, gastric, and pancreatic tumors, while staining on their normal tissue counterparts was limited. Next, human cancer cell lines HT-29 (colon) and BxPC-3 and PANC-1 (both pancreatic) were identified as respectively high, moderate, and low Lewisa/c/x-expressing. Using the clinical NIRF camera system for tumor-bearing mice, a mean tumor-to-background ratio (TBR) of 2.2  $\pm$  0.3 (Pearl: 3.1  $\pm$  0.8) was observed in the HT-29 tumors and a TBR of 1.8  $\pm$  0.3 (Pearl: 1.9  $\pm$  0.5) was achieved in the moderate expression BxPC-3 model. In both models, tumors could be adequately localized and delineated by NIRF for up to 1 week. *Ex vivo* analysis confirmed full tumor penetration of the tracer and low fluorescence signals in other organs.

**CONCLUSION** Using a novel chimeric Lewis<sup>a/c/x</sup>-targeting tracer in combination with a clinical NIRF imager, we demonstrate the potential of targeting Lewis glycans for fluorescence-guided surgery of gastrointestinal tumors.

#### INTRODUCTION

Recent advances in surgical techniques, like laparoscopy and robotics, have reduced the ability for surgeons to directly palpate the surgical field, the second-best sense for recognition of abnormalities after visualization. Consequently, various techniques and technologies have been introduced to aid surgeons in identifying key structures. Targeted image-guided surgery, based on near-infrared fluorescent (NIRF) light, has been shown to be a valuable tool for distinguishing malignant from healthy tissue during oncologic surgery.<sup>2</sup> The key elements of this technique include an efficient tracer-target combination and a dedicated NIRF camera system. Currently, the major challenge in molecular imaging remains the identification of the most suitable target for the tumor of choice. Targeted imaging tracers ideally detect all tumor cells, not only within the primary tumor but also in lymph nodes and distant metastasis and visually occult lesions The potential of established tumor-specific proteins, such as carcinoembryonic antigen (CEA), epidermal growth factor receptor (EGFR), epithelial cell adhesion molecule (EpCAM), human epidermal growth factor receptor 2 (HER2), vascular endothelial growth factor (VEGF) and several integrins, as targets for tumor imaging has been successfully demonstrated in both preclinical and clinical settings.<sup>2-10</sup> Most target/tracer combinations appear to have shortcomings, such as excessive interaction with normal tissues, serum instability or an unsuitable clearance profile, resulting in lack of tumor/background contrast. Therefore, a quest for novel, less conventional imaging targets seems essential, if not indispensable.

Aberrant glycosylation of proteins and lipids is considered a hallmark of cancer. 11,12 During oncogenesis, immature mucin-type O-glycans, such as sialyl-Thomsen-Nouvelle (sTn), and fucosylated glycan antigens, such as sialyl-Lewisa (sLea/CA19.9) and sialyl-Lewisx (sLex/CD15s) are overexpressed on the cell membrane of cancer cells. Some of these antigens, like sLeaand sLex, seem heavily involved in tumor progression, invasion and metastasis, whereas their role in healthy tissue is minimal. 13-15 Therefore, targeting of tumor-associated glycans not only offers opportunities for therapy, but also for molecular imaging. Originating from genetic dysregulation of the enzymes responsible for glycan synthesis, glycan expression is not limited to a single protein. 16 Hence, tracers against tumorassociated glycans will target multiple tumor-associated proteins and lipids simultaneously and may provide a broader tumor-targeting strategy than targeting each tumor marking protein separately. Because glycans are less immunogenic than proteins, the number of specific IgG antibodies against glycans is still limited.<sup>17</sup> Recently Chua et al. developed the novel anti-LecLex, di-Lea, LeaLex and Lea IgG antibody FG88.2, which showed specific immunohistochemical staining on 81% of pancreatic, 71% of colorectal, 54% of gastric, 23% of non-small cell lung, and 31% of ovarian tumor tissues, along with a restricted binding to normal tissues. Subsequently a chimeric (mouse/human) variant was developed, termed CH88.2. This variant is composed of a human Fc region but contains the same mouse-derived antigen binding region as FG88.2, essentially preserving its target specificity. Given the expression of its glycotarget, antibody CH88.2 conjugated with an NIRF dye might constitute a valuable pan-carcinoma tracer for fluorescence-guided surgery (FGS).

In this study, we validate the concept of glycan-based real-time imaging of gastrointestinal tumors by using CH88.2 conjugated with NIR fluorophore IRDye8ooCW. Specific binding of the antibodies was confirmed on human gastrointestinal tissues and a range of gastrointestinal cell lines. The tracer specificity was evaluated *in vivo* using subcutaneous mouse models of gastrointestinal cancers. Using a chimeric antibody in combination with the clinical equivalents of a NIR system, we might pave the way for a rapid clinical translation, not only for this particular tracer, but also for the concept of imaging of cancers using glycan-targeting tracers.

## MATERIALS AND METHODS

## Monoclonal antibodies

Anti-LecLex, di-Lea, LeaLex, and Lea mouse FG88.2 (mIgG3) and its chimeric derivate CH88.2 (hIgG1) were supplied by professor Lindy Durrant (Scancell Ltd, UK).

## Monoclonal antibody conjugation

Mouse FG88.2 and CH88.2 were covalently conjugated with NIR fluorochrome IRDye8ooCW via N-hydroxysuccinimide (NHS)-ester chemistry against primary amines until a degree of labeling (DOL) between 1 and 1.5 was reached, following the manufacturer's protocol (LI-COR, Lincoln, NE, Nebraska). DOLs were estimated by the supplied mathematical formula and confirmed by MALDI-TOF analyses using a Microflex (Bruker, Billerica, MA, USA) and sinnapinic acid as matrix.

## **Immunohistochemistry**

Formalin-fixed, paraffin-embedded tissue blocks from colon tumors (n=4), gastric tumors (n=8), pancreatic tumors (n=10), and pancreatitis (n=2), particularly selected for the presence of healthy appearing adjacent tissue, were obtained from the Pathology department of the Leiden University Medical Center (LUMC). Immunohistochemical staining was performed on 4-µm-thick sections on glass

slides. The sections were deparaffinized in xylene for 15 min, rehydrated in a series of ethanol dilutions, and rinsed in demineralized water. Next, endogenous peroxidase was blocked with 0.3 % hydrogen peroxide in demineralized water. Antigen retrieval was performed by heating sections to 95 °C for 10 min in EnVision Flex Target Retrieval Solution (pH 6.0) using PT Link (Dako, Glostrup, Denmark). After cooling for 5 min in PBS (phosphate-buffered saline, pH 7.4), sections were incubated overnight in a humidified chamber at room temperature with 150 µl primary mouse FG88.2 antibody (0.19 µg/ml). Sections were washed three times in PBS for 5 min and incubated with secondary goat anti-mouse EnVision antibody (Dako, K4001) for 30 min. After secondary incubation and additional washing, sections were incubated with DAB+ substrate buffer (Dako) for 10 min. Sections were counterstained with Mayer's hematoxylin solution (Sigma-Aldrich, Saint Louis, MO, USA), dehydrated in an incubator for 1 h at 37 °C and mounted with Pertex (Leica Microsystems, Wetzlar, Germany). To exclude nonspecific staining, a negative (PBS) and conjugate control (only secondary antibody) were included. Slides were examined under a Zeiss AxioSkop 20 light microscope (Carl Zeiss, Jena, Germany).

## Human cancer cell lines

Cell lines KATO III (signet ring diffuse cell type gastric carcinoma), HT-29, DLD-1, COLO 205, HCT-15 (colon carcinoma), BxPC-3(\_luc2), PANC-1, MIA PaCa-2 (pancreatic carcinoma), and CHO (Chinese hamster ovary) were obtained from ATCC, except for BxPC-3\_luc2 which was purchased from PerkinElmer (Waltham, MA, USA). KATO III, HT-29, DLD-1, COLO 205, HCT-15, and BxPC-3(\_luc2) cells were cultured in RPMI 1640 cell culture medium (Gibco, Invitrogen, Carlsbad, CA, USA). PANC-1, MIA Paca-2, and CHO cells were cultured in DMEM + GlutaMAX<sup>TM</sup> cell culture medium (Gibco, Invitrogen). Both media were supplemented by l-glutamine, 25 mM HEPES, 10 % fetal bovine serum (FBS; Hyclone, Thermo Scientific, Rockford, Il, USA), and penicillin/streptomycin (both 100 IU/ml; Invitrogen). Absence of *Mycoplasma* was confirmed using polymerase chain reaction. Cells were grown to 90 % confluence in a humidified incubator at 37 °C (5 % CO<sub>2</sub>) and detached with trypsin/EDTA. Viability was assessed using Trypan Blue staining in 0.4 % solution (Invitrogen).

## Cell-based plate assay

Binding of FG88.2-8ooCW was evaluated on gastrointestinal cancer cell lines KATO III, HT-29, DLD-1, COLO 205, HCT-15, BxPC-3, PANC-1, and MIA PaCa-2 using a plate assay with CHO as reference cell line. Cells were grown in a 96-well

plate (Corning Costar Inc., Cambridge, MA, USA) at 20,000 cells/well in 100 µl of complete medium until 90 % confluence. Thereafter, cells were incubated with FG88.2-800CW at 10, 5, 2.5, or 1.25 µg/ml for 1 h at 37 °C. After washing twice with medium, fluorescence signal was measured using the Odyssey NIR imaging system (LI-COR Biosciences, 800-nm channel, intensity 10). The 800-nm fluorescence signal was corrected for the number of cells using a nuclear staining. Briefly, cells were fixated and permeabilized with acetone and methanol in a 40/60 mixture for 10 min. After washing, cells were incubated with TO-PRO3 (1/2000, Invitrogen) for 5 min at room temperature, washed, and scanned with the Odyssey NIR imaging system (700-nm channel, intensity 9). The mean fluorescence intensity (MFI) was calculated by dividing the 800CW fluorescence signal by the nuclear 700-nm signal and multiplying the number by 100. Measurements were performed in triplicate.

## Flow Cytometry

After detachment and viability assessment, cells were adjusted to  $0.5 \times 10^6$  cells/ tube in PBS/BSA (PBS/bovine serum albumin) (0.5 %) and incubated with 100 µl FG88.2 antibody (5 µg/ml). Next, cells were washed twice in PBS/BSA 0.5 % and incubated with secondary AF488-labeled goat anti-mouse (A21121, Thermo Scientific, 1/800) or AF647-labeled goat anti-mouse (A21241, Thermo Scientific, 1/800) for 30 min. After washing twice with PBS with 0.5 % BSA, cells were resuspended in 400 µl PBS/BSA containing propidium iodide (1/4000) and measured on a LSRII flow cytometer (BD Biosciences, Franklin Lanes, NJ, USA;  $1.0 \times 10^5$  live cells per tube) using the 530/30 laser for measuring AF488 signals and 695/40 laser for measuring PI or AF647 signals. All incubation steps were done on ice, avoiding exposure to light.

## Chamber slides

After detachment and viability assessment, cells were placed in an 8-well Nunc™ Lab-Tek™ II Chamber Slide (0.7 cm²/well, Thermo Scientific) at 50,000 cells/well. When approximately 90 % confluence was reached, medium was removed and cells were washed twice in PBS for 5 min. Cells were subsequently fixated with 1 % paraformaldehyde for 10 min at room temperature. After washing twice in PBS for 5 min, cells were incubated with respectively primary CH88.2-800CW, secondary polyclonal rabbit anti-human antibody (Ao423, 10 µg/ml; Agilent, Santa Clara, CA, USA), and tertiary goat anti-rabbit F(ab')2-AF488 (Thermo Scientific, A11070, 1/800) for 30 min, with two wash steps (PBS, 5 min) in between incubations. After

additional washing with PBS and demineralized water, slides were dried. Next, the plastic chambers were removed and cell nuclei were stained using ProLong Gold containing DAPI (Thermo Scientific). Antibody binding was analyzed using a DM5500 B fluorescence microscope (Leica Microsystems)) with filter cube A (excitation 340–380, long pass emission 425; exposure time 0.05 s) for visualizing DAPI signals and filter cubes I3 (excitation 450–490, long pass emission 515; exposure time 0.40 s) and CY7 (excitation 710/75, emission 810/90; exposure time 0.70 s) for visualizing AF488 and 800CW fluorescence signals, respectively.

#### Animal models

Mice were kept at the Central Animal Facility of the LUMC, which houses animals per EU Recommendation 2007-526-EC under specific pathogen-free conditions.<sup>19</sup> For all animal handlings, local standard operating procedures were followed. Six- to eight-week-old female BALB/c-Nude (CAnN.Cg-Foxn1<sup>nu</sup>/Crl) mice (Charles River Laboratories, Wilmington, MA, USA) were subcutaneously inoculated on 4 spots on the back with either HT-29 or BxPC-3\_luc2 cells (5.0×10<sup>5</sup> cells/spot; 3 mice per group). Tumor growth was monitored by a digital caliper. Tumors of 50 mm³ were considered large enough for imaging. The local animal welfare body of the LUMC reviewed and approved all animal studies. Animals received humane care in compliance with the Code of Practice Animal Experiments in Cancer Research.

## In vivo NIRF imaging

The tail vein of the mice was injected intravenously with 1 nmol (150  $\mu$ g) CH88.2-800CW. The mice were imaged at 4 h, 24 h, 48 h, 72 h, 96 h, 120 h, 148 h, and 168 h post-injection, using the clinical Artemis NIR Imaging System (Quest Medical Imaging b.v., Middenmeer, The Netherlands; hereafter referred to as "Artemis") using the more sensitive but preclinical Pearl Trilogy Small Animal Imaging System (LI-COR Biosciences; hereafter referred to as "Pearl") as a reference. Mice were kept under 2–4 % isoflurane anesthesia during imaging. After the last measurement, mice were sacrificed and the organs were removed and imaged *ex vivo* using the Pearl.

## **NIRF Imaging Analysis**

MFIs were extracted from images by marking a region of interest on the macroscopic tumor (tumor signal) and on the adjacent skin (background signal) using Spectrum Capture Suite (Quest Medical Imaging b.v.) and ImageJ version 5.2p for Artemis images<sup>20</sup> and Image Studio version 5.2 (LI-COR Biosciences) for Pearl images. Tumor-to-background ratios (TBRs) were calculated *via* the following

formula: TBR=MFI<sub>tumor</sub>/MFI<sub>background</sub>. For biodistribution analysis, mean organ MFIs were calculated in Image Studio by drawing a ROI over the designated organ. Tumor-to-organ ratios were calculated by dividing the tumor MFI by the mean organ MFI of the same mouse (n = 3 for both HT-29 and BxPC-3 mice).

## Histological analysis

After 1 week (168 h), tumors were resected and incubated in 4 % paraformaldehyde which was replaced by 70 % ethanol the next day. Subsequently, tumors were treated with a standard dehydration sequence (ethanol and xylene) and imbedded in paraffin.

For ex vivo imaging and staining, 4-µm-thick tissue sections were deparaffinized in xylene for 15 min and fluorescence imaging was performed using the Odyssey CLx NIR imaging system on the 800-nm channel. Sections were rehydrated as described in the "Immunohistochemistry" section and subsequently stained with standard hematoxylin-eosin staining.

## Statistical analyses

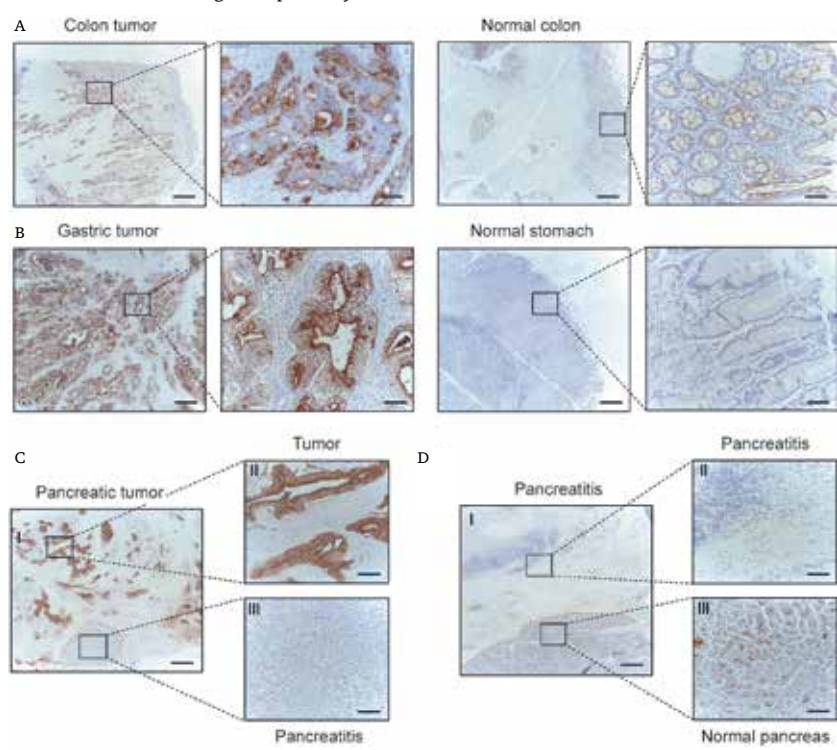
Statistical analyses and graph generation were performed with GraphPad Prism (version 8.01, GraphPad Software Inc., La Jolla, CA, USA). Differences between mean TBRs and tumor/background MFIs for different time points were compared via one-way ANOVA. Correction for multiple comparisons was done using the Holm-Sidak method. Differences in biodistribution between HT-29 and BxPC-3\_luc2 mice were calculated using independent samples t tests. Differences with a P value smaller than 0.05 were regarded significant (NS: not significant; \*:  $p \le$  0.05; \*\*\*:  $p \le$  0.01).

## **RESULTS**

## Immunohistochemistry

Immunohistochemical analysis showed FG88.2 staining in 1 out of 4 colon tumors (Figure 1A), 4 out of 8 gastric tumors (Figure 1B), and 7 out of 10 pancreatic tumors (Figure 1C). FG88.2 was mainly located on the basolateral and apical membrane of cancer cells, and also some staining in cytoplasm was observed. Stromal cells did not stain. FG88.2 on normal colon was mainly located near the apical membrane of epithelial cells and was low to moderate in normal colon (Figure 1A), negative to moderate in normal stomach glands (Figure 1B) and negative to weak in healthy pancreatic acini and ducts (Figure 1C). Very limited FG88.2 staining was found on both pancreatitis tissue samples (Figure 1D).

FIGURE 1 (A) Immunohistochemical FG88.2 staining in a colon tumor and in normal colonic crypts. (B) FG88.2 staining in a gastric tumor and in normal gastric glands. (C,D) FG88.2 staining in pancreatic tumor tissue and pancreatitis tissue (and normal pancreatic tissue derived from the same patient (III)). Red-dotted lines represent the tumor (C) or pancreatitis-normal pancreatic tissue border. (D) Overview images are taken at  $\times$  50 magnification and inserts at  $\times$  200 magnification. Scale bars represent 500  $\mu$ m and 100  $\mu$ m, respectively. Scale bars represent 500  $\mu$ m and 100  $\mu$ m for overview and insert images, respectively.

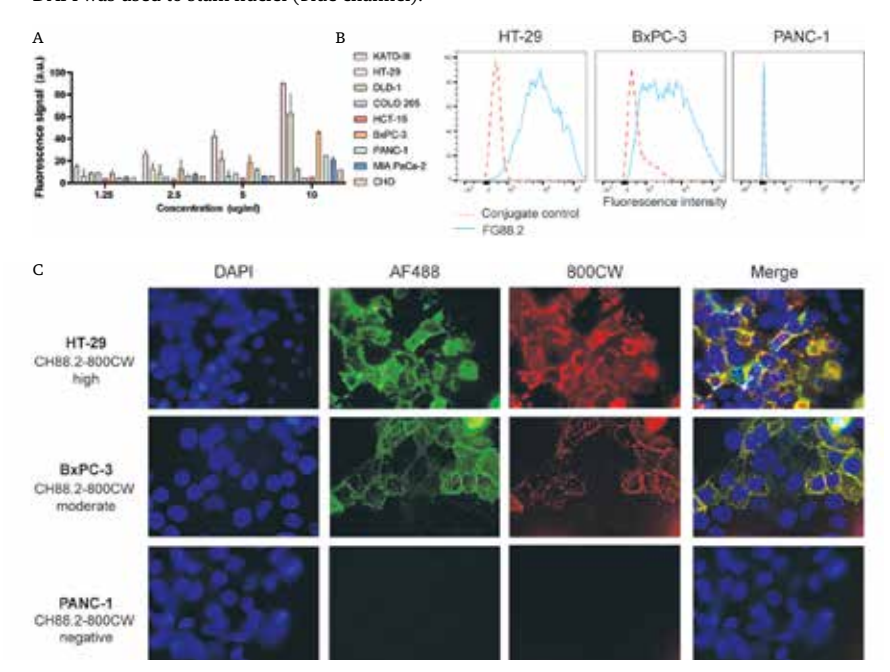


## **Binding specificity**

FG88.2 binding was evaluated on a panel of gastrointestinal carcinoma cell lines using a cell-based plate assay. CHO cells were included as a non-human negative control. Fluorescence signals increased in a dose-dependent manner and no relevant fluorescence signal was observed on CHO cells (Figure 2A). High fluorescence signals were observed on KATO III and HT-29 cells, while fluorescence signal on BxPC-3 cells was moderate. Based on the observed fluorescence signals, HT-29 and BxPC-3 were selected as FG88.2-positive cancer cell lines for further studies

and PANC-1 represented a low control. Next, FG88.2 binding to living cells was further confirmed using flow cytometry. HT-29, BxPC-3, and PANC-1 cells showed respectively high, moderate, and almost negative FG88.2 binding, in accordance with what was found using the plate assays (Figure 2B). The binding specificity to these cells by the chimeric and NIRF conjugated counterpart CH88.2-800CW was performed in chamber slides using immunofluorescence. As expected, CH88.2-800CW expression (in red) was high on HT-29 cells, moderate on BxPC-3 cells, and not detectable on PANC-1 cells. Overlap of the 800CW signal with the AF488 signal (green), indicating the specific presence of anti-human antibodies, confirmed that the binding of 800CW-conjugated CH88.2 was specific (Figure 2C). Based on these *in vitro* data, colon cancer HT-29 and pancreatic cancer BxPC-3 were selected as gastrointestinal cancer cell lines for *in vivo* binding studies with CH88.2-800CW.

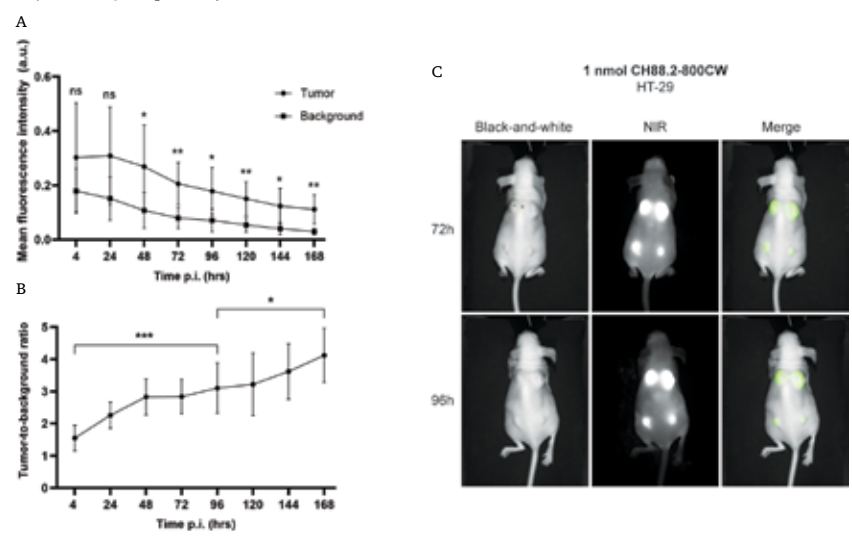
FIGURE 2 (A) Cell-based plate assay of FG88.2-8ooCW at 1.25, 2.5, 5, and 10 µg/ml dilutions on gastrointestinal cell lines. (B) Flow cytometry of FG88.2 on HT-29, BxPC-3, and PANC-1. Red-dotted lines represent conjugate controls and blue lines represent FG88.2 fluorescence signals. (C) Immunofluorescence analysis of CH88.2-8ooCW binding on HT-29, BxPC-3, and PANC-1 cells. AF488 signals and 8ooCW signals are represented in green and red, respectively. DAPI was used to stain nuclei (blue channel).



## In vivo NIRF imaging of subcutaneous HT-29 and BxPC-3 tumors

To evaluate the *in vivo* binding of NIRF tracer CH88.2-8ooCW and establish the optimal imaging window, HT-29 and BxPC-3 tumor-bearing mice were injected with 1 nmol (150 µg) tracer and imaged every 24 h for 7 days (168 h) using the nonclinical Pearl imager. For the HT-29 colonic cancer model, significant differences between tumor and background MFIs could be detected from 48 h (p = 0.011) to 1 week (p = 0.003) and tumor MFIs were sufficient for tumor delineation at all time points onward (Figure 3A). The optimal imaging time frame was defined at 96 h post-injection at which a TBR of  $3.1 \pm 0.8$  was reached (Figure 3B-C). TBRs continued to increase until 7 days post-injection (p = 0.017; Figure 3B). Although the tumor MFI decreased over time, lesions could be clearly visualized during the optimal imaging window, which for many antibody-based tracers lies between 3 and 5 days post-injection.<sup>3</sup>

**FIGURE 3** (A) Average tumor and background MFIs over time in HT-29 colon cancer-bearing mice injected with CH88.2-8ooCW using the Pearl preclinical imager. (B) Mean TBRs over time. (C) Representative black-and-white, NIRF, and merged images of HT-29 tumor-bearing mice at 72 h and 96 h post-injection.



In the BxPC-3 pancreatic cancer model, significant differences between tumor and background MFIs were observed as early as 4 h post-injection (p = 0.031) and remained significant until 168 h (p < 0.001; Figure 4A). At the optimal imaging time point of 96 h post-injection, a TBR of 1.9  $\pm$  0.5 was observed (Figure 4B-C), which was sufficient to clearly localize all tumor lesions (Figure 4C). Both gastrointestinal tumors could be clearly delineated up to 168 h post-injection (Supplementary Figure 1, see ESM1).

Next, NIRF imaging was performed using the clinically used Artemis NIR imaging system to highlight the translational potential of CH88.2-800CW-based tumor imaging. A clinical range exposure time of 150 ms was used, allowing real-time imaging. At the optimal imaging time point of 96 h, a mean TBR of  $2.2 \pm 0.3$  was achieved in the HT-29 colonic model *versus* a mean TBR of  $1.8 \pm 0.3$  in the BxPC-3 pancreatic model (Figure 5, video clips available under ESM 2 and 3). Tumors could be localized and delineated excellently in both gastrointestinal cancer models up to 168 h post-injection (Supplementary Figure 2, see ESM 1).

**FIGURE 4** (A) Average tumor and background MFIs over time in BxPC-3 pancreatic cancerbearing mice injected with CH88.2-8ooCW using the Pearl preclinical imager. (B) Mean TBR over time. (C) Representative black-and-white, NIRF, and merged images of BxPC-3 tumor-bearing mice at 72 h and 96 h post-injection.

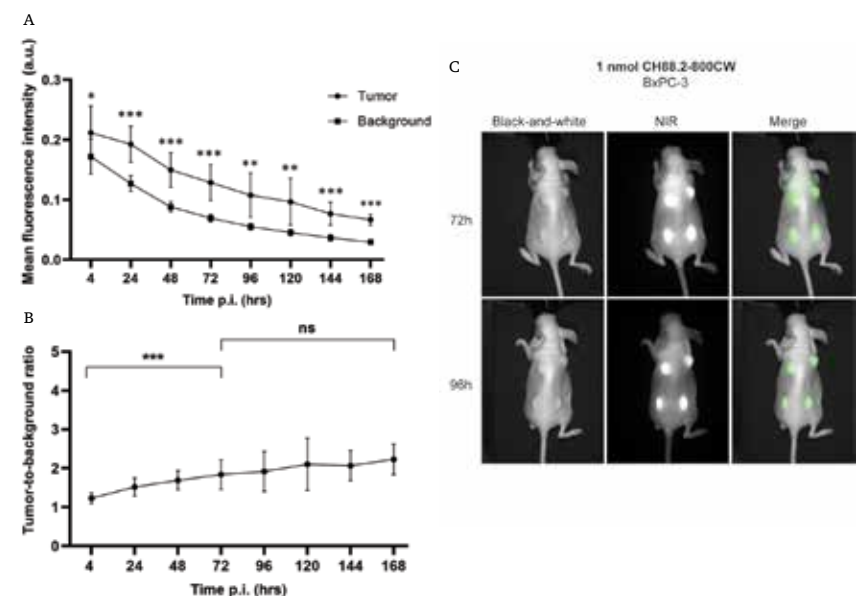
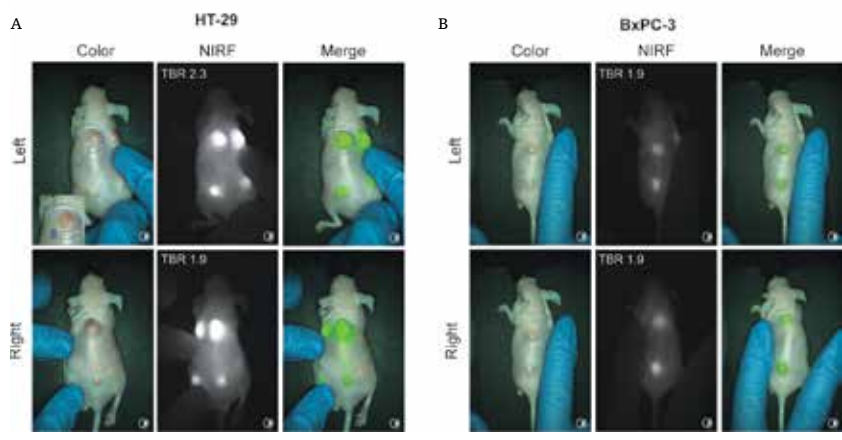


FIGURE 5 (A) Representative color, NIRF, and merged images of CH88.2-800CW binding specificity in a HT-29 tumor-bearing mouse model using the clinical Artemis NIR imaging system at 150-ms exposure. Regions of interest were selected in similar fashion to the Pearl as shown by the red and blue shapes, corresponding to the tumor and background area, respectively (only displayed in the left figure). To allow better visualization of the field of interest, the tumor-bearing skin was manually mobilized to the center of the camera's optical field as is displayed by left and right back images. (B) Representative images of CH88.2-800CW binding specificity in a BxPC-3 tumor-bearing mouse model.

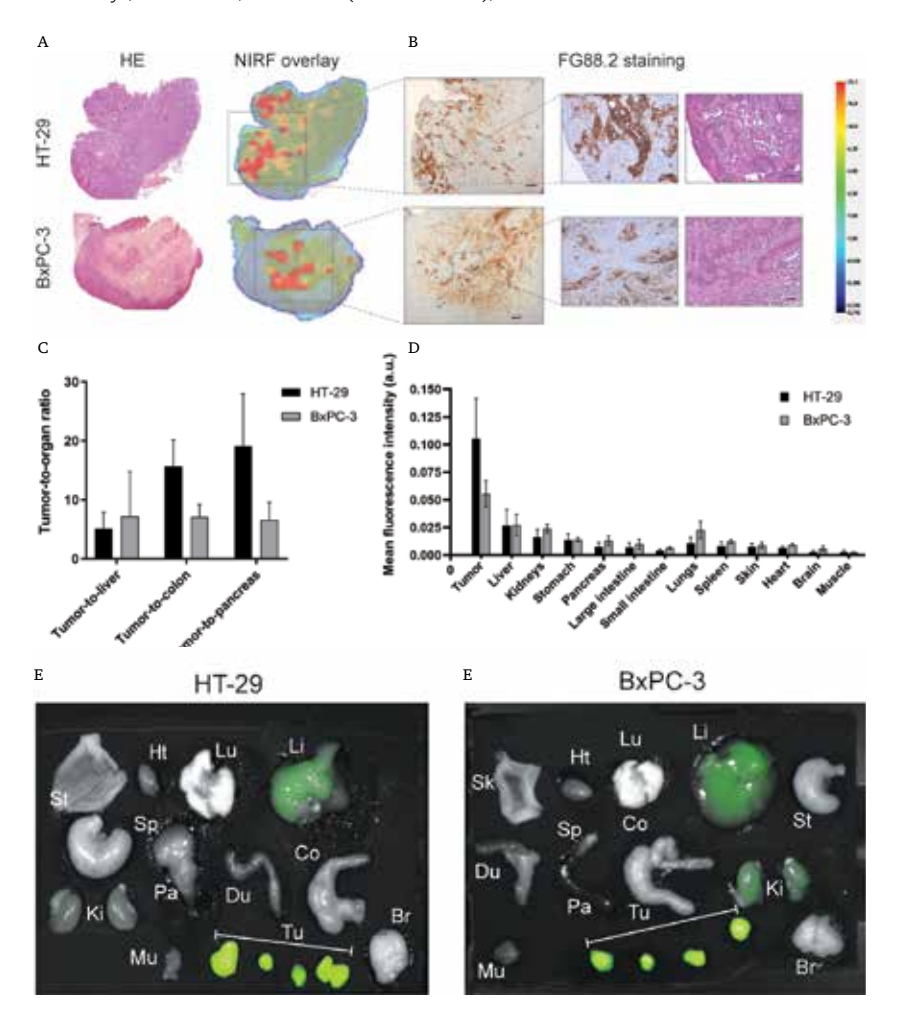


## Ex vivo imaging and histological analysis

At 1 week post-injection, mice were sacrificed and tumors were resected and sectioned. *Ex vivo* analysis showed that CH88.2-8ooCW fully penetrated the tumors, with a higher overall fluorescence signal in HT-29 colon tumors compared with BxPC-3 pancreatic tumors. FG88.2 staining on HT-29 and BxPC-3 tumors showed that Lewis<sup>a/c/x</sup> was expressed in both models and expression correlated with the observed NIR signal (Figure 6A). Of note, healthy mouse colon and pancreas tissues did show specific FG88.2 staining (Supplementary Figure 5, see ESM 1).

Similarly, biodistribution of CH88.2-8ooCW at 1 week showed a high tumor uptake (HT-29:  $0.105\pm0.037$ ; BxPC-3:  $0.056\pm0.012$ ). High tumor-to-liver (HT-29:  $5.1\pm2.8$ ; BxPC-3:  $7.2\pm7.6$ ), tumor-to-colon (HT-29 15.7  $\pm4.4$ ; BxPC-3:  $7.1\pm2.2$ ), and tumor-to-pancreas (HT-29:  $19.1\pm8.8$ ; BxPC-3:  $6.6\pm2.9$ ) ratios were achieved in both mouse models. Mean fluorescence signals in the organs associated with antibody clearing from the circulation were slightly higher than the other organs (liver:  $0.027\pm0.012$  and kidneys:  $0.020\pm0.006$ ). No statistically significant differences in biodistribution were observed between both mouse models (Figure 6B-C).

FIGURE 6 (A) Representative examples of *ex vivo* hematoxylin-eosin (HE) staining, NIR fluorescence heatmap (800 nm), and FG88.2 staining on HT-29 and BxPC-3 tumor tissue sections. Overview images are taken at  $\times$ 25 magnification and inserts at  $\times$ 100 magnification. Scale bars represent 500 µm and 100 µm for overview and insert images, respectively. (B) Average tumor-to-liver, tumor-to-colon, and tumor-to-pancreas ratios in HT-29 and BxPC-3 tumor-bearing mice at 168 h/1 week post-injection. (C) Biodistribution of CH88.2-800CW at 168h/1week post-injection expressed as tumor or organ MFI. (D) *Ex vivo* fluorescent images of resected tumors and organs. Sk: skin, Hrt: heart, Lu: lungs, Li: liver, St: stomach, Sp: spleen, Pa: pancreas, Du: duodenum, Co: colon, Ki: kidneys, Mu: muscle, Tu: tumors (under brackets), Br: brain.



#### DISCUSSION

In this study, we validated the concept of glycan-based tumor imaging, using a novel chimeric anti-Lewis glycan antibody, equipped with a clinically used NIRF dye. Although highest binding of FG88.2 was observed to KATO-III cells, imaging of colorectal and pancreatic tumors was of particular interest considering their expression on well over 80% of tumors. We showed that administration of CH88.2-800CW to human colon or pancreas tumor-bearing mice, resulted in high-contrast tumor delineation using a clinical NIR camera system. Even though the target of FG88.2 is only moderately expressed on BxPC-3 cells, subcutaneous tumors could be localized within the optimal imaging window despite lower TBRs as found for HT-29. At 1 week post-injection of the tracer, tumor lesions could still be localized by the fluorescence signal. Imaging with CH88.2-800CW resulted in 2-3 fold higher TBRs than we have shown with 800CW or rituximab-800CW in the same HT-29 mouse model, suggesting specific binding of CH88.24 [Baart et al, manuscript submitted]. Full tumor penetration was confirmed using ex vivo analysis and tumor uptake seemed dependent on FG88.2 staining. Biodistribution of CH88.2-80oCW showed the highly specific tracer uptake in both tumor types. Tumors could be easily delineated from healthy liver, colon and pancreas tissues with high tumorto-organ ratios. Compared to the low fluorescence signals in other organs, the liver and kidneys showed enhanced signals (<50% of tumor), which should be attributed to tracer clearance from the circulation. Our IHC results confirm the larger dataset previously published by Chua et al. and underscore the great in vitro and in vivo performance of the tracer for imaging of pancreatic, colon and gastric carcinomas.

While surgery remains the cornerstone of cancer therapy, both untargeted and targeted FGS tracers have been implemented within standard-of-care in several centers, greatly affecting intraoperative decision making through identification of tumor tissue and visually occult lesions. <sup>2,8,21</sup> By using a chimeric mAb and a clinically available dye and camera system, we have demonstrated the great translational potential of CH88.2-800CW for NIRF imaging of gastrointestinal tumors. A possible limitation of the current study is that TBRs may have been overestimated as mice do not naturally express Le<sup>a/c/x</sup> glycans, which was supported by our IHC results. <sup>22</sup> Another limitation of the study is that we did not evaluate Le<sup>a/c/x</sup> expression on precursor lesions, tumor-positive lymph nodes and metastases, which should also be distinguished from surrounding tissues. Although we have reported lower FG88.2 staining in normal human tissues than in their malignant tissue counterparts, a more detailed IHC analysis of FG88.2 is essential to define the establish the potential and specific employability of CH88.2-800CW for tumor imaging.

Monoclonal antibody FG88.2 binds the LecLex-glycan and -related glycan clusters, as well as the single Lea subunit. Lea overexpression has been observed in the majority of gastrointestinal cancers<sup>23-28</sup> and gastric lesions, such as gastritis and intestinal metaplasia, suggesting a potential role for CH88.2-800CW in early gastric cancer detection.<sup>29</sup> Additionally, Le<sup>a</sup> expression has been observed in chronic pancreatitis and loss of Lea expression was observed in colonic polyps. 25,30 Therefore, our observation that pancreatitis tissues did not stain for FG88.2, is encouraging a clinical application, since the distinction between pancreatitis and tumor tissue poses a major challenge during surgery for pancreatic cancer. To a lesser extent, Leais also expressed in several normal tissues such as normal pancreas, distal colon and stomach, which may explain the mild FG88.2 reactivity with these human tissues. 26,28,31 Although in principle a non-tumor reactivity can hamper the suitability of a tumor imaging tracer, the ratio of expression between tumor and adjacent normal tissue (TBR) seems to be well over two for most organs, including the lungs. Besides, the limited expression of FG88.2 on normal tissues was largely confined to the apical membrane and it is unlikely that circulating antibodies will reach these locations in vivo. 18 Noteworthy, FGS of human colon tumors targeting the EpCAM glycoprotein resulted in excellent tumor localization despite relatively low TBRs of around two.5

Tumor-associated glycans are of particular interest in the quest for novel, less conventional targets for improved tumor imaging. Several preclinical and clinical studies validated anti-Lewis glycan antibodies for therapy or imaging, particularly focusing on sLea, also known as CA19-9. Preclinically, administration of anti-CA19-9 antibody HuMab-5B1 doubled survival time of COLO 205 (colon carcinoma) tumor-bearing mice and, remarkably, resulted in full survival of two mice at a higher dose without toxicity.<sup>32</sup> The NIR dye- and or <sup>89</sup>Zr-labeled HuMab-5B1 mAb variants were also validated for PET imaging and FGS, with excellent tumor delineation, resection, metastasis imaging and sentinel lymph node mapping possibilities in both a subcutaneous and orthotopic model of pancreatic cancer.<sup>33,34</sup> Phase I trials validating HuMab-5B1 for PET imaging (NCTo2687230), radioimmunotherapy (NCTo3118349) and immunotherapy (NCTo2672917) in pancreatic cancer and other CA19-9 expressing malignancies are currently recruiting in the United States. Although sLea is highly expressed in >90% of pancreatic cancers, it is also overexpressed in normal pancreatic tissue and chronic pancreatitis. Furthermore, sLea serum levels are elevated in benign diseases such as pancreatitis, cholangitis and obstructive jaundice, all making the distinction between cancer and non-cancerous pancreaticobiliary diseases potentially challenging when targeting CA19.9 alone. 35,36 Thus, Lewis glycan-based tumor imaging seems feasible, but using alternative Lewis glycans, such as Le<sup>a/c/x</sup>, are not expressed by normal and benign tissues, may pave the way for an even more specific and or broader tumor targeting strategy.

Altogether, our proof-of-concept study demonstrates the potential of imaging gastrointestinal tumors by targeting Lewis glyco-epitopes present on cancer cells with the novel, NIR dye-conjugated chimeric monoclonal antibody CH88.2-800CW. As the tracer consists of a chimeric mAb and a FDA-approved NIR fluorescent dye, it is ready for clinical use, making a rapid clinical translation by our group feasible.<sup>5,9,10</sup>

#### CONCLUSION

To conclude, our results show that both colorectal and pancreatic tumors can be excellently delineated after administration of Lewis-glycan-specific CH88.2-800CW, with low tracer uptake in other tissues. This promising proof-of-concept research not only paves the way for a more extensive evaluation of the CH88.2-800CW tracer for FGS, but also demonstrates the relevance of glycans for real-time imaging of gastrointestinal tumors. By conducting this study, we form a firm foundation for the introduction of glycan-targeted molecular imaging to the operating room of the future.

#### SUPPLEMENTARY MATERIALS

The following supplementary materials are available online:

ESM 1: https://bit.ly/402Z9T7

**Supplementary Figure 1:** *In vivo* images at all time points of HT-29 colon cancer-bearing mice using the Pearl preclinical imager; **Supplementary Figure 2:** *In vivo* images at all time points of BxPC-3 pancreatic cancer-bearing mice using the Pearl preclinical imager; **Supplementary Figure 3:** *In vivo* images at all time points of HT-29 colon cancer-bearing mice using the clinical Artemis imager; **Supplementary Figure 4:** *In vivo* images at all time points of BxPC-3 pancreatic cancer-bearing mice using the clinical Artemis imager; **Supplementary Figure 5:** FG88.2 staining on healthy mouse colon and pancreatic tissue.

## ESM 2: https://bit.ly/4h1LdQc

 $\label{thm:condition} \mbox{Video clip of NIRF imaging using CH88.2-800CW in HT-29 tumor-bearing mice.}$ 

## ESM 3: https://bit.ly/4fGlAmZ

Video clip of NIRF imaging using CH88.2-800CW in BxPC-3 tumor-bearing mice.

#### REFERENCES

- 1 Verbeek FP, van der Vorst JR, Schaafsma BE, Hutteman M, Bonsing BA, van Leeuwen FW, et al. Image-guided hepatopancreatobiliary surgery using near-infrared fluorescent 16 Fuster MM, Esko JD. The sweet and sour of cancer: light, I Hepatobiliary Pancreat Sci. 2012;19(6):626-37.
- 2 Hernot S, van Manen L, Debie P, Mieog JSD, Vahrmeijer AL. Latest developments in molecular tracers for fluorescence 17 Rabu C, McIntosh R, Jurasova Z, Durrant L. Glycans as image-guided cancer surgery. The Lancet Oncology. 2019;20(7):e354-e67.
- 3 Boonstra MC, Tolner B, Schaafsma BE, Boogerd LS, Prevoo HA, Bhavsar G, et al. Preclinical evaluation of a novel CEA-targeting near-infrared fluorescent tracer delineating colorectal and pancreatic tumors. Int J Cancer. 2015;137(8):1910-20.
- 4 van Driel PBAA, Boonstra MC, Prevoo HAJM, van de Giessen M, Snoeks TJA, Tummers QRJG, et al. EpCAM as multi-tumour target for near-infrared fluorescence guided surgery. BMC Cancer. 2016;16:884.
- 5 Boogerd LSF, Boonstra MC, Prevoo H, Handgraaf HJM, Kuppen PJK, van de Velde CJH, et al. Fluorescenceguided tumor detection with a novel anti-EpCAM targeted antibody fragment: Preclinical validation, Surg Oncol. 2019;28:1-8.
- 6 Diikers EC, Oude Munnink TH, Kosterink IG, Brouwers AH, Jager PL, de Jong JR, et al. Biodistribution of 89Zrtrastuzumab and PET imaging of HER2-positive lesions in patients with metastatic breast cancer. Clin Pharmacol Ther. 2010;87(5):586-92.
- 7 Handgraaf HJM, Boonstra MC, Prevoo H, Kuil J, Bordo MW, Boogerd LSF, et al. Real-time near-infrared fluorescence imaging using cRGD-ZW800-1 for intraoperative visualization of multiple cancer types. Oncotarget. 2017;8(13):21054-66.
- 8 Boogerd LSF, Hoogstins CES, Schaap DP, Kusters M, Handgraaf HJM, van der Valk MJM, et al. Safety and effectiveness of SGM-101, a fluorescent antibody targeting carcinoembryonic antigen, for intraoperative detection of colorectal cancer: a dose-escalation pilot study. Lancet Gastroenterol Hepatol, 2018;3(3):181-91.
- Rosenthal EL, Warram JM, de Boer E, Chung TK, Korb ML, Brandwein-Gensler M, et al. Safety and Tumor Specificity of Cetuximab-IRDye800 for Surgical Navigation in Head and Neck Cancer. Clin Cancer Res. 2015;21(16):3658-66.
- 10 Lamberts LE, Koch M, de Jong JS, Adams ALL, Glatz J, Kranendonk MEG, et al. Tumor-Specific Uptake of Fluorescent Bevacizumab-IRDye8ooCW Microdosing in Patients with Primary Breast Cancer: A Phase I Feasibility Study. Clin Cancer Res. 2017;23(11):2730-41.
- 11 Pinho SS, Reis CA. Glycosylation in cancer: mechanisms and clinical implications. Nat Rev Cancer. 2015;15(9):540-55.
- 12 Munkley J, Elliott DJ. Hallmarks of glycosylation in cancer. Oncotarget. 2016;7(23):35478-89.
- 13 Pinho S, Marcos NT, Ferreira B, Carvalho AS, Oliveira MJ, Santos-Silva F, et al. Biological significance of cancerassociated sialyl-Tn antigen: modulation of malignant phenotype in gastric carcinoma cells. Cancer Lett. 2007;249(2):157-70.
- 14 Munkley J. The Role of Sialyl-Tn in Cancer. Int J Mol Sci. 2016;17(3):275.

- 15 Blanas A, Sahasrabudhe NM, Rodríguez E, van Kooyk Y, van Vliet SJ. Fucosylated Antigens in Cancer: An Alliance toward Tumor Progression, Metastasis, and Resistance to Chemotherapy. 2018;8(39).
- glycans as novel therapeutic targets. Nat Rev Cancer. 2005;5(7):526-42.
- targets for therapeutic antitumor antibodies. Future Oncol. 2012;8(8):943-60.
- 18 Chua IX, Vankemmelbeke M, McIntosh RS, Clarke PA. Moss R, Parsons T, et al. Monoclonal Antibodies Targeting LecLex-Related Glycans with Potent Antitumor Activity. Clin Cancer Res. 2015;21(13):2963-74.
- 19 Mahler Convenor M, Berard M, Feinstein R, Gallagher A, Illgen-Wilcke B, Pritchett-Corning K, et al. FELASA recommendations for the health monitoring of mouse, rat, hamster, guinea pig and rabbit colonies in breeding and experimental units. Lab Anim. 2014;48(3):178-92.
- 20 Rueden CT, Schindelin J, Hiner MC, DeZonia BE, Walter AE, Arena ET, et al. ImageJ2: ImageJ for the next generation of scientific image data. 2017;18(1):529.
- 21 van Manen L, Handgraaf HJM, Diana M, Dijkstra J, Ishizawa T, Vahrmeijer AL, et al. A practical guide for the use of indocvanine green and methylene blue in fluorescence-guided abdominal surgery. J Surg Oncol. 2018;118(2):283-300.
- 22 Gersten KM, Natsuka S, Trinchera M, Petryniak B, Kelly RJ, Hiraiwa N, et al. Molecular cloning, expression, chromosomal assignment, and tissue-specific expression of a murine alpha-(1,3)-fucosyltransferase locus corresponding to the human ELAM-1 ligand fucosyl transferase. J Biol Chem. 1995;270(42):25047-56.
- 23 Tauchi K, Kakudo K, Machimura T, Makuuchi H, Mitomi T. Immunohistochemical studies of blood group-related antigens in human superficial esophageal carcinomas. Cancer. 1991;67(12):3042-50.
- 24 Pour PM, Tempero MM, Takasaki H, Uchida E, Takiyama Y, Burnett DA, et al. Expression of blood group-related antigens ABH, Lewis A, Lewis B, Lewis X, Lewis Y, and CA 19-9 in pancreatic cancer cells in comparison with the patient's blood group type. Cancer Res. 1988;48(19):5422-6.
- 25 Itzkowitz SH, Yuan M, Ferrell LD, Ratcliffe RM, Chung Y-S, Satake K, et al. Cancer-Associated Alterations of Blood Group Antigen Expression in the Human Pancreas2, INCI: Journal of the National Cancer Institute. 1987;79(3):425-34.
- 26 Itzkowitz SH, Yuan M, Fukushi Y, Lee H, Shi ZR, Zurawski V, Jr., et al. Immunohistochemical comparison of Lea, monosialosyl Lea (CA 19-9), and disialosyl Lea antigens in human colorectal and pancreatic tissues. Cancer Res. 1988;48(13):3834-42.
- 27 Schoentag R, Primus FJ, Kuhns W. ABH and Lewis blood group expression in colorectal carcinoma. Cancer Res. 1987;47(6):1695-700.
- 28 Sakamoto S. Watanabe T. Tokumaru T. Takagi H. Nakazato H, Lloyd KO. Expression of Lewisa, Lewisb, Lewisx, Lewisy, siayl-Lewisa, and sialyl-Lewisx blood group antigens in human gastric carcinoma and in normal gastric tissue. Cancer Res. 1989;49(3):745-52.
- 29 Serpa J, Mesquita P, Mendes N, Oliveira C, Almeida R, Santos-Silva F, et al. Expression of Lea in gastric cancer cell

- lines depends on FUT3 expression regulated by promoter methylation. Cancer Lett. 2006;242(2):191-7.
- 30 Itzkowitz SH, Yuan M, Ferrell LD, Palekar A, Kim YS, Cancer-associated alterations of blood group antigen expression in human colorectal polyps. Cancer Res. 1986;46(11):5976-84.
- 31 Blaszczyk M, Pak KY, Herlyn M, Sears HF, Steplewski Z. Characterization of Lewis antigens in normal colon and gastrointestinal adenocarcinomas. Proc Natl Acad Sci U S A. 1985;82(11):3552-6.
- 32 Sawada R, Sun SM, Wu X, Hong F, Ragupathi G, Livingston PO, et al. Human monoclonal antibodies to sialyl-Lewis (CA19.9) with potent CDC, ADCC, and antitumor activity. Clin Cancer Res. 2011;17(5):1024-32.
- 33 Houghton JL, Zeglis BM, Abdel-Atti D, Aggeler R, Sawada R, Agnew BJ, et al. Site-specifically labeled CA19.9-targeted immunoconjugates for the PET, NIRF, and multimodal PET/NIRF imaging of pancreatic cancer. Proc Natl Acad Sci USA. 2015;112(52):15850-5.
- 34 Houghton JL, Abdel-Atti DA, Sawada R, Scholz WW, Lewis IS. Abstract B25: Development of 5B1, an anti-CA19.9 monoclonal antibody, as a near-infrared fluorescent probe for intraoperative imaging of pancreatic cancer. Cancer Research. 2015;75(13 Supplement):B25.
- 35 Ballehaninna UK, Chamberlain RS, Serum CA 19-9 as a Biomarker for Pancreatic Cancer—A Comprehensive Review. Indian journal of surgical oncology. 2011:2(2):88-100.
- 36 Schwenk J, Makovitzky J. Tissue expression of the cancer-associated antigens CA 19-9 and CA-50 in chronic pancreatitis and pancreatic carcinoma. Int J Pancreatol. 1989;5(1):85-98.

## **CHAPTER 7**

Preclinical evaluation of glycantargeting monoclonal antibodies for bimodal near-infrared fluorescence and photoacoustic imaging of gastrointestinal cancers

Ruben D. Houvast, Vincent Q. Sier, Maurice van Duijvenvoorde, Victor M. Baart, Timo Schomann, JiaXin Chua, Mireille Vankemmelbeke, Lindy G. Durrant, Daniëlle Krijgsman, Pieter de Heer, Gert-Jan Hassing, J. Sven D. Mieog, A. Stijn. L. P. Crobach, Jacobus Burggraaf, Peter J.K. Kuppen, Alexander L. Vahrmeijer, Cornelis F.M. Sier

European Journal of Nuclear Medicine and Molecular Imaging Research 2025 Jun 6;15(1):67



#### ABSTRACT

**BACKGROUND** Near-infrared fluorescence (NIRF) imaging assists surgeons intraoperatively to achieve radical resection of malignant tissue with one centimeter depth and can be supplemented with photoacoustic imaging to increase depth-of-view. Tumor-associated carbohydrate antigens are promising targets for tumor imaging with potential advantages over protein targeting. This study preclinically evaluates the anti-glycan tracers CH88.2-800CW (anti-Lea/c/x) and CH129-800CW (anti-sdi-Lea) for bimodal NIRF/PA imaging of gastrointestinal cancers.

**RESULTS** Using immunohistochemistry, we found that  $Le^{a/c/x}$  and sdi- $Le^a$  were highly expressed in gastric and colorectal cancer tissue, with limited expression in healthy surrounding tissue, except for strong  $Le^{a/c/x}$  expression in healthy colorectal epithelium. Bimodal NIRF/PA imaging using CH88.2-800CW and CH129-800CW was performed on subcutaneous and orthotopic HT-29\_luc2 (colon cancer) and BxPC-3\_luc2 (pancreatic cancer) tumor-bearing mice, using rituximab-800CW as a negative control tracer. At 96 hours post-injection, all orthotopic tumors were delineated using the clinical Artemis NIRF imager with mean CH88.2-800CW and CH129-800CW tumor-to-background ratios of  $4.8 \pm 1.4$  and  $4.9 \pm 0.5$  for the HT-29\_luc2 model, and  $2.5 \pm 0.3$  and  $2.9 \pm 0.4$  for the BxPC-3\_luc2 model, respectively. Similarly specific photoacoustic signal was observed within all tumors for both CH88.2-800CW and CH129-800CW. Biodistribution analyses showed high tumor fluorescence with minimal signal in healthy organs, including the liver and kidneys.

**CONCLUSIONS** Bimodal NIRF/PA imaging employing CH88.2-800CW and CH129-800CW facilitates real-time, high-contrast gastrointestinal tumor visualization. Given their strong and mostly tumor-specific expression, both tracers hold promise as effective imaging agents for gastrointestinal cancers, and are compelling candidates for further clinical evaluation.

#### BACKGROUND

Achieving local control through radical surgical resection remains the cornerstone of curative cancer treatment.¹ However, the widespread adoption of non-invasive surgical techniques, such as laparoscopy and robotics, has reduced the surgeon's ability for tumor identification by direct tactile feedback. Fortunately, novel techniques facilitating intraoperative identification of tissues-of-interest have emerged, such as near-infrared fluorescence (NIRF) imaging, also known as fluorescence-guided surgery. This method allows real-time visualization of tissue using a NIRF contrast agent that is visualized through a dedicated camera system.²,³ Its potential in distinguishing malignant tissue from healthy surrounding tissue intraoperatively has been widely demonstrated across various tumor types in both the preclinical and clinical setting.³,⁴

Precise alignment of the NIRF imaging tracer with the tumor type of interest remains a key prerequisite for adequate tumor visualization. As most of the current target-tracer combinations appeared to have their shortcomings, including target expression in healthy surrounding tissues, heterogeneity of target expression and an unsuitable tracer clearance profile, the quest for novel targets continued. Previous work by our group has proposed tumor-associated carbohydrate antigens (TACAs) as an alternative and promising class of tumor-specific targets for NIRF imaging of cancer, with the potential to overcome aforementioned limitations. <sup>5-8</sup>

Aberrant glycosylation of proteins and lipids is a major characteristic of cancer. This results in, among others, the appearance of complex Lewis glycan variants as well as a strong overexpression of Lewis glycans normally expressed in healthy tissue. Most of these TACAs, including sialyl-Lewis<sup>a</sup> (also known as CA19-9) and sialyl-Lewis<sup>x</sup>, play crucial roles in tumor progression, both directly and indirectly by adapting their carrier's configuration. Considering their strong (over)expression in the outmost layer of the cell membrane and on multiple tumor-associated proteins, TACAs possess unique characteristics that make them ideal targets for NIRF imaging. 10-13

Chua and Tivadar et al. described two monoclonal antibodies (mAbs), CH88.2 and CH129, targeting unique sets of Lewis glycan epitopes, Lewisa/c/x (Lea/c/x) and sialyl-di-Lewisa (sdi-Lea), respectively. These targets have been found to be highly-specific for human epithelial cancers, with limited expression in healthy tissue. Our group confirmed the abundance of Lea/c/x (83%) and sdi-Lea (94%) in human pancreatic ductal adenocarcinoma (PDAC) tissue specimens, as well as in tumor-positive lymph nodes and PDAC fine-needle biopsies. Notably, both biomarkers demonstrated significantly lower expression in surrounding healthy

pancreatic tissue and chronic pancreatitis compared to PDAC tissue, establishing both targets as suitable for NIRF imaging.<sup>7,8</sup> In a proof-of-concept *in vivo* study, NIRF imaging using CH88.2-800CW provided high-contrast tumor delineation at 96 hours post-injection in human colon and pancreatic xenograft models using both preclinical and clinical NIRF imagers, thereby establishing the preclinical potential of the tracer for NIRF imaging of cancer.<sup>6</sup>

While NIRF imaging effectively visualizes superficial lesions, its application is less suitable for deeper-located lesions due to the limited penetration depth of NIR light, namely  $\sim 7$  mm. <sup>14</sup> One solution may be augmenting NIRF imaging with another real-time imaging modality, such as photoacoustic (PA) imaging.

PA imaging using ultrasound (US) detects acoustic waves excited by NIRF dyes following exposure with a nanosecond pulsed NIR laser.<sup>15</sup> The technique yields a higher spatial resolution than optical NIRF imaging and allows visualization of tissue up to 7 cm. Bimodal NIRF/PA imaging may synergistically improve tumor detection by supplementing superficial NIRF imaging with the enhanced "depth-of-view" of PA-imaging, using a single tracer administration.<sup>16,17</sup>

Building upon previous work into glycan-targeted tumor imaging, the current study presents the extensive preclinical evaluation of anti-Lewis glycan tracers CH88.2-800CW and its counterpart CH129-800CW for bimodal NIRF/PA imaging of cancer. To accomplish this, expression of their targets, Lea/c/x and sdi-Lea, respectively, is first verified in gastrointestinal malignancies using immunohistochemistry on human tissue specimens of gastric and colorectal cancer, as well ashealthy surrounding tissue. Of note, the abundant and tumor-specific expression of both epitopes in pancreatic cancer has been described elsewhere. Thereafter, binding of CH88.2-800CW and CH129-800CW is evaluated both *in vitro* followed by *in vivo* in human tumor xenograft mouse models.

## **MATERIALS & METHODS**

## Monoclonal antibodies

Anti-Lea/c/x and anti-sdi-Leachimeric mAbs CH88.2 ( $\mathrm{hIgG}_1$ ) and CH129 ( $\mathrm{hIgG}_1$ ) and their murine derivates FG88.2 ( $\mathrm{IgG}_3$ ) and FG129 ( $\mathrm{IgG}_{1k}$ ) were kindly supplied by prof. Lindy Durrant (Scancell Ltd, UK) and produced as described elsewhere. <sup>12,13</sup>

## Conjugation of monoclonal antibodies

CH88.2 and CH129 were covalently conjugated with IRDye 800CW using N-hydroxysuccinimide (NHS)-ester chemistry against primary amino groups until a degree of labeling of 1-1.5 was reached, following the manufacturers protocol (LICOR, Lincoln, NE, Nebraska, USA). Degrees-of-labeling were quantified through

photo spectrophotometry and confirmed using MALDI-TOF analyses. Conjugation results were evaluated using on 4-20% protein gels (Criterion, Bio-Rad laboratories, Veenendaal, The Netherlands). Proteins were stained using Coomassie brilliant blue G-250 (Bio-Rad laboratories). Fluorescence images of the gel were acquired using the Odyssey CLx Infrared Imaging System (LI-COR) with the 800 nm channel.

## Patient selection and specimen selection

Representative formalin-fixed paraffin-embedded tissue blocks of patients diagnosed with gastric (n = 52) or colorectal (n = 36) cancer were obtained. Colorectal and gastric tissue blocks were obtained from the department of Pathology of the Leiden University Medical Center (The Netherlands). Tissue blocks contained tumor tissue and were particularly selected to contain adjacent normal tissue. Clinicopathological data were obtained from the patients' medical records. The research protocol received approval from both the Gastroenterology Biobank Review Committee (protocol reference: 2020-16) and the local Medical Ethical Review Committee (protocol reference: B20.052. The study strictly adhered to the Dutch code of conduct for responsible use of human tissue in medical research. All tissue specimens and associated clinicopathological data were utilized in an anonymized manner and in accordance with the principles outlined in the Declaration of Helsinki (1964).

## Immunohistochemistry

Immunohistochemistry was performed as extensively described elsewhere.<sup>7</sup> Briefly, 4-µm-thick sections were deparaffinized, rehydrated, followed by endogenous peroxidase blocking and antigen retrieval by heating sections in EnVision Flex Target Retrieval Solution (pH 6.0). Sections were incubated overnight with FG88.2 (0.19 µg/ml) or FG129 (0.12 µg/ml) or a pan-cytokeratin-directed antibody (AE1/AE3, Agilent Technologies, Inc., Santa Clara, CA, USA). Slides were incubated with secondary anti-mouse EnVision antibodies (Dako, K4001); staining was visualized using DAB (K3468, Agilent), followed by counterstaining with Mayer's hematoxylin solution and drying. Histological reference slides were stained with Mayer's hematoxylin solution and counterstained with eosin. All slides were mounted with Pertex, digitized using the panoramic digital slide scanner and analyzed using CaseViewer 2.4 (both 3D Histech, Budapest, Hungary).

## **Evaluation of immunohistochemical staining**

Immunohistochemical membranous staining on malignant and healthy tissue was quantified using the total immunostaining score (TIS), which is calculated by multiplying the staining proportion ( $0 \le 9\%$ , 1 = 10 - 25%, 2 = 26 - 50%, 3 = 51 - 75%, 4 = 276%)

by the staining intensity (o = none, 1 = weak, 2 = moderate, 3 = strong). A categorical TIS was constituted as follows: o = negative; 1, 2, 3, 4 = weak expression; 6, 8 = moderate expression; 9, 12 = strong expression. Scoring was performed by three independent observers (RH, MvD. and ASLPC). Samples without agreement were discussed in a consensus meeting, in which the final score was determined.

#### Human cancer cell lines

Cell lines HT-29\_luc2, COLO-320, COLO 205, DLD-1 (colon carcinoma), PANC-1, and MIA PaCa-2 (pancreatic carcinoma) were obtained from ATCC, while BxPC-3\_luc2 was purchased from PerkinElmer (Waltham, MA, USA). HT-29, DLD-1, COLO-320 COLO-205, and BxPC-3(\_luc2) cells were cultured in RPMI 1640 cell culture medium (Gibco, Invitrogen, Carlsbad, CA, USA). PANC-1 and MIA Paca-2 were cultured in DMEM + GlutaMAX™ cell culture medium (Gibco, Invitrogen). The absence of Mycoplasma contamination was confirmed using polymerase chain reaction (PCR) analysis. Cell cultures were maintained in a humidified incubator set at 37°C with 5% CO2, and upon reaching 90% confluence, cells were detached using trypsin/EDTA (0.5% Trypsin-EDTA solution 10×, obtained from Santa Cruz Biotechnology, Inc, Dallas, TX, USA). Viability assessments were conducted using trypan blue staining in a 0.4% solution (Invitrogen).

## Cell-based plate assay

Binding of CH88.2-800CW and CH129-800CW was evaluated on colon carcinoma cell lines HT-29\_luc2, COLO-320, COLO 205, DLD-1 and pancreatic cancer cell lines BxPC-3\_luc2, PANC-1, and MIA PaCa-2 using cell-based plate assays. Cells were cultivated in a 96-well plate at a density of 20,000 cells per well in 100 µl of complete medium (Corning Costar Inc., Cambridge, MA, USA), until reaching 90% confluence. Subsequently, the cells were washed twice with PBS supplemented with 0.5% bovine serum albumin (0.5% PBSA). To assess CH88.2-800CW and CH129-800CW binding, cells were exposed to CH88.2-800CW or CH129-800CW in PBS at concentrations of 3, 6, 12, 25 50, or 100 nM, for 1 hour, on ice and shielded from light. Following incubation, the cells were rinsed twice with 0.5% PBSA to eliminate any unbound tracer. The fluorescence emitted by CH88.2or CH129-800CW was assessed using the Odyssey CLx Infrared Imaging System (LI-COR) with the 800 nm channel (excitation 785 nm, emission filter 812-823) nm). To estimate cell numbers through nuclear fluorescence, cells were permeabilized using 40-60% acetone-methanol for 5 minutes, washed, and then treated with ToPro-3 iodide (1:2000, T3605, Invitrogen, California, USA) for 10 minutes at room temperature. After another washing step, nuclear fluorescence was quantified using the 700 nm channel of the Odyssey (excitation 685 nm, emission filter 710–730 nm). The mean fluorescence intensity (MFI) was computed by dividing the 800-nm fluorescence signal by the nuclear 700-nm signal. All experiments were conducted in triplicate.

## Chamber slides

Following detachment and viability assessment, cells were transferred to an 8-well Nunc™ Lab-Tek™ II Chamber Slide (0.7 cm2/well, Thermo Fisher Scientific) at a density of 40,000 cells per well. Upon achieving 90% confluence, the cell culture medium was aspirated, and the cells underwent two 5-minute washing steps with PBS. Subsequently, cells were fixed using 1% paraformaldehyde at room temperature for 10 minutes, followed by two 5-minute washes with PBS. The cells were then exposed to CH88.2-800CW, CH129-800CW or negative control tracer rituximab (anti-CD20)-800CW on ice (50 nM), shielded from light, for 1 hour, after which they were washed with PBS and demineralized water. The plastic chambers were removed, and the slides were air-dried before staining with ProLong Gold containing DAPI (Thermo Fisher Scientific). Imaging of the slides was performed using the DAPI channel (excitation 376–398 nm, emission filter 417–477 nm) and the Cy7 channel (excitation 773-758 nm, emission filter 776-826 nm) of the Axio Scan Z1 (Carl Zeiss AG, Oberkochen, Germany). Image analysis was performed using Zen Lite software (version 3.5, Zeiss). All experiments were conducted in triplicate.

## Animal models

Mice were housed at the Central Animal Facility of the LUMC, where they were maintained according to EU Recommendation 2007-526-EC guidelines under specific pathogen-free conditions All animal procedures strictly adhered to local standard operating procedures. Female BALB/c-Nude (CAnN.Cg- $Foxn1^{nu}$ /Crl) mice, aged between six to eight weeks, were procured from Charles River Laboratories, Wilmington, MA, USA. For subcutaneous models, mice were subcutaneously injected at four locations on their backs with either HT-29\_luc2 or BxPC-3\_luc2 cells (500,000 cells/spot; n = 3 mice per group). Tumor growth was monitored using a digital caliper, and tumors reaching a volume of 50 mm³ were considered suitable for imaging. Orthotopic HT-29\_luc2 and BxPC-3\_luc2 models were induced as described elsewhere  $^{19}$ .  $^{20}$  Briefly, HT-29\_luc2 tumors were subcutaneously grown, resected, fragmented and kept on ice. After performing a

midline incision, the HT-29\_luc2 fragment was attached to the cecum wall using a 6-o Ethilon suture. For the BxPC-3 model, a left lateral flank incision was performed, after which 500,000 BxPC-3\_luc2 cells (resuspended in 50 μl PBS) were injected into the body of the pancreas. Orthotopic tumors were grown for approximately two weeks and growth was monitored by bioluminescence imaging using the IVIS® Spectrum Preclinical *In Vivo* Imaging System (Spectrum, PerkinElmer, MA, USA). At the end of the experiments, mice were sacrificed using CO<sub>2</sub>. The animal studies underwent thorough review and approval by the local animal welfare body at the LUMC. Animals were cared for in accordance with the Code of Practice Animal Experiments in Cancer Research and guidelines from Directive 2010/63/EU of the European Parliament on the protection of animals used for scientific purposes. The handling of animals adhered to established local standard operating procedures.

#### In vivo NIRF imaging

Once subcutaneous tumors reached a volume of around 50 mm,3 mice were administered either 1 nmol of CH88.2-800CW, CH129-800CW or rituximab-800CW dissolved in PBS via tail vein injection. In the case of orthotopic tumors, tumors emitting a bioluminescence signal exceeding 1.0  $\times$  108 p/sec/cm<sup>2</sup>/sr were deemed appropriate for imaging. Imaging sessions for subcutaneous tumor-bearing mice were conducted at intervals of 4, 24, 48, 72, 96, 120, 144 and 168 hours post-injection. The optimal imaging time point for the orthotopic mice was determined based on the subcutaneous tumor-bearing mice. Both preclinical imaging with the Pearl Trilogy Small Animal Imaging System (LI-COR, 800 nm channel; excitation 785 nm, emission filter 820 nm) and clinical imaging using the Artemis NIR Imaging system (Quest Medical Imaging b.v., Wieringerwerf, The Netherlands; excitation 780 nm, emission filter 805 nm) were employed for all imaging procedures. During imaging, mice were maintained under 2-4% isoflurane anesthesia. After the final measurement, mice were euthanized, and tumors and/or organs were excised for imaging using the Pearl imaging system. Tumor and background MFIs were computed by drawing regions of interest (ROIs) over the tumor area and adjacent normal tissue. These values were then included as individual data points for analysis. Image analysis was conducted using Image Studio (version 5.2, LI-COR) for Pearl images and Spectrum Capture Suite (Quest Medical Imaging b.v.) along with ImageI (version 1.50, National Institutes of Health, Bethesda, MD, USA) for Quest images. Tumor-to-background ratios (TBRs) were determined by the formula:  $TBR = MFI_{tumor}/MFI_{background}$ . For biodistribution analysis, organ MFIs were calculated by drawing a region of interest (ROIs) over the resected organ areas.

#### In vivo PA imaging

PA imaging was conducted 96 hours following the injection using the Vevo 3100 Imaging System (FUJIFILM VisualSonics, Canada), following previously established protocols [33]. The imaging setup consisted of the Vevo LAZR-X cart, Vevo LAZRTight Enclosure, and Vevo Imaging Station. Mice were anesthetized and positioned on a prewarmed imaging table. The MX550D transducer from FUJIFILM VisualSonics was employed for both US and PA imaging (frequency range: 25–55 MHz; axial resolution: 40 µm; excitation at 780 nm). Subsequent image analysis was performed using Vevo LAB software (version: 5.5.o, FUJIFILM, VisualSonics).

#### Histological analysis of resected tumor tissue

Resected tumors were fixed overnight in 4% paraformaldehyde and subsequently dehydrated using ethanol. Afterwards, the tumor tissues were embedded in paraffin. Four-µm-thick formalin-fixed paraffin-embedded tissue sections were deparaffinized in xylene for 15 min, after which fluorescence imaging was performed using the Odyssey CLx Infrared Imaging System on the 800 nm channel. For immunofluorescence, slides were stained with ProLong Gold containing DAPI. Imaging of the slides was performed using the DAPI channel and the Cy7 channel of the Axio Scan Z1, as described before.

## Statistical analysis

GraphPad Prism (version 9.3.1, GraphPad Software Inc., La Jolla, CA, USA) was used for statistical computations and the creation of graphs. IBM SPSS statistics version 29 (IBM Corporation, Armonk, NY, USA) was employed for all statistical analyses of patient characteristics, using a Chi-square test for categorical data, an unpaired t-test for normally distributed data, or the Mann–Whitney U test for nonparametric data. Differences between median TIS values on tumor and healthy tissue were compared using a Mann-Whitney U test. Differences between TBRs at different time points were compared using two-way ANOVA with Šídák correction for multiple comparisons. Differences with a p-value smaller than 0.05 were regarded as significant (ns: not significant. \*:  $p \le 0.001$ , \*\*\*:  $p \le 0.001$ , \*\*\*:  $p \le 0.001$ , \*\*\*:  $p \le 0.001$ .

#### RESULTS

# $Le^{a/c/x}$ and $sdi-Le^a$ expression in malignant and healthy gastric and colorectal tissue

Tissue specimens of fifty-two gastric cancer and thirty-six colorectal cancer patients were obtained. Patient characteristics are summarized in Table 1 and 2 of the Electronic Supplementary Materials (ESM). In total, tumor/healthy surrounding

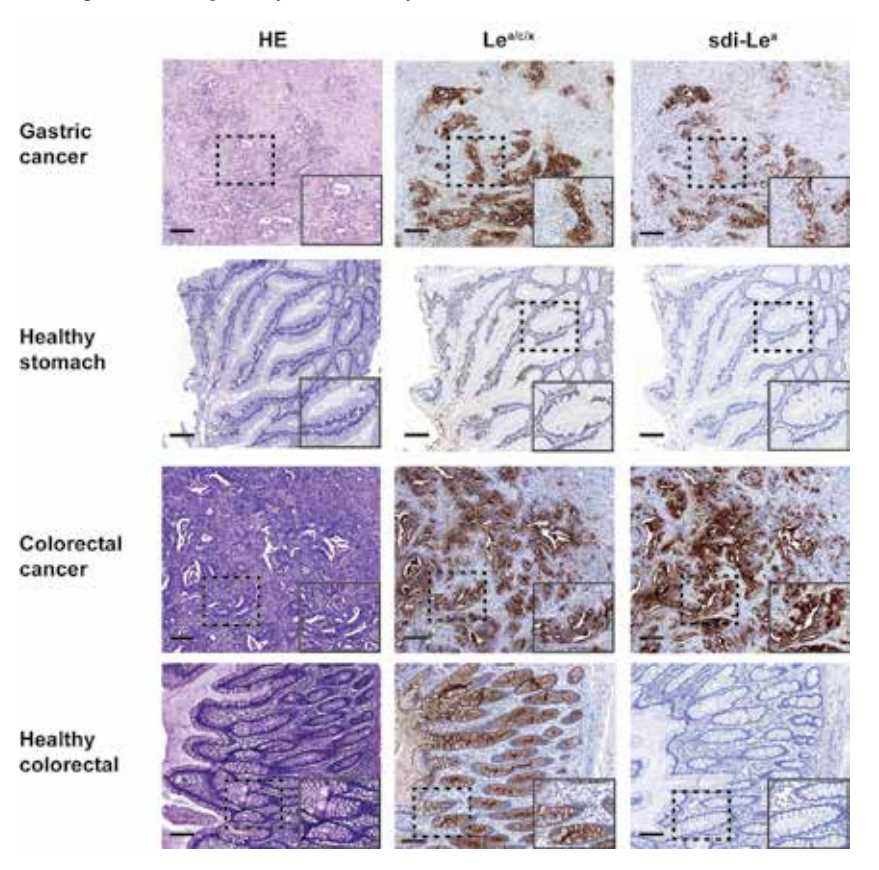
tissue specimens of 35/31 colorectal cancer and 52/43 gastric cancer patients were included for analysis. To evaluate the suitability of CH88.2 and CH129 as targeting moieties for NIRF imaging, the cohort of malignant and healthy tissue specimens was stained for Lea/c/x and sdi-Lea expression (Figure 1) using their (mouse antihuman) counterparts FG88.2 and FG129, respectively. Positive Lea/c/x expression in gastric and colorectal cancer tissue specimens was observed in 81% and 83% of cases, respectively (Table 1). Positive sdi-Le<sup>a</sup> expression was found in 61% and 66% of gastric and colorectal cancer cases, respectively. Staining was mostly located on the cell membrane and showed a relatively homogenous staining distribution throughout the tumor, while some tissue slides showed a more heterogenous staining distribution. Categorized staining distributions on both malignant and healthy gastric and colorectal tissue are also shown in Table 1. Positive staining on tumor tissue specimens was predominantly strong for both biomarkers. While sdi-Lea expression on healthy surrounding tissue specimens was – if present – mostly weak, Lea/c/x expression on healthy surrounding tissue specimens was stronger, especially on healthy surrounding colorectal tissue. As shown in Table 2 and Figure 2, median biomarker staining, as expressed by the TIS, was significantly higher in tumor tissue compared to healthy surrounding tissue for all tumor types and both biomarkers. One exception was Lea/c/x expression in colorectal tissue specimens, which was significantly higher in healthy surrounding colorectal tissue compared to tumor tissue (9.0 vs. 6.0, p = 0.0021).

#### In vitro binding of CH88.2-800CW and CH129-800CW

CH88.2 and CH129 were successfully conjugated to IRDye 8ooCW (see Figure 1 of the ESM). CH88.2-8ooCW and CH129-8ooCW binding was evaluated on a set of colon and pancreatic cancer cell lines using cell-based plate assays, considering their antigens' presence on these human cancers. These tumor types were selected based on the abundant Le<sup>a/c/x</sup> and sdi-Le<sup>a</sup> expression in human tissue, allowing assessment of tracer binding across several relevant gastrointestinal malignancies. As shown in Figure 3A-B, a concentration-dependent MFI increase was observed for both CH88.2-8ooCW and CH129-8ooCW on human colon adenocarcinoma cell line HT-29, as well as human pancreatic adenocarcinoma cell line BxPC-3, which was not observed for the remaining tumor cell lines. Comparison of absolute MFIs for CH88.2-8ooCW showed higher MFIs on HT-29 compared to BxPC-3, while for CH129-8ooCW MFIs were higher on BxPC-3 compared to HT-29 cells. HT-29 and BxPC-3 were selected as suitable cell lines for further *in vivo* evaluation with varying CH88.2 and CH129 binding levels. To confirm binding (localization) of CH88.2-8ooCW and CH129-8ooCW, immunofluorescence using

cell-based chamber slides was performed which showed presence of both tracers on the membrane of HT-29 and BxPC-3 cells (Figure 3C). In contrast, no binding of CH88.2-800CW and CH129-800CW was observed to COLO-320 and PANC-1, which was in line with the cell-based plate assay experiment that showed no MFI increase for these cell lines. Lastly, binding of negative control tracer rituximab-800CW to BxPC-3, HT-29, COLO-320 and PANC-1 cell lines was evaluated and was not observed, thereby establishing rituximab-800CW as a suitable negative control tracer for *in vivo* experiments.

**FIGURE 1** Representative images of HE and immunohistochemical expression of Le<sup>a/c/x</sup> and sdi-Le<sup>a</sup>on malignant and healthy surrounding gastric and colorectal tissue using mAbs FG88.2 and FG129, respectively. Scale bars represent 200  $\mu$ M. Overview images and inserts are taken at 5× and 20× magnification, respectively. HE: hematoxylin-eosin.



#### In vivo binding specificity of CH88.2-800CW and CH129-800CW

To evaluate binding specificity and establish the optimal imaging time point of CH88.2-800CW and CH129-800CW, mice were intravenously injected with 1 nmol of tracer and imaged for 168 hours. For the subcutaneous HT-29\_luc2 model, TBRs of >2.0 were observed from 24 hours post-injection onward for both CH88.2-800CW and CH129-800CW, which continued to increase until 168 hours post-injection (Figure 4A), albeit at the cost of lower tumor MFIs (see Figure 2 of the ESM). From 48 hours and 72 hours onward, significantly higher TBRs were observed for CH88.2-800CW and CH129-800CW, respectively, compared to ritux-imab-800CW, indicating specificity of both glycan-binding tracers.

These *in vivo* results where verified in a BxPC-3\_luc2 model, in which slightly lower TBRs were observed at all time points. From 72 and 48 hours post-injection onward, respectively, TBRs for CH88.2-800CW and CH129-800CW, were significantly higher than those of rituximab-800CW, again indicating target specificity of CH88.2-800CW and CH129-800CW (Figure 4B).

Considering the presence of a sufficiently high TBR as well as tumor MFI to allow clear tumor visualization, 96 hours post-injection was established as the optimal imaging time point for both tracers. At this imaging time point, mean TBRs of  $5.3 \pm 0.8$  and  $3.5 \pm 0.8$  were observed for the subcutaneous HT-29\_luc2 model using CH88.2-800CW and CH129-800CW, respectively, both allowing clear tumor visualization and delineation (CH88.2-800CW vs. rituximab-800CW: 95% CI 1.9; 5.2; p < 0.0001; CH129-800CW vs. rituximab-800CW: 95% CI 0.4; 3.2; p = 0.005) (Figure 4A-C). For the subcutaneous BxPC-3 model, mean TBRs of  $2.2 \pm 0.3$  and  $2.3 \pm 0.3$  were observed for CH88.2-800CW and CH129-800CW, respectively, which also allowed clear tumor visualization (CH88.2-800CW vs. rituximab-800CW: 95% CI 0.2; 0.8; p = 0.0005; CH129-800CW vs. rituximab-800CW: 95% CI 0.4; 0.9; p < 0.0001) (Figure 4A-C).

TABLE 1 Distribution of  $Le^{a/c/x}$  and sdi-Leaexpression levels on gastric and colorectal cancer tissue as well as healthy surrounding tissue, as expressed by the TIS values categorized into negative (TIS = 0), weak (TIS = 1, 2, 3, 4) moderate (TIS = 6, 8) or strong expression (TIS = 9, 12).

		n =	Biomarker	Negative n (%)	Weak n (%)	Moderate n (%)	Strong n (%)
Gastric	Tumor -	52	Lea/c/x	10 (19)	9 (17)	5 (10)	28 (54)
		51	sdi-Le <sup>a</sup>	20 (39)	6 (12)	11 (22)	14 (27)
	Healthy -	43	Le <sup>a/c/x</sup>	26 (61)	4 (9)	3 (7)	10 (23)
		41	sdi-Le <sup>a</sup>	33 (81)	7 (17)	0 (0)	1(2)
Colorectal	Tumor -	35	Lea/c/x	6 (17)	8 (23)	8 (23)	13 (37)
		35	sdi-Le <sup>a</sup>	12 (34)	15 (43)	5 (14)	3 (9)
	Healthy -	31	Le <sup>a/c/x</sup>	3 (10)	0 (0)	8 (26)	20 (65)
		30	sdi-Le <sup>a</sup>	29 (97)	1 (3)	0 (0)	0 (0)

**FIGURE 2** Box plots representing TIS values of Lea/c/x and sdi-Leaexpression on gastric and colorectal cancer as well as healthy surrounding tissue. Horizontal lines represent the median TIS, boxes represent interquartile range and brackets represent total TIS range. ns: not significant, TIS: tumor intensity score. \*:  $p \le 0.05$ , \*\*:  $p \le 0.01$ , \*\*\*:  $p \le 0.001$ , \*\*\*:  $p \le 0.001$ .

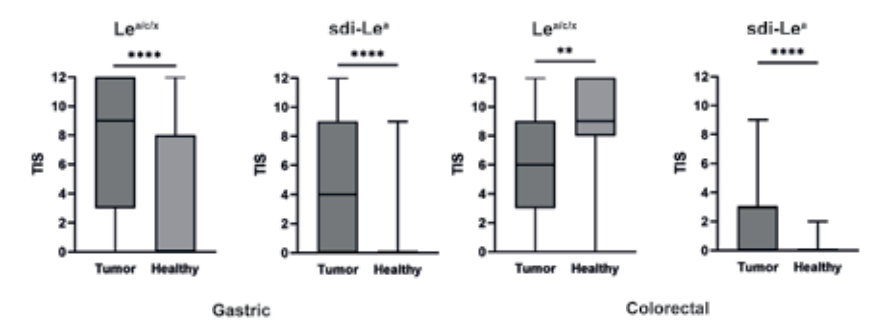


**TABLE 2** Comparison of quantified expression of  $Le^{a/c/x}$  and  $sdi-Le^a$  on gastric and colorectal cancer tissue vs. healthy surrounding tissue as expressed by the median TIS values, as well as their corresponding p-values.

		Le <sup>a/c/x</sup>				sdi-Le <sup>a</sup>		
Tumor type	Tissue	n =	Median (IQR)	<i>p</i> -value	n =	Median (IQR)	<i>p</i> -value	
Castria	Tumor	52	9.0 (9.0)	< 0.0001	51	4.0 (9.0)	<0.0001	
Gastric -	Healthy	43	0.0 (8.0)		41	0.0 (0.0)		
Calamatal	Tumor	35	6.0 (6.0)	0.0021	35	3.0 (3.0)	<0.0001	
Colorectal -	Healthy	31	9.0 (4.0)		30	0.0 (0.0)		

IQR: interquartile range

FIGURE 3 *In vitro* binding of CH88.2-8ooCW and CH129-8ooCW to colon and pancreatic cancer cell lines. (A) Binding of CH88.2-8ooCW and CH129-8ooCW to colon cancer cell lines HT-29 (red), COLO-320 (blue), COLO-205 (green) and DLD-1 (yellow) at increasing concentrations using cell-based plate assays. (B) Binding of CH88.2-8ooCW and CH129-8ooCW to pancreatic cancer cell lines BxPC-3 (red), PANC-1 (blue) and MIA PaCa-2 (green) at increasing concentrations using cell-based plate assays. (C) Immunofluorescence analysis of CH88.2-8ooCW, CH129-8ooCW and rituximab-8ooCW binding to BxPC-3, HT-29, COLO-320 and PANC-1 using cell-based chamber slides. The 8ooCW signal is displayed in red and represents tracer localization. Nuclei are stained using DAPI and are displayed in blue. All experiments were performed in triplicate. a.u.: arbitrary units, MFI: mean fluorescence intensity.

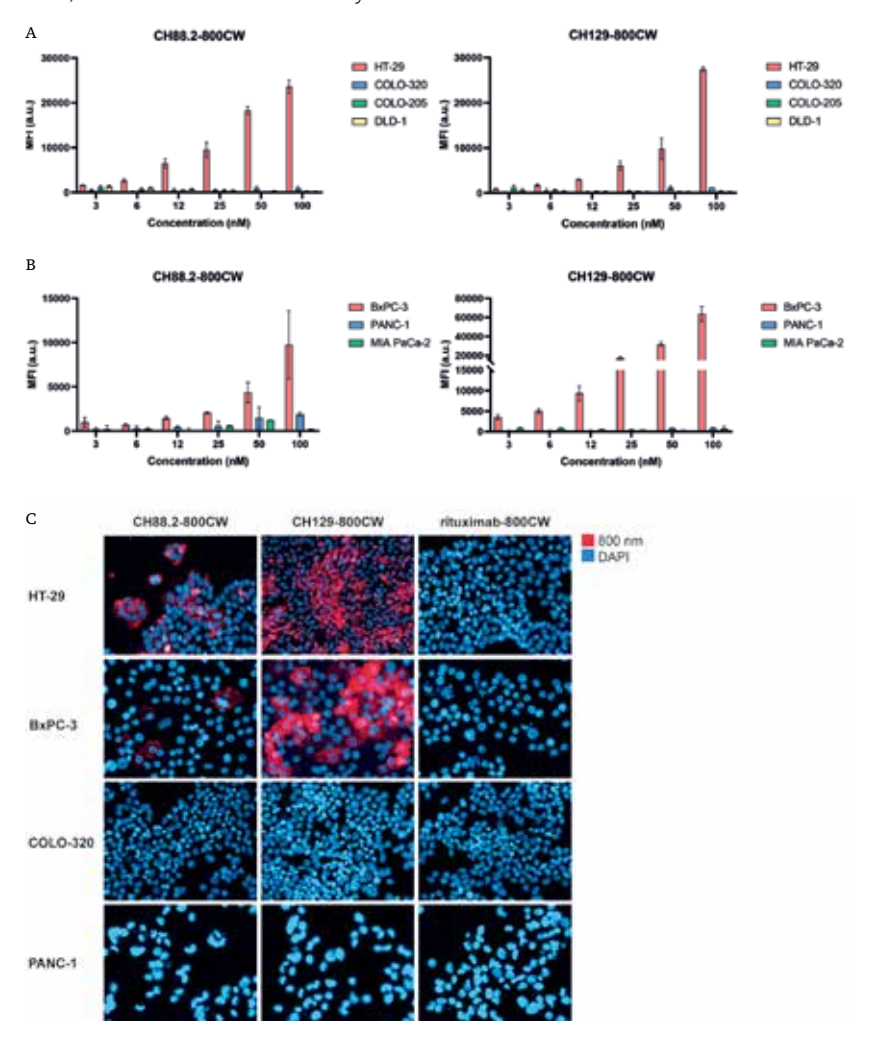
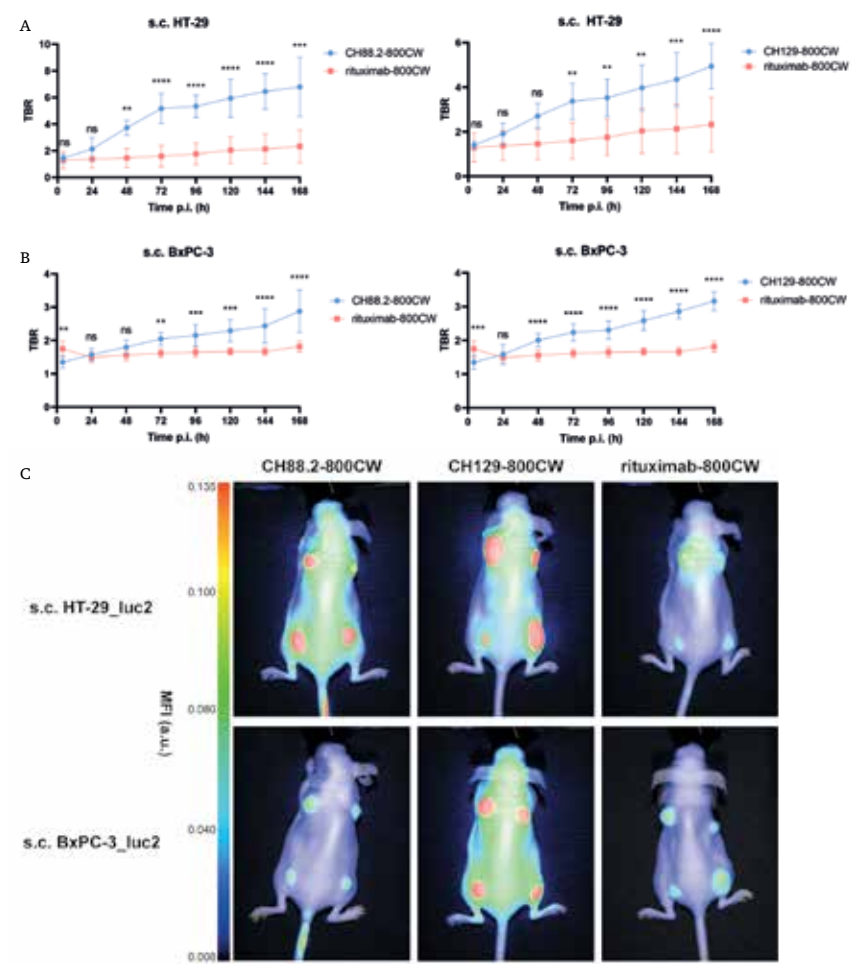


FIGURE 4 In vivo evaluation of CH88.2-8ooCW and CH129-8ooCW using subcutaneous HT-29\_luc2 and BxPC-3\_luc2 tumor-bearing mice. (A) Mean TBRs as a function of time after injection of 1 nmol CH88.2-8ooCW, CH129-8ooCW or rituximab-8ooCW to subcutaneous HT-29\_luc2 tumor-bearing mice (n=3/group). (B) Mean TBRs as a function of time post-injection of 1 nmol CH88.2-8ooCW, CH129-8ooCW or rituximab-8ooCW to subcutaneous BxPC-3\_luc2 tumor-bearing mice (n=3/group). Means are represented by the horizontal line, while error bars represent standard deviations (C) NIRF heatmap-color merge images of subcutaneous HT-29\_luc2 and BxPC-3\_luc2 tumor-bearing mice taken at 96 hours post-injection of 1 nmol CH88.2-8ooCW, CH129-8ooCW or rituximab-8ooCW (n=3/group). Images were captured using the preclinical Pearl NIRF imager and each mouse bears four tumors. MFI: mean fluorescence intensity, ns: not significant, p.i.: post-injection, s.c.: subcutaneous, TBR: tumor-to-background ratio \*\*p<0.01, \*\*\*p<0.001, \*\*\*p<0.0001.



#### In vivo NIRF imaging potential of CH88.2-800CW and CH129-800CW

The NIRF imaging potential of CH88.2-800CW and CH129-800CW was evaluated in a clinically more relevant setting using orthotopic colon and pancreatic models. At 96 hours post-injection of 1 nmol of each tracer, orthotopic HT-29\_luc2 and BxPC-3\_luc2 could be clearly delineated with high contrast using both tracers and the clinical Artemis NIRF imager (Figure 5A-B). For the HT-29\_luc2 model, mean TBRs of 4.8  $\pm$  1.4 and 4.9  $\pm$  0.5 were observed for CH88.2-800CW and CH129-800CW, respectively. For the BxPC-3\_luc2, CH88.2-800CW and CH129-800CW TBRs were 2.5  $\pm$  0.3 and 2.9  $\pm$  0.4, respectively (Figure 5C). This establishes both tracers as suitable for visualization of both higher and lower Lea/c/x and sdi-Lea-expressing tumors.

## In vivo PA imaging potential of CH88.2-800CW and CH129-800CW

The bimodal NIRF/PA imaging potential of CH88.2-8ooCW and CH129-8ooCW was evaluated in orthotopic HT-29\_luc2 and BxPC-3\_luc2 tumor-bearing mice at 96 hours post-injection of 1 nmol of CH88.2-8ooCW or CH129-8ooCW. As shown in Figure 5D, strong PA signal is observed within all tumor ultrasound ROIs for both CH88.2-8ooCW and CH129-8ooCW and both tumor types while PA signal in adjacent tissue is lower, thus allowing tumor-specific PA imaging.

## Biodistribution and histological analysis

Following NIRF/PA imaging, biodistribution of CH88.2-8ooCW and CH129-8ooCW was evaluated by resecting tumors and organs at 96 hours post-injection followed by NIRF imaging. NIRF images of resected tumors and organs for both tracers and tumor types are shown in Figure 6A. Macroscopic fluorescence allowed clear HT-29\_luc2 and BxPC-3\_luc2 identification using both tracers. For both CH88.2-8ooCW and CH129-8ooCW, tumor MFIs were higher compared to fluorescence signal in all remaining organs, including the liver and kidneys (Figure 6A-B).

Histological analysis showed largely overlapping fluorescence with tumor tissue, as well as cytokeratin and FG88.2 or FG129 staining, thereby confirming binding specificity and complete tumor penetration after injection of CH88.2-800CW and CH129-800CW (Figure 7A). While HT-29\_luc2 tumors showed homogenous fluorescence for both tracers, CH88.2-800CW and CH129-800CW fluorescence was more heterogenous in BxPC3\_luc2 tumors. As shown in Figure 7B, immunofluorescence of resected HT-29\_luc2 and BxPC3-luc2 tumors showed membranous localization of CH88.2-800CW and CH129-800CW, thereby confirming specific binding of both NIRF tracers to tumor cells.

FIGURE 5 In vivo evaluation of CH88.2-800CW and CH129-800CW in orthotopic HT-29\_luc2 and BxPC-3\_luc2 tumor-bearing mice. (A) NIRF heatmap-color merge images of orthotopic HT-29\_luc2 tumor-bearing mice taken at 96 hours post-injection of 1 nmol CH88.2-800CW and CH129-800CW. (B) NIRF heatmap-color merge images of orthotopic BxPC-3\_luc2 tumor-bearing mice taken at 96 hours post-injection of 1 nmol CH88.2-800CW and CH129-800CW. Images were captured using the clinical Artemis NIRF imager using an exposure time of 150 ms, allowing real-time imaging. 'T' indicates the tumor location, while 'Cae' indicates healthy cecal tissue, and 'Pan' indicates healthy pancreatic tissue. (C) TBRs of orthotopic HT-29\_luc2 and BxPC-3\_luc2 tumors after injection of 1 nmol of CH88.2-800CW or CH129-800CW. Means are represented by the horizontal line, while error bars represent standard deviations. (D) Representative photoacoustic and ultrasound overlay of orthotopic HT-29\_luc2 and BxPC-3\_luc2 tumors at 96 hours post-injection of 1 nmol of CH88.2-800CW or CH129-800CW. Macroscopically identified tumors are delineated using the green line. Images were captured using a penetration depth of approximately 1.5 cm. NIRF: near-infrared fluorescence, o.t.: orthotopic, TBR: tumor-to-background ratio.

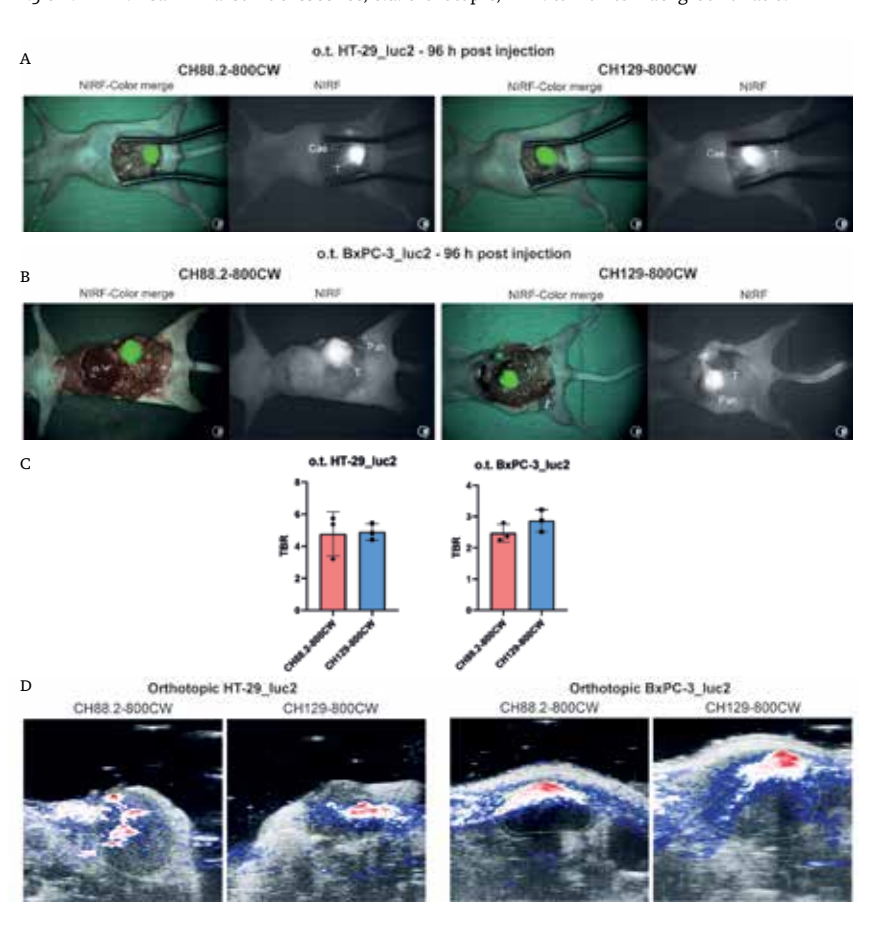


FIGURE 6 Biodistribution of CH88.2-8ooCW and CH129-8ooCW. (A) Macroscopic fluorescence images showing biodistribution in resected orthotopic HT-29\_luc2 and BxPC-3\_luc2 tumors, and healthy organs at 96 hours post-injection of 1 nmol of CH88.2-8ooCW and CH129-8ooCW. Lu: lung, Ht: heart, Pa: pancreas, Sp: spleen, St: stomach, Int: small intestine, "Ce" cecum, Re: rectum, Mu: muscle, Br: brain, Sk: skin, Li: liver, Ki: kidneys, Tu: tumor. Images were captured using the preclinical Pearl NIRF imager. (B) Mean MFIs in resected orthotopic HT-29\_luc2 and BxPC-3\_luc2 tumors, and healthy organs at 96 hours post-injection of 1 nmol of CH88.2-8ooCW and CH129-8ooCW along with their standard deviations. a.u.: arbitrary units, MFI: mean fluorescence intensity, o.t.: orthotopic.

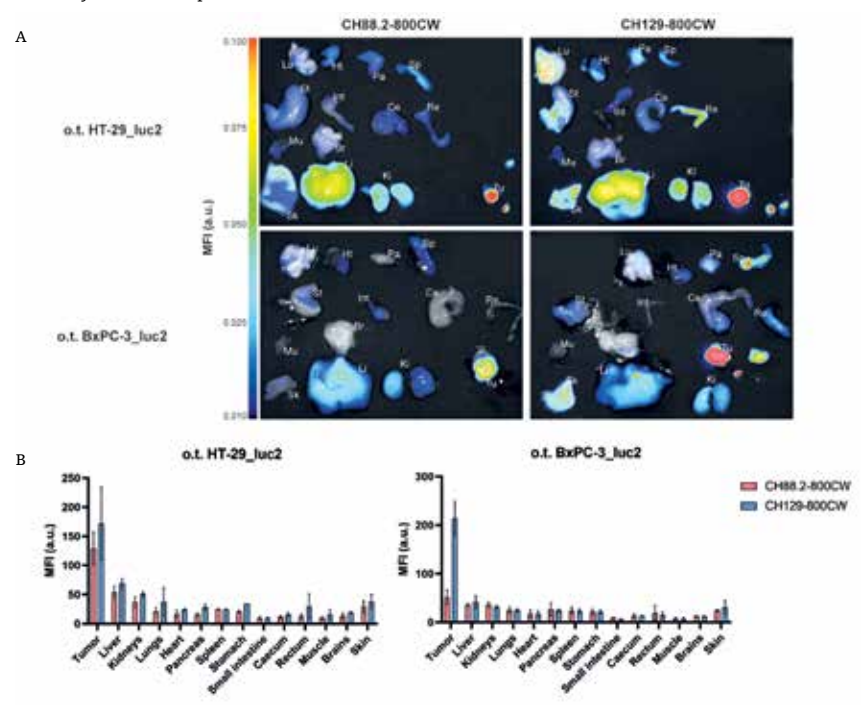
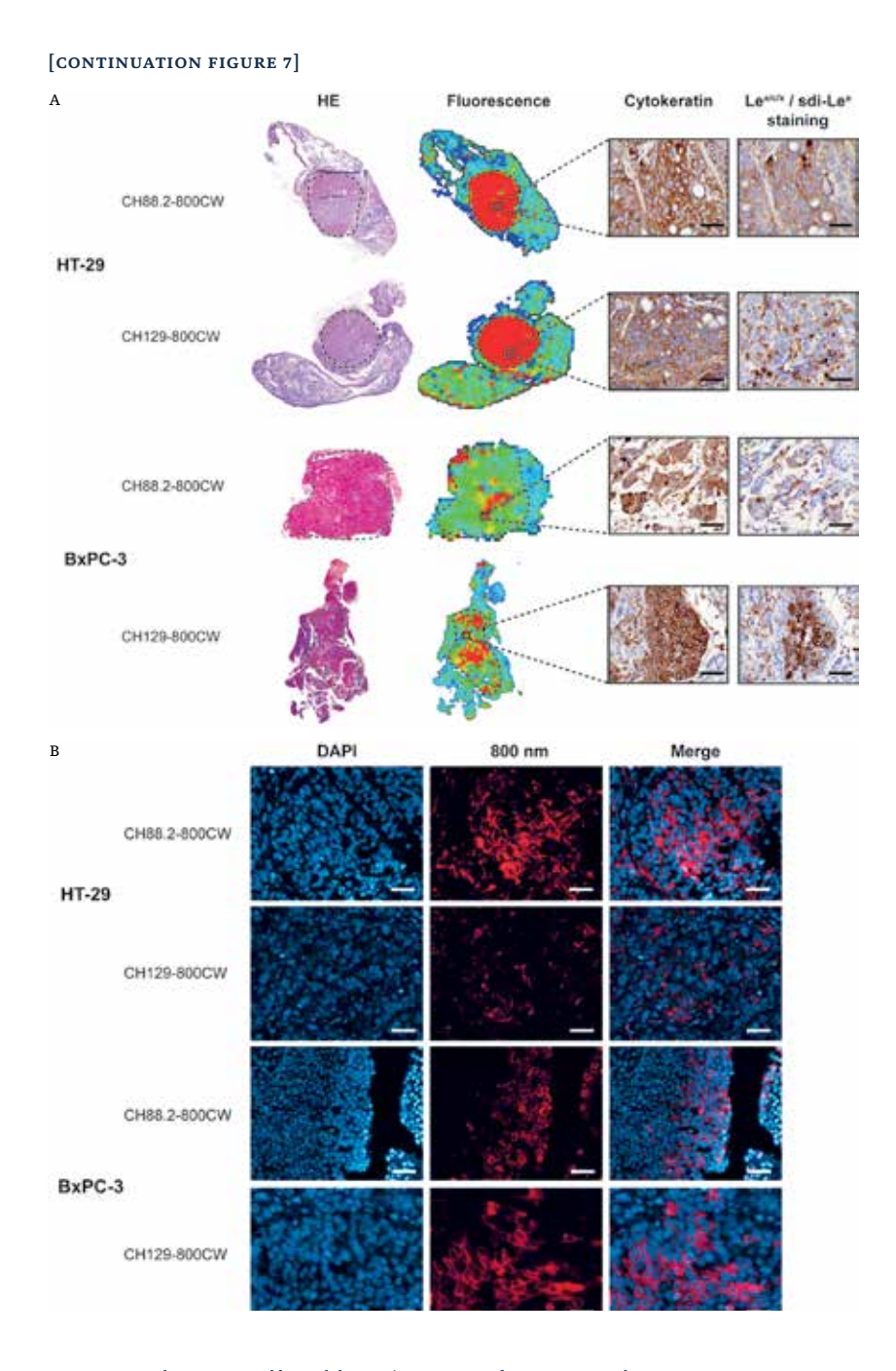


FIGURE 7 Histological analysis of CH88.2-8ooCW and CH129-8ooCW. (A) HE images, NIRF and merged HE-NIRF images, as well as cytokeratin and Lea/c/x or sdi-Lea expression on resected orthotopic HT-29\_luc2 or BxPC-3\_luc2 tumors. Images are taken at 2o× magnification and scale bars represent 50  $\mu$ M. Tumors are delineated using dashed black lines. (B) Microscopic fluorescence images of resected HT-29\_luc2 and BxPC-3\_luc2 96 hours after injection 1 nmol of CH88.2-8ooCW or CH129-8ooCW. Nuclei are stained using DAPI and are displayed in blue. The 8ooCW signal is displayed in red and represents tracer localization and shows a membranous staining pattern. Scale bars represent 25  $\mu$ M. HE: hematoxylin-eosin.



#### DISCUSSION

This study showed that  $Le^{a/c/x}$  and  $sdi-Le^a$ -binding tracers CH88.2-8ooCW and CH129-8ooCW allow high-contrast visualization of tumors using bimodal NIRF/PA imaging at 96 hours post-injection using the clinical Artemis NIRF imager, with low fluorescence signal in healthy surrounding organs. Considering the high and mostly tumor-specific expression of  $Le^{a/c/x}$  and  $sdi-Le^a$  across colorectal and pancreatic cancer, both tracers could be employed for real-time intraoperative imaging for the majority of gastrointestinal cancer patients. $^{7,12,13}$ 

This study built upon the previously published proof-of-concept evaluation of Lea/c/x-specific CH88.2-800CW for NIRF imaging and additionally described the potential of sdi-Lea-specific CH129-800CW, as well as provided an extended immunohistochemical evaluation of their target's expression. 6 Lea/c/x was abundantly expressed in gastric and colorectal cancer tissue, with (mostly) weak expression in healthy surrounding tissue. Noteworthy, as Lea/c/x expression in healthy surrounding colorectal epithelia was higher compared to its malignant counterparts, CH88.2-800CW may be a less suitable tracer for NIRF/PA imaging of colorectal cancer. sdi-Lea, however, showed slightly lower expression in colorectal and gastric cancer tissues, but, more importantly, substantially lower expression in healthy surrounding tissue compared to Lea/c/x, thus classifying this target as more tumor-specific. Therefore, CH129 may provide higher NIRF imaging contrast in vivo, although its target sdi-Lea is expressed in fewer patients compared to CH88.2. These immunohistochemical data are consistent with previous immunohistochemical analyses of Lea/c/x and sdi-Lea expression in tumor and healthy surrounding tissue specimens. 12,13 Although we focused on gastrointestinal cancers, the findings of this study might be extrapolated to other tumor types that expresses Lea/c/x and sdi-Lea glycan epitopes. Notably, the presence of both targets on roughly 20 - 30% of non-small cell lung cancer and ovarian cancer with limited staining on normal surrounding tissue, has been reported, thereby extending the potential application of both tracers beyond gastrointestinal cancers. 12,13

The *in vivo* findings of this study were also consistent with those obtained in the previously published CH88-2-800CW pilot, in which we solely employed subcutaneous HT-29 and BxPC-3 tumor-bearing mice. Compared to the BxPC-3 model, higher MFIs were observed at most time points for both tracers using the HT-29 model, consequently leading to higher TBRs, which was potentially caused by varying CH88.2 and CH129binding to these cell lines. Nevertheless, both tumor models could be excellently delineated using CH88.2-800CW in both the previous and current study, suggesting the suitability of both tracers for

imaging of tumors that express Le<sup>a/c/x</sup> and sdi-Le<sup>a</sup> to a lesser extent. Moreover, our orthotopic models allowed biodistribution analysis at the optimal imaging time point of 96 hours post-injection. The observation that tumor fluorescence exceeded liver fluorescence at this time point is encouraging, as sufficient tumor-to-liver contrast is pivotal for this; a common metastatic site for gastrointestinal cancers.<sup>21</sup> Nevertheless, deeper-located hepatic metastases could be missed using NIRF imaging alone, considering the limited penetration depth of NIR light (~ 7 mm).<sup>14</sup>

As a solution, intraoperative tumor imaging may be enhanced by supplementing NIRF imaging with PA imaging, theoretically allowing detection of tumor tissue located beyond NIRF imaging's penetration depth. Practically, a tumor may be approached using PA imaging and, once reached through PA-guided dissection, high-resolution NIRF imaging can be employed to guide radical tumor resection by overlaying the surgeon's view with a real-time NIRF image. Bimodal NIRF/PA imaging using IRDye 800CW as a photosensitizer has been successfully demonstrated in previous research.<sup>22,23</sup> The clinical application of NIRF/PA imaging was first described by Tummers et al. for pancreatic cancer using cetux-imab-800CW, which provided a nearly 4-fold higher mean PA signal in tumor lesions *ex vivo*, compared to surrounding healthy pancreatic tissue.<sup>24</sup>

Although glycan targeting is still in its infancy, targeting TACAs for imaging may offer advantages over 'conventional' protein targeting methods.<sup>5</sup> Apart from their low abundance in healthy tissue and dense expression in cancer, glycans are expressed at the outmost layer of the cell membrane, making them directly accessible by administered targeting moieties. Also, TACAs are present on multiple proteins simultaneously, enabling indirect targeting of multiple proteins through a single anti-glycan tracer administration. Lewis glycan-targeted molecular imaging has particularly focused on the application of sLea (CA19-9)-targeted agents in pancreatic cancer.<sup>5</sup> sLe<sup>a</sup> is overexpressed in >90% of pancreatic cancers and is commonly used as a serum biomarker for follow-up monitoring in this tumor type.<sup>25</sup> Lohrmann et al. performed a phase 1 PET imaging trial in pancreatic cancer using MVT-2163, which is comprised of the anti-sLea mAb HuMab-5B1 conjugated to 89Zr.26 The tracer was well tolerated, causing mild to moderate side effect on the day of administration and provided high-contrast visualization of primary PDAC as well as metastases. Of note, additional sub-centimeter lesions near common metastatic sites that were invisible on conventional imaging were identified. However, the elevation of sLea in normal pancreatic tissue, chronic pancreatitis, cholangitis, obstructive jaundice and other benign conditions, reduces the potential of sLe<sup>a</sup>-targeted tracers. Therefore, targeting more tumor-specific (gly-can-based) targets for imaging of pancreatic cancer, such as Le<sup>a/c/x</sup> and sdi-Le<sup>a</sup>, may provide superior accuracy.

This study has some limitations. Firstly, the relatively small cohort size of the immunohistochemical evaluation of  $Le^{a/c/x}$  and sdi- $Le^a$  expression hindered comprehensive subgroup analyses. Therefore, we could, for instance, not quantify the effect of neoadjuvant therapy (NAT) on  $Le^{a/c/x}$  and sdi- $Le^a$  expression, which is known to affect biomarker expression in tumors. Powertheless, as a substantial portion of the included gastric and colorectal cancer patients did receive NAT and strong expression was maintained throughout the cohort, we anticipate the effect of NAT on biomarker expression to be limited. This is corroborated by previous research that showed no effect of neoadjuvant therapy on  $Le^{a/c/x}$  and sdi- $Le^a$  expression in PDAC.78

Secondly, the *in vivo* models used in this study provide an estimation of clinical practice. As mice do not naturally express Lewis glycans due to lack of fucosyltransferase-3, the TBRs observed in this study could have been overestimated.30 However, the in vivo findings should be considered alongside our immunohistochemical analysis of Lea/c/x and sdi-Lea expression in human tumors and healthy surrounding tissue specimens, which demonstrated sufficient tumor-specificity for most target/tumor type combinations. This suggests that sufficient imaging contrast could theoretically be achieved intraoperatively. Moreover, glycans such as sLea are known to be shed into the circulation, where they may be bound by a glycan-targeting tracer, thereby diverting away tracer from the tumor and reducing tumor-to-background contrast.31 However, as extent of glycan shedding and its effect on tracer distribution was not investigated in this study, its influence on the in vivo imaging results could not be assessed. Nevertheless, the high TBRs observed in this study suggest that any such effect – if present – did not drastically impede tumor imaging under our experimental conditions. Lastly, the tumor/ stromal composition as well as its heterogeneity is not properly represented in our in vivo tumor models. Given the inverse correlation between the amount of stromal tissue and tumor penetration of tracers, the increased amount of stroma in human tumors may hamper tumor penetration in clinical practice. Although patient-derived xenografts, -organoids or complex co-culture models could better approach the human tumor composition, these still provide an estimation. 32,33 Therefore, clinical evaluation of the CH88.2-800CW and CH129-800CW in gastrointestinal cancer patients is warranted to establish their suitability for bimodal NIRF/PA imaging. Considering the established clinical use of IRDye 800CW, rapid clinical translation is feasible.

#### CONCLUSION

Our findings showed that bimodal NIRF/PA imaging using CH88.2-80oCW and CH129-80oCW allows real-time, high-contrast visualization of tumors at 96 hours post-injection. Considering the strong and tumor-specific expression of Lea/c/x and sdi-Lea on gastric, colorectal, and pancreatic cancer, both tracers may be broadly applied for gastrointestinal cancers. This preclinical evaluation warrants further evaluation of both agents in a clinical setting.

#### SUPPLEMENTARY MATERIALS

The following supplementary materials are available online at: https://bit.ly/3ZBNfAq

**Supplementary Table 1:** Patient characteristics of the gastric cancer cohort (n = 52); **Supplementary Table 2:** Patient characteristics of the colorectal cancer cohort (n = 36); **Supplementary Figure 1:** gel as well as its corresponding fluorescence image of CH88.2, CH88.2-800CW, CH129, and CH129-800CW. **Supplementary Figure 2:** (A) MFIs within tumor (MFI T) and background tissue (MFI B) as a function of time after administration of 1 nmol CH88.2-800CW, CH129-800CW or rituximab-800CW to subcutaneous HT-29\_luc2 tumor-bearing mice.

#### REFERENCES

- 1 1. Khan MA, Hakeem AR, Scott N, Saunders RN. Significance of R1 resection margin in colon cancer resections in the modern era. Colorectal Dis. 2015;17(11):943-53.
- 2 2. Vahrmeijer AL, Frangioni JV. Seeing the invisible during surgery. Br J Surg. 2011;98(6):749.
- 3 3. Mieog JSD, Achterberg FB, Zlitni A, Hutteman M, Burggraaf J, Swijnenburg R-J, Gioux S, Vahrmeijer AL. Fundamentals and developments in fluorescence-guided cancer surgery. Nature Reviews Clinical Oncology. 2021.
- 4 4. Hernot S, van Manen L, Debie P, Mieog JSD, Vahrmeijer 17 17. Vermeulen I, Isin EM, Barton P, Cillero-Pastor B, AL. Latest developments in molecular tracers for fluorescence image-guided cancer surgery. The Lancet Oncology. 2019;20(7):e354-e67.
- 5 5. Houvast RD, Vankemmelbeke M, Durrant LG, Wuhrer M, Baart VM, Kuppen PJK, de Geus-Oei LF, Vahrmeijer AL, Sier CFM. Targeting Glycans and Heavily Glycosylated Proteins for Tumor Imaging. Cancers (Basel). 2020;12(12).
- 6 6. Houvast RD, Baart VM, Bhairosingh SS, Cordfunke RA, Chua JX, Vankemmelbeke M, Parsons T, Kuppen PJK, Durrant LG, Vahrmeijer AL, Sier CFM, Glycan-Based Nearinfrared Fluorescent (NIRF) Imaging of Gastrointestinal Tumors: a Preclinical Proof-of-Concept In Vivo Study, Mol Imaging Biol. 2020.
- 7. Houvast RD, Thijse K, Groen JV, Chua J, Vankemmelbeke M, Durrant LG, Mieog JSD, Bonsing BA, Vahrmeijer AL, Kuppen PJK, Crobach A, Sier CFM. An Immunohistochemical Evaluation of Tumor-Associated Glycans and Mucins as Targets for Molecular Imaging of Pancreatic Ductal Adenocarcinoma. Cancers (Basel). 2021;13(22).
- 8. Houvast RD, van Duijvenvoorde M, Chua J, Vankemmelbeke M. Durrant LG. Inderson A. van Hooft IE. Mieog JSD, Bonsing BA, Sier CFM, Crobach A, Vahrmeijer AL, Kuppen PIK, Prediction of Biomarker Expression on Primary Pancreatic Ductal Adenocarcinoma Tissues Using Fine-Needle Biopsies: Paving the Way for a Patient-Tailored Molecular Imaging Approach, Mol Diagn Ther. 2023;27(2):261-73.
- 9 9. Munkley J, Elliott DJ. Hallmarks of glycosylation in cancer. Oncotarget. 2016;7(23):35478-89.
- 10 10. Fuster MM, Esko JD. The sweet and sour of cancer: glycans as novel therapeutic targets. Nat Rev Cancer. 2005;5(7):526-42.
- 11 11. Contessa JN, Bhojani MS, Freeze HH, Rehemtulla A, Lawrence TS. Inhibition of N-linked glycosylation disrupts receptor tyrosine kinase signaling in tumor cells. Cancer Res. 2008;68(10):3803-9.
- 12 12. Chua JX, Vankemmelbeke M, McIntosh RS, Clarke PA, Moss R, Parsons T, Spendlove I, Zaitoun AM, Madhusudan S, Durrant LG. Monoclonal Antibodies Targeting LecLex-Related Glycans with Potent Antitumor Activity, Clin Cancer Res. 2015;21(13):2963-74.
- 13 13. Tivadar ST, McIntosh RS, Chua JX, Moss R, Parsons T, Zaitoun AM, Madhusudan S, Durrant LG, Vankemmelbeke M. Monoclonal Antibody Targeting Sialyl-di-Lewisa - Containing Internalizing and non-Internalizing Glycoproteins with Cancer Immunotherapy Development Potential. Mol Cancer Ther. 2019.

- 14 14. Vahrmeijer AL, Hutteman M, van der Vorst JR, van de Velde CJH, Frangioni JV. Image-guided cancer surgery using near-infrared fluorescence. Nature reviews Clinical oncology. 2013;10(9):507-18.
- 15 15. Attia ABE, Balasundaram G, Moothanchery M, Dinish US. Bi R. Ntziachristos V. Olivo M. A review of clinical photoacoustic imaging: Current and future trends. Photoacoustics. 2019;16:100144.
- 16 16. Zhao J, Chen J, Ma S, Liu Q, Huang L, Chen X, Lou K, Wang W. Recent developments in multimodality fluorescence imaging probes. Acta Pharm Sin B. 2018;8(3):320-38.
- Heeren RMA. Multimodal molecular imaging in drug discovery and development. Drug Discov Today. 2022;27(8):2086-99.
- 18 18. Mahler Convenor M, Berard M, Feinstein R, Gallagher A, Illgen-Wilcke B, Pritchett-Corning K, Raspa M. FELASA recommendations for the health monitoring of mouse, rat, hamster, guinea pig and rabbit colonies in breeding and experimental units. Lab Anim. 2014;48(3):178-92.
- 19 19. Tseng W, Leong X, Engleman E. Orthotopic mouse model of colorectal cancer. I Vis Exp. 2007(10):484.
- 20 20. Moreno JA, Sanchez A, Hoffman RM, Nur S, Lambros MP. Fluorescent Orthotopic Mouse Model of Pancreatic Cancer. J Vis Exp. 2016(115).
- 21 21. Horn SR, Stoltzfus KC, Lehrer EJ, Dawson LA, Tchelebi L, Gusani NJ, Sharma NK, Chen H, Trifiletti DM, Zaorsky NG. Epidemiology of liver metastases. Cancer Epidemiol. 2020;67:101760.
- 22 22. Baart VM, van der Horst G, Deken MM, Bhairosingh SS, Schomann T, Sier VQ, van der Mark MH, Iamele L, de Jonge H, Resnati M, Mazar AP, Pelger RCM, van der Pluijm G, Kuppen PJK, Vahrmeijer AL, Sier CFM. A multimodal molecular imaging approach targeting urokinase plasminogen activator receptor for the diagnosis, resection and surveillance of urothelial cell carcinoma. Eur I Cancer. 2021:146:11-20.
- 23 23. Houvast RD, Badr N, March T, de Muynck L, Sier VO. Schomann T. Bhairosingh S. Baart VM. Peeters J, van Westen GJP, Plückthun A, Burggraaf J, Kuppen PJK, Vahrmeijer AL, Sier CFM. Preclinical evaluation of EpCAM-binding designed ankyrin repeat proteins (DARPins) as targeting moieties for bimodal near-infrared fluorescence and photoacoustic imaging of cancer. Eur J Nucl Med Mol Imaging. 2023.
- 24 24. Tummers WS, Willmann JK, Bonsing BA, Vahrmeijer AL, Gambhir SS, Swijnenburg RJ. Advances in Diagnostic and Intraoperative Molecular Imaging of Pancreatic Cancer. Pancreas. 2018;47(6):675-89.
- 25 25. Poruk KE, Gay DZ, Brown K, Mulvihill JD, Boucher KM, Scaife CL, Firpo MA, Mulvihill SJ. The clinical utility of CA 19-9 in pancreatic adenocarcinoma: diagnostic and prognostic updates. Curr Mol Med. 2013;13(3):340-51.
- 26 26. Lohrmann C, O'Reilly EM, O'Donoghue JA, Pandit-Taskar N, Carrasquillo JA, Lyashchenko SK, Ruan S, Teng R, Scholz W, Maffuid PW, Lewis JS, Weber WA. Retooling a Blood-Based Biomarker: Phase I Assessment of the High-Affinity CA19-9 Antibody HuMab-5B1 for Immuno-PET Imaging of Pancreatic Cancer. Clin Cancer Res. 2019;25(23):7014-23.

- 27 27. Yan H, Wang R, Yu J. Predictive and Prognostic Value of Smac, VEGF and Ki67 Expression in Locally Advanced Rectal Cancer Treated with Neoadiuvant Chemoradiotherapy. International Journal of Radiation Oncology, Biology, Physics. 2010;78(3):S197.
- 28 28. Boogerd LS, van der Valk MJ, Boonstra MC, Prevoo HA, Hilling DE, van de Velde CJ, Sier CF, Fariña Sarasqueta A, Vahrmeijer AL. Biomarker expression in rectal cancer tissue before and after neoadjuvant therapy. Onco Targets Ther. 2018;11:1655-64.
- 29 29. Mohan SC, Walcott-Sapp S, Lee MK, Srour MK, Kim S, Amersi FF, Giuliano AE, Chung AP. Alterations in Breast Cancer Biomarkers Following Neoadjuvant Therapy. Ann Surg Oncol. 2021;28(11):5907-17.
- 30 30. Gersten KM, Natsuka S, Trinchera M, Petryniak B, Kelly RJ, Hiraiwa N, Jenkins NA, Gilbert DJ, Copeland NG, Lowe JB. Molecular cloning, expression, chromosomal assignment, and tissue-specific expression of a murine alpha-(1,3)-fucosyltransferase locus corresponding to the human ELAM-1 ligand fucosyl transferase. J Biol Chem. 1995;270(42):25047-56.
- 31 31. Houghton JL, Abdel-Atti D, Scholz WW, Lewis JS. Preloading with Unlabeled CA19.9 Targeted Human Monoclonal Antibody Leads to Improved PET Imaging with 89Zr-5B1, Mol Pharm, 2017;14(3):908-15.
- 32. Harryvan TJ, Hawinkels L, Östman A, Ten Dijke P, Strell C. Hornsveld M. A Novel Pancreatic Cancer Minitumor Model to Study Desmoplasia and Myofibroblastic Cancer-Associated Fibroblast Differentiation. Gastro Hep Adv. 2022;1(4):678-81.
- 33. Hakuno SK, Michiels E, Kuhlemaijer EB, Rooman I, Hawinkels L, Slingerland M. Multicellular Modelling of Difficult-to-Treat Gastrointestinal Cancers: Current Possibilities and Challenges. Int J Mol Sci. 2022;23(6).

# **CHAPTER 8**

Preclinical evaluation of EpCAMbinding designed ankyrin repeat proteins (DARPins) as targeting moieties for bimodal near-infrared fluorescence and photoacoustic imaging of cancer

Ruben D. Houvast,\* Nada Badr,\* Taryn March, Lysanne D. A.N. de Muynck, Vincent Q. Sier, Timo Schomann, Shadhvi Bhairosingh, Victor M. Baart, Judith A.H.M. Peeters, Gerard J.P. van Westen, Andreas Plückthun, Jacobus Burggraaf, Peter J.K. Kuppen, Alexander L. Vahrmeijer, Cornelis F.M. Sier \* Shared first authorship

European Journal of Nuclear Medicine and Molecular Imaging. 2024;51(8):2179-92



#### ABSTRACT

**BACKGROUND** Fluorescence-guided surgery (FGS) can play a key role in improving radical resection rates by assisting surgeons to gain adequate visualization of malignant tissue intraoperatively. Designed ankyrin repeat proteins (DARPins) possess optimal pharmacokinetic and other properties for *in vivo* imaging. This study aims to evaluate the preclinical potential of epithelial cancer adhesion molecule (EpCAM)-binding DARPins as targeting moieties for near-infrared fluorescence (NIRF) and photoacoustic (PA) imaging of cancer.

**METHODS** EpCAM-binding DARPins Ac2, Ec4.1 and non-binding control DARPin Off7 were conjugated to IRDye 800CW and their binding efficacy was evaluated on EpCAM-positive HT-29 and EpCAM-negative COLO-320 human colon cancer cell lines. Thereafter, NIRF and PA imaging of all three conjugates were performed in HT-29\_luc2 tumor-bearing mice. At 24 hours post-injection, tumors and organs were resected and tracer biodistributions were analyzed.

**RESULTS** Ac2-800CW and Ec4.1-800CW specifically bound to HT-29 cells, but not to COLO-320 cells. Next, 6 nmol and 24 hours were established as the optimal *in vivo* dose and imaging time point for both DARPin tracers. At 24 hours post-injection, mean tumor-to-background ratios of  $3.0 \pm 0.3$  and  $2.6 \pm 0.3$  were observed for Ac2-800CW and Ec4.1-800CW, respectively, allowing clear tumor delineation using the clinical Artemis NIRF imager. Biodistribution analyses in non-neoplastic tissue solely showed high fluorescence signal in liver and kidney, which reflects the clearance of the DARPin tracers.

**CONCLUSION** Our encouraging results show that EpCAM-binding DARPins are a promising class of targeting moieties for pan-carcinoma targeting, providing clear tumor delineation at 24 hours post-injection. The work described provides the preclinical foundation for DARPin-based bimodal NIRF/PA imaging of cancer.

#### INTRODUCTION

Cancer is a leading cause of death worldwide and the incidence is increasing rapidly.¹ Despite recent therapeutic advances, curative cancer care is still based on achieving local control through radical surgical resection.² For most cancers, the presence of a positive resection margin (R1 resection) is associated with increased local recurrence and distant metastasis, accompanied by a reduced disease-free and overall survival.²-5 Therefore, adequate intraoperative localization of malignant tissue is crucial for effective cancer treatment.

Intraoperatively, delineation of malignant tissue using tactile feedback is challenging and the introduction of laparoscopy and robotics has reduced this ability even further. Alternatively, surgeons can rely on intraoperative tumor imaging techniques, such as fluorescence-guided surgery (FGS).<sup>6,7</sup> FGS provides realtime tumor delineation through untargeted or tumor-targeted near-infrared fluorescent (NIRF) contrast agents which are visualized through a dedicated NIRF camera system. Clinical studies have shown that FGS indeed improves intraoperative tumor detection, regularly leading to a change of the initial surgical plan.<sup>8-10</sup> A limitation of using NIRF contrast is the limited NIRF light tissue penetration depth (~7 mm) due to photon scattering and absorption, which restricts the ability to visualize deeper-located lesions.<sup>11,12</sup> Although NIRF imaging suffices for visualization of superficial lesions and resection margins, for detection of deeper lesions or resection margins, the combination with an additional real-time technique like photoacoustic (PA) imaging would be beneficial.

PA imaging via high-resolution ultrasound (US) relies on the detection of acoustic waves caused by the thermoelastic effect undergone by NIRF dyes after exposure to a nano-second pulsed NIR laser.<sup>13</sup> PA imaging has a higher spatial resolution than optical NIRF imaging and, a deeper tissue penetration of up to 7 cm. By combining 3D information derived from PA imaging with superficial NIRF imaging, the presence of tumor lesions can be verified with increased 'depth-of-view', thereby synergistically enhancing tumor detection.<sup>14,15</sup>

The potential of a bimodal NIRF/PA imaging contrast agent is shaped by the careful selection of a tumor-specific biomarker in combination with a suitable targeting moiety. One promising tumor-specific target is the epithelial cell adhesion molecule (EpCAM). EpCAM is a 40 kDa-transmembrane glycoprotein expressed at the basolateral membrane of human epithelia where it plays a role in key cellular processes including cell adhesion, migration, proliferation, and differentiation. However, in cancer, EpCAM becomes highly and homogenously overexpressed on the entire cell membrane. Although originally identified in

colorectal adenocarcinoma, strong overexpression of EpCAM has been described in virtually all cancer types, such as breast, lung, bladder, prostate, esophageal, gastric, and pancreatic cancer. With regards to EpCAM-based NIRF tumor imaging, monoclonal antibody (mAb) and mAb-derived targeting molecules have previously been evaluated by our group and others, and were shown to provide high-contrast intraoperative tumor delineation of colon, breast and prostate cancer in preclinical *in vivo* models. 20-22

However, the large size of mAbs limits extravasation and tissue penetration, leading to a relatively long time of 3 to 5 days between tracer injection and the optimal imaging time window.<sup>23,24</sup> Consequently, the quest for a novel category of smaller, high-affinity and easy-to-produce targeting moieties has led to the introduction of designed ankyrin repeat proteins (DARPins).<sup>23</sup>

DARPins (~14 kDa) are a novel category of synthetic consensus proteins with a randomized binding surface. They consist of four to six ankyrin repeats that are tightly folded together creating a hydrophobic core and a large, groove-like binding surface. Their high affinity, thermodynamic stability, solubility, as well as low aggregation tendency and easy engineerability have made DARPins a promising tumor-targeting alternative to mAbs. Despite their optimal pharmacokinetics for these applications, the potential of DARPins to serve as targeting moieties for NIRF/PA imaging is still to be elucidated.

This study therefore aimed to evaluate the preclinical potential of EpCAM-binding DARPins as targeting moieties for NIRF and PA imaging of cancer. To accomplish this, the EpCAM-specific DARPins Ec4.1 and Ac2 were conjugated to NIRF dye IRDye 800CW, after which their binding and NIRF imaging potential was evaluated using *in vitro* and *in vivo* tumor models.<sup>28</sup> We focused on colon cancer considering the strong EpCAM overexpression in this tumor type, but consider the findings of this proof-of-concept study as extrapolatable to virtually all EpCAM-expressing cancers.

#### MATERIALS AND METHODS

## **Expression and Purification of DARPins**

The EpCAM-binding DARPins Ac2\_M34L\_cys and Ec4.1\_M34L-cys (both carrying a M34L mutation and a C-terminal Gly-Gly-Cys tail) were expressed and purified by the method previously described. <sup>28-30</sup> Ec4.1 differs from Ec4 by a T54A mutation in a randomized position, which has decreased the dissociation rate constant by a factor 10 (N. Stefan et al., unpublished results) without changing the association

rate constant. The negative control DARPin Off7 was equipped with the same C-terminal Gly-Gly-Cys tail and purified analogously.<sup>31</sup>

#### Conjugation of DARPin-800CW conjugates

DARPins Ac2\_M34L\_cys, Ec4.1\_M34L-cys and Off7-cys (10 mg/mL), each containing a single cysteine residue, were treated with 10 equivalents of Tris (2-carboxyethyl) phosphine (TCEP; 0.11 M in H2O, adjusted to pH7 with NaOH) under an atmosphere of N2 for 1 hour. The TCEP was removed by filtration through Zeba spin filters (Thermo Fisher Scientific, Waltham, MA, USA; MWCO 7K) and the reduced DARPin solutions were adjusted to a concentration of 5 mg/mL with phosphate-buffered saline (PBS). Three equivalents of IRDye 800CW-maleimide (LI-COR, Lincoln, NE, Nebraska) in DMSO were added to each DARPin solution, which were left in the dark for 1-1.5h with occasional shaking. Excess unconjugated dye was removed by double filtration through Zeba spin filters (MWCO 7K), furnishing the mono-800CW substituted DARPins in PBS.

#### Human cancer cell lines

Human colon cancer cell lines HT-29 (EpCAM-positive) and COLO-320 (EpCAM-negative) were obtained from ATCC and cultured in RPMI 1640 cell culture medium (Gibco, Invitrogen, Carlsbad, CA, USA) supplemented with L-glutamine, 25 mM HEPES, 10% fetal bovine serum (FBS; Hyclone, Thermo Fisher Scientific), and penicillin/streptomycin (both 100 IU/ml; Invitrogen). For *in vivo* studies, HT-29 was transfected with luciferase 2 (luc2) to allow monitoring of tumor growth using bioluminescence imaging (BLI). Absence of *Mycoplasma* was evaluated using polymerase chain reaction. Cells were grown in a humidified incubator at 37°C and 5% CO<sub>2</sub>, and subsequently detached with trypsin/EDTA (0.5% Trypsin-EDTA solution 10x; Santa Cruz Biotechnology, Inc, Dallas, TX, USA) when 90% confluence was reached. Viability was assessed using Trypan Blue staining in 0.4% solution (Invitrogen).

#### Cell-based plate assay

Colon cancer cells were grown in a 96-well plate; 20,000 cells/well in 100 µl of complete medium (Corning Costar Inc., Cambridge, MA, USA) until 90% confluency. Cells were then washed twice with PBS supplemented with 0.5% bovine serum albumin (0.5% PBSA). To evaluate DARPin binding to HT-29\_luc2 and COLO-320 cells were incubated with Ac2-800CW, Ec4.1-800CW or non-binding

control Off7-800CW in PBS at concentrations of 1, 10 100 or 1000 nM for 1 hour. Incubation was performed on ice and without exposure to light. Thereafter, cells were washed twice with 0.5% PBSA to wash away unbound DARPin-800CW. For competition experiments, these aforementioned steps were slightly adapted. Washed cells were preincubated with PBS, unconjugated Ac2, Ec4.1 or non-binding control Off7 at a concentration of 200 nM, followed by washing and incubation with Ac2-800CW, Ec4.1-800CW or Off7-800CW at a concentration of 100 nM. DARPin-800CW fluorescence was measured using the Odyssey CLx Infrared Imaging System (LI-COR) using the 800 nm channel (excitation 785 nm, emission filter 812 - 823 nm). For cell number estimation via nuclear fluorescence, cells were permeabilized with 40%-60% acetone-methanol for 5 minutes, washed once, and incubated with ToPro-3 iodide (1:2000, T3605, Invitrogen, California, USA) at room temperature for 10 minutes. After one washing step, nuclear fluorescence was quantified using the 700 nm channel of the Odyssey (excitation 685 nm, emission filter 710-730 nm). The mean fluorescence intensity (MFI) was calculated by dividing the 800 nm fluorescence signal by the nuclear 700 nm signal. Measurements were performed in triplicate.

## Flow cytometry

After detaching and viability assessment, cells were resuspended in ice-cold 0.5% PBSA at 500,000 cells/tube followed by 2 washings. Thereafter, cells were incubated with 100 nM Ac2-800CW, Ec4.1-800CW or Off7-800CW for 1 hour. After washing twice, cells were resuspended in 400 µl PBSA containing propidium iodide (1/4000) and measured on a LSRFortessa flow cytometer (BD Biosciences, Franklin Lanes, NJ, USA; 1.0×10⁴ living cells per tube) using FACS DIVA software version 7 (BD Biosciences). All incubation steps were performed on ice, without exposure to light. Data were analyzed using FlowJo™ (version 10.8.1, BD Biosciences).

#### Chamber slides

After detachment and viability assessment, cells were transferred to an 8-well Nunc™ Lab-Tek™ II Chamber Slide (0.7 cm²/well, Thermo Fisher Scientific) at 40,000 cells/well. Once 90% confluence was reached, the medium was removed and the cells were washed twice in PBS for 5 minutes, followed by fixation with 1% paraformaldehyde at room temperature for 10 minutes. Next, cells were washed twice in PBS for 5 minutes and incubated with 200 nM Ac2-800CW, Ec4.1-800CW or Off7-800CW on ice and without exposure to light for 1 hour, followed by washing with PBS and demineralized water. Thereafter, plastic chambers were

removed, slides were dried and subsequently stained with ProLong Gold containing DAPI (Thermo Fisher Scientific). Slides were scanned using the DAPI (excitation 376-398 nm, emission filter 417-477 nm) and Cy7 channel (excitation 773-758 nm, emission filter 776 - 826 nm) of the Axio Scan Z1 (Carl Zeiss AG, Oberkochen, Germany). Images were analyzed using Zen Lite (version 3.5, Zeiss). Measurements were performed in triplicate.

#### Animal models

Mice were kept at the Central Animal Facility of the LUMC, housing animals per EU Recommendation 2007-526-EC under specific pathogen-free conditions [19]. Six- to twelve-week-old female CD-1® Nude (Crl:CD1-Foxn1<sup>nu</sup>) mice (Charles River Laboratories, Wilmington, MA, USA) were subcutaneously inoculated on 4 spots on the back with HT-29\_luc2 cells (5.0×10<sup>5</sup> cells/spot; 3 mice per group). Tumor growth was monitored by a digital caliper. Orthotopic HT-29\_luc2 models were induced as previously described.³² Orthotopic tumor growth was monitored by bioluminescence imaging using the IVIS® Spectrum Preclinical *In Vivo* Imaging System (Spectrum, PerkinElmer, MA, USA). The local animal welfare body of the LUMC reviewed and approved all animal studies. Animals were humanely cared for in accordance with the Code of Practice Animal Experiments in Cancer Research and guidelines from Directive 2010/63/EU of the European Parliament on the protection of animals used for scientific purposes. Local standard operating procedures were followed for handling of animals.

#### In vivo NIRF imaging

Once subcutaneous tumors reached approximately 50 mm³ in size, the mice were injected with either 3, 6, or 9 nmol of Ac2-8ooCW, Ec4.1-8ooCW, or non-binding control Off7-8ooCW dissolved in PBS by tail vein injection. For orthotopic tumors, tumors providing a BLI signal of > 1.0×10<sup>8</sup> p/sec/cm²/sr were regarded as suitable for imaging. Subcutaneous tumor-bearing mice were imaged at 1, 2, 4, 8, 24, 48 and or 72 hours post-injection, while orthotopic tumor-bearing mice were imaged at the optimal imaging time point as determined using the subcutaneous tumor-bearing mice. All mice were imaged using both the preclinical Pearl Trilogy Small Animal Imaging System (LI-COR, 800 nm channel; excitation 785 nm, emission filter 820 nm) and the clinical Artemis NIR Imaging system (Quest Medical Imaging b.v., Middenmeer, The Netherlands; excitation 780 nm, emission filter 805 nm). Mice were kept under 2–4 % isoflurane anesthesia during imaging. After the last measurement, the mice were sacrificed and the tumors and/or organs were resected, followed by imaging using the Pearl imaging system. Tumor and

background MFIs were calculated by drawing a region-of-interest over the tumor area and adjacent normal tissue, respectively, and included as separate data points for analysis. Pearl images were analyzed using Image Studio (version 5.2, LI-COR), while Quest images were analyzed using Spectrum Capture Suite (Quest Medical Imaging b.v.) and subsequently ImageJ (version 1.50, National Institutes of Health, Bethesda, MD, USA). Tumor-to-background ratios (TBRs) were calculated using the following formula: TBR = MFI<sub>tumor</sub>/MFI<sub>background</sub>. For biodistribution analysis, organ MFIs were calculated by drawing a ROI over the resected organ.

#### In vivo PA imaging

PA imaging was performed at 24 hours post-injection using the Vevo 3100 Imaging System (FUJIFILM VisualSonics, Canada) as described before. The system was equipped with Vevo LAZR-X cart, a Vevo LAZRTight Enclosure, and a Vevo Imaging Station. Mice were anesthetized and placed on a preheated imaging table. The MX550D transducer was used for US and PA imaging (FUJIFILM, VisualSonics; 25–55 MHz; axial resolution: 40  $\mu$ m; excitation 780 nm). Images were analyzed using Vevo LAB (version: 5.5.0, FUJIFILM, VisualSonics). Tumor-to-background ratios (TBRs) were calculated using the following formula: TBR = PAtumor/PAbackground.

### Histological analysis

Resected tumors were embedded in 4% paraformaldehyde and replaced by ethanol the next day, after which tumor tissues were embedded in paraffin. Four µm-thick formalin-fixed paraffin-embedded tissue sections were deparaffinized in xylene for 15 min followed by fluorescence imaging using the Odyssey CLx Infrared Imaging System on the 800 nm channel. For immunohistochemical staining, sections were rehydrated in a series of decreasing ethanol dilutions and rinsed in demineralized water. Endogenous peroxidase was blocked with 0.3% hydrogen peroxide in demineralized water. Antigen retrieval was subsequently performed by heating sections at 95 °C for 10 min in EnVision Flex Target Retrieval Solution (pH 6.0) using PT Link (Dako, Glostrup, Denmark). After cooling in PBS, sections were incubated overnight in a humidified chamber at room temperature with 120 µL primary antibody: MOC31 (Acris antibodies, Herford, Germany; 0.06 µg/ml) and AE1/AE3 (Dako; o.o8 mg/ml) were used for, respectively, EpCAM and pan-cytokeratin. Next, slides were washed three times in PBS for 5 min and incubated with secondary goat anti-mouse EnVision antibody (Dako, K4001) at room temperature for 30 min, followed by an additional washing step. Staining was effected by incubation with 3,3-diaminobenzidine tetrahydrochloride solution (DAB, K3468, Agilent Technologies, Inc., Santa Clara, CA, USA) at room temperature for 10 min.

Sections were then counterstained with Mayer's hematoxylin solution (Sigma-Aldrich, Saint Louis, MO, USA). After dehydration in an incubator at 37°C for 1 h, slides were mounted with Pertex (Leica Microsystems, Wetzlar, Germany). As histological reference, rehydrated slides were stained with Mayer's hematoxylin solution (Sigma-Aldrich, Saint Louis, MO, USA) for 2 minutes and counterstained with eosin for 2 minutes, followed by dehydrating and mounting with Pertex. All slides were digitalized with the Panoramic Digital slide Scanner and analyzed using CaseViewer 2.4 (both 3D Histech, Budapest, Hungary).

#### Statistical analyses

Statistical analyses and graph generation were performed with GraphPad Prism (version 9.3.1 GraphPad Software Inc., La Jolla, CA, USA). Differences between mean MFI and TBRs at different time points were compared using two-way ANOVA with Šídák correction for multiple comparisons. For the *in vitro* binding competition experiment, one-way ANOVA with Dunnett correction for multiple comparisons was used to calculate MFI differences. Differences with a p-value smaller than 0.05 were regarded as significant (NS: not significant; \*:  $p \le 0.005$ ; \*\*:  $p \le 0.001$ , \*\*\*\*  $p \le 0.0001$ , \*\*\*\*  $p \le 0.0001$ ).

#### RESULTS

#### In vitro binding of DARPin-800CW conjugates

EpCAM-binding DARPins Ac2 and Ec4.1, an affinity-improved version of Ec4, and the negative control DARPin Off7 were successfully conjugated to IRDye 800CW, with the absence of free dye in the conjugate solution verified via sodium dodecyl sulfate-polyacrylamide gel electrophoresis (not shown). Next, binding to EpCAMpositive HT-29 and EpCAM-negative COLO-320 cell lines was evaluated in vitro. Using cell-based plate assays, a concentration-dependent increase in 800 nm meanfluorescence intensity (MFI) was observed for Ac2-800CW and Ec4.1-800CW on HT-29 cells, and a significantly lower signal on EpCAM-negative COLO-320 cells (Figure 1A). In contrast, Off7-800CW MFI did not show a substantial concentrationdependent MFI increase on either HT-29 or COLO-320 cells. Therefore, Ac2-800CW and Ec4.1-800CW specifically bind to EpCAM-positive HT-29 cells, while Off7-800CW does not. While the specific binding of Ac2 and Ec4.1 has been shown before, the present experiments show that 800CW conjugation neither sterically interferes with binding, nor does it induce non-specific binding through a hydrophobic effect.<sup>28</sup> Binding specificity was confirmed on single cells using flow cytometry, which showed a substantial right-shift for Ac2-800CW and Ec4.1-800CW on HT-29 cells, but not on COLO-320 cells, thereby validating the observed binding specificity of Ac2-800CW and Ec4.1-800CW (Figure 1B). As expected, Off7-800CW did not show any right-shift for either cell line.

Immunofluorescence microscopy was subsequently performed on cell-based chamber slides to evaluate the localization of DARPin-8ooCW binding on HT-29 and COLO-320 cells, which showed that Ac2-8ooCW and Ec4.1-8ooCW were present on the cell membrane of HT-29 cells, while neither tracer bound to COLO-320 cells (Figure 1C). Again, Off7-8ooCW did not bind to HT-29 nor COLO-320 cells.

#### In vitro binding competition of DARPin-800CW conjugates

To evaluate the differential epitope specificity of DARPin-8ooCW conjugates, *in vitro* binding competition between Ac2-8ooCW, Ec4.1-8ooCW and Off7-8ooCW was assessed on HT-29 and COLO-320 cells using a plate assay. While Ac2-8ooCW and Ec4.1-8ooCW showed competition with their unconjugated counterpart on HT-29 cells, w between Ec4.1 and Ac2 was absent, confirming that the two DARPins target different EpCAM epitopes,<sup>28</sup> also when conjugated to 8ooCW (Figure 2). Competition of both EpCAM-targeting DARPins by Off7 was not significant. Moreover, no binding and or competition was found for all DARPin-8ooCW conjugates on COLO-320 cells. Based on the above, HT-29 was selected as a suitable EpCAM-positive cell line for *in vivo* experiments.

## In vivo dose and time window optimization of DARPin-800CW conjugates

To establish the suitable *in vivo* dose and time window of DARPin-8ooCW conjugates, HT-29\_luc2 tumor-bearing mice were injected with either 3, 6, or 9 nmol of Ac2-800CW or Ec4.1-800CW using tail vein injection followed by NIRF imaging at 1, 2, 4, 8, 24, 48, and 72 hours post-injection using the preclinical Pearl imager. The tumor MFI<sub>max</sub> as measured by the Pearl imager was observed at 1 hour postinjection, followed by an exponential decrease (Figure 3A). For Ac2-80oCW, no substantial tumor MFI difference was observed for the 6 and 9 nmol group, whereas for Ec4.1-800CW, the highest tumor MFI was observed with the 9 nmol dose. Next, tumor-to-background ratios (TBRs) were calculated to quantify the relative tumor MFI compared to the surrounding healthy tissue. For Ac2-80oCW, the highest TBRs were observed in the 6 nmol group, while for Ec4.1-80oCW, comparable TBRs were observed in the 3 nmol and 6 nmol groups (Figure 3B). The TBR<sub>max</sub>, as measured by the preclinical Pearl imager, was observed in the 6 nmol group at 24 hours post-injection for Ac2-800CW and Ec4.1-800CW, with 2.3 + 0.2 and 2.3 + 0.1, respectively. Therefore, 6 nmol and 24 hours were selected as the optimal dose and imaging time point for both DARPin tracers.

FIGURE 1 In vitro binding of EpCAM DARPin-8ooCW conjugates. (A) Binding of Ac2-8ooCW, Ec4.1-8ooCW, and Off7-8ooCW to HT-29 (black) and COLO-320 (grey) colon cancer cell lines at various concentrations using cell-based plate assays. Experiments were performed in triplicate. (B) Binding of Ac2-8ooCW, Ec4.1-8ooCW, and Off7-8ooCW (each at 100 nM) to HT-29 and COLO-320 cells using flow cytometry using the 800 nm channel. Dark grey curves display DARPin-8ooCW binding, whereas light grey curves represent unstained cells. (C) Immunofluorescence analysis of Ac2-8ooCW, Ec4.1-8ooCW, and Off7-8ooCW binding to HT-29 and COLO-320 cells. The 8ooCW signal representing DARPin-8ooCW localization is displayed in red. DAPI stained nuclei are displayed in blue. ns: not significant, \*\*\*\*: p < 0.001.

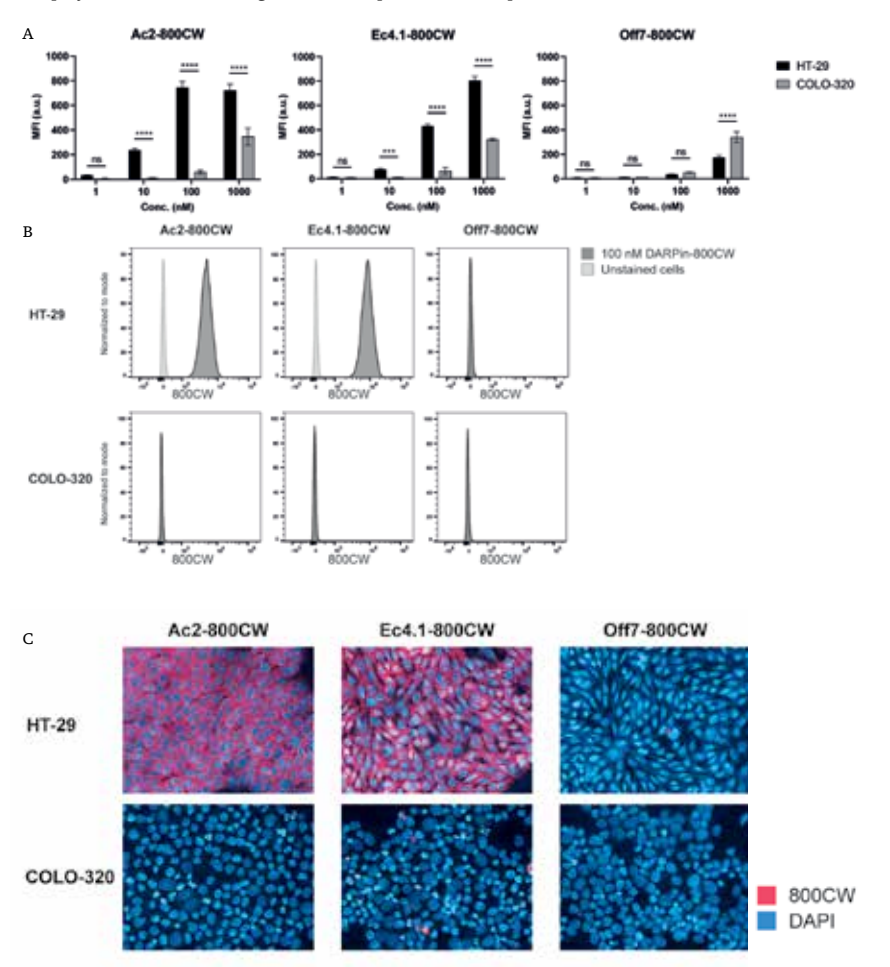
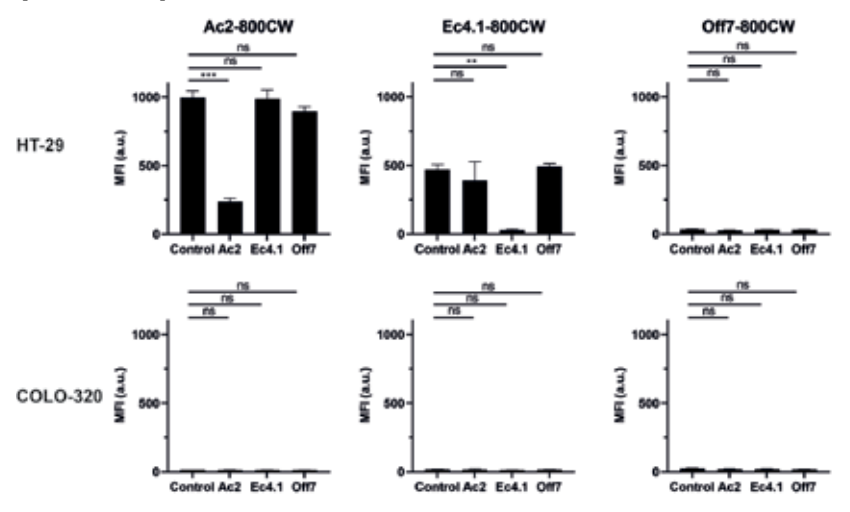


**FIGURE 2** *In vitro* binding competition of DARPin-8ooCW conjugates on HT-29 and COLO-320 cells. Cells were preincubated with PBS (control), unconjugated Ac2, Ec4.1 or Off7 (each at 200 nM), followed by incubation with DARPin-8ooCW conjugates (100 nM). a.u: arbitrary units, MFI: mean fluorescence intensity, ns: not significant, \*\*: p < 0.01, \*\*\*: p < 0.001. Experiments were performed in triplicate.



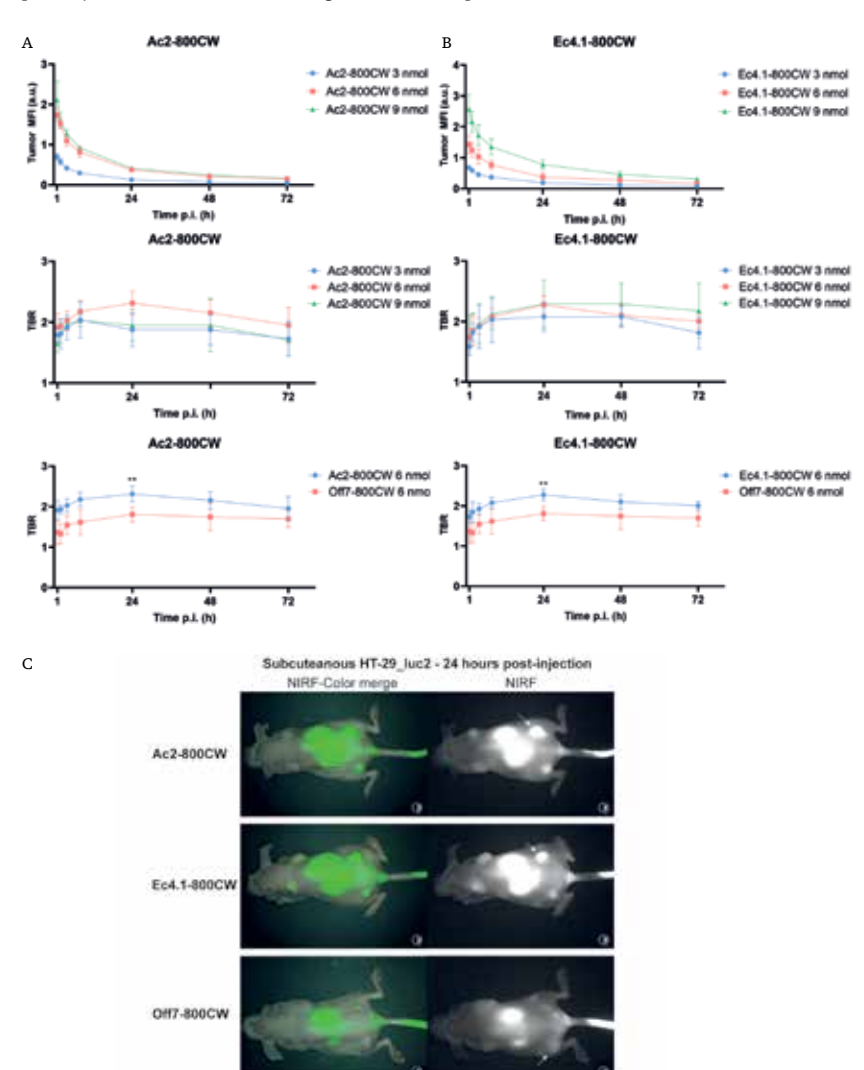
# In vivo binding specificity of DARPin-800CW conjugates

To verify *in vivo* binding specificity, HT-29\_luc2 tumor-bearing mice were administered with 6 nmol Ac2-8ooCW, Ac2-8ooCW or control Off7-8ooCW and imaged using the preclinical Pearl and clinical Artemis NIRF imagers at 1, 2, 4, 8, 24, 48, and 72 hours post-injection. At 24 hours post-injection, a significantly higher TBR was found for Ac2-8ooCW and Ec4.1-8ooCW compared to Off7-8ooCW, suggesting *in vivo* specificity of both EpCAM-targeting DARPin tracers (Ac2-8ooCW vs. Off7-8ooCW:  $2.3 \pm 0.2$  vs.  $1.8 \pm 0.2$ , p = 0.003; Ec4.1-8ooCW vs. Off7-8ooCW:  $2.3 \pm 0.1$  vs.  $1.8 \pm 0.2$ , p = 0.003) (Figure 3C). As shown in Figure 3D, HT-29\_luc2 tumors can be clearly delineated using the clinical Artemis NIRF imager after injection of Ac2-8ooCW and Ec4.1-8ooCW, while tumors can be less clearly localized using Off7-8ooCW. Moreover, kidney uptake was pronounced for all EpCAM-targeting DARPin tracers.

FIGURE 3 In vivo dose and time window optimization of DARPin-8ooCW conjugates. (A) Tumor MFIs and TBRs as a function of time after intravenous administration of 3, 6, or 9 nmol Ac2-8ooCW or Ec4.1-8ooCW in subcutaneous HT-29\_luc2 tumor-bearing mice. (B) TBRs as a function of time after intravenous administration of 6 nmol Ac2-8ooCW, Ec4.1-8ooCW and negative control tracer Off7-8ooCW in subcutaneous HT-29\_luc2 tumor-bearing mice. (C)

#### [CONTINUATION FIGURE 3]

NIRF-color merge and NIRF images of subcutaneous HT-29\_luc2 tumor-bearing mice at 24 hours post-injection of Ac2-8ooCW, Ec4.1-8ooCW or Off7-8ooCW. Images were captured using the clinical Artemis NIRF imager at a similar exposure time of 150 ms, allowing real-time imaging. White arrows indicate an example of a representative tumor. NIRF: near-infrared fluorescence, p.i.: post-injection, TBR: tumor-to-background ratio, \*\*: p < 0.01.



#### In vivo NIRF imaging potential of DARPin-800CW conjugates

To evaluate the *in vivo* NIRF imaging potential of Ac2-8ooCW and Ec4.1-8ooCW in a more clinically relevant colon cancer model, mice were orthotopically inoculated with HT-29\_luc2 tumors in the caecum and injected with 6 nmol Ac2-8ooCW or Ec4.1-8ooCW. For both tracers, orthotopic HT-29\_luc2 tumors could be localized with high contrast at 24 hours post-injection using the clinical Artemis NIRF imager (Figure 4A). Mean Pearl TBRs of  $4.2 \pm 0.7$  and  $5.3 \pm 0.5$  were observed for Ac2-8ooCW and Ec4.1-8ooCW, respectively. Using the clinical Artemis NIRF imager, slightly lower mean TBRs of  $3.0 \pm 0.3$  and  $2.6 \pm 0.3$  were observed for Ac2-8ooCW and Ec4.1-8ooCW, respectively (Figure 4B).

#### In vivo PA imaging potential of DARPin-800CW conjugates

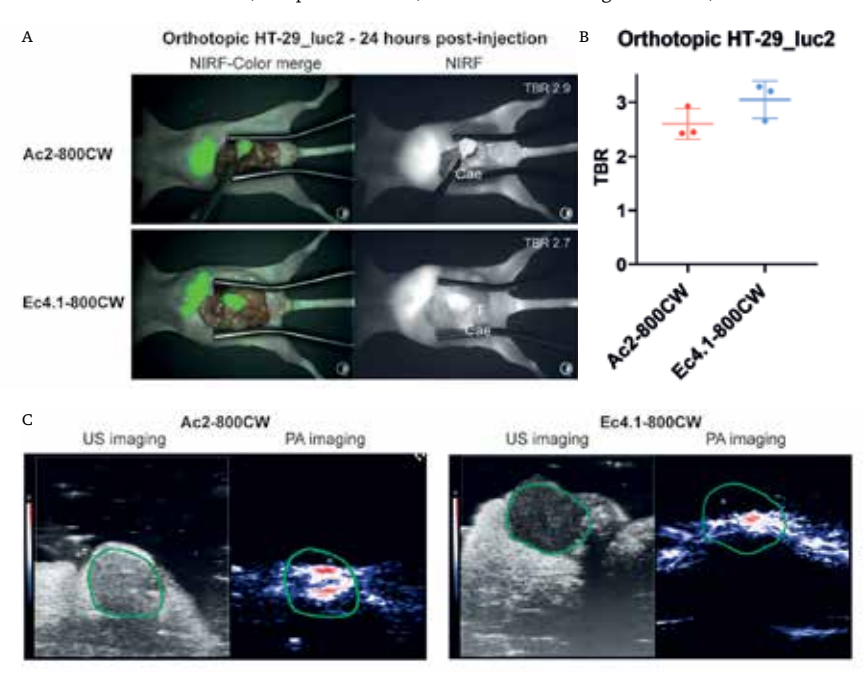
To establish the potential of DARPin-8ooCW conjugates as tracers for bimodal NIRF/PA imaging, PA imaging using Ac2-8ooCW or Ec4.1-8ooCW was performed in orthotopic HT-29\_luc2 tumor-bearing mice at 24 hours post-injection. As shown in Figure 4C, PA signal is located inside the tumor lesions with high intensity for both Ac2-8ooCW and Ec4.1-8ooCW, while PA signal in surrounding tissues is limited. PA imaging TBRs of 2.7 and 2.3 were observed for Ac2-8ooCW and Ec4.1-8ooCW, respectively.

## Biodistribution and histological analysis

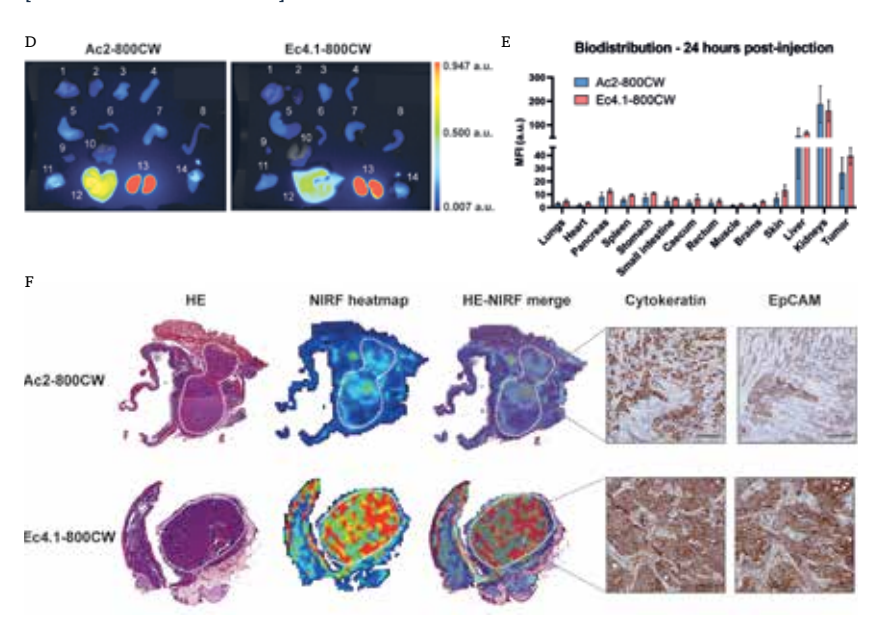
To verify the biodistribution of the tracers, tumors and organs were resected at 24 hours post-injection followed by NIRF imaging. For both Ac2-800CW and Ec4.1-800CW, biodistribution analysis showed higher fluorescence signal in excretory organs such as the kidneys and liver than in tumor tissues. The tumor MFI for Ac2-800CW  $26 \pm 12$  was lower compared than that of Ec4.1-800CW  $(39 \pm 6)$ , although this difference was not statistically significant (95% CI: -9, 35; p = 0.17). Macroscopic fluorescence allowed clear tumor visualization for both tracers with low fluorescence signal in remaining healthy organs (Figure 4D-E).

Histological analysis showed that NIRF signals for both Ac2-800CW and Ec4.1-800CW largely overlapped with microscopically identified tumor areas, as well as cytokeratin and EpCAM staining, thereby confirming binding specificity of both tracers and indicating complete tumor penetration (Figure 4F). As outlined above, intratumoral fluorescence of Ac2-800CW was lower than Ec4.1-800CW fluorescence.

FIGURE 4 In vivo NIRF imaging and PA imaging using DARPin-800CW conjugates. (A)NIRFcolor merge and NIRF images of orthotopic HT-29\_luc2 tumor-bearing mice at 24 hours postinjection of Ac2-800CW or Ec4.1-800CW. Images were captured using the clinical Artemis NIRF imager at an exposure time of 150 ms. 'T' indicates the tumor localization, while 'Cae' indicates the corresponding background tissue (caecum). Mouse-specific TBRs are indicated in white in the right-upper quadrant of the NIRF images. (B) TBRs of orthotopic HT-29\_luc2 tumors 24 hours after intravenous administration of 6 nmol Ac2-80oCW or Ec4.1-80oCW as measured using the clinical Artemis NIRF imager. Mean TBRs are represented by the horizontal line together with their error bars representing the standard deviation. (C) Representative US and PA images of orthotopic HT-29\_luc2 tumor-bearing mice at 24 hours post-injection of Ac2-80oCW or Ec4.1-800CW. Images were captured using a penetration depth of approximately 1.5 cm. Tumors are delineated with a green line. (D) Biodistribution in orthotopic HT-29\_luc2 tumors and healthy organs of mice at 24 hours post-injection of Ac2-80oCW or Ec4.1-80oCW. 1: lungs, 2: heart, 3: pancreas, 4: spleen, 5: stomach, 6: small intestine, 7: caecum, 8: rectum, 9: muscle, 10: brain, 11: skin, 12: liver, 13: kidneys, 14: tumor. (E) Macroscopic fluorescence biodistribution of orthotopic HT-29\_ luc2 tumors and healthy organs at 24 hours post-injection of Ac2-80oCW or Ec4.1-80oCW (Pearl imager). (F) HE staining, 800 nm heatmap and merge, as well as cytokeratin and EpCAM stainings of sequential tissue sections derived from orthotopic HT-29\_luc2 tumors at 24 hours post-injection of Ac2-800CW or Ec4.1-800CW. Tumors are delineated by dashed white lines. HE-NIRF and cytokeratin-EpCAM images are taken at 2× and 15× magnification, respectively. Scale bars represent 100 µm. a.u: arbitrary units, HE: hematoxylin-eosin, MFI: mean fluorescence intensity, NIRF: near-infrared fluorescence, PA: photoacoustic, TBR: tumor-to-background ratio, US: ultrasound.



#### [CONTINUATION FIGURE 4]



#### **DISCUSSION**

176

Fluorescence-guided surgery can play a key role in improving radical resection rates by assisting surgeons with intraoperative visualization of malignant tissue. The quest for adequate tumor-targeting moieties for FGS tracers has shifted from antibodies towards strategically designed targeting molecules with optimal pharmacokinetics for *in vivo* imaging, such as DARPins. Using real-time NIRF imaging and PA imaging, we showed that EpCAM-binding DARPins Ac2-800CW and Ec4.1-800CW provided high-contrast tumor delineation in a clinically relevant *in vivo* model at 24 hours post-injection, accompanied by low signals in healthy surrounding organs. This study thereby provides the first preclinical substantiation that EpCAM-binding DARPins are promising targeting molecules for NIRF and PA imaging of cancer. Considering the strong abundance of EpCAM in a wide variety of epithelial cancer types, EpCAM-targeted DARPin-based NIRF/PA imaging tracers may be deployed in a broad, pan-carcinoma clinical context.

Intraoperatively, combining NIRF with PA imaging provides a powerful diagnostic and screening tool, allowing detection of malignant tissue located beyond NIRF imaging's penetration capability using a single contrast agent injection. Once a lesion is identified and approached guided by PA imaging, NIRF

imaging allows tumor identification and removal with higher accuracy by overlaying the actual surgeon's view with real-time fluorescence. The synergy between PA and NIRF imaging thus provides an improved intraoperative tumor imaging approach, where the strengths of each modality complement and compensate for their individual limitations. Several studies have successfully described the use of 800CW-based contrast agents for bimodal NIRF/PA imaging.33,34 Intraoperatively, Tummers et al. demonstrated an 3.7-fold mean PA signal in primary pancreatic cancer lesions compared to normal pancreatic tissue using anti-EGFR tracer cetuximab-800CW, providing the first clinical evidence of the combined NIRF/PA imaging approach. Despite these promising findings, routine implementation is hampered by, among others, the clinical availability of PA imaging systems.<sup>35</sup> In contrast to NIRF/PA imaging, research into DARPins as tumor imaging agents has primarily focused on nuclear imaging, which has already yielded multiple encouraging results.<sup>28,36-40</sup> Recently, a first-in-human study evaluating the anti-HER2 DARPin tracer 99mTc-(HE)3-G3 for SPECT imaging of breast cancer reported a favorable safety and tolerability profile, and it showed clear visualization of both primary and metastatic HER2-positive lesions (NCTo4277338).41 Interestingly, clinically defined HER2-negative tumors could also be visualized, albeit with lower contrast. Vorobyeva et al. evaluated, in a preclinical setting, the PET imaging potential of the EpCAM-binding DARPin Ec1 conjugated to [125] I-PIB in a human ovarian cancer xenograft model and observed a tumor-to-blood ratio of 19 at 6 hours post-injection, which increased to 31 at 24 hours post-injection, thereby providing high-contrast tumor localization.38 Although lower TBRs were achieved using NIRF instead of radiation, we observed a TBR increase to >2 in the subcutaneous model until 24 hours post-injection, providing clear tumor localization.

Obviously, tumor-to-blood ratios from nuclear imaging studies cannot be directly compared to tumor-to-background tissue ratios in NIRF imaging. This is largely caused by the presence of endogenous autofluorescence and NIR light absorption/scattering which can increase background signal, decreasing the TBR.<sup>42-44</sup> Of note, TBRs in the range from 2 to 3 are typically observed using NIRF-labeled, tumor targeted nanobodies, which share similar pharmacokinetic properties with DARPins, further substantiating our findings.<sup>45,46</sup> Moreover, even though Off7-800CW binding was not observed *in vitro*, some tumor fluorescence was observed *in vivo*, albeit at lower levels compared to Ec4.1/Ac2-800CW. The phenomenon that untargeted tracers show low, non-specific intratumoral uptake in human tumors grown in mice is common and attributed to the enhanced permeability and retention (EPR) effect.<sup>47</sup>

Besides the contrast between the primary tumor and direct background (TBR), sufficient contrast between other healthy organs and common (distant) metastatic sites is crucial to decrease false-positivity and allow adequate NIRF/PA imagingbased intraoperative staging. 48,49 For colon carcinoma, common metastatic sites are the liver and peritoneum. 50 Our biodistribution analysis at 24 hours post-injection showed high fluorescence in the liver and kidneys, in line with previous reports on DARPin-based imaging. 38,51 As high liver fluorescence was observed for both DARPin tracers, visualization of hepatic metastases could potentially be impaired in the clinical setting, which should be considered when choosing suitable applications. In contrast, the high kidney fluorescence, which can be attributed to renal clearance of the construct, will be reduced in humans due to the presence of a more pronounced retroperitoneal perinephric fat layer along with Gerota's fascia. 45 Moreover, renal metastases are rarely observed for any cancer type.<sup>52</sup> Nonetheless and in line with previous literature, DARPin-800CW conjugate fluorescence in peritoneal organs has been found to be low, theoretically allowing visualization of EpCAM-expressing peritoneal depositions using both DARPins tracers. 37,38,40

The use of mAbs has dominated the molecular imaging field for years as the first targeting molecule-of-choice. 53,54 Despite their favorable stability, specificity and target affinity, mAb-based tumor imaging is complicated by high costs, limited extravasation, and poor tissue penetration, resulting in a relatively long time frame (3 to 5 days) between tracer injection and imaging.<sup>23,24</sup> The use of smaller targeting molecules may improve extravasation and tissue penetration and shorten the time between injection and imaging, however their size reduction should be compensated by enhanced target affinity (Kd), in order to achieve similar tumor uptake compared to larger molecules. 55,56 Despite relevant affinity differences between Ac2 (Kd: 130 nM) and Ec4.1 (Kd: 0.2 nM, ca. 10-fold improved over the previously published Ec4, cf. Materials and Methods<sup>28</sup>) we found that TBRs and tumor MFIs of both DARPin tracers were sufficiently high to allow adequate tumor visualization. Nonetheless, both TBRs and MFIs were somewhat higher for the high-affinity Ec4.1, albeit only at the border of statistical significance. Of note, Ac2 and Ec4.1 affinities are comparable or higher than those of therapeutic EpCAM mAbs, such as adecatumumab (Kd: 91 nM) or edrecolomab (Kd: 1530 nM).57

In line with these findings, Zahnd et al.<sup>58</sup> systematically investigated the influence of molecular mass and affinity on tumor accumulation of DARPins. A strong correlation of tumor accumulation with affinity was found for these small proteins, when accumulation was evaluated by radioactivity accumulation as a

function of time. Interestingly, increasing the size of the DARPins to 30 kDa resulted in significantly lower tumor accumulation after 24 h, similar to the lower values observed for scFvs, whereas valency as such had no influence on accumulation for molecules with already very high affinity.<sup>58</sup> For larger proteins (such as PEGylated DARPins) affinity became less important. In modelling studies, these experimental findings were completely replicated and explained by the need to avidly retain molecules of fast diffusion.<sup>59</sup>

Although the potential effect of IRDye8ooCW conjugation on affinity was not quantified, the retained specificity is consistent, with the dye not interacting with the target, nor impeding the interaction. Previous studies have already indicated that DARPin selectivity and affinity was retained after conjugation.<sup>30,58,60</sup> The quantitative influence of affinity and size on total accumulation, however, strongly depends on the tumor model used, regarding accessibility (orthotopic versus subcutaneous) and target expression level.

The fact that DARPins can easily be equipped with a free and unique C-terminal cysteine moiety, to enable site-specific labeling, is an important advantage of recombinant proteins above conventional, non-recombinant antibodies. Traditionally, mAbs are conjugated in a random manner using N-hydroxysuccinimide ester chemistry to link the dye to primary amino groups, generating a heterogenous conjugate in which individual mAbs contain a varying number of dye molecules and exhibit different pharmacokinetics. Site-specific labeling, as used for DARPins, generates homogenous conjugates and prevents steric hindrance of the antigenbinding domain as well as quenching of fluorescence due to high localized fluorophore density. As both Ac2-800CW and Ec4.1-800CW allowed clear visualization of malignant tissue using a clinical NIRF camera system, no detrimental effect of site-specific conjugation was observed.

This study has some limitations. First, any *in vivo* tumor model is only an approximation of clinical practice. While EpCAM is expressed in most normal human epithelia, mice do not naturally express the human EpCAM protein, which might lead to an overestimation of the TBR.<sup>65</sup> However, previous research has shown that EpCAM is overexpressed up to 1000-fold on human tumor tissue compared to healthy tissue, thereby compensating for this potential overestimation.<sup>19,21,66</sup> Furthermore, the level of heterogeneity in human carcinomas is not replicated well in our *in vivo* model and therefore the extent of tumor penetration and diffusion of the tracers cannot be extrapolated. Since the amount of extracellular matrix is inversely correlated with the tumor penetration potential of targeting molecules, the tumor penetration capacity by DARPins reported herein could be reduced in

clinical practice.<sup>55</sup> Even the use of clinically relevant tumour models, such as patient-derived xenografts or complex co-culture models could not compensate for this issue.<sup>67,68</sup> Secondly, it is possible that the optimal time window was outside the measured imaging times. However, ethical standards for animal care limited the number of possible measurements. Therefore, imaging times were chosen based on their clinical practicality. Of note, a time frame of 24 hours between injection and imaging has been extensively used in clinical practice for NIRF imaging of liver metastasis using ICG and was found to be practical.<sup>69</sup>

Our experiments confirmed that Ac2 and Ec4.1 target different EpCAM epitopes with different affinity. Because high affinity is not per se the most important characteristic for tumor targeting, future research could therefore focus on the development of a bivalent Ac2-Ec4.1 DARPin dimer or other construct that may have even better binding potential for tumor-associated EpCAM. However, the opposing effects of avidity and hindered diffusion with the larger size<sup>58</sup> will require an experimental testing of this strategy. The flexible engineerability of DARPins allows for the creation of additional conjugation sites, enabling simultaneous conjugation with additional NIRF dyes or (radio) labels. This may provide opportunities for dual-labeled DARPins that may be used for trimodal NIRF/PA/nuclear imaging and or therapeutic applications via one single administration. For instance, Van Den Brand et al. evaluated the potential for photodynamic therapy of IRDye700DXconjugated EpCAM-binding DARPins Ac2 and Ec1 and showed effective in vitro cytotoxicity on EpCAM-positive human ovarian cancer cell lines. 70 Lastly, considering the clinical availability of IRDye 800CW, a rapid clinical translation of both EpCAM-binding DARPin tracers evaluated herein is feasible.

#### CONCLUSION

To conclude, our findings show that bimodal NIRF/PA imaging using EpCAM-binding DARPin tracers Ac2-8ooCW and Ec4.1-8ooCW allows for clear colon tumor delineation at a rapid and clinically practical time window of 24 hours post-injection. Thanks to both the tumor-specific expression pattern of EpCAM and the optimal pharmacokinetics and flexible manufacturability of DARPins, EpCAM-binding DARPins form a promising class of pan-carcinoma targeting agents. This study provides the preclinical foundation for DARPin-based bimodal NIRF/PA imaging of cancer and paves the way for further optimization, evaluation, and clinical translation of such agents.

#### REFERENCES

- Sung H, Ferlay J, Siegel RL, Laversanne M, Soerjomataram I, Jemal A, et al. Global Cancer Statistics 2020: GLOBOCAN Estimates of Incidence and Mortality Worldwide for 36 Cancers in 185 Countries. CA Cancer J Clin. 2021;71(3):209-49.
- 2 Khan MA, Hakeem AR, Scott N, Saunders RN. Significance of R1 resection margin in colon cancer resections in the modern era. Colorectal Dis. 2015;17(11):943-53.
- 3 Nagtegaal ID, Quirke P. What is the role for the circumferential margin in the modern treatment of rectal cancer? J Clin Oncol. 2008;26(2):303-12.
- 4 Osipov A, Nissen N, Rutgers J, Dhall D, Naziri J, Chopra S, et al. Redefining the Positive Margin in Pancreatic Cancer: Impact on Patterns of Failure, Long-Term Survival and Adjuvant Therapy. Ann Surg Oncol. 2017;24(12):3674-82.
- 5 Osarogiagbon RÜ, Lin CC, Smeltzer MP, Jemal A.
  Prevalence, Prognostic Implications, and Survival
  Modulators of Incompletely Resected Non-Small Cell Lung 21
  Cancer in the U.S. National Cancer Data Base. J Thorac
  Oncol. 2016;11(1):e5-16.
- 6 Vahrmeijer AL, Frangioni JV. Seeing the invisible during surgery. Br J Surg. 2011;98(6):749-50.
- Mieog JSD, Achterberg FB, Zlitni A, Hutteman M, Burggraaf J, Swijnenburg RJ, et al. Fundamentals and developments in fluorescence-guided cancer surgery. Nat Rev Clin Oncol. 2022;19(1):9-22.
- 8 Mieog JSD, Achterberg FB, Zlitni A, Hutteman M, Burggraaf J, Swijnenburg RJ, et al. Fundamentals and developments in fluorescence-guided cancer surgery. Nat Rev Clin Oncol. 2021.
- 9 Handgraaf HJM, Boogerd LSF, Höppener DJ, Peloso A, Sibinga Mulder BG, Hoogstins CES, et al. Longterm follow-up after near-infrared fluorescence-guided resection of colorectal liver metastases: A retrospective multicenter analysis. Eur J Surg Oncol. 2017;43(8):1463-71.
- 10 de Valk KS, Deken MM, Schaap DP, Meijer RP, Boogerd LS, Hoogstins CE, et al. Dose-Finding Study of a CEA-Targeting Agent, SGM-101, for Intraoperative Fluorescence Imaging of Colorectal Cancer. Ann Surg Oncol. 2021;28(3):1832-44.
- 11 Vahrmeijer AL, Hutteman M, van der Vorst JR, van de Velde CJH, Frangioni JV. Image-guided cancer surgery using near-infrared fluorescence. Nature reviews Clinical oncology. 2013;10(9):507-18.
- 12 Almarhaby A, Lees J, Bugby S, Alqahtani M, Jambi L, McKnight W, et al. Characterisation of a near-infrared (NIR) fluorescence imaging systems intended for hybrid gamma-NIR fluorescence image guided surgery. Journal of Instrumentation. 2019;14(07):P07007.
- 13 Attia ABE, Balasundaram G, Moothanchery M, Dinish US, Bi R, Ntziachristos V, et al. A review of clinical photoacoustic imaging: Current and future trends. Photoacoustics. 2019;16:100144.
- 14 Zhao J, Chen J, Ma S, Liu Q, Huang L, Chen X, et al. Recent developments in multimodality fluorescence imaging probes. Acta Pharm Sin B. 2018;8(3):320-38.
- 15 Vermeulen I, Isin EM, Barton P, Cillero-Pastor B, Heeren RMA. Multimodal molecular imaging in drug discovery and development. Drug Discoy Today. 2022;27(8):2086-99.

- 16 Sankpal NV, Brown TC, Fleming TP, Herndon JM, Amaravati AA, Loynd AN, et al. Cancer-associated mutations reveal a novel role for EpCAM as an inhibitor of cathepsin-L and tumor cell invasion. BMC Cancer. 2021;21(1):541.
- 17 Patriarca C, Macchi RM, Marschner AK, Mellstedt H. Epithelial cell adhesion molecule expression (CD326) in cancer: a short review. Cancer Treat Rev. 2012;38(1):68-75.
- 18 Munz M, Baeuerle PA, Gires O. The emerging role of EpCAM in cancer and stem cell signaling. Cancer Res. 2009;69(14):5627-9.
- 19 Spizzo G, Fong D, Wurm M, Ensinger C, Obrist P, Hofer C, et al. EpCAM expression in primary tumour tissues and metastases: an immunohistochemical analysis. J Clin Pathol. 2011;64(5):415-20.
- 20 van Driel PBAA, Boonstra MC, Prevoo HAJM, van de Giessen M, Snoeks TJA, Tummers QRJG, et al. EpCAM as multi-tumour target for near-infrared fluorescence guided surgery. BMC Cancer. 2016;16:884.
- Boogerd LSF, Boonstra MC, Prevoo H, Handgraaf HJM, Kuppen PJK, van de Velde CJH, et al. Fluorescenceguided tumor detection with a novel anti-EpCAM targeted antibody fragment: Preclinical validation. Surg Oncol. 2019;28:1-8.
- 22 Hall MA, Pinkston KL, Wilganowski N, Robinson H, Ghosh P, Azhdarinia A, et al. Comparison of mAbs targeting epithelial cell adhesion molecule for the detection of prostate cancer lymph node metastases with multimodal contrast agents: quantitative small-animal PET/CT and NIRF. J Nucl Med. 2012;3(9):1427-37.
- 23 Plückthun A. Designed Ankyrin Repeat Proteins (DARPins): Binding Proteins for Research, Diagnostics, and Therapy. Annual Review of Pharmacology and Toxicology. 2015;55(1):489-511.
- 24 Sousa F, Castro P, Fonte P, Kennedy PJ, Neves-Petersen MT, Sarmento B. Nanoparticles for the delivery of therapeutic antibodies: Dogma or promising strategy? Expert Opin Drug Deliv. 2017;14(10):1163-76.
- 25 Stumpp MT, Binz HK, Amstutz P. DARPins: a new generation of protein therapeutics. Drug Discov Today. 2008;13(15-16):695-701.
- 26 Stumpp MT, Amstutz P. DARPins: a true alternative to antibodies. Curr Opin Drug Discov Devel. 2007;10(2):153-9
- 27 Shilova ON, Deyev SM. DARPins: Promising Scaffolds for Theranostics. Acta Naturae. 2019;11(4):42-53.
- 28 Stefan N, Martin-Killias P, Wyss-Stoeckle S, Honegger A, Zangemeister-Wittke U, Plückthun A. DARPins recognizing the tumor-associated antigen EpCAM selected by phage and ribosome display and engineered for multivalency. J Mol Biol. 2011;413(4):826-43.
- 29 Tamaskovic R, Simon M, Stefan N, Schwill M, Plückthun A. Designed ankyrin repeat proteins (DARPins) from research to therapy. Methods Enzymol. 2012;503:101-34.
- 30 Simon M, Zangemeister-Wittke U, Plückthun A. Facile double-functionalization of designed ankyrin repeat proteins using click and thiol chemistries. Bioconjug Chem. 2012;23(2):279-86.
- 31 Binz HK, Amstutz P, Kohl A, Stumpp MT, Briand C, Forrer P, et al. High-affinity binders selected from designed ankyrin repeat protein libraries. Nat Biotechnol. 2004;22(5):575-82.

- 32 Tseng W, Leong X, Engleman E. Orthotopic mouse model of colorectal cancer. J Vis Exp. 2007(10):484.
- 33 Baart VM, van der Horst G, Deken MM, Bhairosingh SS, Schomann T. Sier VO. et al. A multimodal molecular imaging approach targeting urokinase plasminogen activator receptor for the diagnosis, resection and surveillance of urothelial cell carcinoma. Eur J Cancer. 2021;146:11-20.
- 34 Tummers WS, Miller SE, Teraphongphom NT, Gomez A, Steinberg I, Huland DM, et al. Intraoperative Pancreatic Cancer Detection using Tumor-Specific Multimodality Molecular Imaging. Ann Surg Oncol. 2018;25(7):1880-8.
- 35 Tummers WS, Willmann JK, Bonsing BA, Vahrmeijer AL, Gambhir SS, Swijnenburg RJ. Advances in Diagnostic and Intraoperative Molecular Imaging of Pancreatic Cancer. Pancreas. 2018;47(6):675-89.
- 36 Martin-Killias P, Stefan N, Rothschild S, Plückthun A, Zangemeister-Wittke U. A novel fusion toxin derived from an EpCAM-specific designed ankyrin repeat protein has potent antitumor activity. Clin Cancer Res. 2011;17(1):100-10.
- 37 Vorobyeva A. Konovalova E. Xu T. Schulga A. Altai M. Garousi J, et al. Feasibility of Imaging EpCAM Expression in Ovarian Cancer Using Radiolabeled DARPin Ec1. Int I Mol Sci. 2020;21(9).
- 38 Vorobyeva A, Bezverkhniaia E, Konovalova E, Schulga A, Garousi J, Vorontsova O, et al. Radionuclide Molecular Imaging of EpCAM Expression in Triple-Negative Breast Cancer Using the Scaffold Protein DARPin Eci. Molecules. 53 He K, Zeng S, Qian L. Recent progress in the molecular
- 39 Tolmachev V, Bodenko V, Orlova A, Schulga A, Deyev SM, Vorobyeva A. Visualization of epithelial cell adhesion molecule-expressing renal cell carcinoma xenografts using designed ankyrin repeat protein Ec1 labelled with (99m)Tc and (125)I. Oncol Lett. 2023;25(1):12.
- 40 Deyev SM, Xu T, Liu Y, Schulga A, Konovalova E, Garousi J, et al. Influence of the Position and Composition of Radiometals and Radioiodine Labels on Imaging of Epcam Expression in Prostate Cancer Model Using the DARPin Ec1. Cancers (Basel). 2021;13(14).
- 41 Bragina O. Chernov V. Schulga A. Konovalova E. Garbukov E, Vorobyeva A, et al. Phase I Trial of (99m)Tc-(HE)(3)-G3, a DARPin-Based Probe for Imaging of HER2 Expression in Breast Cancer. J Nucl Med. 2022;63(4):528-35.
- 42 Zhang Y, Hong H, Severin GW, Engle JW, Yang Y, Goel S, et al. ImmunoPET and near-infrared fluorescence imaging of CD105 expression using a monoclonal antibody dual-labeled with (89)Zr and IRDye 800CW. Am J Transl Res. 2012;4(3):333-46.
- 43 Hu Z, Chen WH, Tian J, Cheng Z. NIRF Nanoprobes for Cancer Molecular Imaging: Approaching Clinic. Trends Mol Med. 2020;26(5):469-82.
- 44 Gioux S, Choi HS, Frangioni JV. Image-guided surgery using invisible near-infrared light; fundamentals of clinical 60 Brandl F, Busslinger S, Zangemeister-Wittke U, Plückthun translation. Mol Imaging. 2010;9(5):237-55.
- 45 Lwin TM, Hernot S, Hollandsworth H, Amirfakhri S, Filemoni F, Debie P, et al. Tumor-specific near-infrared nanobody probe rapidly labels tumors in an orthotopic mouse model of pancreatic cancer. Surgery. 2020:168(1):85-91.
- 46 van Driel PB, van der Vorst JR, Verbeek FP, Oliveira S, Snoeks TJ, Keereweer S, et al. Intraoperative fluorescence

- delineation of head and neck cancer with a fluorescent anti-epidermal growth factor receptor nanobody. Int J Cancer. 2014;134(11):2663-73.
- 47 Nichols IW. Bae YH. EPR: Evidence and fallacy. I Control Release. 2014;190:451-64.
- 48 Emile SH, Elfeki H, Shalaby M, Sakr A, Sileri P, Laurberg S, et al. Sensitivity and specificity of indocyanine green nearinfrared fluorescence imaging in detection of metastatic lymph nodes in colorectal cancer: Systematic review and meta-analysis. J Surg Oncol. 2017;116(6):730-40.
- 49 Harlaar NJ, Koller M, de Jongh SJ, van Leeuwen BL, Hemmer PH, Kruijff S, et al. Molecular fluorescenceguided surgery of peritoneal carcinomatosis of colorectal origin: a single-centre feasibility study. Lancet Gastroenterol Hepatol. 2016;1(4):283-90.
- 50 Pretzsch E, Bösch F, Neumann J, Ganschow P, Bazhin A, Guba M, et al. Mechanisms of Metastasis in Colorectal Cancer and Metastatic Organotropism: Hematogenous versus Peritoneal Spread. J Oncol. 2019;2019:7407190.
- 51 Deyev S, Vorobyeva A, Schulga A, Proshkina G, Güler R, Löfblom J, et al. Comparative Evaluation of Two DARPin Variants: Effect of Affinity, Size, and Label on Tumor Targeting Properties. Mol Pharm. 2019;16(3):995-1008.
- 52 Zhou C, Urbauer DL, Fellman BM, Tamboli P, Zhang M, Matin SF, et al. Metastases to the kidney: a comprehensive analysis of 151 patients from a tertiary referral centre. BJU Int. 2016;117(5):775-82.
- imaging of therapeutic monoclonal antibodies. J Pharm Anal. 2020;10(5):397-413.
- 54 Dammes N, Peer D. Monoclonal antibody-based molecular imaging strategies and theranostic opportunities. Theranostics. 2020;10(2):938-55.
- 55 Xenaki KT, Oliveira S, van Bergen En Henegouwen PMP. Antibody or Antibody Fragments: Implications for Molecular Imaging and Targeted Therapy of Solid Tumors. Front Immunol. 2017:8:1287.
- 56 Schmidt MM, Wittrup KD, A modeling analysis of the effects of molecular size and binding affinity on tumor targeting, Mol Cancer Ther, 2009;8(10):2861-71.
- 57 Münz M, Murr A, Kvesic M, Rau D, Mangold S, Pflanz S, et al. Side-by-side analysis of five clinically tested anti-EpCAM monoclonal antibodies. Cancer Cell Int. 2010;10:44.
- 58 Zahnd C, Kawe M, Stumpp MT, de Pasquale C, Tamaskovic R, Nagy-Davidescu G, et al. Efficient tumor targeting with high-affinity designed ankyrin repeat proteins: effects of affinity and molecular size. Cancer Res. 2010;70(4):1595-605.
- 59 Wittrup KD, Thurber GM, Schmidt MM, Rhoden II. Practical theoretic guidance for the design of tumortargeting agents. Methods Enzymol. 2012;503:255-68.
- A. Optimizing the anti-tumor efficacy of protein-drug conjugates by engineering the molecular size and half-life. J Control Release. 2020;327:186-97.
- 61 Sato K, Gorka AP, Nagaya T, Michie MS, Nani RR, Nakamura Y, et al. Role of Fluorophore Charge on the In Vivo Optical Imaging Properties of Near-Infrared Cyanine Dye/Monoclonal Antibody Conjugates. Bioconjug Chem. 2016;27(2):404-13.

- 62 Cilliers C, Nessler I, Christodolu N, Thurber GM. Tracking Antibody Distribution with Near-Infrared Fluorescent Dyes: Impact of Dye Structure and Degree of Labeling on Plasma Clearance. Mol Pharm. 2017;14(5):1623-33.
- 63 Agarwal P, Bertozzi CR. Site-specific antibody-drug conjugates: the nexus of bioorthogonal chemistry, protein engineering, and drug development. Bioconjug Chem. 2015;26(2):176-92.
- 64 Zhegalova NG, He S, Zhou H, Kim DM, Berezin MY. Minimization of self-quenching fluorescence on dves conjugated to biomolecules with multiple labeling sites via asymmetrically charged NIR fluorophores. Contrast Media Mol Imaging. 2014;9(5):355-62.
- 65 Trzpis M, McLaughlin PM, Popa ER, Terpstra P, van Kooten TG, de Leij LM, et al. EpCAM homologues exhibit epithelial-specific but different expression patterns in the kidney. Transgenic Res. 2008;17(2):229-38.
- 66 Went P, Vasei M, Bubendorf L, Terracciano L, Tornillo L, Riede U, et al. Frequent high-level expression of the immunotherapeutic target Ep-CAM in colon, stomach, prostate and lung cancers. Br J Cancer. 2006;94(1):128-35.
- 67 De Angelis ML, Francescangeli F, Nicolazzo C, Xhelili E. La Torre F, Colace L, et al. An Orthotopic Patient-Derived Xenograft (PDX) Model Allows the Analysis of Metastasis-Associated Features in Colorectal Cancer, Front Oncol. 2022;12:869485.
- 68 Dolznig H. Rupp C. Puri C. Haslinger C. Schweifer N. Wieser E, et al. Modeling colon adenocarcinomas in vitro a 3D co-culture system induces cancer-relevant pathways upon tumor cell and stromal fibroblast interaction. Am J Pathol. 2011;179(1):487-501.
- 69 van Manen L, Handgraaf HJM, Diana M, Dijkstra J, Ishizawa T, Vahrmeijer AL, et al. A practical guide for the use of indocyanine green and methylene blue in fluorescence-guided abdominal surgery. J Surg Oncol. 2018;118(2):283-300.
- 70 van den Brand D. van Lith SAM, de Jong JM, Gorris MAJ. Palacio-Castañeda V, Couwenbergh ST, et al. EpCAM-Binding DARPins for Targeted Photodynamic Therapy of Ovarian Cancer, Cancers (Basel), 2020:12(7).

# PART III Summary, general discussion and future perspectives

# **CHAPTER 9**

Summary



Despite recent therapeutic advances, radical surgery remains the cornerstone of curative treatment of gastrointestinal cancers, including esophageal, gastric, pancreatic and colorectal cancer. Preoperatively, adequate tumor staging is pivotal for selecting patients for surgery. Several surgical and diagnostic challenges currently are currently encountered and should be overcome to further optimize surgical treatment of gastrointestinal cancers. Preoperatively, current imaging methods such as, MRI and FDG-PET imaging provide crucial information on tumor size, invasion, nodal involvement and metastases, but insufficient sensitivity/specificity for some tumor types hampers adequate surgical planning. This may lead to unnecessary resections or biopsies, additional imaging procedures, and futile administration of systemic therapy, thereby increasing burden for patients and healthcare costs. Intraoperatively, distinguishing tumor tissue from healthy surrounding tissue, especially after neoadjuvant therapy, is challenging and the increased adoption of minimally invasive surgery has complicated this process even more. This may lead to irradical resections, which are associated with increased local recurrence rates and reduced patient survival for most tumor types.

As a solution, targeted molecular imaging, thus directed at biomarkers expressed in the tumor, may enhance tumor identification. Preoperatively, targeted PET imaging is of particular interest. Intraoperatively, near-infrared fluorescence (NIRF) imaging, also known as fluorescence-guided surgery, is increasingly employed. By providing real-time visualization of tissue of interest without interfering with the visible surgical field, NIR fluorescence (NIRF) imaging, optionally combined with photoacoustic (PA) imaging, aids surgeons in 1) intraoperative staging by detection of (clinically occult) disease, including metastases, and 2) tumor-free margin assessment.

This thesis aimed to address challenges related to biomarkers and targeting moieties encountered during molecular imaging in gastrointestinal cancers, with a focus on pancreatic and gastric cancer. While the findings of Part I of this thesis may be extrapolatable to both NIRF imaging and targeted PET imaging, Part II focuses on bimodal NIRF/PA imaging of gastrointestinal cancers.

# Part I: Evaluation of biomarkers for molecular imaging in gastrointestinal tumors

Despite technical dissimilarities between both PET and NIRF imaging, selecting the suitable biomarkers remains a key perquisite for successful tumor visualization of both techniques. Biomarkers of some promising molecular imaging tracers appear to have drawbacks, including heterogenic expression and presence on non-malignant tissue. These drawbacks necessitate a continuous need for exploration of novel, less-conventional biomarkers, including tumor-associated glycans and highly glycosylated proteins, such as mucins.

Chapter 2 provides a narrative review on the most promising glycans and highly glycosylated proteins and highlights the potential of these structures as imaging targets by discussing the recent preclinical and clinical research into glycan-related tumor imaging. Aberrant glycosylation of proteins and lipids is a fundamental hallmark of almost all cancer types and contributes to tumor progression. Additionally, overexpression of glycoproteins that carry aberrant glycans, such as mucins and proteoglycans, is observed. Considering their low abundance or absence in healthy tissues and very dense expression on tumor cells, tumorassociated glycans are of particular interest as biomarkers for molecular imaging of tumors. This potential is further augmented by their presence on the outermost layer of the cell membrane, thereby making glycans easily accessible by targeting moieties, as well as their presence on multiple tumor-associated proteins simultaneously. This theoretically allows targeting of multiple proteins simultaneously using an imaging tracer directed at a single glycan. As described in this chapter, several glycan and heavily glycosylated proteins have been evaluated as targets for imaging in both preclinical and early-phase clinical studies. Promising glycan for imaging of gastrointestinal carcinomas identified in this chapter include: Lewisa/c/x (Lea/c/x), sialyl-di-Lewisa (sdi-Lea), sialyl-Lewisx (sLex), sialyl-Lewisa(sLea, also known as CA19-9), and sialyl-Thomsen-Nouveau (sTn). Regarding, highly glycosylated proteins, mucin-1 (MUC1) and mucin-5AC (MUC5AC) are of particular interest for imaging of gastrointestinal cancers.

The knowledge of Chapter 2 was applied in Chapter 3 which evaluates the potential of these glycans and mucins to serve as targets for imaging of pancreatic ductal adenocarcinoma (PDAC) using immunohistochemistry on human tissue specimens. Expression level in human PDAC tissue specimens was determined using immunohistochemical staining and was quantified using a semi-automated digital image analysis workflow. Expression of Lea/c/x, sdi-Lea, sLea, sLex, sTn, MUC1 and MUC5AC on primary PDAC tissue was high and was similar between patients who received neoadjuvant therapy (NAT) and patients who did not. Moreover, all biomarkers were significantly lower expressed on chronic pancreatitis, healthy pancreatic and duodenal tissue specimens, except for sTn and MUC1, which showed a strong expression on duodenum and healthy pancreatic tissue, respectively. These biomarkers are therefore considered less suitable for PDAC imaging. With moderate to high sensitivity and specificity for

189 CHAPTER 9 • Summary 189

distinguishing tumor-positive from tumor-negative lymph nodes, all biomarkers seem promising biomarkers for staging of nodal involvement in PDAC. This chapter paves the way for the development and evaluation of  $Le^{a/c/x}$ -,  $sdi-Le^{a}$ -,  $sLe^{x}$ - and MUC5AC-specific tracers for molecular imaging of PDAC imaging and their subsequent introduction into the clinic.

A second challenge involves the underexploration of the relative expression between malignant and non-malignant tissue types of some established imaging biomarkers, which can be considered crucial data for determining suitability of imaging biomarkers. Therefore, **Chapter 4** evaluates the potential of  $\alpha_V \beta_6$ , CEACAM5, EGFR, epithelial cell adhesion molecular (EpCAM) and human epidermal growth factor receptor- 2 (HER2), as targets for imaging of primary gastric cancer and metastases. For this purpose, immunohistochemistry on human tissue specimens was used. Positive biomarker expression in primary gastric tumors was observed in 71% to 93% of patients between the biomarkers. Tumor expression of CEACAM5, EGFR and EpCAM was higher compared to healthy stomach tissue expression, while this was not the case for  $\alpha_V \beta_6$  and HER2, making these biomarkers unsuitable for gastric cancer imaging. Tumor-positive lymph nodes could be distinguished from tumor-negative lymph nodes with accuracy ranging from 82% to 93% between biomarkers. Also, CEACAM5, EGFR and EpCAM expression were abundantly expressed on distant metastases, with positive expression in 88% to 95% of tissue specimens. These findings show that CEACAM5, EGFR and EpCAM are promising biomarkers for molecular imaging of primary gastric cancer, as well as visualization of both lymph node and distant metastases.

The third and last challenge regarding imaging biomarkers addressed in Part I concerns the heterogenic expression of established imaging biomarkers, which hampers universal application of molecular imaging tracers. This could be addressed by screening for biomarker expression preoperatively. However, for some tumor types, it remains unknown whether biopsy specimens can be used to predict primary tumor expression. Therefore, Chapter 5 evaluates the concordance and correlation of integrin  $\alpha_V\beta_6$ , CEACAM5, epidermal growth factor receptor (EGFR), mesothelin, Lea/c/x, and sdi-Lea expression between preoperatively obtained fine-needle biopsy (FNB) and primary PDAC tissue specimens. Concordance was found to be moderate to high for all biomarkers, ranging from 61% to 85%. Correlation between FNB tissue specimen expression and primary PDAC expression was also evaluated and was moderate to strong for CEACAM5, EGFR, mesothelin, sdi-Lea and Lea/c/x, suggesting that biomarker expression on FNB tissues is predictive for expression level in primary PDAC tissue specimens.

However, although no correlation was observed for  $\alpha\nu\beta_6$ , its expression was consistently high on both FNB and primary PDAC tissue specimens. Importantly, NAT had limited effect on concordance for all biomarkers. Moreover, no effect on correlation of biomarker expression between FNB and primary PDAC tissue specimens was observed, except for mesothelin. This chapter demonstrates that biomarker expression in FNB tissues is, for most of the investigated biomarkers, predictive for primary tumor expression, irrespective of the application of NAT. These findings thereby provide the preclinical foundation for the clinical application of a FNB-based biomarker-screening workflow, eventually facilitating a patient-specific approach of molecular imaging tracer administration in PDAC.

# Part II: Preclinical evaluation of novel tracers for near-infrared fluorescence and photoacoustic imaging of gastrointestinal tumors

Part II of this thesis extends the work of Part I by providing a preclinical evaluation of novel tracers for bimodal NIRF/photoacoustic (PA) imaging. Chapter 6 describes the preclinical proof-of-concept of targeting tumor-associated glycans for NIRF imaging of gastrointestinal cancers using a tracer directed at Lea/c/x (evaluated for PDAC in Chapter 3). Using immunohistochemistry on human tissue specimens of primary gastric, pancreatic and colon tumors and tissue specimens containing healthy surrounding stomach, colon and pancreas tissue, respectively, high tumor expression and limited expression on healthy surrounding tissue was confirmed. However, expression of Lea/cxwas moderate in some cases. Thereafter, the Lea/c/x-targeting chimeric antibody CH88.2 was conjugated to NIR fluorophore IRDye 800CW and intravenously administered to HT-29 (human colon carcinoma) and BxPC-3 (human pancreatic carcinoma) tumor-bearing mice at a dose on 1 nmol. Using the clinical NIRF camera system, a mean tumor-to-background ratio (TBR) of 2.2  $\pm$  0.3 was observed in the HT-29 tumors and a TBR of 1.8  $\pm$  0.3 (Pearl:  $1.9 \pm 0.5$ ) was achieved in the moderate Lea/c/x-expressing BxPC-3 model at 96 hours after injection. In both models, tumors could be adequately localized and delineated by NIRF for up to 1 week. Ex vivo analysis confirmed full tumor penetration of the tracer and low fluorescence signals in other organs. This chapter demonstrates the potential of targeting Lewis glycans for fluorescence-guided surgery of gastrointestinal cancers.

This promising work was confirmed and extended in **Chapter 7**, in which we describe the preclinical evaluation of CH88.2-800CW as well as sdi-Lea-targeting tracer CH129-800CW for bimodal NIRF/PA imaging of gastrointestinal carcinomas. An extensive immunohistochemical evaluation was performed in which

Lea/c/x and sdi-Lea expression was quantified on a larger tissue specimen cohort compared to **Chapter 6**. Lea/c/x and sdi-Lea were highly expressed on pancreatic, gastric and colorectal cancer tissue, with limited expression on healthy surrounding tissue. However, Lea/c/x expression on healthy colorectal epithelium was strong, making this biomarker less suitable for imaging of colorectal cancer. At 96 hours (4 days) post-injection, all orthotopic tumors could be excellently identified with the clinical Artemis NIRF imager with mean CH88.2-800CW and CH129-800CW tumor-to-background ratios of  $4.8 \pm 1.4$  and  $4.9 \pm 0.5$  for the HT-29\_luc2 model, and  $2.5 \pm 0.3$  and  $2.9 \pm 0.4$  for the BxPC-3\_luc2 (pancreatic cancer) model, respectively. Strong PA signal was observed within all tumor for both CH88.2-800CW and CH129-800CW. Biodistribution analyses showed high tumor fluorescence with minimal signal in healthy organs, including the liver and kidneys. These findings show that bimodal NIRF/PA imaging employing CH88.2-800CW and CH129-800CW facilitates real-time, high-contrast tumor visualization. Given their target's strong and tumor-specific expression, both tracers hold promise as effective imaging agents for imaging of selected gastrointestinal cancers.

Part II focuses on a second topic of research, namely the targeting moieties of molecular imaging tracers. Despite advantages of monoclonal antibodies as targeting moieties for molecular imaging, such as high specificity, affinity and stability, they may not fully penetrate tumors and their long half-life in the circulation leads to a suboptimal time between injection and the optimal imaging timepoint of 3-5 days. As a solution, alternative targeting vehicles are considered, including designed ankyrin repeat proteins (DARPins), but their potential for molecular imaging in gastrointestinal cancers is underexplored. Chapter 8 evaluates preclinical potential of EpCAM-binding DARPins as targeting moieties for bimodal NIRF/PA of gastrointestinal cancers. EpCAM is considered a promising biomarker for target imaging, with overexpression described in most carcinomas. EpCAM-binding DARPins Ac2, Ec4.1, and non-binding control DARPin Off7 were conjugated to IRDye 800CW. Using an in vivo dose comparison study, 6 nmol and 24 h were established as the optimal in vivo dose and imaging time point for both DARPin tracers. At 24 h post-injection, mean tumor-to-background ratios of 2.6 ± 0.3 and 3.1 ± 0.3 were observed for Ac2-800CW and Ec4.1-800CW, respectively, allowing clear tumor delineation using the clinical Artemis NIRF imager. Also, strong PA signal was present in the tumors. Biodistribution analyses in non-neoplastic tissue showed high fluorescence signal in the liver and kidney, reflecting clearance of the DARPin tracers. These results show that EpCAMbinding DARPins are a promising class of targeting moieties for pan-carcinoma NIRF/PA imaging, providing clear tumor delineation at 24 hours post-injection.

192 CHAPTER 9 • Summary 193

# **CHAPTER 10**

General discussion and future perspectives



This thesis evaluated biomarkers and novel tracers for molecular imaging in gastrointestinal cancers, with a focus on pancreatic and gastric cancer. This chapter reflects on the key findings and implications of this thesis as well as on future perspectives.

# Exploration of novel imaging biomarkers: tumor-associated glycans and mucins

In the search for novel biomarkers suitable for molecular imaging, this thesis identified tumor-associated glycans and heavily glycosylated proteins, including mucins, as targets of particular interest (Chapters 2 and 3). Moreover, due to their superior tumor-specificity and expression in most patients,  $Le^{a/c/x}$  and sdi-Lea were identified as promising biomarkers for molecular imaging of PDAC (Chapter 3), as well as gastric and colorectal tumors (Chapters 6 and 7). While tumor expression of Lea/c/x and sdi-Lea was mostly strong, their main strength lies in the differential expression between tumor and benign/healthy surrounding tissues, except for Lea/c/x in colorectal tumors. In PDAC, for instance, this differential expression was larger compared to EGFR, HER2, EpCAM and VEGF in PDAC, and, in gastric cancer, compared to  $\alpha_V \beta_6$  and HER2 (Chapter 3).<sup>1,2</sup> This indicates that imaging tracers targeting tumor-associated glycans Lea/c/x and sdi-Lea may offer superior imaging capabilities compared to several established molecular imaging tracers. Nevertheless, intratumoral heterogeneity of Lea/c/x and sdi-Lea expression was still observed in **Chapters 3, 5, 6 and 7**, indicating that some limitations of current imaging targets have not yet been overcome. Although identifying a 'perfect' imaging biomarker may be an utopia, targeting tumor-associated glycans is currently in an early stage, partially relating to the intrinsic complexity of the glycome accompanied by a lack of robust glycoanalytical methods.<sup>3</sup> It is expected that advances in glycobiology research, such as the application of MALDI-TOF mass spectrometry imaging, will contribute to the discovery of novel tumor-associated glycans, potentially with superior suitability for molecular imaging.<sup>3,4</sup>

## Targeting the tumor stroma

Apart from tumor-associated glycans and mucins, stromal targets represent another promising class of biomarkers for tumor imaging. As the stromal compartment comprises up to 90% of the mass of some pancreatic tumors, these targets are of particular interest in PDAC.<sup>5</sup> One example of such a target is fibroblast activating protein (FAP), which has been found promising not only for pancreatic cancer,

but is also expressed on cancer-associated fibroblasts of more than 90% of carcinomas. <sup>6,7</sup> Regarding FAP-targeted positron emission tomography (PET) imaging, several clinical trials have been performed for many tumor types, with encouraging results. <sup>8,9</sup> For instance, the FAP-targeting PET tracer <sup>18</sup>F-FAPI-04 has shown to outperform conventional [<sup>18</sup>F]Fluorodeoxyglucose (FDG)-PET imaging of primary and metastatic PDAC in the clinical setting. <sup>10,11</sup> A notable limitation of FAP, however, is its expression in tissue remodeling processes, such as wound healing and chronic inflammation, which can compromise the distinction between benign and malignant. <sup>12</sup> This of particular importance in patients who have received neoadjuvant therapy (NAT), a treatment known to induce increased fibrosis and necrosis. <sup>13</sup> The extent to which FAP expression is altered by NAT in PDAC remains insufficiently studied. Given the growing application of NAT in this tumor type, it is crucial to identify and target biomarkers that remain consistently expressed after NAT, such as the targets investigated in Chapters 3 and 5.

## Underexplored differential expression of current imaging biomarkers

Chapter 4 identified CEACAM5, EGFR and EpCAM as suitable imaging biomarkers for gastric cancer. Several targeted PET and NIRF imaging tracers targeting these biomarkers have been evaluated in clinical trials. For instance, a phase 1 trial evaluating CEACAM5-targeted tracer [111In]In-DOTA-labetuzumab-IRDye8ooCW for multimodal preoperative PET and intraoperative radioguidance and NIRF imaging in peritoneal metastases of colorectal cancer was recently conducted and allowed pre- and intraoperative identification of previously undetected lesions, altering clinical strategy in three patients. Also, EGFR-targeting panitumumab-IRDye 8ooCW allowed detection of occult lymph node metastases using bimodal NIRF/PA imaging in proof-of-concept study in head and neck cancer. These encouraging clinical results, supplemented with the immunohistochemical (IHC) data presented in Chapter 4, allow and necessitate rapid clinical evaluation of such tracers in gastric cancer.

As development and characterization of novel molecular imaging tracers can take years, it is crucial to evaluate the potential of current imaging tracers' targets across different tumor types to maximize their utility. IHC studies can provide sufficient evidence to apply (clinically evaluated) imaging tracers in other tumor types. Given the limitations of most biomarkers for molecular imaging, identifying novel biomarkers also remains essential. The optimal strategy combines both approaches, through which we can provide short-term solutions for

pre- and intraoperative tumor visualization, while simultaneously investing in the development of novel tracers which may offer superior specificity or sensitivity. This ensures that patients could benefit from the latest advances without unnecessary delays.

# Selecting molecular imaging biomarkers: revised criteria and implications for practice

Chapter 3 and 4 show that it is crucial to investigate expression of biomarkers in the full anatomical context of the tumor to establish their potential as imaging biomarkers. Traditionally, however, most IHC studies investigating biomarker expression in human tissue specimens have solely investigated the 'tumor-versus-normal' expression of biomarkers. Instead, their expression should be evaluated in primary tumors after neoadjuvant therapy, in healthy surrounding tissues frequently invaded by the primary tumor (eg. duodenum in distal gastric cancer), in tumor-positive and -negative lymph nodes, distant metastases, as well as on benign surrounding tissue (eg. pancreatitis in PDAC). Lastly, but not evaluated in this thesis, biomarkers could be selected based on their expression in premalignant tissue, such as pancreatic intraepithelial neoplasia (PanIN) lesions or polyps with high-grade dysplasia in the case of PDAC and colorectal cancer, respectively. Future work should investigate these 'revised' criteria to guide tracer development.

Besides demonstrating (un)suitability of biomarkers for molecular imaging, these data also facilitate selective employment of tracers in certain conditions. For instance, application of a CEACAM5-targeted imaging tracer would not be recommended in proximal gastric cancer invading the gastro-esophageal junction (Chapter 4). Nevertheless, as limitations of IHC are present (discussed in detail below), it remains to be clarified to what extent quantified IHC staining truly reflects protein expression. Clinical imaging studies are therefore required to definitely establish the true impact of biomarker expression on surrounding tissue on a tracer's imaging potential.<sup>16</sup>

## Addressing heterogenetic expression of current imaging biomarkers

This thesis additionally evaluated a workflow for preoperative biomarker screening using IHC in PDAC (Chapter 5). Although the predictive value of FNB expression for primary tumor expression was considerable for most biomarkers, concordance was not always present. This may have been caused by intratumoral heterogeneity of biomarker expression in PDAC, which was also described in Chapter 3. Assuming heterogeneity, biomarker expression in biopsy material may not invariably

include positive biomarker expression in the tumor, and vice versa (**Chapter 5**). Diminishing intratumor heterogeneity as a source of bias could, for instance, be achieved by taking multiple core biopsies of the tumor, however this may not be feasible in clinical practice.<sup>17</sup>

Also, heterogeneity of biomarker expression between multiple tumor lesions in one patient may be present, which could complicate adequate tumor staging as not all lesions show positive signal during imaging.<sup>18,19</sup> Although the workflow described in **Chapter 5** cannot fully address this, concordance between biomarker expression in biopsies, primary tumors and (lymph node) metastases could be studied for the biomarkers evaluated in **Chapter 5**, as was performed for folate receptor-α by Boogerd et al. in breast and lung cancer.<sup>19</sup> Alternatively, targeted PET imaging could be performed to validate expression of an imaging biomarker, followed by administration of a NIRF imaging tracer. Another solution to the heterogeneity problem may be the employment of multiple tracers simultaneously or using a bispecific tracer. As demonstrated by the co-expression analyses of **Chapters 3 and 4**, a theoretical bispecific tracer could increase imaging capabilities, for some biomarker combinations, to virtually all patients within a single tumor type. Of note, targeting two biomarkers simultaneously has shown to increase tumor uptake *in vivo*.<sup>20</sup>

As more molecular imaging tracers become available for a single tumor type, biomarker screening will play a central role in personalizing imaging approaches, allowing suitable tracer selection to optimize tumor visualization. Upon clinical validation, the biomarker screening workflow could be conveniently integrated into clinical practice, as IHC is commonly performed on FNB tissue specimens for histological diagnosis of PDAC.<sup>21</sup> It is crucial that future studies investigate similar biomarker screening workflows in other gastrointestinal cancers. However, several drawbacks of IHC should be considered which will be discussed below.

#### IHC and scoring: critical evaluation

Technical biases of IHC, a technique extensively used in **Part I** of this thesis, include, but are not limited to tissue fixation and processing, antigen retrieval methods, endogenous peroxidase activity, and the secondary antibody used in the process, all of which can affect final staining results.<sup>22</sup> Moreover, primary antibodies used in IHC often bind different epitopes on the protein than the associated molecular imaging tracer. As different epitopes on the same protein may exhibit varying expression in tissues, the translational value of IHC studies may become

compromised.<sup>23,24</sup> IHC studies must therefore align the IHC antibody's epitope with the epitope targeted by the imaging tracer.

Another issue is the manual scoring of IHC staining, which suffers from intra- and interobserver variability, especially when staining is heterogenous, as was observed for some biomarkers evaluated in **Chapters 3**, 4 and 5.25-27 Semiautomated image analysis provides a solution, allowing highly reproducible and accurate cell detection and staining quantification using the H-score (range: o-300), as was demonstrated in Chapters 3 and 5 using QuPath.28 However, training such software is labor intensive and still requires involvement of a dedicated pathologist for classification of tumor and non-malignant tissue, as well as validation of cell detection classifier algorithms. Despite these challenges, using QuPath offers significant advantages, especially for difficult-to-identify tumor types such as PDAC, and holds promise for clinical application. Although limitations of IHC warrant cautious interpretation of results, it offers a flexible, efficient and low-cost approach to evaluate biomarker expression in human tissue specimens, offering crucial information for suitability of molecular imaging biomarkers, as demonstrated in Part I of this thesis. Lastly, while selecting an appropriate biomarker is essential for successful tumor visualization, effective molecular imaging hinges on a complex interplay between biomarker properties, (photo) chemical properties and pharmacokinetics of the tracer, imaging system characteristics, to name just a few. This highlights the relevance of thorough in vitro and in vivo testing of imaging tracers, as was performed in Part II.

# Targeting tumor-associated glycans for NIRF/PA imaging of gastrointestinal tumors

In **Part II** of this thesis, the preclinical potential of tumor-associated glycan-binding tracers CH88.2-8ooCW and CH129-8ooCW for bimodal NIRF and photoacoustic (PA) imaging of gastrointestinal cancers was demonstrated (**Chapters 6 and 7**). Thereby, combined with the findings from **Chapters 2, 3 and 5**, this thesis brought the concept of glycan targeting an important step forward. Despite the potential of tumor-associated glycans as biomarkers for imaging, a limited number of preclinical and clinical studies into glycan imaging has been conducted, as was discussed in **Chapter 2**. Clinically, sLe<sup>a</sup> (also known as CA19-9), a glycan structurally related to Le<sup>a/c/x</sup> and sdi- Le<sup>a</sup>, has been targeted for PET imaging in pancreatic cancer using the antibody-based tracer [89Zr]-DFO-HuMab-5B1, and was able to detect primary tumors and distant metastases, as well as sub-centimeter lymph node

metastases not visible with conventional imaging.<sup>29,30</sup> As demonstrated in **Chapter** 3, expression of Le<sup>a/c/x</sup> and sdi-Le<sup>a</sup>on chronic pancreatitis was lower compared to sLe<sup>a</sup> expression, thereby suggesting the superiority of both glycans as PDAC imaging biomarkers. Further clinical evaluation of CH88.2-800CW and CH129-800CW for bimodal NIRF/PA imaging of gastrointestinal cancers is warranted.

# DARPins as targeting moieties for NIRF/PA imaging of gastrointestinal tumors

Chapter 8 provided the first preclinical evidence that bimodal NIRF/PA imaging of tumors using DARPins is feasible. DARPin-based molecular imaging has particularly focused on PET imaging.<sup>31</sup> The first in-human DARPin imaging study used HER2-targeted tracer 99mTc-(HE)3-G3 for SPECT imaging of breast cancer and showed clear visualization of both primary and metastatic breast cancer, with a favorable safety and tolerability profile.<sup>31</sup> Preclinically, the EpCAM-targeting DARPin tracer [125] I-PIB-Ec1 was evaluated for PET imaging in an ovarian cancer xenograft model and showed a tumor-to-blood ratio of 31 at 24 hours post-injection, providing high-contrast tumor delineation.<sup>32</sup> Also, the tracer showed similarly promising results for SPECT/CT of triple-negative breast cancer. 33 A phase 1 trial evaluating this tracer for PET imaging of the tracer in ovarian and lung cancer is currently ongoing (NCTo6386653) and the results are eagerly awaited. The promising clinical findings of DARPin-based imaging tracers combined with the (over)expression of EpCAM in virtually all gastrointestinal malignancies, including gastric cancer (Chapter 4), lung, breast, prostate, bladder, ovarian, thyroid and head and neck carcinomas, suggest broad application of EpCAM-binding DARPins as molecular imaging tracers.34

# Selecting targeting moieties

Although mAbs have been the first targeting moiety of choice for molecular imaging, owing to their high specificity, affinity and stability, an increasing number of smaller-sized alternatives, such as DARPins, have become available.<sup>35</sup> Although this thesis did not directly compare mAbs and DARPins, as their targets were different, various factors should be considered when choosing a targeting moiety, which include molecular size, conjugation method, and several practical aspects.

As the hydrodynamic volume of a targeting moiety is inversely correlated with its extravasation and tumor penetration potential, tumor accumulation of mAbs take longer compared to DARPins, often requiring 3-5 days between injection and

imaging.<sup>36</sup> Conversely, DARPins extravasate quickly and allow a shorter interval between injection and imaging but require a higher (picomolar) affinity for similar tumor uptake to prevent backflow into the circulation and subsequent renal elimination.<sup>36,38</sup> Also, DARPins may provide better tumor penetration compared to mAbs due to their smaller size.<sup>39</sup>

The conjugation method, i.e. the attachment of a dye/radiolabel to a targeting moiety, is a second critical factor. The heterogeneous mixture after N-hydroxy succinimide-ester coupling of mAbs is susceptible to self-quenching and blocking of antigen-binding domains, thereby reducing brightness and binding potential of the construct, respectively.<sup>40-42</sup> Conversely, DARPins can be conjugated site-specifically through maleimide labelling using free cysteines that can be introduced site-specifically.<sup>39</sup> Simultaneously, a synthetic amino acids such as azidohomoalanine (Aha) can be introduced to allow coupling of effector moieties via click chemistry, allowing conjugation of two different dyes and allowing multimodal tumor imaging.<sup>43</sup>

Thirdly, practical aspects should be considered, such as production costs, which are substantially higher for mAbs compared to DARPins. However, retooling therapeutic mAbs for imaging purposes through conjugation with approved dyes or radiolabels, may reduce production costs and speed-up clinical translation.<sup>44,45</sup> Also, the interval time between injection and imaging longer than one day requires patient to make two hospitals visits, which is less attractive from a practical standpoint. Noteworthy, this timing has proven feasible in clinical practice, as indocyanine green (ICG) is also administrated 24 hours before colorectal liver metastasis resection.<sup>46</sup>

Eventually, it is to the end-user who decides if the benefits outweigh the draw-backs. In our experience, mAbs tend to show higher tumor signal than smaller targeting moieties, but tumor-to-background ratios may be similar.<sup>47</sup> High tumor signal remains a key condition for adequate tumor visualization, especially of smaller lesions that may not be expected to be present based on preoperative imaging. Conversely, DARPins offer a highly promising alternative to mAbs for molecular imaging considering their optimal pharmacokinetic profile, rapid production, and versatile engineerability.<sup>38</sup>

# Tumor models in preclinical molecular imaging research

A final topic of discussion involves the tumor models used during *in vivo* experiments. While tumor models, by definition, aim to approximate clinical practice,

several drawbacks of the *in vivo* models used in **Chapters 6, 7 and 8** can be identified. First, these models do not reflect the level tumor heterogeneity and histomorphology of human tumors, including their vascular, lymphatic and immune compartments.<sup>48</sup> Consequently, the enhanced permeability and retention (EPR) effect - which results in intratumoral uptake and trapping of tracers due to hyperpermeable tumor vasculature and inadequate lymphatic drainage - is not well modeled.<sup>49</sup> This can lead to aberrant tumor uptake of imaging tracers in preclinical models, potentially under- or overestimating their clinical utility.<sup>36</sup> This underlines the importance of a negative control tracer, ideally consisting of a similar targeting vehicle conjugated to the same fluorophore but directed at a target that is not expressed in the tumor, which would theoretically suffer similarly from the EPR effect.

Despite these limitations, our preclinical *in vivo* studies provide crucial information for the clinical translation of molecular imaging tracers. After all, the primary aim of *in vivo* studies in molecular imaging research is to determine whether an imaging tracer reaches its intended molecular target on the tumor in a living organism and can be visualized using a dedicated imaging system. A second application of *in vivo* studies is to study pharmacokinetic properties of the tracer, including hepatic or renal clearance. Lastly, while preclinical molecular imaging studies remain indispensable, one must realize that the true potential of a molecular imaging tracer can only be assessed in the clinical setting.

#### **FUTURE PERSPECTIVES**

The field of molecular imaging is rapidly evolving and increasingly adopted within surgical oncological care. The current arsenal of targeting imaging biomarkers needs to be expanded to overcome limitations of current biomarkers. To achieve this, future studies could employ innovative biomarker discovery strategies such as multi-omics analysis, which offers high-throughput biomarker screening across multiple molecular levels. <sup>50,51</sup> Research has shown the suitability this approach for molecular imaging biomarkers, but acknowledged the need of validating such targets on the protein level, for instance using IHC (De Muynck et al., manuscript in preparation).

This thesis highlighted the potential of glycan-targeted tumor imaging, however the field will advance further once novel targeting vehicles against promising tumor-associated glycan biomarkers have been developed. Glycan targeting has been hindered by the low immunogenicity and structural similarity of glycans, requiring the employment of complex immunization strategies to develop suitable glycan-specific antibodies.<sup>52</sup> Therefore, an additional focus on non-mAb-derived vehicles is crucial. The development of glycan-targeting DARPins has not yet been successful despite substantial efforts.<sup>53</sup> It may be that the emerging class of glycan-targeting nanobodies could offer a promising, smaller-sized targeting alternative to mAbs.<sup>54</sup>

Several interesting developments regarding NIRF imaging are currently taking place. For instance, pH-activable tracers have become available for NIRF imaging, which owe their efficacy to the acidic environment of the tumor. <sup>55,56</sup> Such tracers may eventually circumvent the need for tumor targeting through tumor-specific biomarkers. Also, topical application of tracers is an interesting development as this can be done instantaneously and theoretically results in low or absent systemic exposure. In animal models, topically applied NIRF tracers have successfully visualized nerves, a development with potential applications in rectal or aortic surgery. <sup>57</sup> In addition to tumor imaging, future research should focus on intraoperative imaging of anatomical structures that should be avoided during surgery, such as ureters or nerves, which could enhance surgical safety by reducing iatrogenic damage. <sup>57,58</sup>

To overcome the limited penetration depth of NIRF imaging (NIR-I; 700-900 nm), NIR-II imaging has gained significant attention (1000-1400 nm). Due to reduced autofluorescence and scattering, NIR-II imaging may result in higher tumor-to-background ratios, allowing improved tumor detection with an increased depth of up to 20 mm. <sup>59,60</sup> As spectral characterization studies have shown long emission tails of ICG and IRDye 800CW in the NIR-II spectrum, applicability of current tracers for NIR-II without the immediate need for development of novel dyes is feasible. <sup>61</sup> However, as for PA imaging, suitable clinical camera systems capable of NIR-II imaging are required to bring this closer to the clinic. Close collaboration with developers of imaging systems is therefore essential. A last development of particular interest are molecular imaging tracers that allow bimodal NIRF/PET imaging. <sup>62</sup> Although currently in preclinical development, it is expected that such tracers will make their way to the clinic in the foreseeable future to allow pre- and intraoperative imaging using a single tracer injection.

As may be deducted from this thesis and developments outlined above, it appears that molecular imaging holds great promise for revolutionizing surgical oncological care. With the first NIRF imaging tracer being FDA-approved (OTL-38 in ovarian cancer), the results of the phase 3 trial evaluating CEACAM5-targeting SGM-101 in colorectal cancer are eagerly anticipated (NCT03659448). To arrive at

a bright future, it is pivotal for researchers to adopt a truly multidisciplinary approach to pursue future endeavors. Such within the molecular imaging research field hinge on the reciprocal collaboration between preclinical and clinical researchers, as well as industrial partners and physicians from various clinical disciplines. Ultimately, problems must originate from the clinic and suggested solutions must be clinically feasible. On a personal note, the Green Light Leiden research group exemplified this collaborative approach, resulting in notable successes, with numerous studies currently ongoing.<sup>63</sup>

#### CONCLUSION

Molecular imaging may enhance pre- and intraoperative tumor identification. Preoperatively, targeted PET imaging is of particular interest. Intraoperatively, NIRF imaging, optionally combined with PA imaging, holds great promise. This thesis addressed several challenges regarding biomarkers and tracers for molecular imaging in gastrointestinal cancers, with a focus on pancreatic and gastric cancer. By evaluating biomarkers - such as tumor-associated glycans - and innovative tracers - such as glycan-binding and DARPin-based NIRF/PA tracers - this thesis contributed to the groundwork for improved pre- and intraoperative visualization of gastrointestinal cancers. Further development, optimization and clinical evaluation of molecular imaging tracers directed at the biomarkers identified in this work, and novel tracers evaluated in this thesis is warranted. Ultimately, such tracers may optimize surgical care and improve patient outcomes.

#### REFERENCES

- 1 de Geus SW, Boogerd LS, Swijnenburg RJ, Mieog JS, Tummers WS, Prevoo HA, et al. Selecting Tumor-Specific Molecular Targets in Pancreatic Adenocarcinoma: Paving the Way for Image-Guided Pancreatic Surgery. Mol Imaging Biol. 2016;18(6):807-19.
- 2 Tummers WS, Farina-Sarasqueta A, Boonstra MC, Prevoo HA, Sier CF, Mieog JS, et al. Selection of optimal molecular targets for tumor-specific imaging in pancreatic ductal adenocarcinoma. Oncotarget. 2017;8(34):56816-28.
- 3 Mereiter S, Balmaña M, Gomes J, Magalhães A, Reis CA. Glycomic Approaches for the Discovery of Targets in Gastrointestinal Cancer. Front Oncol. 2016;6:55.
- 4 Heijs B, Holst S, Briaire-de Bruijn IH, van Pelt GW, de Ru AH, van Veelen PA, et al. Multimodal Mass Spectrometry Imaging of N-Glycans and Proteins from the Same Tissue Section. Anal Chem. 2016;88(15):7745-53.
- 5 Tian C, Clauser KR, Öhlund D, Rickelt S, Huang Y, Gupta M, et al. Proteomic analyses of ECM during pancreatic ductal adenocarcinoma progression reveal different contributions by tumor and stromal cells. Proc Natl Acad Sci U S A. 2019;116(39):19609-18.
- 6 Zhao X, Zhang G, Chen J, Li Z, Shi Y, Li G, et al. A rationally designed nuclei-targeting FAPI 04-based molecular probe with enhanced tumor uptake for PET/ CT and fluorescence imaging. Eur J Nucl Med Mol Imaging. 2024;51(6):1593-604.
- 7 Liu R, Li H, Liu L, Yu J, Ren X. Fibroblast activation protein: A potential therapeutic target in cancer. Cancer biology & therapy. 2012;13(3):123-9.
- 8 Gilardi L, Airò Farulla LS, Demirci E, Clerici I, Omodeo Salè E, Ceci F. Imaging Cancer-Associated Fibroblasts (CAFs) with FAPi PET. Biomedicines. 2022;10(3).
- 9 Arçay Öztürk A, Flamen P. FAP-targeted PET imaging in gastrointestinal malignancies: a comprehensive review. Cancer Imaging. 2023;23(1):79.
- 10 Li X, Lu N, Lin L, Chen Y, Yang S, Wang H, et al. (18) F-FAPI-04 Outperforms (18)F-FDG PET/CT in Clinical Assessments of Patients with Pancreatic Adenocarcinoma. J Nucl Med. 2024;65(2):206-12.
- 11 van Dam MA, Vuijk FA, Stibbe JA, Houvast RD, Luelmo SAC, Crobach S, et al. Overview and Future Perspectives on Tumor-Targeted Positron Emission Tomography and Fluorescence Imaging of Pancreatic Cancer in the Era of Neoadjuvant Therapy. Cancers. 2021;13(23):6088.
- 12 Kessler L, Ferdinandus J, Hirmas N, Zarrad F, Nader M, Kersting D, et al. Pitfalls and Common Findings in (68)Ga-FAPI PET: A Pictorial Analysis. J Nucl Med. 2022;63(6):890-6.
- 13 Vuijk FA, de Muynck L, Franken LC, Busch OR, Wilmink JW, Besselink MG, et al. Molecular targets for diagnostic and intraoperative imaging of pancreatic ductal adenocarcinoma after neoadjuvant FOLFIRINOX treatment. Sci Rep. 2020;10(1):16211.
- 14 de Gooyer JM, Elekonawo FMK, Bremers AJA, Boerman OC, Aarntzen E, de Reuver PR, et al. Multimodal CEAtargeted fluorescence and radioguided cytoreductive surgery for peritoneal metastases of colorectal origin. Nat Commun. 2022;13(1):2621.

- 15 Vonk J, Kukačka J, Steinkamp PJ, de Wit JG, Voskuil FJ, Hooghiemstra WTR, et al. Multispectral optoacoustic tomography for in vivo detection of lymph node metastases in oral cancer patients using an EGFRtargeted contrast agent and intrinsic tissue contrast: A proof-of-concept study. Photoacoustics. 2022;26:100362.
- 16 Muynck L, Gaarenstroom KN, Sier CFM, Duijvenvoorde MV, Bosse T, Mieog JSD, et al. Novel Molecular Targets for Tumor-Specific Imaging of Epithelial Ovarian Cancer Metastases. Cancers (Basel). 2020;12(6).
- 17 Goethals L, Perneel C, Debucquoy A, De Schutter H, Borghys D, Ectors N, et al. A new approach to the validation of tissue microarrays. J Pathol. 2006;208(5):607-14.
- 18 Lower EE, Glass E, Blau R, Harman S. HER-2/neu expression in primary and metastatic breast cancer. Breast Cancer Res Treat. 2009;113(2):301-6.
- 19 Boogerd LS, Boonstra MC, Beck AJ, Charehbili A, Hoogstins CE, Prevoo HA, et al. Concordance of folate receptor-α expression between biopsy, primary tumor and metastasis in breast cancer and lung cancer patients. Oncotarget. 2016;7(14):17442-54.
- 20 Kwon LY, Scollard DA, Reilly RM. (64) Cu-Labeled Trastuzumab Fab-PEG(24)-EGF Radioimmunoconjugates Bispecific for HER2 and EGFR: Pharmacokinetics, Biodistribution, and Tumor Imaging by PET in Comparison to Monospecific Agents. Mol Pharm. 2017;14(2):492-501.
- 21 Luu TT. Review of Immunohistochemistry Biomarkers in Pancreatic Cancer Diagnosis. Front Oncol. 2021;11:799025.
- 22 Matos LL, Trufelli DC, de Matos MG, da Silva Pinhal MA. Immunohistochemistry as an important tool in biomarkers detection and clinical practice. Biomark Insights. 2010;5:9-20.
- 23 Gan HK, Burgess AW, Clayton AH, Scott AM. Targeting of a conformationally exposed, tumor-specific epitope of EGFR as a strategy for cancer therapy. Cancer Res. 2012;72(12):2924-30.
- 24 Baeuerle PA, Gires O. EpCAM (CD326) finding its role in cancer. Br J Cancer. 2007;96(3):417-23.
- 25 Loughrey MB, Bankhead P, Coleman HG, Hagan RS, Craig S, McCorry AMB, et al. Validation of the systematic scoring of immunohistochemically stained tumour tissue microarrays using QuPath digital image analysis. Histopathology. 2018;73(2):327-38.
- 26 Adams EJ, Green JA, Clark AH, Youngson JH. Comparison of different scoring systems for immunohistochemical staining. J Clin Pathol. 1999;52(1):75-7.
- 27 Feuchtinger A, Stiehler T, Jütting U, Marjanovic G, Luber B, Langer R, et al. Image analysis of immunohistochemistry is superior to visual scoring as shown for patient outcome of esophageal adenocarcinoma. Histochem Cell Biol. 2015;143(1):1-9.
- 28 Bankhead P, Loughrey MB, Fernández JA, Dombrowski Y, McArt DG, Dunne PD, et al. QuPath: Open source software for digital pathology image analysis. Sci Rep. 2017;7(1):16878.
- 29 Lohrmann C, O'Reilly EM, O'Donoghue JA, Pandit-Taskar N, Carrasquillo JA, Lyashchenko SK, et al. Retooling a

- Blood-Based Biomarker: Phase I Assessment of the High-Affinity CA19-9 Antibody HuMab-5B1 for Immuno-PET Imaging of Pancreatic Cancer. Clin Cancer Res. 2019;25(23):7014-23.
- 30 Lwin TM, Hoffman RM, Bouvet M. The development of fluorescence guided surgery for pancreatic cancer: from bench to clinic. Expert Rev Anticancer Ther. 2018;18(7):651-62.
- 31 Bragina O, Chernov V, Schulga A, Konovalova E, Garbukov E, Vorobyeva A, et al. Phase I Trial of (99m)Tc-(HE)(3)-G3, a DARPin-Based Probe for Imaging of HER2 Expression in Breast Cancer. J Nucl Med. 2022;63(4):528-35.
- 32 Vorobyeva A, Konovalova E, Xu T, Schulga A, Altai M, Garousi J, et al. Feasibility of Imaging EpCAM Expression in Ovarian Cancer Using Radiolabeled DARPin Ec1. Int J Mol Sci. 2020;21(a).
- 33 Vorobyeva A, Bezverkhniaia E, Konovalova E, Schulga A, Garousi J, Vorontsova O, et al. Radionuclide Molecular Imaging of EpCAM Expression in Triple-Negative Breast Cancer Using the Scaffold Protein DARPin Ec1. Molecules. 2020;25(20).
- 34 Gires Ö, Pan M, Schinke H, Canis M, Baeuerle PA. Expression and function of epithelial cell adhesion molecule EpCAM: where are we after 40 years? Cancer Metastasis Rev. 2020;30(3):060-87.
- 35 Ryman JT, Meibohm B. Pharmacokinetics of Monoclonal Antibodies. PETT: Pharmacometrics & Systems Pharmacology. 2017;6(9):576-88.
- 36 Xenaki KT, Oliveira S, van Bergen En Henegouwen PMP. Antibody or Antibody Fragments: Implications for Molecular Imaging and Targeted Therapy of Solid Tumors. Front Immunol. 2017;8:1287.
- 37 Schmidt MM, Wittrup KD. A modeling analysis of the effects of molecular size and binding affinity on tumor targeting. Mol Cancer Ther. 2009;8(10):2861-71.
- 38 Plückthun A. Designed Ankyrin Repeat Proteins (DARPins): Binding Proteins for Research, Diagnostics, and Therapy. Annual Review of Pharmacology and Toxicology. 2015;55(1):489-511.
- 39 Stumpp MT, Binz HK, Amstutz P. DARPins: A new generation of protein therapeutics. Drug Discovery Today. 2008;13(15):695-701.
- 40 Mädler S, Bich C, Touboul D, Zenobi R. Chemical crosslinking with NHS esters: a systematic study on amino acid reactivities. J Mass Spectrom. 2009;44(5):694-706.

  Commun. 2020;11(1):3257.

  Gollianin J, Amin A, Moshnikova A, Brito JM, Tran TY,
  Adochite RC, et al. Targeted imaging of urothelium
- 41 Agarwal P, Bertozzi CR. Site-specific antibody-drug conjugates: the nexus of bioorthogonal chemistry, protein engineering, and drug development. Bioconjug Chem. 2015;26(2):176-92.
- 42 Zhegalova NG, He S, Zhou H, Kim DM, Berezin MY. Minimization of self-quenching fluorescence on dyes conjugated to biomolecules with multiple labeling sites via asymmetrically charged NIR fluorophores. Contrast Media Mol Imaging. 2014;9(5):355-62.
- 43 Simon M, Zangemeister-Wittke U, Plückthun A. Facile double-functionalization of designed ankyrin repeat proteins using click and thiol chemistries. Bioconjug Chem. 2012;23(2):279-86.
- 44 Lyu X, Zhao Q, Hui J, Wang T, Lin M, Wang K, et al. The global landscape of approved antibody therapies. Antib Ther. 2022;5(4):233-57.

- 45 Hernot S, van Manen L, Debie P, Mieog JSD, Vahrmeijer AL. Latest developments in molecular tracers for fluorescence image-guided cancer surgery. The Lancet Oncology. 2019;20(7):e354-e67.
- 46 van Manen L, Handgraaf HJM, Diana M, Dijkstra J, Ishizawa T, Vahrmeijer AL, et al. A practical guide for the use of indocyanine green and methylene blue in fluorescence-guided abdominal surgery. J Surg Oncol. 2018;118(2):283-300.
- 47 Baart VM, van Manen L, Bhairosingh SS, Vuijk FA, Iamele L, de Jonge H, et al. Side-by-Side Comparison of uPAR-Targeting Optical Imaging Antibodies and Antibody Fragments for Fluorescence-Guided Surgery of Solid Tumors. Mol Imaging Biol. 2021.
- 48 Gengenbacher N, Singhal M, Augustin HG. Preclinical mouse solid tumour models: status quo, challenges and perspectives. Nat Rev Cancer. 2017;17(12):751-65.
- 49 Danhier F. To exploit the tumor microenvironment: Since the EPR effect fails in the clinic, what is the future of nanomedicine? J Control Release. 2016;244(Pt A):108-21.
- 50 Das T, Andrieux G, Ahmed M, Chakraborty S. Integration of Online Omics-Data Resources for Cancer Research. Front Genet. 2020;11:578345.
- 51 Biswas N, Chakrabarti S. Artificial Intelligence (AI)-Based Systems Biology Approaches in Multi-Omics Data Analysis of Cancer. Front Oncol. 2020;10:588221.
- 52 Prendergast JM, Galvao da Silva AP, Eavarone DA, Ghaderi D, Zhang M, Brady D, et al. Novel anti-Sialyl-Tn monoclonal antibodies and antibody-drug conjugates demonstrate tumor specificity and anti-tumor activity. mAbs: Taylor & Francis; 2017. p. 615-27.
- 53 Warkentin R. Toward the use of Ankyrins and Affibodies as Scaffolds for Glycan Binding Proteins: A Directed Evolution and Computational Approach. Concordia University: 2022.
- 54 Khilji SK, Goerdeler F, Frensemeier K, Warschkau D, Lühle J, Fandi Z, et al. Generation of glycan-specific nanobodies. Cell Chem Biol. 2022;29(8):1353-61.e6.
- 55 Voskuil FJ, Steinkamp PJ, Zhao T, van der Vegt B, Koller M, Doff JJ, et al. Exploiting metabolic acidosis in solid cancers using a tumor-agnostic pH-activatable nanoprobe for fluorescence-guided surgery. Nat Commun. 2020;11(1):3257.
- 56 Golijanin J, Amin A, Moshnikova A, Brito JM, Tran TY, Adochite RC, et al. Targeted imaging of urothelium carcinoma in human bladders by an ICG pHLIP peptide ex vivo. Proc Natl Acad Sci U S A. 2016;113(42):11829-34.
- 57 Barth CW, Rizvi SZH, Masillati AM, Chakraborty S, Wang LG, Montaño AR, et al. Nerve-Sparing Gynecologic Surgery Enabled by A Near-Infrared Nerve-Specific Fluorophore Using Existing Clinical Fluorescence Imaging Systems. Small. 2023;e2300011.
- 58 de Valk KS, Handgraaf HJ, Deken MM, Sibinga Mulder BG, Valentijn AR, Terwisscha van Scheltinga AG, et al. A zwitterionic near-infrared fluorophore for real-time ureter identification during laparoscopic abdominopelvic surgery. Nature Communications. 2019;10(1):3118.
- 59 Hu Z, Fang C, Li B, Zhang Z, Cao C, Cai M, et al. First-in-human liver-tumour surgery guided by multispectral fluorescence imaging in the visible and near-infrared-I/II windows. Nat Biomed Eng. 2020;4(3):259-71.

- 60 He S, Song J, Qu J, Cheng Z. Crucial breakthrough of second near-infrared biological window fluorophores: design and synthesis toward multimodal imaging and theranostics. Chem Soc Rev. 2018;47(12):4258-78.
- 61 Guo X, Li C, Jia X, Qu Y, Li M, Cao C, et al. NIR-II fluorescence imaging-guided colorectal cancer surgery targeting CEACAM5 by a nanobody. EBioMedicine. 2023;89:104476.
- 62 Schouw H, Huisman L, Janssen Y, Slart R, Borra R,
  Willemsen A, et al. Targeted optical fluorescence imaging:
  a meta-narrative review and future perspectives. European
  journal of nuclear medicine and molecular imaging.
  2021:1-21.
- 63 Mieog JSD, Achterberg FB, Zlitni A, Hutteman M, Burggraaf J, Swijnenburg R-J, et al. Fundamentals and developments in fluorescence-guided cancer surgery. Nature Reviews Clinical Oncology. 2021.



#### NEDERLANDSE SAMENVATTING

Ondanks recente therapeutische vooruitgang blijft radicale chirurgie de hoeksteen van de curatieve behandeling van gastro-intestinale tumoren, waaronder maag-, pancreas- en colorectale carcinomen. Preoperatief is een goede stadiëring van de tumor cruciaal voor het selecteren van patiënten voor chirurgie. Om de chirurgische behandeling van gastro-intestinale tumoren verder te optimaliseren, zijn er verschillende chirurgische en diagnostische uitdagingen die overwonnen moeten worden. Preoperatief bieden de huidige beeldvormingstechnieken, zoals CT, MRI en FDG-PET, essentiële informatie over tumorgrootte, invasiviteit, lymfeklierbetrokkenheid en metastasen. De adequate chirurgische planning bij bepaalde tumortypes wordt echter bemoeilijkt door een gebrek aan voldoende sensitiviteit en specificiteit van deze beeldvormingstechnieken. Dit kan leiden tot onnodige resecties of biopsieën, extra beeldvormingsprocedures en nodeloze toediening van systemische therapieën, wat de belasting voor patiënten vergroot en de kosten voor de gezondheidszorg verhoogt. Intra-operatief is het onderscheiden van tumorweefsel van gezond omliggend weefsel een uitdaging, vooral na neoadjuvante therapie (NAT). De toegenomen inzet van minimaal invasieve chirurgie heeft dit proces verder bemoeilijkt. Dit kan leiden tot irradicale resecties, wat bij de meeste tumortypen is geassocieerd met verhoogde lokale recidiefpercentages en een verminderde overleving van patiënten.

Als oplossing kan gerichte moleculaire beeldvorming, gericht op biomarkers die tot expressie komen in de tumor, worden ingezet om de identificatie van de tumor te verbeteren. Preoperatief is gerichte PET beeldvorming van bijzonder belang. Intraoperatief wordt nabij-infraroodfluorescentie (NIRF) beeldvorming, ook wel fluorescentie-geleide chirurgie genoemd, steeds vaker toegepast. Door real-time visualisatie van weefsel te faciliteren zonder het zichtbare chirurgische veld te verstoren, ondersteunt NIRF beeldvorming, al dan niet gecombineerd met foto-akoestische (PA) beeldvorming, chirurgen bij 1) intraoperatieve stadiëring door detectie van (klinisch occulte) ziekte, inclusief metastasen, en 2) het beoordelen van tumorvrije marges.

Dit proefschrift heeft als doel om uitdagingen met betrekking tot biomarkers en targeting-moleculen bij moleculaire beeldvorming van gastro-intestinale tumoren aan te pakken, met een focus op pancreas- en maagkanker. Hoewel de bevindingen van **Deel I** van dit proefschrift extrapoleerbaar zijn naar zowel NIRF beeldvorming als gerichte PET beeldvorming, richt **Deel II** zich op bimodale NIRF/PA-beeldvorming van gastro-intestinale tumoren.

# Deel I: Evaluatie van biomarkers voor moleculaire beeldvorming van gastro-intestinale tumoren

Ondanks de technische verschillen tussen PET en NIRF beeldvorming blijft de keuze van geschikte biomarkers een cruciale voorwaarde voor succesvolle tumorvisualisatie bij beide technieken. Biomarkers van enkele veelbelovende moleculaire beeldvormingstracers blijken nadelen te hebben, zoals heterogene expressie en aanwezigheid op niet-kwaadaardig weefsel. Deze nadelen benadrukken de voortdurende noodzaak om nieuwe, minder conventionele biomarkers te onderzoeken, zoals tumor-geassocieerde glycanen en sterk geglycosyleerde eiwitten, waaronder mucines.

Hoofdstuk 2 biedt een narratief overzicht van de meest veelbelovende glycanen en sterk geglycosyleerde eiwitten en belicht het potentieel van deze structuren als targets voor beeldvorming door recente preklinische en klinische onderzoeken naar glycaan-gerelateerde tumorbeeldvorming te bespreken. Abnormale glycosylering van eiwitten en lipiden is een fundamenteel kenmerk van bijna alle kankertypen en draagt bij aan tumorprogressie. Bovendien wordt overexpressie beschreven van glycoproteïnen die abnormale glycanen dragen, zoals mucines en proteoglycanen. Gezien hun beperkte aanwezigheid of afwezigheid in gezond weefsel en hun zeer dichte expressie op tumorcellen zijn tumor-geassocieerde glycanen bijzonder interessant als biomarkers voor moleculaire beeldvorming van tumoren. Dit potentieel wordt verder versterkt door hun aanwezigheid op de buitenste laag van het celmembraan, waardoor glycanen gemakkelijk toegankelijk zijn voor targeting-moleculen, evenals door hun aanwezigheid op meerdere tumor-geassocieerde eiwitten tegelijkertijd. Dit maakt het theoretisch mogelijk om meerdere eiwitten tegelijk te targeten met een beeldvormingstracer die gericht is op een enkele glycaan. Zoals beschreven in dit hoofdstuk, zijn verschillende glycanen en sterk geglycosyleerde eiwitten onderzocht als targets voor beeldvorming in zowel preklinische als vroege-fase klinische studies. Veelbelovende glycanen voor beeldvorming van gastro-intestinale tumoren die in dit hoofdstuk worden geïdentificeerd, zijn: Lewisa/c/x (Lea/c/x), sialyl-di-Lewisa (sdi-Lea), sialyl-Lewisx (sLex), sialyl-Lewisa (sLea, ook bekend als CA19-9), en sialyl-Thomsen-Nouveau (sTn). Wat betreft sterk geglycosyleerde eiwitten zijn mucine-1 (MUC1) en mucine-5AC (MUC5AC) interessant voor beeldvorming van gastro-intestinale tumoren.

De kennis uit **Hoofdstuk 2** wordt toegepast in **Hoofdstuk 3**, waarin het potentieel van deze glycanen en mucines als targets voor beeldvorming van het ductaal adenocarcinoom van de pancreas (PDAC) wordt geëvalueerd. Het

expressieniveau in humaan PDAC-weefsel werd bepaald middels immunohistochemische kleuringen en gekwantificeerd met een semi-geautomatiseerde workflow voor digitale beeldanalyse. De expressie van Lea/c/x, sdi-Lea, sLea, sLex, sTn, MUC1 en MUC5AC op primair PDAC-weefsel was hoog en vergelijkbaar tussen patiënten die NAT hadden ontvangen en patiënten die dit niet hadden ontvangen. Bovendien was de expressie van alle biomarkers significant lager op chronische pancreatitis, gezond pancreasweefsel en duodenumweefsel, met uitzondering van sTn en MUC1, die respectievelijk een sterke expressie vertoonden op duodenum- en gezond pancreasweefsel. Deze biomarkers worden daarom als minder geschikt beschouwd voor PDAC-beeldvorming. Alle biomarkers lijken echter veelbelovend voor het vaststellen van lymfeklierbetrokkenheid bij PDAC, gezien de matige tot hoge sensitiviteit en specificiteit om tumor-positieve van tumor-negatieve lymfeklieren te onderscheiden. Dit hoofdstuk baant de weg voor de ontwikkeling en evaluatie van Lea/c/x-, sdi-Lea-, sLea-, sLex- en MUC5AC-specifieke tracers voor moleculaire beeldvorming van PDAC en hun daaropvolgende introductie in de kliniek.

Een tweede uitdaging betreft het gebrek aan onderzoek naar de relatieve expressie tussen maligne en niet-maligne weefseltypes van enkele gevestigde biomarkers voor moleculaire beeldvorming. Dit kan worden beschouwd als cruciale informatie om de geschiktheid van biomarkers voor beeldvorming te bepalen. Daarom evalueert **Hoofdstuk** 4 het potentieel van  $\alpha_V \beta_6$ , CEACAM5, EGFR, epitheliaal celadhesiemolecuul (EpCAM) en humane epidermale groeifactorreceptor-2 (HER2) als targets voor beeldvorming van primaire maagkanker, lymfeklier- en afstandsmetastasen. Voor dit doel werd immunohistochemie toegepast op humaan weefsel. Positieve biomarkerexpressie in primaire maagtumoren werd waargenomen bij 71% tot 93% van de patiënten, afhankelijk van de biomarker. Tumorexpressie van CEACAM5, EGFR en EpCAM was hoger in vergelijking met de expressie in gezond maagweefsel, terwijl dit niet het geval was voor ανβ<sub>6</sub> en HER2, waardoor deze biomarkers ongeschikt zijn voor beeldvorming van maagkanker. Tumor-positieve lymfeklieren konden worden onderscheiden van tumor-negatieve lymfeklieren met een nauwkeurigheid variërend van 82% tot 93%, afhankelijk van de biomarker. Bovendien werden CEACAM5, EGFR en EpCAM overvloedig tot expressie gebracht in afstandsmetastasen, met positieve expressie in 88% tot 95% van de patiënten. Deze bevindingen tonen aan dat CEACAM5, EGFR en EpCAM veelbelovende biomarkers zijn voor moleculaire beeldvorming van primaire maagkanker, evenals voor de visualisatie van zowel lymfeklier- als afstandsmetastasen.

De derde en laatste uitdaging met betrekking tot biomarkers, besproken in **Deel I**, betreft de heterogene expressie van gevestigde biomarkers voor moleculaire beeldvorming, wat de universele toepassing van moleculaire beeldvormingstracers belemmert. Dit kan worden aangepakt door patiënten preoperatief voor expressie van biomarkers te screenen. Voor sommige tumortypen is het echter onbekend of biopsieën kunnen worden gebruikt om de expressie in de primaire tumor te voorspellen. Daarom evalueert **Hoofdstuk 5** de concordantie en correlatie van de expressie van integrine  $\alpha_V \beta_6$ , CEACAM5, epidermale groeifactorreceptor (EGFR), mesotheline, Lea/c/x en sdi-Lea tussen preoperatief verkregen fijne-naaldbiopten (FNB) en primair PDAC weefsel. De concordantie bleek matig tot hoog voor alle biomarkers, variërend van 61% tot 85%. De correlatie tussen de expressie in FNB-weefsel en primaire PDAC-expressie werd ook geëvalueerd en was matig tot sterk voor CEACAM5, EGFR, mesotheline, sdi-Lea en Lea/c/x Dit suggereert dat de biomarkerexpressie in FNB-weefsel voorspellend is voor het expressieniveau in primair PDAC weefsel. Hoewel er geen correlatie werd waargenomen voor  $\alpha v \beta_6$ , was de expressie hiervan consequent hoog in zowel FNB- als primair PDACweefsel. Belangrijk is dat NAT een beperkte invloed had op de concordantie van alle biomarkers. Daarnaast werd geen effect waargenomen op de correlatie van biomarkerexpressie tussen FNB- en primair PDAC weefsel, behalve voor mesotheline. Dit hoofdstuk toont aan dat biomarkerexpressie in FNB-weefsel, voor de meeste onderzochte biomarkers, voorspellend is voor de expressie in de primaire tumor, ongeacht de toepassing van NAT. Deze bevindingen bieden daarmee de preklinische basis voor de klinische toepassing van een FNB-gebaseerde biomarker screeningsworkflow, wat uiteindelijk een patiënt-specifieke benadering van de toediening van tracers voor moleculaire beeldvorming bij PDAC kan faciliteren.

# Deel II: Preklinische evaluatie van nieuwe tracers voor nabij-infraroodfluorescentie en foto-akoestische beeldvorming van gastro-intestinale tumoren

Deel II van dit proefschrift bouwt voort op het werk van Deel I en presenteert een preklinische evaluatie van nieuwe tracers voor bimodale NIRF/PA beeldvorming. Hoofdstuk 6 beschrijft een preklinische proof-of-concept van het targeten van tumor-geassocieerde glycanen voor NIRF beeldvorming van gastro-intestinale tumoren met behulp van een tracer gericht op Lea/c/x (geëvalueerd voor PDAC in Hoofdstuk 3). Immunohistochemie op humaan weefsel van primaire maag-, pancreas- en coloncarcinomen en gezonde omliggende weefsels bevestigde een hoge tumorexpressie en beperkte expressie in gezond weefsels. In sommige gevallen was de Lea/c/x-expressie op gezond weefsel echter matig. Vervolgens werd het

Lea/c/x-specifieke chimere antilichaam CH88.2 geconjugeerd aan de NIR-fluorofoor IRDye 800CW en intraveneus toegediend aan HT-29 (humaan coloncarcinoom) en BxPC-3 (humaan pancreascarcinoom) tumor-dragende muizen met een dosis van 1 nmol. Met de klinische Artemis NIRF imager werden tumor-achtergrond-ratios (TBRs) van 2.2  $\pm$  0.3 en 1.8  $\pm$  0.3 gemeten in respectievelijk het HT-29 model en BxPC-3 model met matige Lea/c/x expressie. Tumoren werden tot 1 week na injectie succesvol gelokaliseerd en afgebakend. *Ex vivo*-analyse bevestigde volledige tumorpenetratie en lage fluorescentiesignalen in andere organen. Dit hoofdstuk toont het potentieel aan van het targeten van Lewis-glycanen voor fluorescentie-geleide chirurgie van gastro-intestinale tumoren.

In **Hoofdstuk 7** werd dit werk bevestigd en uitgebreid met een preklinische evaluatie van CH88.2-800CW en een sdi-Lea-specifieke tracer, CH129-800CW, voor bimodale NIRF/PA-beeldvorming van gastro-intestinale tumoren. Een uitgebreide immunohistochemische evaluatie toonde aan dat Lea/c/x en sdi-Lea sterk tot expressie kwamen in maag- en colorectaal tumorweefsel, met beperkte expressie in gezond weefsel. Lea/c/x-expressie was echter sterk in gezond colonepitheel, waardoor dit target minder geschikt is voor beeldvorming van colorectale carcinomen. 96 uur na injectie van CH88.2-800CW of CH129-800CW konden alle orthotope tumoren uitstekend worden geïdentificeerd met de Artemis NIRF imager, met TBRs van respectievelijk 4.8  $\pm$  1.4 en 4.9  $\pm$  0.5 (HT-29\_luc2-model) en 2.5±0.3 en 2.9±0.4 (BxPC-3\_luc2-model). Een sterk PA-signaal werd waargenomen in alle tumoren voor zowel CH88.2-800CW als CH129-800CW. Biodistributieanalyse toonde hoge tumorfluorescentie met minimale signalen in gezonde organen. Deze resultaten bevestigen dat bimodale NIRF/PA-beeldvorming met CH88.2-800CW en CH129-800CW een veelbelovende benadering is voor real-time, hoog-contrast tumorvisualisatie van gastro-intestinale tumoren.

Het tweede onderzoeksgebied in **Deel II** richt zich op het targeting-molecuul van moleculaire beeldvormingstracers. Hoewel monoklonale antilichamen voordelen bieden, zoals hoge specificiteit en stabiliteit, hebben ze beperkingen, zoals slechte tumorpentratie en lange halfwaardetijden in de circulatie. Alternatieve targeting-moleculen, zoals 'Designed Ankyrin Repeat Proteins' (DARPins), bieden mogelijk een oplossing, maar hun potentieel voor moleculaire beeldvorming van gastro-intestinale tumoren is nog onvoldoende onderzocht. **Hoofdstuk** 8 presenteert de preklinische evaluatie van EpCAM-bindende DARPins als targeting-moleculen voor bimodale NIRF/PA-beeldvorming van gastro-intestinale tumoren. EpCAM wordt beschouwd als een veelbelovende biomarker

voor beeldvorming, met overexpressie beschreven in de meeste carcinomen. De DARPins Ac2, Ec4.1 en de niet-bindende controle DARPin Off7 werden geconjugeerd met IRDye 800CW. Met behulp van een *in vivo* dosisvergelijkingsstudie werden 6 nmol en 24 uur vastgesteld als de optimale *in vivo* dosis en het optimale tijdstip voor beeldvorming voor beide DARPins. 24 uur post-injectie toonden Ac2-800CW en Ec4.1-800CW duidelijke tumordelineatie middels de klinische Artemis imager, met TBRs van respectievelijk  $2.6 \pm 0.3$  en  $3.1 \pm 0.3$ . Een sterk PA-signaal werd ook in de tumoren waargenomen voor beide tracers. Biodistributieanalyse toonde hoge fluorescentiesignalen in de lever en nieren, wat klaring van de tracers weerspiegelde. Deze resultaten suggereren dat EpCAM-bindende DARPins veelbelovende targeting-moleculen zijn voor NIRF/PA-beeldvorming van een breed scala aan tumortypen, met duidelijke tumorvisualisatie binnen 24 uur na injectie.

216 APPENDICES • Nederlandse samenvatting 217

#### LIST OF PUBLICATIONS

- Baart VM, **Houvast RD**, de Geus-Oei LF, Quax PHA, Kuppen PJK, Vahrmeijer AL, Sier CFM. Molecular imaging of the urokinase plasminogen activator receptor: opportunities beyond cancer. EJNMMI Res. 2020;10(1):87.
- Houvast RD, Baart VM, Bhairosingh SS, Cordfunke RA, Chua JX, Vankemmelbeke M, Parsons T, Kuppen PJK, Durrant LG, Vahrmeijer AL, Sier CFM. Glycan-Based Near-infrared Fluorescent (NIRF) Imaging of Gastrointestinal Tumors: a Preclinical Proof-of-Concept In Vivo Study. Mol Imaging Biol. 2020.
- Wellens LM, Deken MM, Sier CFM, Johnson HR, de la Jara Ortiz F, Bhairosingh SS, **Houvast RD**, Kholosy WM, Baart VM, Pieters A, de Krijger RR, Molenaar JJ, Wehrens EJ, Dekkers JF, Wijnen M, Vahrmeijer AL, Rios AC. Anti-GD2-IRDye8ooCW as a targeted probe for fluorescence-guided surgery in neuroblastoma. Sci Rep. 2020;10(1):17667.
- Attia JVD, Dessens CE, van de Water R, **Houvast RD**, Kuppen PJK, Krijgsman D. The Molecular and Functional Characteristics of HLA-G and the Interaction with Its Receptors: Where to Intervene for Cancer Immunotherapy? Int J Mol Sci. 2020;21(22).
- **Houvast RD**, Vankemmelbeke M, Durrant LG, Wuhrer M, Baart VM, Kuppen PJK, de Geus-Oei LF, Vahrmeijer AL, Sier CFM. Targeting Glycans and Heavily Glycosylated Proteins for Tumor Imaging. Cancers (Basel). 2020;12(12).
- van de Water RB, Krijgsman D, **Houvast RD**, Vahrmeijer AL, Kuppen PJK. A Critical Assessment of the Association between HLA-G Expression by Carcinomas and Clinical Outcome. Int J Mol Sci. 2021;22(15).
- Houvast RD, Thijse K, Groen JV, Chua J, Vankemmelbeke M, Durrant LG, Mieog JSD, Bonsing BA, Vahrmeijer AL, Kuppen PJK, Crobach A, Sier CFM. An Immunohistochemical Evaluation of Tumor-Associated Glycans and Mucins as Targets for Molecular Imaging of Pancreatic Ductal Adenocarcinoma. Cancers (Basel). 2021;13(22).
- van Dam MA, Vuijk FA, Stibbe JA, **Houvast RD**, Luelmo SAC, Crobach S, Shahbazi Feshtali S, de Geus-Oei L-F, Bonsing BA, Sier CFM, Kuppen PJK, Swijnenburg R-J, Windhorst AD, Burggraaf J, Vahrmeijer AL, Mieog JSD. Overview and Future Perspectives on Tumor-Targeted Positron Emission Tomography and Fluorescence Imaging of Pancreatic Cancer in the Era of Neoadjuvant Therapy. Cancers. 2021;13(23):6088.

- van Manen L, Schmidt I, Inderson A, **Houvast RD**, Boonstra JJ, Dijkstra J, van Hooft JE, Nagengast WB, Robinson DJ, Vahrmeijer AL, Mieog JSD. Single fiber reflectance spectroscopy for pancreatic cancer detection during endoscopic ultrasound guided fine needle biopsy: a prospective cohort study. Int J Med Sci. 2022;19(2):205-12.
- Vuijk F, **Houvast R**, Baart V, van de Velde C, Vahrmeijer A, Hilling D, Mieog J, Slingerland M, de Geus-Oei L, Hawinkels L. Molecular Imaging of the Tumor Stroma and Beyond. The Tumor Stroma. Jenny Stanford Publishing; 2022. p. 315-57.
- Houvast RD, van Duijvenvoorde M, Chua J, Vankemmelbeke M, Durrant LG, Inderson A, van Hooft JE, Mieog JSD, Bonsing BA, Sier CFM, Crobach A, Vahrmeijer AL, Kuppen PJK. Prediction of Biomarker Expression on Primary Pancreatic Ductal Adenocarcinoma Tissues Using Fine-Needle Biopsies: Paving the Way for a Patient-Tailored Molecular Imaging Approach. Mol Diagn Ther. 2023;27(2):261-73.
- Houvast RD, Badr N, March T, de Muynck L, Sier VQ, Schomann T, Bhairosingh S, Baart VM, Peeters J, van Westen GJP, Plückthun A, Burggraaf J, Kuppen PJK, Vahrmeijer AL, Sier CFM. Preclinical evaluation of EpCAM-binding designed ankyrin repeat proteins (DARPins) as targeting moieties for bimodal near-infrared fluorescence and photoacoustic imaging of cancer. Eur J Nucl Med Mol Imaging. 2024;51(8):2179-92.
- Houvast RD, van Duijvenvoorde M, Thijse K, de Steur WO, de Geus-Oei LF, Crobach A, Burggraaf J, Vahrmeijer AL, Kuppen PJK. Selecting Targets for Molecular Imaging of Gastric Cancer: An Immunohistochemical Evaluation. Mol Diagn Ther. 2024.
- Badr N, Elshof LT, **Houvast RD**, de Muynck L, Crobach A, van Westen GJP, van Vlierberghe RLP, Mieog JSD, Vahrmeijer AL, Kuppen PJK. Evaluation of tumor targets selected from public genomic databases for imaging of pancreatic ductal adenocarcinoma. Sci Rep. 2025;15(1):17102.
- Houvast RD, Sier VQ, van Duijvenvoorde M, Baart VM, Schomann T, Chua J, Vankemmelbeke M, Durrant LG, Krijgsman D, de Heer P, Hassing GJ, Mieog JSD, Crobach A, Burggraaf J, Kuppen PJK, Vahrmeijer AL, Sier CFM. Preclinical evaluation of glycan-targeting monoclonal antibodies for bimodal near-infrared fluorescence and photoacoustic imaging of gastrointestinal cancers. EJNMMI Res. 2025;15(1):67.

218 Cancers. 2021;13(23):6088.

#### **CURRICULUM VITAE**

Ruben Douwe Houvast werd geboren op 15 december 1996 in Zwolle. Na het behalen van zijn vwo-diploma aan het Meander College in Zwolle, startte hij in 2014 met de studie Geneeskunde aan de Universiteit Leiden. Al vroeg in zijn studie raakte hij geïnteresseerd in de chirurgie en wetenschappelijk onderzoek, waarna hij als student-onderzoeker betrokken raakte bij de Green Light Leiden onderzoeksgroep. Naast zijn studie volgde hij het driejarige Practicum Musicae-programma in de richting Jazz piano aan het Koninklijk Conservatorium in Den Haag.

Na afronding van zijn wetenschapsstage startte hij in 2020 met zijn promotietraject bij de Green Light Leiden onderzoeksgroep. Onder supervisie van prof. dr. J. Burggraaf, prof. dr. A.L. Vahrmeijer en dr. P.J.K. Kuppen verrichtte hij preklinisch onderzoek naar de selectie en evaluatie van (nieuwe) moleculaire targets voor beeldvorming van gastro-intestinale tumoren, evenals de ontwikkeling en het testen van nieuwe tracers voor fluorescentie-geleide chirurgie.

In 2022 startte hij met zijn coschappen, die hij afsloot met een klinische stage op de Trauma Unit van het Tygerberg Hospital in Kaapstad, Zuid-Afrika. Tijdens zijn coschappen rondde hij ook de master Health Care Management af aan de Erasmus Universiteit Rotterdam. Zijn masterscriptie onderzocht het concept van 'Just Culture' binnen de chirurgie en de bevindingen hiervan verschenen in het Nederlands Tijdschrift voor Heelkunde.

In 2025 is hij gestart als arts-assistent (ANIOS) chirurgie in het Alrijne Ziekenhuis in Leiderdorp. Ruben woont in Amsterdam, samen met zijn vriendin Renske.

APPENDICES • Curriculum Vitae

#### DANKWOORD

Promoveren is teamwork. Dit proefschrift is dan ook tot stand gekomen door steun van en samenwerking met velen. Ik zou een aantal personen in het bijzonder willen bedanken.

Prof. dr. Burggraaf, beste Koos, bedankt voor je nauwe betrokkenheid en onmisbare hulp bij het schrijven van mijn artikelen en de afronding van mijn promotie. Jouw motiverende, pragmatische en informele begeleiding gaf mij steeds weer richting en energie.

Prof. dr. Vahrmeijer, beste Lex, jouw vermogen om te blijven innoveren en mensen te verbinden is bewonderenswaardig en werkt enorm enthousiasmerend. Heel veel dank voor je positiviteit, vertrouwen en de vele kansen die je mij hebt geboden om mijn promotie vorm te geven en af te kunnen afronden.

Dr. Kuppen, beste Peter, allereerst wil ik je bedanken voor de mogelijkheid die je mij hebt gegeven om te gaan promoveren. Ik heb je kritische blik op mijn projecten en het preklinisch onderzoek altijd erg gewaardeerd en deze heeft mij scherp gehouden. Dank voor je zeer prettige begeleiding en de vrijheid die je mij hebt gegeven om mijn projecten in te vullen.

Dr. Sier, beste Kees, toen ik als jonge student bij jou binnenkwam heb je me mee op sleeptouw genomen in de wereld van de fluorescentie-geleide chirurgie. Je wetenschappelijke drive is aanstekelijk en ik heb een hoop van je geleerd. Dank daarvoor.

Victor, Labrinus, Lizzie, Marion en Nada, mijn preklinische maten. Ik kijk met veel plezier terug op alle uren die we in het donker op de Eo hebben doorgebracht. Dank voor jullie hulp bij mijn *in vivo* experimenten. Lizzie, altijd beschikbaar aan de andere kant van de lijn om van gedachten te wisselen. Geweldig dat de Greenlight nog lang van jouw kennis en kunde gebruik gaat maken.

Uiteraard ook veel dank aan alle studenten die mij hebben geholpen, Maurice en Kira in het bijzonder. Zonder jullie harde werk had dit proefschrift er niet gelegen.

Dr. Crobach, beste Stijn, bedankt voor de tijd die je hebt genomen om mij wegwijs te maken in de pathologie. Jouw expertise bij het scoren van de kleuringen was absoluut onmisbaar.

Shadhvi, Geeske en Ronald, analisten van het Heelkunde Research Lab. Ook aan jullie veel dank voor de ondersteuning in het lab en jullie flexibiliteit bij het plannen en uitvoeren van de experimenten. Taryn, many thanks for your assistance and perseverance during the DARPin conjugations.

Greenlighters van de J3 en de bungalow, dank voor alle mooie momenten. Jullie hebben mijn promotie tot de geweldige tijd gemaakt die het was. We gaan elkaar nog veel zien. Martijn en Mats, mijn paranimfen, wat hebben we gelachen. Een betere opstelling kan ik me op deze bijzondere dag niet wensen.

Annelieke, Sophie, Meaghan, Floris, kamergenoten van de C7, en vrienden van 'De Borrelclub', Merel, Sofieke, Nynke, Daphne, en Weller in het bijzonder. Ook jullie ontzettend bedankt voor de fantastische tijd. Er zullen nog veel borrels volgen.

Boyd, Paul en Thijs, ooit vier ambitieuze broekies, inmiddels allemaal aan het werk in de kliniek. Ik vind het mooi hoe wij elkaar door de jaren heen hebben gemotiveerd om te doen waar ons hart ligt. Ik ben trots op jullie.

Clubgenoten van Panenka en huisgenoten van De Drukkerij, vrienden van het eerste uur. Dank voor de fantastische Leidse jaren en jullie oprechte interesse in mijn onderzoek. Ik kijk enorm uit naar al het moois dat we samen nog gaan meemaken.

Siem, *mien breur* en een van mijn beste maten. Wat geniet ik altijd van onze weekendwandelingen door de stad. Ik ben ontzettend trots op je. Ga zo door!

Lieve pap en mam, dit is voor jullie. Dank voor jullie onbegrensde liefde, steun en interesse. Jullie hebben mij de kans gegeven om alles te doen waar ik gelukkig van word. Wat ben ik trots op hoe jullie je leven leiden.

Lieve Renske, de laatste woorden zijn voor jou. Jouw liefde, humor, nuchterheid en relativeringsvermogen maken het leven geweldig. Dankjewel dat jij er altijd bent.

APPENDICES • Dankwoord 223

